MEMBRANE STRUCTURE AND DYNAMICS STUDIED WITH NEUTRON SCATTERING

EDITED BY: Olaf Holderer, Alexandros Koutsioumpas, Christopher Garvey and Tommy Nylander

PUBLISHED IN: Frontiers in Chemistry and Frontiers in Physics

frontiers Research Topics

ISSN 1664-8714
ISBN 978-2-88971-463-6
DOI 10.3389/978-2-88971-463-6

About Frontiers

Frontiers is more than just an open-access publisher of scholarly articles: it is a pioneering approach to the world of academia, radically improving the way scholarly research is managed. The grand vision of Frontiers is a world where all people have an equal opportunity to seek, share and generate knowledge. Frontiers provides immediate and permanent online open access to all its publications, but this alone is not enough to realize our grand goals.

Frontiers Journal Series

The Frontiers Journal Series is a multi-tier and interdisciplinary set of open-access, online journals, promising a paradigm shift from the current review, selection and dissemination processes in academic publishing. All Frontiers journals are driven by researchers for researchers; therefore, they constitute a service to the scholarly community. At the same time, the Frontiers Journal Series operates on a revolutionary invention, the tiered publishing system, initially addressing specific communities of scholars, and gradually climbing up to broader public understanding, thus serving the interests of the lay society, too.

Dedication to Quality

Each Frontiers article is a landmark of the highest quality, thanks to genuinely collaborative interactions between authors and review editors, who include some of the world's best academicians. Research must be certified by peers before entering a stream of knowledge that may eventually reach the public - and shape society; therefore, Frontiers only applies the most rigorous and unbiased reviews.
Frontiers revolutionizes research publishing by freely delivering the most outstanding research, evaluated with no bias from both the academic and social point of view. By applying the most advanced information technologies, Frontiers is catapulting scholarly publishing into a new generation.

What are Frontiers Research Topics?

Frontiers Research Topics are very popular trademarks of the Frontiers Journals Series: they are collections of at least ten articles, all centered on a particular subject. With their unique mix of varied contributions from Original Research to Review Articles, Frontiers Research Topics unify the most influential researchers, the latest key findings and historical advances in a hot research area! Find out more on how to host your own Frontiers Research Topic or contribute to one as an author by contacting the Frontiers Editorial Office: frontiersin.org/about/contact

MEMBRANE STRUCTURE AND DYNAMICS STUDIED WITH NEUTRON SCATTERING

Topic Editors:
Olaf Holderer, Helmholtz-Verband Deutscher Forschungszentren (HZ), Germany
Alexandros Koutsioumpas, Helmholtz Association of German Research Centers (HZ), Germany
Christopher Garvey, Technical University of Munich, Germany
Tommy Nylander, Lund University, Sweden

Citation: Holderer, O., Koutsioumpas, A., Garvey, C., Nylander, T., eds. (2021). Membrane Structure and Dynamics Studied With Neutron Scattering. Lausanne: Frontiers Media SA. doi: 10.3389/978-2-88971-463-6

Table of Contents

frontiers in Chemistry

EDITORIAL
published: 19 August 2021
doi: 10.3389/fchem.2021.732062

Editorial: Membrane Structure and Dynamics Studied With Neutron Scattering

O. Holderer[1]*, *A. Koutsioubas*[1], *C. J. Garvey*[2,3] and *T. Nylander*[2,4]

[1]Jülich Centre for Neutron Science (JCNS) at Heinz Maier-Leibnitz Zentrum (MLZ), Forschungszentrum Jülich GmbH, Garching, Germany, [2]Lund Institute for Advanced Neutron and X-ray Science, Lund, Sweden, [3]Heinz Maier-Leibnitz Zentrum (MLZ), Technische Universität München, Garching, Germany, [4]Department of Chemistry, Lund University, Lund, Sweden

Keywords: microemulsions, lipid membranes, bending elasticity, neutron scattering, neutron spin echo, reflectometry, small angle neutron scattering

Editorial on the Research Topic

Membrane Structure and Dynamics Studied With Neutron Scattering

Self-assembled phospholipid bilayers are ubiquitous in biology and chemistry. In biological systems they constitute membranes that act as cell barriers that mediate the exchange of compounds, energy and information with the extra-cellular environement and essentially act as a host for membrane proteins that carry out a multitude of critical taks. In modern chemistry, self-assembled surfactant or lipid membranes in dispersed lamellar or non-lamellar phases (cubic and hexagonal) or bicontinuous microemulsions are frequently used in health care or consumer products to encapsulate and deliver active substances for controlled pharmacokinetics. Thanks to their generally well defined structure and properties, and using nature as an inspiration they can also be used to formulate nano-scale reactors for sustainable synthesis.

Neutron scattering provides a unique view on nanoscopic and mesoscopic structure of self-assembled membranes, for example with Small Angle Neutron Scattering (SANS) in solution or with Neutron Reflectivity (NR) using contrast variation through deuterium labelling (**Figure 1**). Thermal membrane fluctuations are measured with Neutron Spin Echo (NSE) spectroscopy, allowing us to study how changes in environment, for example adding diblock copolymers or changing solvent properties, can influence membrane elasticity. Recent advances in instrumentation have also provided access to membrane dynamics at the solid-liquid interface with grazing incidence NSE (GINSES).

Contrast variation by deuteration in neutron scattering provides a tool to get insight into the properties of individual components in the liquid state on nanometer length scales that is not accessible through other techniques.

The collection of papers in this issue only covers a fraction of the plethora of membrane properties that can be studied with state-of-the-art neutron scattering techniques.

The interaction of ionic liquids (ILs) with cellular membranes is studied in the Article of Sharma et al. ILs as solvents with increasing importance in chemical engineering processes of various kinds are generally toxic to living organisms. The article aims therefore in a better understanding of the interaction if ILs with lipid membranes by studying the influence of ILs on the membrane fluidity and molecular motion and learning in this way how to work with or use safely ILs. Quasi elastic neutron scattering was the method of choice to get insight into the molecular dynamics at the membrane-IL-interface.

A completely different environment is studied in the contribution of LoRicco et al. with neutron diffraction. Apolar molecules stabilize the membrane of archea for survival in the most extreme conditions of high temperatures and pressures.

The interaction of lipase with microemulsion membranes has been investigated by Engelskirchen et al. in view of understanding and improving lipase catalyzed reactions. Combining structural and spectroscopic investigations were essential for getting hints on the residence time of the lipase at the surfactant membrane.

OPEN ACCESS

Edited and reviewed by:
Moyuan Cao,
Tianjin University, China

***Correspondence:**
O. Holderer
o.holderer@fz-juelich.de

Specialty section:
This article was submitted to Physical Chemistry and Chemical Physics, a section of the journal Frontiers in Chemistry

Received: *28 June 2021*
Accepted: *06 August 2021*
Published: *19 August 2021*

Citation:
Holderer O, Koutsioubas A, Garvey CJ and Nylander T (2021) Editorial: Membrane Structure and Dynamics Studied With Neutron Scattering. Front. Chem. 9:732062. doi: 10.3389/fchem.2021.732062

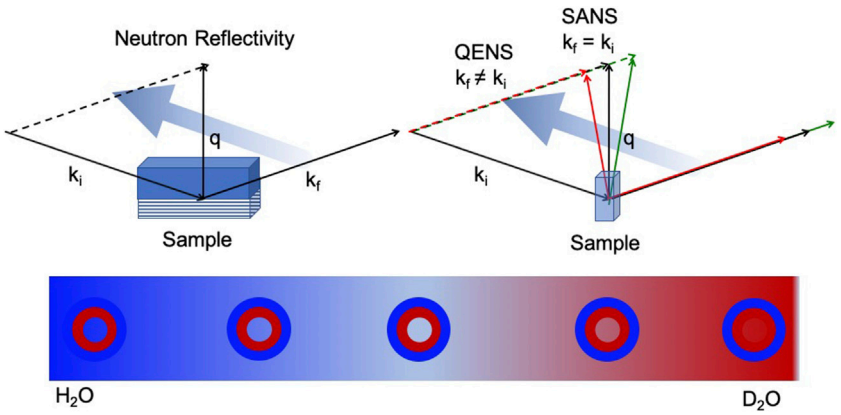

FIGURE 1 | Self assembled membranes are ubiquious in chemical systems, such as surfactant membranes, and biological systems as for example phospholipid membranes. Neutron reflectivity **(left)** and scattering **(right)** allows to study the structure and motion in a realistic environment, e.g., physiological conditions. By isotop substitution it is possible to highlight different parts of the sample under chemically quasi identical conditions **(bottom)**.

The strength of neutron scattering in soft matter and biology is the accessibility to parts of a complex sample through contrast variation. This has been used by Conn et al. to study membrane proteins, here in the bicontinuous cubic phase of phospholipid bilayers.

Thermally driven motion of membranes or incorporated proteins can be investigated with neutron spin echo (NSE) spectroscopy on nanometer and nanosecond length- and time-scales under physiologically relevant conditions. Subtleties of modern NSE experiments are discussed in the Article of Hoffmann.

An example of studies of the membrane dynamics with NSE is found in the contribution of Jaksch et al., where, in combination with reflectometry, the influence of salt on phospholipid membranes is studied.

Also plant cells contain membranes, and photosynthetic membranes are eminently important for nature and thus studied since long time. Combining different techniques such as microscopy and x-ray or neutron scattering provides an added value helping to understand nature, when the experimental results are properly modelled, as is shown in the paper of Jakubauskas et al..

Use of (partial) deuteration is a strong argument for neutron scattering techniques, which is applied for studying the interplay between high density lipoproteins (HDLs), cholesterol and the lipid membrane to help understanding the factors for deseases as Altzheimer's or atherosclerosis in the article by Waldie et al.).

Neutron diffraction on stacks of lipid multilayers allowed Luchini et al. to characterize different preparation methods, an important prerequisite for reliable data analysis, and further on the existence of different lipid phases could be proven by the diffraction data attributed to the heterogeneity of their acyl chain composition. Using natural extracts with the ability of producing deuterated lipid mixtures plays again with the power of adjustable contrast for biological samples.

Neutron reflectivity is mainly used in the contribution by Krugmann et al. in order to investigate the nanoscopic details of the role of myelin basic protein in the formation of the sheath that wraps around axons. Combination of static and kinetic measurements together with theoretical arguments provide insights concerning the myelination process.

Finally the review article by Kinnun et al. highlights the advantages of contrast variation availiable in various neutron methods for accessing structural and dynamic information about the in-plane and out-of-plane structure of a variety of biomembrane systems.

With this research topic we hope to provide a useful and interesting overview over some recent advances in membrane studies with different neutron scattering techniques and to illustrate the potential of the different techniques of diffraction, reflectivity and spectroscopy measurements which allow together with the unique contrast variation possibilities with isotope substitution a nanoscopic view into the details of artificial and natural self assembled membranes.

AUTHOR CONTRIBUTIONS

All authors listed have made a substiancial, direct and intellectual contribution to the work, and approved it for publication.

Conflict of Interest: The authors declare that the research was conducted in the absence of any commercial or financial relationships that could be construed as a potential conflict of interest.

Publisher's Note: All claims expressed in this article are solely those of the authors and do not necessarily represent those of their affiliated organizations, or those of the publisher, the editors and the reviewers. Any product that may be evaluated in this article, or claim that may be made by its manufacturer, is not guaranteed or endorsed by the publisher.

frontiers in Chemistry

ORIGINAL RESEARCH
published: 12 November 2020
doi: 10.3389/fchem.2020.594039

Apolar Polyisoprenoids Located in the Midplane of the Bilayer Regulate the Response of an Archaeal-Like Membrane to High Temperature and Pressure

Josephine G. LoRicco[1], *Marta Salvador-Castell*[1†], *Bruno Demé*[2], *Judith Peters*[2,3*] *and Philippe M. Oger*[1*]

[1] Univ Lyon, INSA de Lyon, CNRS, MAP UMR 5240, Villeurbanne, France, [2] Department of Large Scale Structures, Institut Laue-Langevin, Grenoble, France, [3] Department of Spectroscopy, Université Grenoble Alpes, LiPhy, Grenoble, France

Archaea are known to inhabit some of the most extreme environments on Earth. The ability of archaea possessing membrane bilayers to adapt to high temperature (>85°C) and high pressure (>1,000 bar) environments is proposed to be due to the presence of apolar polyisoprenoids at the midplane of the bilayer. In this work, we study the response of this novel membrane architecture to both high temperature and high hydrostatic pressure using neutron diffraction. A mixture of two diether, phytanyl chain lipids (DoPhPC and DoPhPE) and squalane was used to model this novel architecture. Diffraction data indicate that at high temperatures a stable coexistence of fluid lamellar phases exists within the membrane and that stable coexistence of these phases is also possible at high pressure. Increasing the amount of squalane in the membrane regulates the phase separation with respect to both temperature and pressure, and also leads to an increase in the lamellar repeat spacing. The ability of squalane to regulate the ultrastructure of an archaea-like membrane at high pressure and temperature supports the hypothesis that archaea can use apolar lipids as an adaptive mechanism to extreme conditions.

Keywords: archaea, archaeal lipids, high pressure, phase coexistence, membrane architecture, adaptation, membrane

OPEN ACCESS

Edited by:
Olaf Holderer,
Helmholtz Association of German Research Centers (HZ), Germany

Reviewed by:
Arkaprabha Konar,
Kent State University, United States
Maikel Rheinstadter,
McMaster University, Canada

****Correspondence:***
Judith Peters
jpeters@ill.fr
Philippe M. Oger
philippe.oger@insa-lyon.fr

†Present address:
Marta Salvador-Castell,
University of California, San Diego, La Jolla, CA, United States

Specialty section:
This article was submitted to Physical Chemistry and Chemical Physics, a section of the journal Frontiers in Chemistry

Received: *12 August 2020*
Accepted: *13 October 2020*
Published: *12 November 2020*

Citation:
LoRicco JG, Salvador-Castell M, Demé B, Peters J and Oger PM (2020) Apolar Polyisoprenoids Located in the Midplane of the Bilayer Regulate the Response of an Archaeal-Like Membrane to High Temperature and Pressure. Front. Chem. 8:594039. doi: 10.3389/fchem.2020.594039

INTRODUCTION

According to the Singer-Nicolson model, cell membranes are composed of a "mosaic" of proteins embedded in a fluid, lipid bilayer (Singer and Nicolson, 1972). Our understanding of cell membranes has developed further since then, for example we now recognize the importance of other lipid phases in addition to the fluid lamellar phase (bilayer phase), and that there can be substantial lateral heterogeneity within the membrane (Goñi, 2014). Membrane structural lipids, typically phospholipids, are diverse and display varied properties owing to the differences in both the lipid polar head groups and the hydrophobic tails. In aqueous solution, these lipids, driven by the hydrophobic effect, self-assemble into structures in which the hydrophilic heads can interact with the solution and the hydrophobic tails are excluded. The most biologically common phases, seen in familiar lipid bilayer structures, are lamellar phases in which the lipids assemble into flat

sheets (zero membrane curvature) (Cullis et al., 1991; Perutková et al., 2009; Frolov et al., 2011; Goñi, 2014). However, the ability of membrane to form phases with non-zero curvature, such as cubic or inverted hexagonal phases, is also important and plays a role in many cellular processes such as membrane fission and fusion (Jouhet, 2013; McMahon and Boucrot, 2015; Jarsch et al., 2016). Membrane lipids can prefer different membrane curvatures based on their shape, and this preferred curvature can vary with environmental conditions such as pressure and temperature. The presence of diverse lipids within a membrane can even promote phase separation and domain formation within the membrane (Jouhet, 2013). Domains are laterally organized membrane regions with distinct lipid compositions and specialized functions such as interacting with specific proteins, or adopting a specific curvature (Tayebi et al., 2012; Arumugam and Bassereau, 2015; Marquardt et al., 2015). Such lateral membrane domains have been well-characterized in eukaryotic and bacterial cells (Baumgart et al., 2003; Heberle and Feigenson, 2011; Heberle et al., 2013; McCarthy et al., 2015; Schmid, 2017).

Life has been found at some of the most extreme conditions on Earth such as temperatures above 100°C and pressures up to 120 MPa (Yayanos et al., 1981; Takai et al., 2008; Zeng et al., 2009; Dalmasso et al., 2016; Siliakus et al., 2017). All aspects of these organisms must be specially adapted to tolerate such conditions. Cell membranes, in particular, are highly sensitive to pressure and temperature (Winter and Jeworrek, 2009; Oger and Jebbar, 2010; Brooks and Seddon, 2014). In order to maintain functionality of the membrane under extreme conditions cells adjust the composition of their membranes to cope with environmental changes, in a process known as homeoviscous adaptation (Sinensky, 1974). High temperature tends to increase membrane fluidity, permeability, and promote more negative membrane curvature whereas increasing pressure tends to have the opposite effects (Brooks, 2014). To compensate, bacteria and eukaryotes are known to regulate the length, saturation, and branching of the hydrophobic chains as well as the proportion of different polar headgroups (Jebbar et al., 2015; Siliakus et al., 2017). In archaea the mechanisms of adaptation are less well-understood, in part due to their unique membrane lipids. Archaeal lipids have methyl-branched phytanyl chains rather than straight chain fatty acids which are linked via ether rather than ester bonds to the glycerol backbone (De Rosa et al., 1986; Gambacorta et al., 1995). These lipids have higher temperature stability, and lowered proton permeability (Gliozzi et al., 1983; Yamauchi et al., 1993) compared with typical bacterial/eukaryotic lipids.

In addition to bilayer forming lipids, archaea are known to produce bipolar, tetra-ether lipids capable of forming lipid monolayers with high stability and low permeability (De Rosa et al., 1983; Elferink et al., 1994). Archaea have been shown to increase the quantity of tetra-ether lipids in the membrane in response to temperature (Matsuno et al., 2009; Cario et al., 2015). Even some bacteria have shown to produce membrane spanning tetraether or tetraester lipids in response to high-temperature conditions (Damsté et al., 2007; Schouten et al., 2007; Siliakus et al., 2017). Despite the link to high temperature adaption, tetra-ether lipids are not found solely in thermophiles but have also been observed in mesophilic archaea. In addition, not all organisms living at high temperatures produce large quantities, if any tetra-ether lipids (Tornabene and Langworthy, 1979; Hafenbradl et al., 1996; Sako et al., 1996; Sprott et al., 1997; Siliakus et al., 2017). Some insight into the ability of archaea with bilayer forming lipids to live at temperatures up to 100°C can be found in the study by Cario et al. (2015) on the piezo-hyperthermophilic archaeon, *Thermococcus barophilus*. The quantity and saturation of isoprenoid derivatives (such as lycopane, squalane) were shown to vary in response to temperature and pressure. In order to explain the ability of *T. barophilus* to live at high temperature in presence of bilayer forming lipids, it was hypothesized that apolar lipids sit at the midplane of the bilayer and provide enhanced stability (Cario et al., 2015). The ability of apolar lipids such as squalane to localize to the midplane of the lipid bilayer has been confirmed in model membranes of both bacterial-like and archaea-like lipids (Hauß et al., 2002; Salvador-Castell et al., 2020b). The presence of apolar molecules is capable of modulating membrane physicochemical properties, for example, the presence of squalane at the bilayer midplane has been shown to increase permeability to water and decrease proton permeability (Haines, 2001). Apolar molecules at the midplane have been shown to increase the tendency toward negative membrane curvature by reducing packing frustration (Salvador-Castell et al., 2020a,b) and to play a role in phase separation and domain formation (Gilmore et al., 2013; Salvador-Castell et al., 2020b). Such isoprenoid hydrocarbons are found in all archaea (Langworthy et al., 1982) suggesting this hypothesis could be extended to explain adaptation to high temperature and pressure in other archaea processing lipid bilayers.

In this work we studied the behavior of an archaeal-like bilayer with the proposed novel architecture composed of 1,2-di-O-phytanyl-*sn*-glycero-3-phosphocholine (DoPhPC) and 1,2-di-O-phytanyl-*sn*-glycero-3-phosphoethanolamine (DoPhPE) and 2,6,10,15,19,23-hexamethyltetracosane (squalane) under high temperature and high pressure conditions, mimicking the extreme conditions in which some archaea live. Using neutron diffraction, we are able to see the localization of squalane in the midplane bilayer, and to detect the presence of coexisting lamellar phases within the membrane. The structure of each phase as well as the phase coexistence were shown to vary in response to temperature and pressure. The response of the membrane ultrastructure to temperature and pressure could be modulated by varying the quantity of the apolar lipid squalane present in the membrane.

MATERIALS AND METHODS

Chemicals

1,2-di-O-phytanyl-*sn*-glycero-3-phosphocholine (DoPhPC) and 1,2-di-O-phytanyl-*sn*-glycero-3-phosphoethanolamine (DoPhPE) were both purchased from Avanti Polar Lipids (Alabaster, USA) in the lyophilized form and utilized without further purification. The isoprenoid used, 2,6,10,15,19,23-hexamethyltetracosane (squalane) was bought from Sigma—Aldrich Co (Montana, USA) in its hydrogenated

form and from CDN Isotopes (Pointe-Claire, Canada), in its deuterated form.

Sample Preparation

Three milligram of DoPhPC:DoPhPE (9:1 molar) and the corresponding amount of either hydrogenated squalane (h-squalane) or deuterated squalane (d-squalane) were dissolved in chloroform:methanol (2:1) and were spread on a silicon wafer using the "rock and roll" method (Tristram-Nagle, 2007) and dried overnight under high vacuum. Next, the sample was hermetically sealed inside an aluminum sample holder containing a 1:1 ratio of H_2O:D_2O (50% D_2O). The sample was left at 50°C for 48 h to allow for complete hydration.

Neutron Diffraction

Neutron diffraction experiments were performed on D16 (Cristiglio et al., 2015) at the Institut Laue-Langevin (Grenoble, France). The incident wavelength was 4.52 Å. The accessible q-range was from 0.06 $Å^{-1}$ to 0.51 $Å^{-1}$. The H_2O/D_2O contrast was 50% D_2O. 50% D_2O was previously found to give both strong diffraction signal and good resolution between the first order peaks of the two lamellar phases. The temperature was carefully controlled by placing the sample holder in a cryostat. Samples were either measured in a high temperature (HT) sample holder or in a HT-high hydrostatic pressure (HHP) cell (Peters et al., 2018). Data obtained at ILL are identified by Salvador-Castell et al. (2019).

Data treatment was performed by LAMP (Richard et al., 1996) and Origin Pro (Version 2019, OriginLab Corperation, Northampton, MA, USA). The integrated intensities of the Bragg peaks were corrected according to the absorption and analyzed by a Gaussian function, as done previously (Salvador-Castell et al., 2020c). The angle (θ) of a Bragg peak is related to the scattering vector (q) by:

$$q = \frac{4\pi \sin(\theta)}{\lambda} \tag{1}$$

where λ is the wavelength. In cases where many orders of diffraction were visible, a linear fit of the form y = a + bx was performed on a plot of peak location (q) vs. diffraction order (h). The slope of the line (Δq) was used to determine the d-spacing using the following equation:

$$d = \frac{2\pi}{\Delta q} \tag{2}$$

In cases where only a single Bragg order was visible, the d-spacing was calculated using the first order peak and corrected based on the y-intercept determined for each sample under conditions where multiple peaks were present.

To locate squalane in the membrane we used the method described in Hauß et al. (2002, 2005) taking advantage of difference scattering density between hydrogen and deuterium. Neutron scattering length density (NSLD) profiles are constructed from the sum of the neutron scattering lengths per unit volume (Marquardt et al., 2015). The NSLD profiles were calculated from a discrete set of Fourier coefficients (F_h) using the following equation (Katsaras, 1995):

$$\rho(z) = \frac{2}{d}\sum_{h=1}^{h_{max}} |F_h|\, \nu_n cos\left(\frac{2h\pi}{d} z\right) \tag{3}$$

where d is the lamellar spacing of the bilayer in the z direction, $z \in \left[\frac{-d}{2}, \frac{d}{2}\right]$, $|F_h| = \pm\sqrt{I_h Q_z}$, Q_z is the Lorentz correction factor equal to q for oriented bilayers, I_h is the integrated intensity of the hth Bragg peak and ν_n is the phase of the structure factor. The assigned phases of structure factors 1 to 4 (–, +, +, –) were based on those previously determined for this [DoPhPC:DoPhPE(9:1) + squalane] (Salvador-Castell et al., 2020a).

RESULTS AND DISCUSSION

Stable Phases Coexist Within Archaeal-Like Membrane at High Temperature and Pressure

Cario et al. (2015) proposed a novel membrane architecture to explain the stability of archaea lipid bilayers under high pressure and temperatures. In this novel membrane architecture, apolar lipids act as structural lipids, sitting at the midplane of the lipid bilayer and leading to enhanced membrane stability under extreme conditions (Oger and Cario, 2013; Cario et al., 2015; Salvador-Castell et al., 2020a). A synthetic archaeal-like membrane composed of a mixture of diphytanyl lipids (DoPhPC and DoPhPE in a 9 to 1 molar ratio) and the apolar lipid squalane was used to model this novel architecture. The chemical structures of these lipids are shown in **Supplementary Figure 1**. In order to probe how this membrane behaves under the extreme conditions of temperature and pressure faced by archaea, neutron diffraction was performed on oriented stacked bilayers at temperatures up to 85°C and pressures up to 1,000 bar. Experiments were performed with both hydrogenated squalane (h-squalane) and deuterated squalane (d-squalane) in order to take advantage of the differential neutron scattering between hydrogen and deuterium (Hauß et al., 2002, 2005). The neutron scattering length density (NSLD) for membranes containing h-squalane and d-squalane was plotted as a function of distance (**Supplementary Figure 2**). For convenience, 0 Å represents the midplane of the bilayer. These plots exhibit two characteristic maxima corresponding to the glycerol backbone and a minimal intensity near the terminal methyl groups. The spectra for the membrane containing h-squalane and d-squalane overlap fairly well except within the region corresponding to the midplane of the bilayer (−10 to 10 Å) where the sample containing d-squalane shows an excess of scattering density. This indicates that squalane is located in the midplane of the bilayer and is in agreement with the findings of Salvador-Castell et al. (2020b). In this work we see that this localization of squalane is seen in both $Phase_{LT}$ and $Phase_{HT}$ at low (20 bar) and high (1,000 bar) pressure.

The stacked multilayers were sufficiently ordered in the membrane to give rise to Bragg peaks in the diffraction data. **Figure 1A** shows the 1D neutron diffraction profiles for a membrane composed of DoPhPC:DoPhPE (9:1) + 5 mol% h-squalane at 20 bar (black spectra). The temperature increased

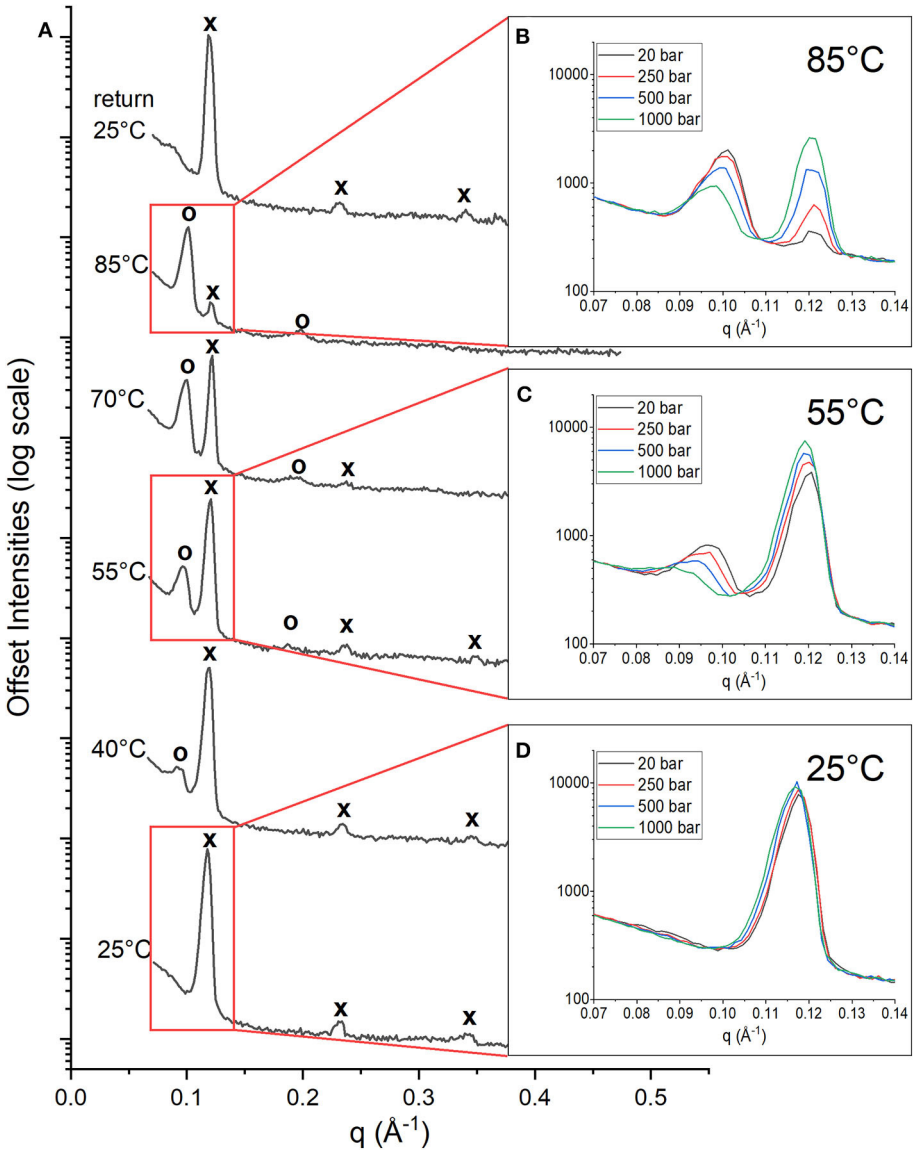

FIGURE 1 | 1D Neutron diffractograms of DoPhPC:DoPhPE (9:1) + 5 mol% h-squalane membrane. **(A)** Diffractograms at 20 bar and temperatures increasing from 25 to 85°C and after returning to 25°C. Diffraction peaks corresponding to $Phase_{LT}$ are denoted with an "x" and peaks corresponding to $Phase_{HT}$ are denoted with an "o." First order diffraction peaks at 85°C **(B)**, 55°C **(C)**, and 25°C **(D)** measured at 20 bar (black), 250 bar (red), 500 bar (blue), and 1,000 bar (green).

from 25°C (bottom) to 85°C (top). At 25°C, there were three orders of diffraction for the sample at low pressure (20 bar). The first order diffraction peak was located at q = ∼0.12 $Å^{-1}$, the second order peak at q = ∼0.23 $Å^{-1}$, and the third order peak at q = ∼0.34 $Å^{-1}$. The location of peaks in the ratio of (1, 2, 3...) indicates a lamellar phase (Tyler et al., 2015). As the temperature increased, the peaks corresponding to the original phase were still present at similar values of q (marked with an "x"), although with diminished intensities. At higher temperatures (above 40°C) a second set of peaks appeared at lower values of q corresponding to a new phase (marked with an "o"). The first order diffraction peak of this new phase is located at q = ∼0.09 $Å^{-1}$ and the second order diffraction peak at q = ∼0.18 $Å^{-1}$. The spacing of the peaks indicates that this new phase is also lamellar. We will refer to the new phase as $Phase_{HT}$ because it appeared at high temperatures (HT) compared to the original phase, which is also present at low temperatures (LT) and will therefore be referred to as $Phase_{LT}$. Increasing temperature leads to an increase in the intensity of the $Phase_{HT}$ peaks indicating that temperature stabilizes $Phase_{HT}$, and leads to a decrease in the intensity of $Phase_{LT}$ indicating that temperature destabilizes $Phase_{LT}$. Upon returning the membrane to 25°C and 20 bar, the initial state, is restored indicating that this change in phase is fully reversible (**Figure 1A**).

At each temperature, the diffraction of the DoPhPC:DoPhPE (9:1) + 5 mol% h-squalane membrane was measured at 20, 250, 500, and 1,000 bar. The **Figure 1** insets show the first order

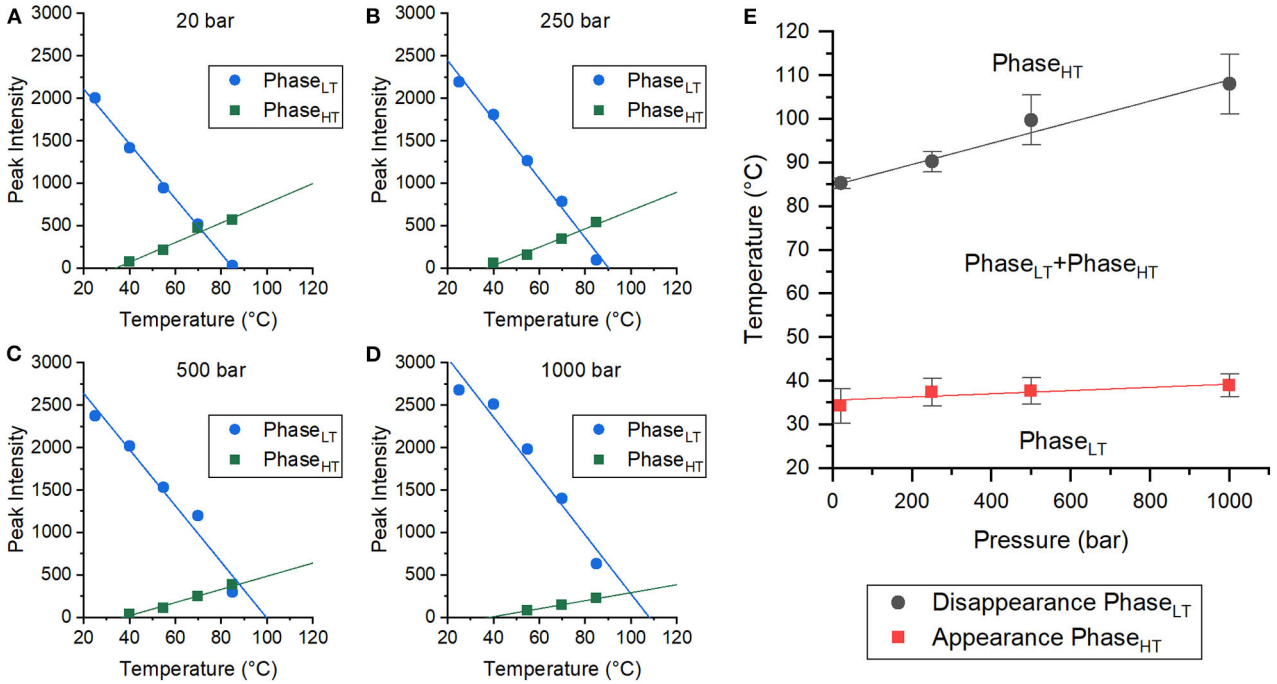

FIGURE 2 | Coexistence of phases in DoPhPC:DoPhPE (9:1) membrane containing 5 mol% h-squalane. **(A–D)** Plots of peak intensities of Phase$_{LT}$ (blue circles) and Phase$_{HT}$ (green squares) as a function of temperature. Pressures were 20 bar **(A)**, 250 bar **(B)**, 500 bar **(C)**, and 1,000 bar **(D)**. Error bars are within symbols. **(E)** Pressure-Temperature diagram of the coexistence of Phase$_{LT}$ and Phase$_{HT}$. Error bars indicate standard errors.

diffraction peaks, indicated by the red boxes, seen at pressures of 20 bar (black), 250 bar (red), 500 bar (blue) and 1,000 bar (green). At 85 and 55°C, two first order diffraction peaks are seen, representing the two phases. The area of the Phase$_{HT}$ peak (found at lower q) decreases and the area of the Phase$_{LT}$ peak (found at higher q) increases as a function of pressure (**Figures 1B,C**). This indicates that high pressure has a stabilizing effect on Phase$_{LT}$ and a destabilizing effect on Phase$_{HT}$. Although it is well-established that increasing pressure causes an effect similar to decreasing the temperature, our results show that even 1,000 bar is not enough to completely replace Phase$_{HT}$ and return to the lipid organization present at lower temperatures. At 25°C, the membrane is exclusively in Phase$_{LT}$. Again, there is a slight increase in the intensity of the Phase$_{LT}$ peak with pressure indicating that pressure stabilizes Phase$_{LT}$ (**Figure 1D**).

Both pressure and temperature play an important role in the stability of each phase and their ability to coexist. In order to better quantify the temperature and pressure range at which these phases coexist, the change in the integrated peak intensities was monitored as a function of temperature at each pressure (20, 250, 500, and 1,000 bar). The changes in the peak intensities of the first order peaks of both Phase$_{LT}$ and Phase$_{HT}$ have a linear dependence on temperature (**Figures 2A–D**, **Supplementary Figure 3**). A linear fit could be used to extrapolate/interpolate when the peak intensity would be zero and thus to determine the temperature at which the corresponding phase was no longer present in the membrane for each pressure, as shown in **Figure 2**.

The integrated peak intensities of Phase$_{LT}$ (blue) and Phase$_{HT}$ (green) at 20 bar were analyzed as a function of temperature (**Figure 2A**). A linear fit of the integrated Phase$_{HT}$ peak intensities determined that the peak intensity would equal zero at 34.3 ± 3.9°C, signifying that Phase$_{HT}$ appears above this temperature. Below this temperature, the membrane is exclusively in Phase$_{LT}$. A linear fit of the Phase$_{LT}$ peak intensities determined that the peak intensity would reach zero at 85.3 ± 1.2°C. Above this temperature, Phase$_{LT}$ would disappear and the membrane would be entirely in Phase$_{HT}$. Between these two temperatures, both phases coexist. This analysis was repeated with the data taken at 250, 500, and 1,000 bar (**Figures 2B–D**), allowing the determination of a pressure-temperature diagram of the phase coexistence of Phase$_{LT}$ and Phase$_{HT}$ (**Figure 2E**). The temperature at which Phase$_{HT}$ appears (T_{HT}) increased with increasing pressure from 34.3 ± 3.9°C at 20 bar to 37.4 ± 3.2°C at 250 bar, 37.7 ± 3.0°C at 500 bar, and to 38.9 ± 2.6°C at 1,000 bar. The increase in T_{HT} with pressure was small (∼5°C/kbar) and was not statistically significant. The temperature at which Phase$_{LT}$ disappeared (T_{LT}) also increased with increasing pressure from 85.3 ± 1.2°C at 20 bar, to 90.2 ± 2.3°C at 250 bar, 99.7 ± 5.7°C at 500 bar, and finally to 108.0 ± 6.9°C at 1,000 bar. The increase in T_{LT} as a function of pressure was much larger (∼24°C/kbar) (**Figure 2E**). Here we demonstrate that although the phases are pressure sensitive, phase coexistence is possible at pressures up to, and presumably above, 1,000 bar. Based on the phase diagram, at high temperatures (> 85°C), the application of pressure

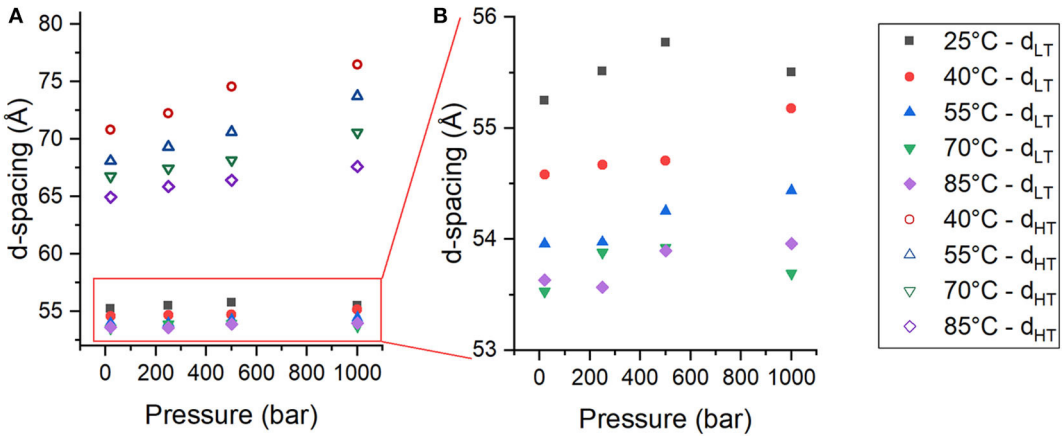

FIGURE 3 | (A,B) Membrane d-spacing as a function of pressure for $Phase_{LT}$ (solid symbols) and $Phase_{HT}$ (open symbols) in DoPhPC:DoPhPE (9:1) membrane containing 5 mol% h-squalane. Temperature was 25°C (black squares), 40°C (red circles), 55°C (blue triangles), 70°C (green inverted triangles), or 85°C (purple diamonds). Error for d-spacing measurements is ± 0.5 Å.

is predicted to induce phase separation from solely $Phase_{HT}$ at low pressure to a coexistence of $Phase_{HT}$ and $Phase_{LT}$ at high pressure and high temperature. Pressure induced phase separation is not a novel concept, as high pressure has been previously shown to be capable of inducing phase separation and domain formation (McCarthy et al., 2015). Our results suggest that this is also possible in membranes composed of archaeal lipids. It should be noted that the T_{HT} and T_{LT} reported here were calculated only as the sample being heated, and that the transition temperature upon cooling was not explicitly tracked. Membranes are known to exhibit hysteresis near phase transitions meaning that the transition temperatures upon heating and cooling are different. A similar effect has also been seen in membranes upon pressurization/depressurization (Trovaslet-Leroy et al., 2016).

From the changes in peak intensity, it could be determined that pressure destabilizes $Phase_{HT}$ and stabilizes $Phase_{LT}$. In addition to changes in the integrated intensities of the peaks, there were also changes in the location of the peaks with pressure that reflect changes in the lamellar repeat structure. The multilayer organization of the membranes makes it simple to determine the repeat spacing (d), which includes the thickness of the bilayer and its associated water layer (Nagle and Tristram-Nagle, 2000), from the location of the Bragg peaks of each phase. For a lamellar phase, the repeat spacing (d) can be calculated simply by Equation (3), where q is the location of the first order lamellar peak. The d-spacing of both $Phase_{LT}$ (solid symbols) and $Phase_{HT}$ (open symbols) increase as a function of pressure (**Figure 3A**). The d-spacing of $Phase_{LT}$ with increasing pressure is shown again in **Figure 3B** using a different scale to better visualize the changes. $Phase_{LT}$ exhibits either a small increase or negligible change in d-spacing with increasing pressure. Linear fitting of the data determined that the d-spacing of $Phase_{LT}$ increases at a rate of 0.23 ± 0.32 Å/kbar at 25°C, 0.61 ± 0.13 Å/kbar at 40°C, 0.53 ± 0.11 at 55°C, 0.09 ± 0.30 at 70°C and 0.40 ± 0.16 at 85°C. An increase in membrane d-spacing with pressure has been observed previously (Winter and Jeworrek, 2009; Trapp et al., 2013; Brooks and Seddon, 2014). Increasing pressure provokes a lateral compression of membrane lipids and an increase in membrane thickness due to extension of the hydrocarbon chains. The d-spacing of $Phase_{HT}$ also increases with pressure (**Figure 3A**). The d-spacing increased at a rate of 5.84 ± 0.81 Å/kbar at 40°C, 5.78 ± 0.19 Å/kbar at 55°C, 3.91 ± 0.36 Å/kbar at 70°C, and 2.62 ± 0.22 Å/kbar at 85°C. The changes in d-spacing for $Phase_{HT}$ were almost an order of magnitude greater than that seen in $Phase_{LT}$ showing that $Phase_{HT}$ is much more sensitive to changes in pressure. It is interesting to note that the swelling of $Phase_{HT}$ decreases with temperature.

The formation of a new phase, $Phase_{HT}$, is most likely due to the presence of lipids with different preferred curvatures within the membrane as seen by Salvador-Castell et al. (2020b). The bilayer is made up of two phytanyl lipids with different polar head groups (DoPhPC and DoPhPE) and the apolar isoprenoid squalane. The phosphoethanolamine (PE) headgroup is small, so the lipid has a conical geometry and favors a negative curvature (favoring the formation of non-lamellar structure such as inverted hexagonal phases/cubic phases/inverted micelles). The phosphocholine (PC) headgroup is larger and the lipid has a cylindrical geometry which favors zero-curvature (favoring the formation of lamellar structures such as bilayers). The PC headgroup can stabilize the lamellar phase of PE lipids (Kates and Manson, 1984). The phase separation can be explained by partitioning of DoPhPC and DoPhPE into different phases based on preferred curvature which can be triggered, for example, by temperature which favors more negative membrane curvatures. The presence of squalane also promotes negative lipid curvature and was found to forward the formation of non-lamellar phases in a DoPhPC:DoPhPE (9:1) membrane (Salvador-Castell et al., 2020a,b). Increasing pressure, on the other hand, tends to increase the preferred membrane curvature (Shearman et al., 2006; Brooks, 2014). In our model membrane, phase separation was triggered by increasing temperature, which could be due to the differences in curvature between the lipids becoming

TABLE 1 | Membrane d-spacing for $Phase_{LT}$ (left table) and $Phase_{HT}$ (right table) for DoPhPC:DoPhPE (9:1) membrane containing h-squalane.

$Phase_{LT}$	+2.5% squalane	+5% squalane	+10% squalane	$Phase_{HT}$	+2.5% squalane	+5% squalane	+10% squalane
25°C 20 bar	55.6 Å	55.2 Å	56.0 Å	25°C 20 bar	N.P.	N.P.	82.3 Å
25°C 250 bar	56.2 Å	55.5 Å	57.0 Å	25°C 250 bar	N.P.	N.P.	86.7 Å
25°C 500 bar	56.1 Å	55.8 Å	57.1 Å	25°C 500 bar	N.P.	N.P.	88.9 Å
25°C 1,000 bar	56.2 Å	55.5 Å	57.2 Å	25°C 1000bar	N.P.	N.P.	90.6 Å
40°C 20 bar	55.2 Å	54.6 Å	55.7 Å	40°C 20 bar	N.P.	70.8 Å	78.6 Å
40°C 250 bar	55.2 Å	54.7 Å	55.8 Å	40°C 250 bar	N.P.	72.2 Å	79.8 Å
40°C 500 bar	55.0 Å	54.7 Å	56.0 Å	40°C 500 bar	N.P.	74.6 Å	82.6 Å
40°C 1,000 bar	55.6 Å	55.2 Å	56.4 Å	40°C 1,000 bar	N.P.	76.5 Å	83.6 Å
55°C 20 bar	54.1 Å	54.0 Å	55.3 Å	55°C 20 bar	67.1 Å	68.1 Å	74.7 Å
55°C 250 bar	54.8 Å	54.0 Å	55.7 Å	55°C 250 bar	68.5 Å	69.3 Å	75.9 Å
55°C 500 bar	55.2 Å	54.3 Å	55.3 Å	55°C 500 bar	69.4 Å	70.6 Å	77.3 Å
55°C 1,000 bar	55.2 Å	54.4 Å	56.1 Å	55°C 1,000 bar	72.2 Å	73.7 Å	80.0 Å
70°C 20 bar	53.8 Å	53.5 Å	54.4 Å	70°C 20 bar	65.7 Å	66.8 Å	72.4 Å
70°C 250 bar	54.0 Å	53.9 Å	55.3 Å	70°C 250 bar	65.7 Å	67.5 Å	74.3 Å
70°C 500 bar	54.2 Å	53.9 Å	55.2 Å	70°C 500 bar	67.7 Å	68.2 Å	74.1 Å
70°C 1,000 bar	54.8 Å	53.7 Å	55.2 Å	70°C 1,000 bar	70.1 Å	70.6 Å	75.3 Å
85°C 20 bar	53.5 Å	53.6 Å	N.P.	85°C 20 bar	64.9 Å	65.0 Å	74.1 Å
85°C 250 bar	53.5 Å	53.6 Å	54.3 Å	85°C 250 bar	65.4 Å	65.9 Å	75.4 Å
85°C 500 bar	53.6 Å	53.9 Å	54.5 Å	85°C 500 bar	65.9 Å	66.4 Å	74.8 Å
85°C 1,000 bar	53.7 Å	54.0 Å	54.8 Å	85°C 1,000 bar	67.3 Å	67.6 Å	76.3 Å

N.P., not present. Error is ± 0.5 Å.

too great to remain within the same phase. Increasing pressure hinders the phase separation and favors $Phase_{LT}$, lending further support to the idea that the phase separation is driven by components of different curvature.

Increasing negative curvature favors a transition from a lamellar phase to a non-lamellar phase. Although no such phases were seen by neutron diffraction, non-lamellar phases in this membrane system have been detected by SAXS (Salvador-Castell et al., 2020a). Neutron scattering was performed on multi-stacks of bilayers on a silicon wafer, whereas for the SAXS the sample was not ordered on a substrate but rather was self-assembled in bulk. These differences in lipid preparation may explain why in one case the DoPhPC:DoPhPE (9:1) + 5 mol% squalane membrane separates into two lamellar phases and in the other case the membrane separates into a lamellar phase and an inverted hexagonal phase. The ordering of the lipids on a solid support for neutron diffraction may impede the formation of non-lamellar phases. For both phases seen by neutron diffraction, increasing pressure leads to an increase in the membrane d-spacing, however, the magnitude of the pressure-induced swelling was significantly different between the phases. The changes in $Phase_{LT}$ are small, generally within the error of the measurements for the d-spacing. The changes in $Phase_{HT}$ are quite large (2–6 Å/kbar). The pressure-induced swelling of the $Phase_{HT}$ seen by neutron diffraction is unusually large for a lamellar phase which is typically <2 Å/kbar (Brooks, 2014). Interestingly, the magnitude of the pressure-induced swelling seen in $Phase_{HT}$ is similar to that seen in the inverted hexagonal phase seen by SAXS (Salvador-Castell et al., 2020a). **Supplementary Figure 4** illustrates how the membrane lattice parameter (equal to d for lamellar phase and 2/3 d for inverted hexagonal phase) increases as a function of pressure. The similarities in the response to pressure of $Phase_{HT}$ and the inverted hexagonal phase seen in SAXS could be due to the partitioning of lipid headgroups and squalane in a similar manner.

Squalane Regulates Membrane Ultrastructure Under High Temperature and Pressure

Archaea are thought to regulate their membranes response to extreme conditions with apolar lipids. For this reason, the neutron diffraction experiments were repeated with two additional concentrations of hydrogenated squalane, 2.5 and 10 mol% in order to determine what effect the amount of squalane would have on the membrane structure at high temperatures and pressures. Two coexisting phases are also present in membranes containing 2.5 or 10 mol% squalane at elevated temperatures (**Supplementary Figures 5, 6**).

The repeat spacing of $Phase_{LT}$ and $Phase_{HT}$ was calculated for the membranes containing 2.5, 5, and 10 mol% squalane and the values are displayed in **Table 1**. In all membranes, there is an increase in the membrane d-spacing with increasing pressure, and $Phase_{HT}$ is again found to be the more pressure-sensitive phase (**Figure 4**). The pressure induced swelling of $Phase_{LT}$ remains small (≤1Å/kbar) for all squalane concentrations and is not significantly different with changes in temperature. The pressure induced swelling of $Phase_{HT}$ is much larger (2–8 Å/kbar) and the swelling of $Phase_{HT}$ is temperature dependent.

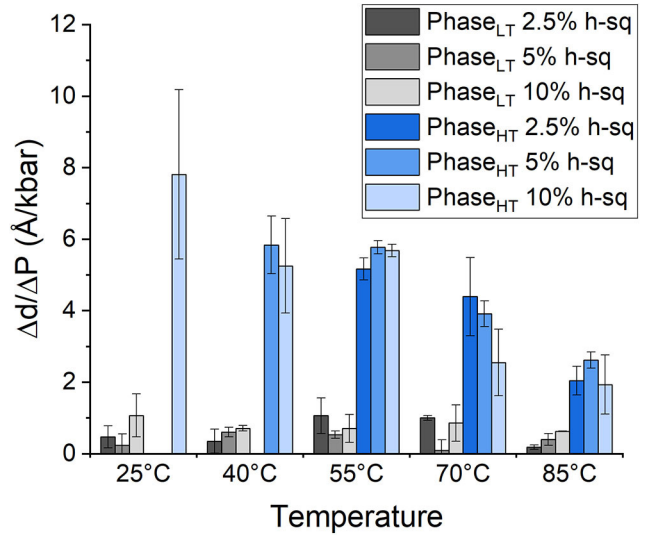

FIGURE 4 | Pressure induced swelling of DoPhPC:DoPhPE (9:1) membrane containing different quantities of h-squalane. Swelling of $Phase_{LT}$ containing 2.5 mol% (dark gray), 5 mol% (gray), or 10 mol% (light gray) h-squalane. Swelling of $Phase_{HT}$ containing 2.5 mol% (dark blue), 5 mol% (blue), or 10 mol% (light blue) h-squalane.

TABLE 2 | Temperature at which $Phase_{HT}$ appears in DoPhPC:DoPhPE (9:1) membrane containing h-squalane.

Pressure	2.5% squalane	5% squalane	10% squalane
20 bar	44.7 ± 4.0°C	34.3 ± 3.9°C	23.9 ± 3.4°C
250 bar	49.3 ± 1.5°C	37.4 ± 3.2°C	28.8 ± 3.3°C
500 bar	49.2 ± 0.1°C	37.7 ± 3.0°C	31.8 ± 1.6°C
1,000 bar	50.8 ± 1.2°C	38.9 ± 2.6°C	32.2 ± 2.6°C

The swelling is significantly larger at low temperatures and smaller at high temperatures. Although the percentage of squalane does not change the swelling of $Phase_{HT}$, the amount of squalane does play an important role in affecting the temperature range at which $Phase_{HT}$ is present. At ≥55°C, $Phase_{HT}$ is seen in membranes containing 2.5, 5, and 10 mol% squalane. At 40°C, $Phase_{HT}$ is no longer capable of forming the membrane containing 2.5 mol% squalane and at 25°C, $Phase_{HT}$ is only seen in the membrane containing 10 mol% squalane.

The temperatures at which $Phase_{HT}$ appears for a membrane containing either 2.5 or 10 mol% squalane are determined from a linear fit of integrated peak intensity vs. temperature (**Supplementary Figure 3**). As seen previously with the membrane containing 5 mol% squalane, pressure leads to an increase in T_{HT} and T_{LT} (**Supplementary Figure 7**). Increasing the quantity of squalane promotes the formation of $Phase_{HT}$ at lower temperatures. For example, at 20 bar $Phase_{HT}$ appears at 44.7 ± 4.0°C for the membrane containing 2.5 mol% squalane, 34.3 ± 3.9°C for the membrane containing 5 mol% squalane and 23.9 ± 3.4°C for the membrane containing 10 mol% squalane. The concentration of squalane has a similar effect on T_{HT} at elevated pressures (**Table 2**).

This agrees with previous findings that squalane promotes negative membrane curvature, favoring the formation of $Phase_{HT}$ and phase separation at lower temperatures (Salvador-Castell et al., 2020a,b). Here we show that squalane is also capable of promoting the formation of $Phase_{HT}$ at high pressures. Previously at ambient pressure, it was shown that the phase coexistence and lateral organization within a DoPhPC:DoPhPE membrane was squalane dependent leading to the hypothesis that squalane may promote the formation of membrane domains (Salvador-Castell et al., 2020b). That would mean that the ability of squalane to favor phase separation at high pressures, may indicate that squalane could also promote domain formation in archaea that live at such high-pressure conditions.

In addition to regulating the phase coexistence within the membrane, increasing the amount of squalane in the membrane also affects the d-spacing. The d-spacing of the membrane is typically higher when the membrane contains a higher quantity of squalane for $Phase_{HT}$ (**Table 1**, **Supplementary Figure 8**). For example, in $Phase_{HT}$ at 20 bar/55°C the d-spacing is 67.1 Å when the membrane contains 2.5 mol% squalane compared with 68.1 Å when the membrane contains 5 mol% squalane and 74.7 Å when the membrane contains 10 mol% squalane. In this experiment, we did not see a significant change in the d-spacing of $Phase_{LT}$ with increasing squalane concentration which was seen previously, at ambient pressure and temperature (Salvador-Castell et al., 2020b). The increase in d-spacing with increasing squalane for $Phase_{LT}$ was only seen up to 5 mol% squalane at which point the phase is thought to reach saturation. It is conceivable that the amount of squalane required to reach saturation within membrane could change with pressure and temperature and this may be one of the reason we did not see any change in the d-spacing of $Phase_{LT}$ with increasing squalane in this experiment.

At temperatures at which $Phase_{HT}$ was present, $Phase_{HT}$ was always found to increase in d-spacing with increasing squalane. Previously it was shown that increasing the percentage of squalane leads to an increase in the d-spacing in $Phase_{LT}$ due to an increase in the hydrophobic core thickness (Salvador-Castell et al., 2020b). The localization of squalane to the midplane of the bilayer is confirmed for $Phase_{HT}$ as well as $Phase_{LT}$ (**Supplementary Figure 2**). This could indicate that the increase in the d-spacing for $Phase_{HT}$ is also due to an increase in hydrophobic core thickness although this cannot be directly confirmed from this data. Increasing squalane promotes changes in membrane structure of both phases, even at high pressures and temperatures, indicating that squalane could act as a membrane regulator under the extreme conditions at which many archaea live.

CONCLUSIONS

It was proposed by Cario et al. (2015) that apolar lipids, such as squalane, sit at the midplane of the lipid bilayer, and provide a means of enhancing the stability of archaeal membrane bilayers under extreme conditions. This localization of apolar lipids to the midplane of an archaeal-like bilayer was then confirmed by the work of Salvador-Castell et al. (2020b). The aims of this

study were to determine how an archaeal-like membrane with this novel membrane architecture behaves in response to the high temperatures and high hydrostatic pressures and to determine how the quantity of apolar lipid present in the membrane modulates this behavior. To model the proposed membrane architecture in which apolar molecules sit in the midplane of the bilayer, we used an artificial archaea-like membrane composed of DoPhPC, DoPhPE, and squalane. The use of neutron diffraction allowed us to confirm the localization of the apolar lipid squalane and to further study the coexistence of two distinct lamellar phases previously reported by Salvador-Castell et al. (2020b). The phase separation within the membrane is most likely due to the partitioning of lipids (DoPhPC/DoPhPE) with different preferred curvatures and the presence of the apolar molecule (squalane). The two phases are capable of coexisting at a wide range of temperatures and pressure. High temperature favors the formation of a swollen lamellar phase ($Phase_{HT}$) and high pressure favors a thinner lamellar phase ($Phase_{LT}$). The temperature and pressure range of the phase coexistence is regulated by the percentage of squalane present in the membrane. Increasing the percentage of squalane favors the formation of $Phase_{HT}$ at lower temperatures, for pressures up to 1,000 bar. Coexistence and lateral organization of these phases was seen previously at ambient pressure (Salvador-Castell et al., 2020b). Here we have shown that phase coexistence is also seen at high pressure which could indicate the possibility of domain formation in archaea living at high pressure in addition to high temperature. Increasing the amount of squalane also leads to an increase in the membrane lamellar repeat spacing for $Phase_{HT}$. The ability of squalane to modify the membrane ultrastructure at both high pressure and temperature supports the hypothesis that apolar lipids play a role in adaptation of archaea to extreme conditions.

DATA AVAILABILITY STATEMENT

The datasets generated for this study can be found in online repositories. The names of the repository/repositories and accession number(s) can be found at: http://dx.doi.org/10.5291/ILL-DATA.8-02-852.

AUTHOR CONTRIBUTIONS

PO, MS-C, and JP conceived the project. MS-C, BD, JP, and PO carried out the experiments. JL performed the data analysis and wrote the initial draft. All authors contributed to the final manuscript.

FUNDING

This work was supported by the French National Research Agency programme ANR 17-CE11-0012-01 to PO and JP. MS-C was supported by a Ph.D. grant from the French Ministry of Research.

ACKNOWLEDGMENTS

The authors thank the Institut Laue-Langevin for the allocation of beamtime (Salvador-Castell et al., 2019) and for technical support with the high temperature and pressure setup.

SUPPLEMENTARY MATERIAL

The Supplementary Material for this article can be found online at: https://www.frontiersin.org/articles/10.3389/fchem.2020.594039/full#supplementary-material

REFERENCES

Arumugam, S., and Bassereau, P. (2015). Membrane nanodomains: contribution of curvature and interaction with proteins and cytoskeleton. *Essays Biochem.* 57, 109–119. doi: 10.1042/bse0570109

Baumgart, T., Hess, S. T., and Webb, W. W. (2003). Imaging coexisting fluid domains in biomembrane models coupling curvature and line tension. *Nature* 425, 821–824. doi: 10.1038/nature02013

Brooks, N. J. (2014). Pressure effects on lipids and bio-membrane assemblies. *IUCrJ* 1, 470–477. doi: 10.1107/S2052252514019551

Brooks, N. J., and Seddon, J. M. (2014). High pressure x-ray studies of lipid membranes and lipid phase transitions. *Zeitschr. Phys. Chem.* 228, 987–1004. doi: 10.1515/zpch-2014-0602

Cario, A., Grossi, V., Schaeffer, P., and Oger, P. M. (2015). Membrane homeoviscous adaptation in the piezo-hyperthermophilic archaeon *Thermococcus barophilus*. *Front. Microbiol.* 6:1152. doi: 10.3389/fmicb.2015.01152

Cristiglio, V., Giroud, B., Didier, L., and Demé, B. (2015). D16 is back to business: more neutrons, more space, more fun. *Neutron News* 26, 22–24. doi: 10.1080/10448632.2015.1057051

Cullis, P. R., Tilcock, C. P., and Hope, M. J. (1991). "Lipid polymorphism," in *Membrane Fusion*, eds J. Wilschut and D. Hoekstra (New York, NY: CRC Press), 35–64.

Dalmasso, C., Oger, P., Courtine, D., Georges, M., Takai, K., Maignien, L., et al. (2016). Complete genome sequence of the hyperthermophilic and piezophilic archeon *Thermococcus piezophilus* CDGST, able to grow under extreme hydrostatic pressures. *Genome Announc.* 4:e00610-16. doi: 10.1128/genomeA.00610-16

Damsté, J. S. S., Rijpstra, W. I. C., Hopmans, E. C., Schouten, S., Balk, M., and Stams, A. J. M. (2007). Structural characterization of diabolic acid-based tetraester, tetraether and mixed ether/ester, membrane-spanning lipids of bacteria from the order thermotogales. *Arch. Microbiol.* 188, 629–641. doi: 10.1007/s00203-007-0284-z

De Rosa, M., Gambacorta, A., and Gliozzi, A. (1986). Structure, biosynthesis, and physicochemical properties of archaebacterial lipids. *Microbiol. Rev.* 50, 70–80. doi: 10.1128/MMBR.50.1.70-80.1986

De Rosa, M., Gambacorta, A., and Nicolaus, B. (1983). A new type of cell membrane, in thermophilic archaebacteria, based on bipolar ether lipids. *J. Memb. Sci.* 16, 287–294. doi: 10.1016/S0376-7388(00)81316-2

Elferink, M. G. L., De Wit, J. G., Driessen, A. J. M., and Konings, W. N. (1994). Stability and proton-permeability of liposomes composed of archaeal tetraether lipids. *Biochim. Biophys. Acta* 1193, 247–254. doi: 10.1016/0005-2736(94)90160-0

Frolov, V. A., Shnyrova, A. V., and Zimmerberg, J. (2011). Lipid polymorphisms and membrane shape. *Cold Spring Harb. Perspect. Biol.* 3:a004747. doi: 10.1101/cshperspect.a004747

Gambacorta, A., Gliozzi, A., and De Rosa, M. (1995). Archaeal lipids and their biotechnological applications. *World J. Microbiol. Biotechnol.* 11, 115–131. doi: 10.1007/BF00339140

Gilmore, S. F., Yao, A. I., Tietel, Z., Kind, T., Facciotti, M. T., and Parikh, A. N. (2013). Role of squalene in the organization of monolayers derived

from lipid extracts of *Halobacterium salinarum*. *Langmuir* 29, 7922–7930. doi: 10.1021/la401412t

Gliozzi, A., Paoli Mario Rosa, G. D. E., and Gambacorta, A. (1983). Effect of isoprenoid cyclization on the transition temperature of lipids in thermophilic archaebacteria. *Biochem. Biophys. Acta* 735, 234–242. doi: 10.1016/0005-2736(83)90298-5

Goñi, F. M. (2014). The basic structure and dynamics of cell membranes: an update of the Singer-Nicolson model. *Biochim. Biophys. Acta Biomembr*. 1838, 1467–1476. doi: 10.1016/j.bbamem.2014.01.006

Hafenbradl, D., Keller, M., and Stetter, K. O. (1996). Lipid analysis of *Methanopyrus kandleri*. *FEMS Microbiol. Lett*. 136, 199–202. doi: 10.1111/j.1574-6968.1996.tb08049.x

Haines, T. H. (2001). Do sterols reduce proton and sodium leaks through lipid bilayers? *Prog. Lipid Res*. 40, 299–324. doi: 10.1016/S0163-7827(01)00009-1

Hauß, T., Dante, S., Dencher, N. A., and Haines, T. H. (2002). Squalane is in the midplane of the lipid bilayer: implications for its function as a proton permeability barrier. *Biochem. Biophys. Acta* 1556, 149–154. doi: 10.1016/S0005-2728(02)00346-8

Hauß, T., Dante, S., Haines, T. H., and Dencher, N. A. (2005). Localization of coenzyme Q10 in the center of a deuterated lipid membrane by neutron diffraction. *Biochim. Biophys. Acta Bioenerg*. 1710, 57–62. doi: 10.1016/j.bbabio.2005.08.007

Heberle, F. A., and Feigenson, G. W. (2011). Phase separation in lipid membranes. *Cold Spring Harb. Perspect. Biol*. 3, 1–13. doi: 10.1101/cshperspect.a004630

Heberle, F. A., Petruzi1'1elo, R. S., Pan, J., Drazba, P., Kučerka, N., Standaert, R. F., et al. (2013). Bilayer thickness mismatch controls domain size in model membranes. *J. Am. Chem. Soc*. 135, 6853–6859. doi: 10.1021/ja3113615

Jarsch, I. K., Daste, F., and Gallop, J. L. (2016). Membrane curvature in cell biology: an integration of molecular mechanisms. *J. Cell Biol*. 214, 375–387. doi: 10.1083/jcb.201604003

Jebbar, M., Franzetti, B., Girard, E., and Oger, P. (2015). Microbial diversity and adaptation to high hydrostatic pressure in deep-sea hydrothermal vents prokaryotes. *Extremophiles* 19, 721–740. doi: 10.1007/s00792-015-0760-3

Jouhet, J. (2013). Importance of the hexagonal lipid phase in biological membrane organization. *Front. Plant Sci.* 4:494. doi: 10.3389/fpls.2013.00494

Kates, M., and Manson, L. A. (1984). *Membrane Fluidity*. New York, NY: Plenum Press.

Katsaras, J. (1995). X-ray diffraction studies of oriented lipid bilayers. *Biochem. Cell Biol*. 73, 209–218. doi: 10.1139/o95-025

Langworthy, T. A., Tornabene, T. G., and Holzer, G. (1982). Lipids of Archaebacteria. *Zent. Bakteriol. Angew. Okol. Microbiol. Abt. L. Orig. C. Hyg*. 3, 228–244.

Marquardt, D., Heberle, F. A., Nickels, J. D., Pabst, G., and Katsaras, J. (2015). On scattered waves and lipid domains: detecting membrane rafts with X-rays and neutrons. *Soft Matter*. 11, 9055–9072. doi: 10.1039/C5SM01807B

Matsuno, Y., Sugai, A., Higashibata, H., Fukuda, W., Ueda, K., Uda, I., et al. (2009). Effect of growth temperature and growth phase on the lipid composition of the archaeal membrane from Thermococcus kodakaraensis. *Biosci. Biotechnol. Biochem*. 73, 104–108. doi: 10.1271/bbb.80520

McCarthy, N. L. C., Ces, O., Law, R. V., Seddon, J. M., and Brooks, N. J. (2015). Separation of liquid domains in model membranes induced with high hydrostatic pressure. *Chem. Commun*. 51, 8675–8678. doi: 10.1039/C5CC02134K

McMahon, H. T., and Boucrot, E. (2015). Membrane curvature at a glance. *J. Cell Sci*. 128, 1065–1070. doi: 10.1242/jcs.114454

Nagle, J. F., and Tristram-Nagle, S. (2000). Structure of lipid bilayers. *Biochim. Biophys. Acta* 1469, 159–195. doi: 10.1016/S0304-4157(00)00016-2

Oger, P. M., and Cario, A. (2013). Adaptation of the membrane in archaea. *Biophys. Chem*. 183, 42–56. doi: 10.1016/j.bpc.2013.06.020

Oger, P. M., and Jebbar, M. (2010). The many ways of coping with pressure. *Res. Microbiol*. 161, 799–809. doi: 10.1016/j.resmic.2010.09.017

Perutková, Š., Daniel, M., Dolinar, G., Rappolt, M., Kralj-Iglič, V., and Iglič, A. (2009). Stability of the inverted hexagonal phase, *Adv. Planar Lipid Bilayers Liposomes*, 9, 237–278. doi: 10.1016/S1554-4516(09)09009-7

Peters, J., Golub, M., Demé, B., Gonthier, J., Maurice, J., Payre, C., et al. (2018). New pressure cells for membrane layers and systems in solutions up to 100°C. *J. Neutron Res*. 20, 1–10. doi: 10.3233/JNR-180055

Richard, D., Ferrand, M., and Kearley, G. J. (1996). Analysis and visualisation of neutron-scattering data. *J. Neutron Res*. 4, 33–39. doi: 10.1080/10238169608200065

Sako, Y., Nomura, N., Uchida, A., Ishida, Y., Morii, H., Koga, Y., et al. (1996). *Aeropyrum pernix* gen. nov., sp. nov., a novel aerobic hyperthermophilic archaeon growing at temperatures up to 100°C. *Int. J. Syst. Bacteriol*. 46, 1070–1077. doi: 10.1099/00207713-46-4-1070

Salvador-Castell, M., Brooks, N. J., Peters, J., and Oger, P. (2020a). Induction of non-lamellar phases in archaeal lipids at high temperature and high hydrostatic pressure by apolar polyisoprenoids. *Biochim. Biophys. Acta Biomembr*. 1862:183130. doi: 10.1016/j.bbamem.2019.183130

Salvador-Castell, M., Déme, B., Misuraca, L., Oger, P., and Peters, J. (2019). *Novel High-Pressure/High-Temperature Phases in Archaeal Membranes*. Institut Laue-Langevin (ILL). doi: 10.5291/ILL-DATA.8-02-852

Salvador-Castell, M., Demé, B., Oger, P., and Peters, J. (2020b). Lipid phase separation induced by the apolar polyisoprenoid squalane demonstrates its role in membrane domain formation in archaeal membranes. *Langmuir* 36, 7375–7382. doi: 10.1021/acs.langmuir.0c00901

Salvador-Castell, M., Demé, B., Oger, P., and Peters, J. (2020c). Structural characterization of an archaeal lipid bilayer as a function of hydration and temperature. *Int. J. Mol. Sci*. 21:1816. doi: 10.3390/ijms21051816

Schmid, F. (2017). Physical mechanisms of micro- and nanodomain formation in multicomponent lipid membranes. *Biochim. Biophys. Acta* 1859, 509–528. doi: 10.1016/j.bbamem.2016.10.021

Schouten, S., Van Der Meer, M. T. J., Hopmans, E. C., Rijpstra, W. I. C., Reysenbach, A. L., Ward, D. M., et al. (2007). Archaeal and bacterial glycerol dialkyl glycerol tetraether lipids in hot springs of Yellowstone National Park. *Appl. Environ. Microbiol*. 73, 6181–6191. doi: 10.1128/AEM.00630-07

Shearman, G. C., Ces, O., Templer, R. H., and Seddon, J. M. (2006). Inverse lyotropic phases of lipids and membrane curvature. *J. Phys. Condens. Matter* 18:S1105–24. doi: 10.1088/0953-8984/18/28/S01

Siliakus, M. F., van der Oost, J., and Kengen, S. W. M. (2017). Adaptations of archaeal and bacterial membranes to variations in temperature, pH and pressure. *Extremophiles* 21, 651–670. doi: 10.1007/s00792-017-0939-x

Sinensky, M. (1974). Homeoviscous adaptation: a homeostatic process that regulates the viscosity of membrane lipids in *Escherichia coli*. *Proc. Natl. Acad. Sci. U.S.A*. 71, 522–525. doi: 10.1073/pnas.71.2.522

Singer, S. J., and Nicolson, G. L. (1972). The fluid mosaic model of the structure of cell membranes. *Science* 175, 720–731. doi: 10.1126/science.175.4023.720

Sprott, G. D., Agnew, B. J., and Patel, G. B. (1997). Structural features of ether lipids in the archaeobacterial thermophiles pyrococcus furiosus, *Methanopyrus kandleri*, *Methanothermus fervidus*, and *Sulfolobus acidocaldarius*. *Can. J. Microbiol*. 43, 467–476. doi: 10.1139/m97-066

Takai, K., Nakamura, K., Toki, T., Tsunogai, U., Miyazaki, M., Miyazaki, J., et al. (2008). Cell proliferation at 122°C and isotopically heavy CH4 production by a hyperthermophilic methanogen under high-pressure cultivation. *Proc. Natl. Acad. Sci. U.S.A*. 105, 10949–10954. doi: 10.1073/pnas.0712334105

Tayebi, L., Ma, Y., Vashaee, D., Chen, G., Sinha, S. K., and Parikh, A. N. (2012). Long-range interlayer alignment of intralayer domains in stacked lipid bilayers. *Nat. Mater*. 11, 1074–1080. doi: 10.1038/nmat3451

Tornabene, T. G., and Langworthy, T. A. (1979). Diphytanyl and dibiphytanyl glycerol ether lipids of methanogenic archaebacteria. *Science* 203, 51–53. doi: 10.1126/science.758677

Trapp, M., Marion, J., Tehei, M., Demé, B., Gutberlet, T., and Peters, J. (2013). High hydrostatic pressure effects investigated by neutron scattering on lipid multilamellar vesicles. *Phys. Chem. Chem. Phys*. 15, 20951–20956. doi: 10.1039/c3cp52762j

Tristram-Nagle, S. A. (2007). Preparation of oriented, fully hydrated lipid samples for structure determination using X-ray scattering. *Methods Mol. Biol*. 400, 63–75. doi: 10.1007/978-1-59745-519-0_5

Trovaslet-Leroy, M., Martinez, N., Marion, J., and Peters, J. (2016). "Hautes pressions et dynamique des systems bilogiques," in *Mesures en Conditions Extrêmes*, eds Y. Le Godec, H. Cardon, T. Hammouda, and Y. Morizet (Paris: Éditions des Archives Contemporaines), 51–64.

Tyler, A. I. I., Law, R. V., and Seddon, J. M. (2015). "X-Ray diffraction of lipid model membranes," in *Methods in Membrane Lipids*, ed D. M. Owen (New York, NY: Humana Press), 199–225.

Winter, R., and Jeworrek, C. (2009). Effect of pressure on membranes. *Soft Matter*. 5, 3157–3173. doi: 10.1039/b901690b

Yamauchi, K., Doi, K., Yoshida, Y., and Kinoshita, M. (1993). Archaebacterial lipids: highly proton-impermeable membranes from 1,2-diphytanyl-sn-glycero-3-phosphocholine. *Biochim. Biophys. Acta* 1146, 178–182. doi: 10.1016/0005-2736(93)90353-2

Yayanos, A. A., Dietz, A. S., and Van Boxtel, R. (1981). Obligately barophilic bacterium from the mariana trench. *Proc. Natl. Acad. Sci. U.S.A.* 78, 5212–5215. doi: 10.1073/pnas.78.8.5212

Zeng, X., Birrien, J. L., Fouquet, Y., Cherkashov, G., Jebbar, M., Querellou, J., et al. (2009). Pyrococcus CH1, an obligate piezophilic hyperthermophile: extending the upper pressure-temperature limits for life. *ISME J.* 3, 873–876. doi: 10.1038/ismej.2009.21

Conflict of Interest: The authors declare that the research was conducted in the absence of any commercial or financial relationships that could be construed as a potential conflict of interest.

frontiers in Chemistry

ORIGINAL RESEARCH
published: 19 November 2020
doi: 10.3389/fchem.2020.577508

Enhanced Microscopic Dynamics of a Liver Lipid Membrane in the Presence of an Ionic Liquid

Veerendra K. Sharma[1,2]*, *Sajal K. Ghosh*[3], *Victoria García Sakai*[4] and *R. Mukhopadhyay*[1,2]

[1] Solid State Physics Division, Bhabha Atomic Research Centre, Mumbai, India, [2] Homi Bhabha National Institute, Mumbai, India, [3] Department of Physics, School of Natural Sciences, Shiv Nadar University, Greater Noida, India, [4] Rutherford Appleton Laboratory, ISIS Pulsed Neutron and Muon Facility, Science and Technology Facilities Council, Didcot, United Kingdom

Ionic liquids (ILs) are an important class of emerging compounds, owing to their widespread industrial applications in high-performance lubricants for food and cellulose processing, despite their toxicity to living organisms. It is believed that this toxicity is related to their actions on the cellular membrane. Hence, it is vital to understand the interaction of ILs with cell membranes. Here, we report on the effects of an imidazolium-based IL, 1-decyl-3-methylimidazolium tetrafluoroborate (DMIM[BF4]), on the microscopic dynamics of a membrane formed by liver extract lipid, using quasielastic neutron scattering (QENS). The presence of significant quasielastic broadening indicates that stochastic molecular motions of the lipids are active in the system. Two distinct molecular motions, (i) lateral motion of the lipid within the membrane leaflet and (ii) localized internal motions of the lipid, are found to contribute to the QENS broadening. While the lateral motion could be described assuming continuous diffusion, the internal motion is explained on the basis of localized translational diffusion. Incorporation of the IL into the liver lipid membrane is found to enhance the membrane dynamics by accelerating both lateral and internal motions of the lipids. This indicates that the IL induces disorder in the membrane and enhances the fluidity of lipids. This could be explained on the basis of its location in the lipid membrane. Results are compared with various other additives and we provide an indication of a possible correlation between the effects of guest molecules on the dynamics of the membrane and its location within the membrane.

Keywords: ionic liquids, lipid membrane, neutron scattering, lateral motion, internal motion

OPEN ACCESS

Edited by:
Olaf Holderer, Helmholtz Association of German Research Centers (HZ), Germany

Reviewed by:
Siddharth Surajbhan Gautam, The Ohio State University, United States
Rolf Hempelmann, Saarland University, Germany

***Correspondence:**
Veerendra K. Sharma
sharmavk@barc.gov.in;
vksphy@gmail.com

Specialty section:
This article was submitted to Physical Chemistry and Chemical Physics, a section of the journal Frontiers in Chemistry

Received: *29 June 2020*
Accepted: *01 October 2020*
Published: *19 November 2020*

Citation:
Sharma VK, Ghosh SK, García Sakai V and Mukhopadhyay R (2020) Enhanced Microscopic Dynamics of a Liver Lipid Membrane in the Presence of an Ionic Liquid. Front. Chem. 8:577508. doi: 10.3389/fchem.2020.577508

INTRODUCTION

Ionic liquids (ILs) are a particular class of organic salts in which the ions are poorly coordinated, which results in low melting temperatures (Hayes et al., 2015; Egorova et al., 2017). ILs are non-explosive, non-flammable and have good thermal stability and high ionic conductivity (Hayes et al., 2015; Egorova et al., 2017). These ILs have various widespread industrial applications, such as in high-performance lubricants, in chemical and polymer synthesis, in energy harvesting, and in food and cellulose processing (Plechkova and Seddon, 2008; Plechkova et al., 2009; Hayes et al., 2015; Egorova et al., 2017). However, recent studies (Matzke et al., 2007; Jeong et al., 2012; Liang et al., 2013; Bakshi et al., 2020) have suggested that ILs are toxic to various organisms. It has been shown that toxicity strongly depends on the lipophilicity of the IL, generally increasing with IL chain length (Matzke et al., 2007; Jeong et al., 2012; Liang et al., 2013). The origin

of the toxicity of the IL is mainly attributed to their interaction with the cellular membrane (Jeong et al., 2012; Benedetto and Ballone, 2016; Bakshi et al., 2020), which provides the interface between an organelle or a cell, and the surrounding external environment. It is a heterogeneous mixture of various lipids, proteins, and other small molecules. The main constituents of the cell membrane are the lipids and thus a lipid membrane can be used as a model cell membrane system.

Imidazolium-based cations are a popular class of ILs which have shown high levels of toxicity against several classes of organisms (Pendleton and Gilmore, 2015). Recently (Bakshi et al., 2020), we have studied the effects of various imidazolium-based ILs $[C_nMIM]^+[BF4]$ (*n* varies from 2 to 10) on different cancerous cells such as human breast, colon and liver cells. Our work showed that 1-decyl-3-methylimidazolium tetrafluoroborate $[C_{10}MIM]^+[BF4]$ [or [DMIM][BF4]] has the highest toxicity toward liver cancerous cells, which we suggest is due to the modulation of the structure and dynamics of the liver membrane due to the incorporation of IL (Bakshi et al., 2020). In the present study, we investigate this possible modulation in more detail, specifically on the effect of [DMIM][BF4] on the dynamics of a membrane from liver extract lipid. The structure of the IL is shown in **Figure 1**. We choose this as our model system instead of a simpler more commonly used single lipid model membrane, since it more physiologically relevant. The liver lipid extract membrane contains the commonly found lipids in all eukaryotic cells, namely a mixture of lipids including phosphatidylcholine (PC), phosphatidylethanolamine (PE), phosphatidylinositol (PI), and cholesterol.

Membrane dynamics play a key role in the viscoelastic properties of the cell membrane, which are important in various physiological processes such as cell signaling, protein-protein interaction, etc. Lipid membranes exhibit a complex hierarchical dynamical behavior owing to multiple relaxation processes on the local and global scales (Tocanne et al., 1994; Lipowsky and Sackmann, 1995; Marquardt et al., 2017; Nagao et al., 2017; Sharma et al., 2019a,b). For example, at a local scale, an individual lipid molecule performs distinct motions such as vibrations, conformational changes, protrusions, molecular rotations, lateral motions within the leaflet, flip flop motions from one leaflet to another, etc. On the other hand, at a larger and more global scale, the whole lipid bilayer may undergo bending motions, thickness fluctuations, shape fluctuations, etc. These motions occur in a wide range of time scales ranging from vibrations at ∼fs to flip flop motions which take a few hours, and over a wide variety of length scales, from molecular rotations at a few Å to the macroscopic deformation of the vesicles at the micrometer scale. To investigate these motions, various experimental methods have been used, such as dynamic light scattering (Hassan et al., 2015; Sharma et al., 2020), fluorescence spectroscopy (Machán and Hof, 2010; Singh et al., 2019), electron paramagnetic resonance (McConnell and Kornberg, 1971), nuclear magnetic resonance (Perlo et al., 2011), quasielastic neutron scattering (Busch et al., 2010; Armstrong et al., 2011; Sharma et al., 2015a, 2017a,b; Dubey et al., 2018; Sharma and Mukhopadhyay, 2018), neutron spin echo (Boggara et al., 2010; Lee et al., 2010; Woodka et al., 2012; Nickels et al., 2015). Each method has limited accessible temporal and spatial regimes. For example, dynamic light scattering is more suitable to study motions at time scales of the order of microseconds while quasielastic neutron scattering (QENS) is suitable to study dynamics from nanoseconds to sub-picoseconds and length scales from Angstroms to a few nanometers (Gardner et al., 2020). Furthermore, neutron spin echo (NSE) is more suitable to prove the relatively slower motions, up to 0.1 μs, taking place at large spatial scales, up to 0.1 μm (Gardner et al., 2020). It is therefore evident that to obtain the detailed dynamical landscape one needs to combine results from different experimental methods.

Here, we report the effects of [DMIM][BF4] IL on the microscopic dynamics of liver lipid membrane studied using QENS techniques. Two distinct motions, (i) lateral motion of the lipid within the leaflet and (ii) localized internal motions of the lipid are observed (A schematic of a lipid bilayer and these motions are shown in **Figure 1**). Our measurements suggest that the incorporation of the IL in the membrane modulates both of these dynamical processes. We note that the dynamics of ILs have also been investigated using the QENS technique (Triolo et al.,

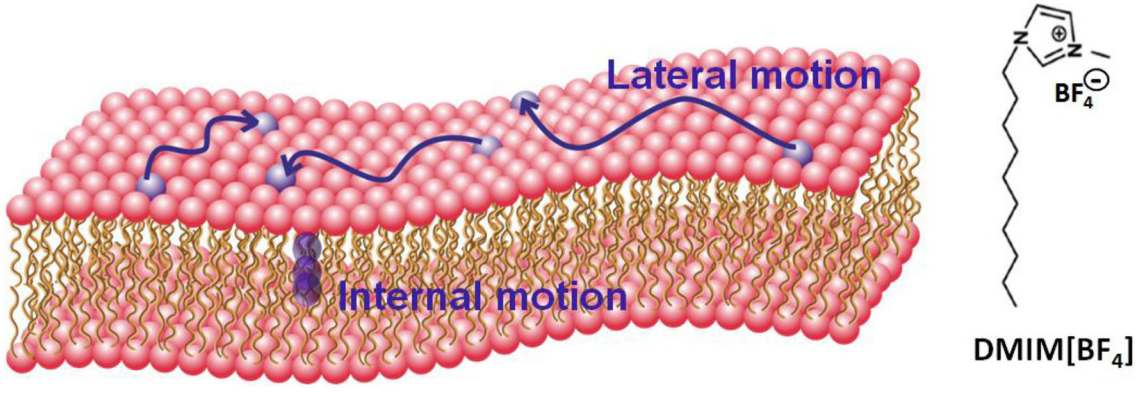

FIGURE 1 | Schematic of a lipid bilayer and molecular configuration of the ionic liquid DMIM[BF4]. Two distinct motions (i) lateral motion within the leaflet and (ii) localized internal motion in the lipids are also shown.

2006; Mamontov et al., 2009; Aoun et al., 2010; Burankova et al., 2018; Nemoto et al., 2018), however in this work we focus on the dynamics of the lipids and how they are affected by the presence of IL, and not on the dynamics of the IL themselves, since the concentration is small (see experimental details).

EXPERIMENTAL METHODS

Preparation of Unilamellar Vesicles

Liver lipid extract (bovine) solution in chloroform was procured from Avanti Polar Lipids (USA). This extract is a mixture of various lipids PC:PE:PI:lysoPI:Cholesterol:other lipids = 42:26:9:1:5:17 (weight%). The ionic liquid [DMIM][BF4], and D_2O (99.9%) were obtained from Sigma Aldrich (USA). Deuterated water was used in order to minimize the scattering contribution from the solvent, since the neutron scattering cross-section of deuterium is lower than hydrogen by more than an order of magnitude ($\sigma_D << \sigma_H$). Large unilamellar vesicles (LUV) composed of liver lipids were prepared using the extrusion method (Sharma et al., 2015b, 2016a,b; Mitra et al., 2020). Briefly, organic solvent was evaporated to obtain lipid films. These films were hydrated by D_2O which followed 3 freeze-thaw cycles by keeping the lipid suspension in a warm water bath (50°C) and in a freezer (−80°C). The suspension was extruded 21 times through a 100 nm pore sized polycarbonate filter using a mini extruder from Avanti Polar Lipids Inc. Two different samples, 5% (*w/w*) liver lipid LUV, and 5% (*w/w*) liver lipid LUV with 10 wt% [DMIM][BF4] (with respect to liver lipid) were used. It should be noted that the main contribution to the quasielastic scattering signal comes from the liver lipid and that only ∼7% is from the DMIM IL, making it small enough to be neglected from the analysis.

Quasi-Elastic Neutron Scattering (QENS) Experiment

QENS experiments were carried out on the liver lipid-based LUVs with and without [DMIM][BF4], using the time-of-flight neutron backscattering spectrometer, IRIS (Carlile and Adams, 1992) at ISIS facility, UK. To minimize multiple scattering effects, both samples were filled into annular aluminum sample holders with an annular spacing of 0.5 mm to ensure a sample transmission of more than 90%. The IRIS spectrometer was used with the PG(002) analyzer giving an energy resolution of $\Delta E = 17$ μeV (full width at half-maximum), and with a detector coverage spanning a wave vector transfer range of 0.5–1.8 $Å^{-1}$. In the offset mode, the spectrometer provided an energy transfer range of −0.3 to +1.0 meV. To estimate the solvent contribution, QENS measurements were also carried out on pure D_2O. Measurements were carried out at two distinct temperatures, 37°C (physiological temperature) and 57°C. A QENS measurement was also carried out on vanadium, a good elastic incoherent scatterer, to obtain the instrument resolution. Standard data reduction was carried out using MANTID software (Taylor et al., 2012).

RESULTS AND DISCUSSION

In a quasielastic neutron scattering experiment, the scattered intensity is proportional to the double scattering cross section, which gives the probability of scattered neutrons within the solid angle element d**Ω**, about the direction **Ω** and with an energy exchange of $dE = E_f$-E_i (E_f and E_r are the final and initial energy of the neutron, respectively). The double scattering cross section can be written as Bee (1988)

$$\frac{d^2\sigma}{dEd\Omega} \propto \frac{k_f}{k_i}[\sigma_{coh}S_{coh}(\boldsymbol{Q},E) + \sigma_{inc}S_{inc}(\boldsymbol{Q},E)] \quad (1)$$

where, S_{coh} and S_{inc} are the coherent and incoherent scattering laws, and σ_{coh} and σ_{inc} are the coherent and incoherent scattering cross sections; and $\boldsymbol{Q}$ is the momentum transfer in the scattering process. In the case of hydrogenous samples, the scattered intensity is dominated by incoherent scattering from the hydrogen atoms in the sample, which is due to their exceptionally high incoherent scattering cross section compared to the coherent or incoherent scattering cross-section of any other atoms ($\sigma_{inc}^{H} >> \sigma_{inc/coh}^{any\ atom}$). In this case, Equation (1) can be written as

$$\frac{d^2\sigma}{dEd\Omega} \propto \frac{k_f}{k_i}\sigma_{inc}S_{inc}(\boldsymbol{Q},E) \quad (2)$$

The incoherent scattering law S_{inc} (Q,ω) is the double Fourier transform of $G_s(r, t)$ which provides the probability of finding a particle at position r and time t provided the same particle was at position $r = 0$ at $t = 0$. Hence, a QENS experiment from a hydrogenous system provides information about the self-diffusion or single particle motion of the protons in the system. Since our interest lies in the study of the dynamics of the liver lipid membrane, D_2O was used as a solvent while preparing the LUVs to minimize the solvent contribution. The contribution to the measured scattering signal from the dynamics of the lipid liver was extracted by subtracting the weighted D_2O signal from the solution data (Sharma et al., 2015b, 2016b).

D_2O subtracted QENS spectra for the liver lipid membrane at both the temperatures are shown in **Figure 2** at a typical Q-value of 1.22 $Å^{-1}$. The instrument resolution, as measured using a standard vanadium sample, is also shown in the figure. For direct comparison, spectra are normalized to 1 by dividing the respective spectra by the peak value, S(Q,0). Significant quasielastic (QE) broadening is observed for the liver lipid membrane at both temperatures, indicating the presence of stochastic molecular motions of the lipid in the temporal window accessible by the IRIS spectrometer.

Plotting the data in terms of the dynamic susceptibility is a useful way to find out the number of relaxation processes without employing any detailed data analysis. This approach is possible since a relaxation process with a characteristic time (τ) shows a peak in the dynamic susceptibility at energy transfer $E = \hbar/\tau$, where $\hbar$ is the reduced Planck's constant. The scattering data are converted into the imaginary component of the dynamic susceptibility, $\chi''(E)$, by dividing the Q-averaged intensity, $S(E)$, by the Bose population factor, $n_B(E) \approx k_BT/E$ (under the

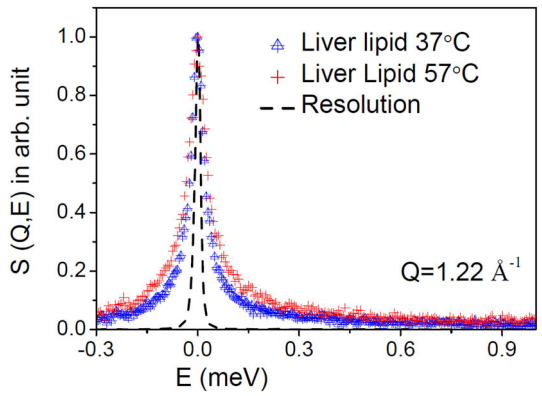

FIGURE 2 | Typical measured QENS spectra at a representative $Q = 1.22$ Å^{-1} for the liver lipid membrane at 37 and 57°C. The evolution of the dynamics at higher temperature is evident. The contribution of the solvent (D_2O) has been subtracted, and the resultant spectra are plotted normalized to the peak amplitudes. Instrument resolution is shown by a dashed line.

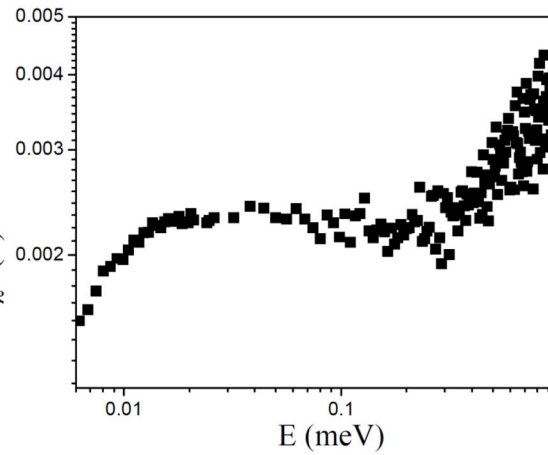

FIGURE 3 | Dynamic susceptibility, $\chi''(E)$, for the liver lipid membrane at 37°C.

approximation that $E << k_BT$), where k_B is the Boltzmann's constant and $E = \hbar\omega$ is the energy transfer. The resulting profile of $\chi''(E)$ vs. E for liver lipid membrane obtained at 37°C is shown in **Figure 3**. It can be inferred from the susceptibility spectra that the dynamics of the liver lipid membrane cannot be viewed as a single relaxation process. The existence of a minimum in the susceptibility spectra indicates the presence of two relaxation processes.

As mentioned before, molecular motions in the time scale from nanoseconds to picoseconds and length scales from Angstroms to few nanometers can be probed by QENS. On these length and time scales, two different motions which can contribute to the observed data are: (i) the lateral motion of lipid molecules within the leaflet and (ii) relatively faster internal motions (Sharma et al., 2015b, 2016a,b; Mitra et al., 2020). Assuming both motions are independent of each other, the scattering law for the lipid membrane can be written as

$$S_{mem}(Q,E) = S_{lat}(Q,E) \otimes S_{\text{int}}(Q,E) \tag{3}$$

where, $S_{lat}(Q,E)$ and $S_{int}(Q,E)$ are the scattering functions corresponding to the lateral and internal motions, respectively. The nature of the lateral motion of the lipid in the membrane is debatable as a number of different models have been proposed, such as continuous diffusion (Armstrong et al., 2011), ballistic flow-like motions (Busch et al., 2010), localized diffusion (Wanderlingh et al., 2014), sub-diffusive motion (Flenner et al., 2009; Srinivasan et al., 2018), etc. We have assumed the simple continuous diffusion model, based on the recent study (Armstrong et al., 2011), which has shown that this is the case for the temporal and spatial scales accessible by QENS and valid at least, for distances greater than a lipid molecule diameter. The scattering law corresponding to the lateral motion is then expressed as:

$$S_{lat}(Q,E) = L_{lat}(\Gamma_{lat},E) \tag{4}$$

where $L_{lat}(\Gamma_{lat}, E)$ is a Lorentzian function, corresponding to the lateral motion of the lipid, and Γ_{lat} is its HWHM, which is inversely proportional to the timescale of the motion.

The internal motions of the lipid molecules correspond to motions that are spatially restricted by the chemical structure of the lipid molecule. Thus, after a relatively long relaxation time, there is a finite probability of finding the scattering center within a given molecular volume. This leads to an elastic component in the scattering law and we can write the scattering law for the internal motions as,

$$S_{\text{int}}(Q,E) = A(Q)\delta(E) + (1 - A(Q))L_{\text{int}}(\Gamma_{\text{int}},E) \tag{5}$$

The first term represents the elastic part where $A(Q)$ is the elastic incoherent structure factor (EISF). The second term corresponds to the quasielastic part which is characterized by a single Lorentzian $L_{int}(\Gamma_{int}$,E) function with Γ_{int} is its HWHM.

Combining Equations (4) and (5), the resultant scattering law (Equation 3) can be written as

$$S_{mem}(Q,E) = \left[A(Q)\,L_{lat}(\Gamma_{lat},E) + (1 - A(Q))\,L_{tot}(\Gamma_{lat} + \Gamma_{\text{int}},E)\right] \tag{6}$$

Convoluting Equation (6) with the resolution function (obtained by measuring the data from a standard vanadium sample), the parameters $A(Q)$, Γ_{lat}, and Γ_{int} were determined by least squares fit of the measured spectra. DAVE software (Azuah et al., 2009) developed at the NIST Center for Neutron Research has been used to analyze the QENS data. It is found that the scattering law given in Equation (6) describes the observed QENS data quite well for liver lipid membrane in the absence and presence of the IL for the entire Q range at both temperatures. Typical fitted QENS spectra for liver lipid membrane at 57°C at different Q values are shown in **Figure 4**. To gain more insight into the different dynamical processes, the fit parameters are used to obtain some more dynamical characteristic parameters for each of the processes (such as diffusion coefficients and extent of mobility).

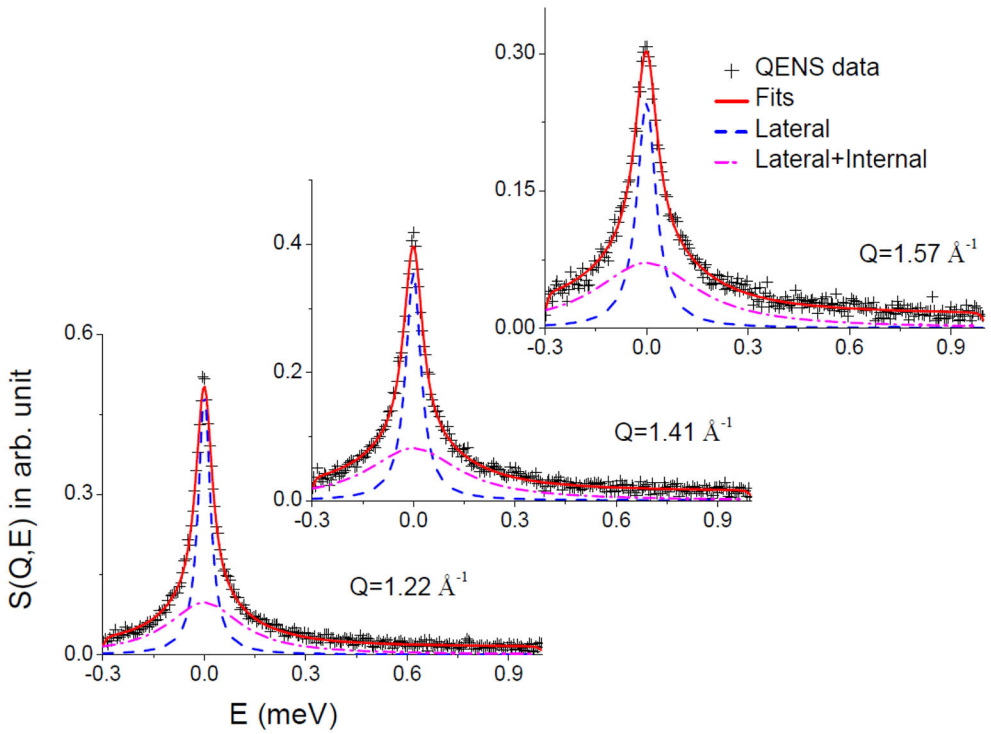

FIGURE 4 | Typical fitted QENS spectra for liver lipid membrane at 57°C. Individual components corresponding to lateral and lateral with internal motions are also shown.

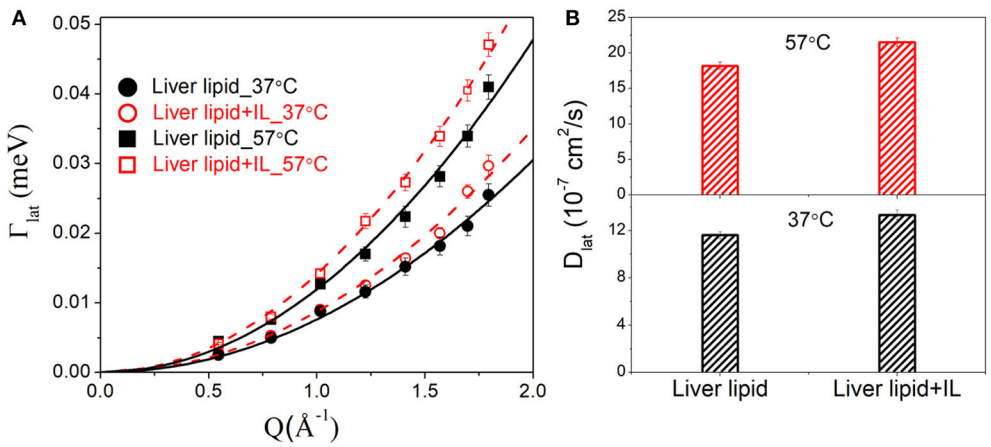

FIGURE 5 | (A) Variation of HWHM's of Lorentzian corresponding to the lateral motion of liver lipid in the absence and presence of [DMIM][BF4] IL at 37 and 57°C. The solid and dashed lines the fits assuming Fick's law of diffusion. **(B)** Lateral diffusion coefficient D_{lat} for liver lipids in absence and presence of [DMIM][BF4] IL at 37 and 57°C.

Lateral Motion

The lateral motion of the lipid molecules within the leaflet is of principal interest since it plays a key role in various physiologically relevant membrane processes, such as cell signaling, membrane trafficking, location and activity of membrane proteins, cell recognition, etc. HWHM's of the Lorentzian corresponding to the lateral motion, Γ_{lat} for the liver lipid with and without [DMIM][BF4], at 37 and 57°C, are shown in **Figure 5A**. At both temperatures, addition of the IL increases the values of HWHM, indicating an enhancement in lateral diffusion. It is evident that for liver lipid in the absence and presence of [DMIM][BF4], Γ_{lat} increases quadratically with Q at both temperatures, passing through the origin, which indicates that the lateral motion of the lipid molecules can be

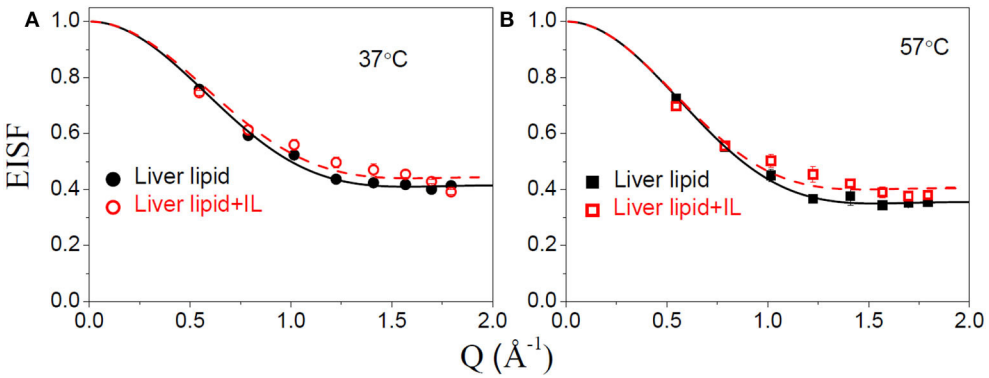

FIGURE 6 | Elastic incoherent structure factor (EISF) corresponding to the internal motion of liver lipid in the pristine membrane and membrane with IL at **(A)** 37°C and **(B)** 57°C. The solid and dashed lines correspond to the fit assuming localized translational diffusion model as discussed in the text.

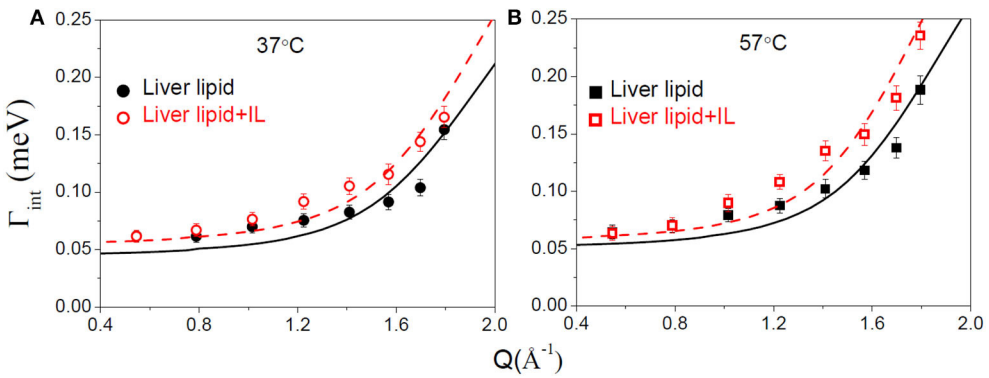

FIGURE 7 | Variation of the HWHM, Γ_{int}, corresponding to internal motions of liver lipid in the pristine membrane and membrane with IL at **(A)** 37°C and **(B)** 57°C. The solid and dashed lines correspond to the fits as per the localized translational diffusion model as discussed in the text.

described as a continuous diffusion, described by Fick's law $\Gamma_{lat} = D_{lat}Q^2$. A least squares fitting method is used to determine the lateral diffusion coefficient, D_{lat}, for liver lipid with and without [DMIM][BF4] at both temperatures. **Figure 5B** shows that the incorporation of the IL accelerates the lateral motion of the lipids at both temperatures by about 15–20%. At the physiological temperature of 37°C, D_{lat} is found to be $11.6(\pm0.3) \times 10^{-7}$ cm^2/s which increases to $13.3(\pm0.4) \times 10^{-7}$ cm^2/s due to the incorporation of [DMIM][BF4]. At 57°C, D_{lat} is found to be $18.2(\pm0.5) \times 10^{-7}$ cm^2/s which increases to $21.5(\pm0.6) \times 10^{-7}$ cm^2/s.

Internal Motion

The internal motion of the lipid is characterized by two parameters, the EISF and the HWHM, Γ_{int}. **Figures 6A,B** show the EISFs for the liver lipids in the absence and presence of [DMIM][BF4] at 37 and 57°C, respectively. The internal motions of liver lipids are expected to be a complex mixture of motion, including reorientation of lipids, conformational motions, large amplitude oscillations, etc. The variation of Γ_{int} with Q, as shown in **Figure 7**, is very different to that observed for Γ_{lat}. It may be noted that at low Q, Γ_{int} is nearly constant and approaches a non-zero value as Q tends to zero. At higher Q, Γ_{int} increases and follows Q^2 variation. This is a signature of localized translational diffusion within a spherical volume. We have successfully described the internal motions in similar systems (Sharma et al., 2010, 2015a; Dubey et al., 2018) by a model where all these various motions have been effectively taken into account. In this model, it is assumed that the hydrogen atoms belonging to lipids undergo localized translation diffusion (LTD) within a confined volume (Sharma et al., 2015a; Dubey et al., 2018). At lower Q ($QR < \pi$; where R is radius of confining spherical domain), that is when larger distances are probed, the behavior of Γ_{int} is independent of Q. At this length of scale, hydrogen atoms in the lipid molecules perform localized motions. Therefore, the behavior of Γ_{int} in this Q range is similar to that of rotational motions. However, at larger Q values ($QR > \pi$), where small distances are probed within the spherical domain, the usual DQ^2 behavior corresponding to translational motion in an infinite medium is observed. It is likely that at a given temperature, all the hydrogen atoms belonging to a lipid molecule are not dynamically active. Assuming that on average only a fraction of hydrogen atoms are participating in the internal motions, the EISF can be written as

TABLE 1 | Fraction of immobile hydrogen atoms (p_x), radius of the spherical domain (R) and diffusivity correspond to the internal motion of the liver lipids in the membrane in the absence and presence of [DMIM][BF4].

T (°C)	Liver lipids			Liver lipids + [DMIM][BF4]		
	p_x (%)	R (Å)	D_{int} (×10^{-6} cm^2/s)	p_x	R (Å)	D_{int} (×10^{-6} cm^2/s)
37	41 (3)	2.8 (2)	12.3 (4)	43 (3)	2.8 (2)	14.9 (4)
57	35 (2)	2.9 (2)	15.0 (5)	39 (3)	3.0 (3)	18.4 (6)

Volino and Dianoux (1980)

$$A(Q) = p_x + (1 - p_x)\left[\frac{3j_1(QR)}{QR}\right]^2 \tag{7}$$

where p_x is the fraction of hydrogen atoms that are immobile on the observation time scale, R is the radius of the spherical domain and j_1 is the first-order spherical Bessel function. It was found that the experimentally observed EISF could be described very well using Equation (7) for the liver lipid membranes with and without [DMIM][BF4] at both temperatures, as shown by the solid lines in **Figures 6A,B**. The obtained fitting parameters, p_x and R are given in **Table 1**. At 37°C, values of $p_x = 0.41$ and $R = 2.8$ Å indicate that on average about 59% of the hydrogen atoms participate in the localized translational diffusion, within a sphere with a radius of 2.8 Å. The size of the confining domain is correlated with the bilayer structure, more specifically with the area per lipid molecule and found to be consistent with studies on other lipid membranes (Busch et al., 2010; Mitra et al., 2020). Due to the addition of the IL, the fraction of immobile hydrogen atoms increases very slightly, but the radius of the spherical domain remains more or less unchanged. It is evident that addition of DMIM[BF4] does not affect the nature of the internal dynamics.

For any model to be considered robust it should simultaneously describe both EISF and HWHM. The scattering law for the localized translational diffusion model as described above can be written as Volino and Dianoux (1980):

$$\begin{aligned} S_{\text{int}}(Q,E) \;=\; & \left[p_x + (1-p_x)\left[\frac{3j_1(QR)}{QR}\right]^2\right]\delta(\omega) \\ & +\; (1-p_x)\left[\frac{1}{\pi}\sum_{\{l,n\}\neq\{0,0\}}\left(2l\right.\right. \\ & \left.\left.+\;1\;\right)A_n^l(QR)\frac{\hbar(x_n^l)^2 D_{\text{int}}/R^2}{\left[\hbar(x_n^l)^2 D_{\text{int}}/R^2\right]^2 + E^2}\right] \end{aligned} \tag{8}$$

Where $A_n^l(QR)$; $(n,\, l \neq \;\; 0{,}0)$ is the quasielastic structure factor and values of it for different n and l can be calculated by using the values of x_n^l which are given in Volino and Dianoux (1980) and are obtained by the numerical solution of the equations as described therein. Here, D_{int} is the diffusion coefficient for internal motion. Equation (8) involves an infinite sum of the Lorentzian whose widths are independent of Q, but whose weight factors depend on Q or more specifically on (QR) (Volino and Dianoux, 1980). In practice, the summation series in the above equation can be truncated at those values of n and l for which A_n^l do not contribute up to $Q_{\max}R$. In the present case, $Q_{\max} = 1.8$ Å^{-1} and $R \sim 3$Å, hence $Q_{\max}R = 5.4$. It has been shown (Volino and Dianoux, 1980) that for $QR \sim 20$ (which is sufficiently larger than the present case), one needs to take into account about 100 terms to obtain a numerical accuracy of $\sim 10^{-3}$. In the present case where $Q_{\max}R = 5.4$ we have used first 100 terms of the summation series.

To estimate the time scale of the internal motion of the lipid, a detailed analysis of the $\Gamma_{\text{int}}(Q)$ has been carried out. Since no analytical expression exists for $\Gamma_{\text{int}}(Q)$ within the LTD model, it was numerically calculated using the quasielastic term of Equation (8). D_{int} is obtained from the least-squares fitting of $\Gamma_{\text{int}}(Q)$ (**Figure 7**). The p_x and R as obtained from the description of EISF have been used in the fitting. As evident from **Figure 7**, that model could describe the obtained HWHM quite well. The obtained diffusion coefficients D_{int} for both the systems are given in **Table 1**. Again a $\sim$ 20% increase in D_{int} is found at both temperatures suggesting an enhancement of the internal motions in the presence of the IL.

The data obtained here indicates that [DMIM][BF4] does affect the dynamics of the liver membrane, by enhancing both lateral motions within the leaflet and also the localized internal motion of the lipids. A recent molecular dynamics (MD) simulation study (Yoo et al., 2014) has shown that the imidazolium based ILs penetrate within the lipid membrane and have a preferred orientation in the lipid membrane. Alkyl chains prefer to orient parallel to the lipid molecules and the imidazolium group interacts with the head group. This was further supported by Isothermal Titration Calorimetry (ITC) measurements which showed stoichiometry ratios for IL of ∼2. Incorporation of IL inside the membrane creates disorder, supported by neutron and x-ray reflectivity measurements (Benedetto et al., 2014; Bhattacharya et al., 2017) which showed that addition of IL leads to membrane thinning.

These results are in contrast with the recent QENS studies on membranes with antimicrobial peptides (AMPs), where it was reported that the addition of cationic antimicrobial peptides in zwitterionic PC (Sharma et al., 2015b, 2016b) as well as in anionic PG (Mitra et al., 2020) restricts the dynamics of the membrane. Moreover, these peptides have shown that the restriction is mainly on the lateral motion of the lipid, while the internal motion of the lipids remained unchanged. Observed differences between the action of ILs and antimicrobial peptides on the membranes can be explained on the basis of their locations within the membrane. Using orientated circular dichroism (OCD), it has been shown that at low concentrations, cationic AMPs bind on the surface of the lipid membrane (Sharma et al., 2016b). These observations were also supported by ITC data which showed that stoichiometry ratio for these AMP is high (∼few tens of the lipid), further indicating that these AMPs bind on the surface on the lipid membrane (Mitra et al., 2020). As the lateral motion of the lipid involves diffusion of the whole lipid within the leaflet and the internal motion of the lipid is

localized, the AMPs affect mainly the lateral motion of the lipid. Comparing the results with other membrane active molecules such as NSAIDs (Sharma et al., 2019b, 2020), vitamins (Sharma et al., 2016a), cholesterol (Sharma et al., 2015b) etc., it can be concluded that effects of the membrane active molecules are correlated with the location of the molecules in the lipid membrane. If the additive molecules are located on the surface of the membrane it mainly affects the lateral motion of the lipid molecules. However, if molecules penetrate within the lipid membrane, both lateral and internal motions of the lipid are affected. Addition of these molecules enhances or restricts the membrane dynamics depending on their nature. It is worth mentioning that cholesterol also penetrates into the membrane core similar to the IL, but in contrast, it restricts both the lateral and internal motions of the lipid in the fluidic phase of membrane (Sharma et al., 2015b). This can be understood as the incorporation of cholesterol in the membrane's fluidic phase brings more order in the membrane while IL brings disorder in the membrane. These studies reveal that membrane dynamics are highly sensitive to the presence of membrane active molecules and can be used to decipher interactions of these additives with the cell membrane.

CONCLUSIONS

Quasielastic neutron scattering (QENS) has been used to study the effects of an ionic liquid (IL) on the dynamics of the membrane formed by liver extract lipid. A prototype imidazolium based IL [DMIM][BF4], has been used for the present study. QENS data analysis indicates the presence of two distinct lipid motions, (i) lateral motion of the lipid within the leaflet and (ii) internal motions of the lipid, in the ps timescale. The lateral motion of the lipid follows a continuous diffusion whereas the internal motions can be described using localized translational diffusion. Incorporation of IL in the liver lipid membrane is found to enhance the dynamics in the membrane, indicating an increase in membrane fluidity. Both lateral and internal motions of the lipid are accelerated due to the addition of the IL. This is explained on the basis of the location of the IL within the lipid membrane. As the IL goes into the membrane core and adopts a preferred orientation parallel to the lipid, increasing the disorder of the lipids and leading to enhanced mobility. Results are compared with various membrane active bio-molecules such as antimicrobial peptides, cholesterol, drugs, and vitamins. This comparison suggests a strong correlation between the location of the additive inside a lipid membrane and the microscopic dynamics of the lipid membrane. The present study also shows that a more physiologically relevant bio-membrane model system can be used for the study of the interaction of foreign molecules with cellular membranes. In particular, this model system would be an excellent one in which to incorporate trans- and peripheral membrane proteins to figure out if the effects of an ionic liquid on a living organism is related to purely the membrane reorganization or to a possible denaturation of the structure of proteins, or a combination of both.

DATA AVAILABILITY STATEMENT

The data that support the findings of this study are available from the corresponding author upon reasonable request. The QENS raw data can be found in Dr. Ramaprosad Mukhopadhyay et al. (2017): Dynamics in Bovine Lipid with ionic liquid, STFC ISIS Neutron and Muon Source, https://doi.org/10.5286/ISIS.E.89903473.

AUTHOR CONTRIBUTIONS

VS, RM, and SG designed the research project. VS, RM, and VG carried out experiments. VS wrote the manuscript with the inputs from all the authors. All authors contributed to the article and approved the submitted version.

REFERENCES

Aoun, B., González, M. A., Ollivier, J., Russina, M., Izaola, Z., Price, D. L., et al. (2010). Translational and reorientational dynamics of an imidazolium-based ionic liquid. *J. Phys. Chem. Lett*. 1, 2503–2507. doi: 10.1021/jz100856t

Armstrong, C. L., Trapp, M., Peters, J., Seydel, T., and Rheinstädter, M. C. (2011). Short range ballistic motion in fluid lipid bilayers studied by quasi-elastic neutron scattering. *Soft Matter* 7, 8358–8362. doi: 10.1039/c1sm05691c

Azuah, R. T., Kneller, L. R., Qiu, Y., Tregenna-Piggott, P. L. W., Brown, C. M., Copley, J. R. D., et al. (2009). DAVE: a comprehensive software suite for the reduction, visualization, and analysis of low energy neutron spectroscopic data. *J. Res. Natl. Inst. Stan. Technol*. 114:341. doi: 10.6028/jres.114.025

Bakshi, K., Mitra, S., Sharma, V. K., Jayadev, M. S. K., Sakai, V. G., Mukhopadhyay, R., et al. (2020). Imidazolium-based ionic liquids cause mammalian cell death due to modulated structures and dynamics of cellular membrane. *BBA Biomembr*. 1862:183103. doi: 10.1016/j.bbamem.2019.183103

Bee, M. (Ed.). (1988). "Quasielastic neutron scattering: principles and applications in solid state chemistry," in *Biology and Materials Science*, (Bristol: Adam Hilger).

Benedetto, A., and Ballone, P. (2016). Room temperature ionic liquids meet biomolecules: a microscopic view of structure and dynamics. *ACS Sustain. Chem. Eng.* 4, 392–412. doi: 10.1021/acssuschemeng.5b01385

Benedetto, A., Heinrich, F., Gonzalez, M. A., Fragneto, G., Watkins, E., and Ballone, P. (2014). Structure and stability of phospholipid bilayers hydrated by a room-temperature ionic liquid/water solution: a neutron reflectometry study. *J. Phys. Chem. B* 118, 12192–12206. doi: 10.1021/jp507631h

Bhattacharya, G., Giri, R. P., Saxena, H., Agrawal, V. V., Gupta, A., Mukhopadhyay, M. K., et al. (2017). X-ray reflectivity study of the interaction of an imidazolium-based ionic liquid with a soft supported lipid membrane. *Langmuir* 33, 1295–1304. doi: 10.1021/acs.langmuir.6b03192

Boggara, M. B., Faraone, A., and Krishnamoorti, R. (2010). Effect of pH and ibuprofen on the phospholipid bilayer bending modulus. *J. Phys. Chem. B* 114, 8061–8066. doi: 10.1021/jp100494n

Burankova, T., Cardozo, J. F. M., Rauber, D., Wildes, A., and Embs, J. P. (2018). Linking structure to dynamics in protic ionic liquids: a neutron scattering study of correlated and single-particle motions. *Sci. Rep*. 8, 16400–16410. doi: 10.1038/s41598-018-34481-w

Busch, S., Smuda, C., Pardo, L. C., and Unruh, T. (2010). Molecular mechanism of long-range diffusion in phospholipid membranes studied by quasielastic neutron scattering. *J. Am. Chem. Soc*. 132, 3232–3233. doi: 10.1021/ja907581s

Carlile, C. J., and Adams, M. A. (1992). The design of the IRIS inelastic neutron spectrometer and improvements to its analysers. *Phys. B* 182, 431–440. doi: 10.1016/0921-4526(92)90047-V

Dubey, P. S., Srinivasan, H., Sharma, V. K., Mitra, S., Sakai, V. G., and Mukhopadhyay, R. (2018). Dynamical transitions and diffusion mechanism in dodab bilayer. *Sci. Rep.* 8:1862. doi: 10.1038/s41598-018-19899-6

Egorova, K. S., Gordeev, E. G., and Ananikov, V. P. (2017). Biological activity of ionic liquids and their application in pharmaceutics and medicine. *Chem. Rev.* 117, 7132–7189. doi: 10.1021/acs.chemrev.6b00562

Flenner, E., Das, J., Rheinstädter, M. C., and Kosztin, I. (2009). Subdiffusion and lateral diffusion coefficient of lipid atoms and molecules in phospholipid bilayers. *Phys. Rev. E* 79:011907. doi: 10.1103/PhysRevE.79.011907

Gardner, J. S., Ehlers, G., Faraone, A., and Sakai, V. G. (2020). High-resolution neutron spectroscopy using backscattering and neutron spin-echo spectrometers in soft and hard condensed matter. *Nat. Rev. Phys.* 2, 103–116. doi: 10.1038/s42254-019-0128-1

Hassan, P. A., Rana, S., and Verma, G. (2015). Making sense of brownian motion: colloid characterization by dynamic light scattering. *Langmuir* 31, 3–12. doi: 10.1021/la501789z

Hayes, R., Warr, G. G., and Atkin, R. (2015). Structure and nanostructure in ionic liquids. *Chem. Rev.* 115, 6357–6426. doi: 10.1021/cr500411q

Jeong, S., Ha, S. H., Han, S.-H., Lim, M.-C., Kim, S. M., Kim, Y.-R, et al. (2012). Elucidation of molecular interactions between lipid membranes and ionic liquids using model cell membranes. *Soft Matter* 8, 5501–5506. doi: 10.1039/c2sm25223f

Lee, J. H., Choi, S. M., Doe, C., Faraone, A., Pincus, P. A., and Kline, S. R. (2010). Thermal fluctuation and elasticity of lipid vesicles interacting with pore-forming peptides. *Phys. Rev. Lett.* 105:038101. doi: 10.1103/PhysRevLett.105.038101

Liang, C. H., Ho, W. Y., Yeh, L. H., Cheng, Y. S., and Chou, T. H. (2013). Effects of 1-hexadecyl-3-methylimidazolium ionic liquids on the physicochemical characteristics and cytotoxicity of phosphatidylcholine vesicles. *Colloids Surf. A* 436, 1083–1091. doi: 10.1016/j.colsurfa.2013.08.040

Lipowsky, R., and Sackmann, E. (Eds.). (1995). "Structure and dynamics of membranes from cells to vesicles," in *Handbook of Biological Physics*, Vol. 1 (North Holland: Elsevier).

Machán, R., and Hof, M. (2010). Lipid diffusion in planar membranes investigated by fluorescence correlation spectroscopy. *Biochim. Biophys. Acta* 1798, 1377–1391. doi: 10.1016/j.bbamem.2010.02.014

Mamontov, E., Luo, H., and Dai, S. (2009). Proton dynamics in N,N,N′,N′-tetramethylguanidinium bis(perfluoroethylsulfonyl)imide protic ionic liquid probed by quasielastic neutron scattering. *J. Phys. Chem. B* 113, 159–169. doi: 10.1021/jp808102k

Marquardt, D., Heberle, F. A., Miti, T., Eicher, B., London, E., Katsaras, J., et al. (2017). 1H NMR shows slow phospholipid flip-flop in gel and fluid bilayers. *Langmuir* 33, 3731–3741. doi: 10.1021/acs.langmuir.6b04485

Matzke, M., Stolte, S., Thiele, K., Juffernholz, T., Arning, J., Ranke, J., et al. (2007). The influence of anion species on the toxicity of 1-alkyl-3-methylimidazolium ionic liquids observed in an (eco)toxicological test battery. *Green Chem.* 9, 1198–1207. doi: 10.1039/b705795d

McConnell, H. M., and Kornberg, R. D. (1971). Inside-outside transitions of phospholipids in vesicle membranes. *Biochemistry* 10, 1111–1120. doi: 10.1021/bi00783a003

Mitra, J. B., Sharma, V. K., Mukherjee, A., Sakai, V. G., Dash, A., and Kumar, M. (2020a). Ubiquicidin-derived peptides selectively interact with the anionic phospholipid membrane, *Langmuir* 36, 397. doi: 10.1021/acs.langmuir.9b03243

Nagao, M., Kelley, E. G., Ashkar, R., Bradbury, R., and Butler, P. D. (2017). Probing elastic and viscous properties of phospholipid bilayers using neutron spin echo spectroscopy. *J. Phys. Chem. Lett.* 8, 4679–4684. doi: 10.1021/acs.jpclett.7b01830

Nemoto, F., Kofu, M., Nagao, M., Ohishi, K., Takata, S., Suzuki, J. et al. (2018). Neutron scattering studies on short- and long-range layer structures and related dynamics in imidazolium-based ionic liquids. *J. Chem. Phys.* 149:054502. doi: 10.1063/1.5037217

Nickels, J. D., Cheng, X., Mostofian, B., Stanley, C., Lindner, B., Heberle, F. A., et al. (2015). Mechanical properties of nanoscopic lipid domains. *J. Am. Chem. Soc.*, 137, 15772–15780. doi: 10.1021/jacs.5b08894

Pendleton, J. N., and Gilmore, B. F. (2015). The antimicrobial potential of ionic liquids: a source of chemical diversity for infection and biofilm control. *Int. J. Antimicrob. Agents* 46, 131–139. doi: 10.1016/j.ijantimicag.2015.02.016

Perlo, J., Meledandri, C. J., Anoardo, E., and Brougham, D. F. (2011). Temperature and size-dependence of membrane molecular dynamics in unilamellar vesicles by fast field-cycling NMR relaxometry. *J. Phys. Chem. B* 115, 3444–3451. doi: 10.1021/jp2009034

Plechkova, N. V., Rogers, R. D., and Seddon, K. R. (2009). *Ionic Liquids: From Knowledge to Applications*. ACS Symposium Series no. 1030. Washington, DC: American Chemical Society.

Plechkova, N. V., and Seddon, K. R. (2008). Applications of ionic liquids in the chemical industry. *Chem. Soc. Rev.* 37, 123–150. doi: 10.1039/B006677J

Sharma, V. K., Ghosh, S. K., Mandal, P., Yamada, T., Shibata, K., Mitra, S., et al. (2017a). Effects of ionic liquids on the nanoscopic dynamics and phase behaviour of a phosphatidylcholine membrane. *Soft Matter* 13, 8969–8979. doi: 10.1039/C7SM01799E

Sharma, V. K., Mamontov, E., Anunciado, D. B., O'Neill, H., and Urban, V. (2015a). Nanoscopic dynamics of phospholipid in unilamellar vesicles: effect of gel to fluid phase transition. *J. Phys. Chem. B* 119, 4460–4470. doi: 10.1021/acs.jpcb.5b00220

Sharma, V. K., Mamontov, E., Anunciado, D. B., O'Neill, H., and Urban, V. S. (2015b). Effect of antimicrobial peptide on the dynamics of phosphocholine membrane: role of cholesterol and physical state of bilayer. *Soft Matter* 11, 6755–6767. doi: 10.1039/C5SM01562F

Sharma, V. K., Mamontov, E., Ohl, M., Tyagi, M., and Urban, V. S. (2017b). Incorporation of aspirin modulates the dynamical and phase behavior of the phospholipid membrane. *Phys. Chem. Chem. Phys.* 19, 2514–2524. doi: 10.1039/C6CP06202D

Sharma, V. K., Mamontov, E., and Tyagi, M. (2020). Effects of NSAIDs on the nanoscopic dynamics of lipid membrane. *BBA Biomembr.* 2:183100. doi: 10.1016/j.bbamem.2019.183100

Sharma, V. K., Mamontov, E., Tyagi, M., Qian, S., Rai, D. K., and Urban, V. S. (2016b). Dynamical and phase behavior of a phospholipid membrane altered by an antimicrobial peptide at low concentration. *J. Phys. Chem. Lett.* 7, 2394–2401. doi: 10.1021/acs.jpclett.6b01006

Sharma, V. K., Mamontov, E., Tyagi, M., and Urban, V. S. (2016a). Effect of α-tocopherol on the microscopic dynamics of dimyristoyl phosphatidylcholine membrane. *J. Phys. Chem. B* 120, 154–163. doi: 10.1021/acs.jpcb.5b10417

Sharma, V. K., Mitra, S., Verma, G., Hassan, P. A., Sakai, V. G., and Mukhopadhyay, R. (2010). Internal dynamics in SDS micelles: neutron scattering study. *J. Phys. Chem. B* 114, 17049–17056. doi: 10.1021/jp108274y

Sharma, V. K., Mitra, S., and and Mukhopadhyay, R. (2019a). Dynamic landscape in self-assembled surfactant aggregates. *Langmuir* 35:14151. doi: 10.1021/acs.langmuir.8b03596

Sharma, V. K., and Mukhopadhyay, R. (2018). Deciphering interactions of ionic liquids with biomembrane. *Biophys. Rev.* 10:721. doi: 10.1007/s12551-018-0410-y

Sharma, V. K., Nagao, M., Rai, D. K., and Mamontov, E. (2019b). Membrane softening by nonsteroidal anti-inflammatory drugs investigated by neutron spin echo. *Phys. Chem. Chem. Phys.* 21, 20211–20218. doi: 10.1039/C9CP03767E

Singh, P., Sharma, V. K., Singha, S., Sakai, V. G., Mukhopadhyay, R., Das, R., et al. (2019). Unraveling the role of monoolein in fluidity and dynamical response of a mixed cationic lipid bilayer. *Langmuir* 35, 4682–4692. doi: 10.1021/acs.langmuir.9b00043

Srinivasan, H., Sharma, V. K., Mitra, S., and Mukhopadhyay, R. (2018). Heterogeneity in dynamics of dioctadecyldimethylammonium bromide bilayers: molecular dynamics simulation and neutron scattering study. *J. Phys. Chem. C* 122:20419. doi: 10.1021/acs.jpcc.8b06216

Taylor, J., Arnold, O., Bilheaux, J., Buts, A., Campbell, S., et al. (2012). Mantid, a high performance framework for reduction and analysis of neutron scattering data. *Bull. Am. Phys. Soc.* 57:W26.

Tocanne, J. F., Dupou-Ciézanne, L., and Lopez, A. (1994). Lateral diffusion of lipids in model and natural membranes. *Prog. Lipid Res.* 33, 203–237. doi: 10.1016/0163-7827(94)90027-2

Triolo, A., Mandanici, A., Russina, O., Rodriguez-Mora, V., Cutroni, M., Hardacre, C., et al. (2006). Thermodynamics, structure, and dynamics in

room temperature ionic liquids: the case of 1-Butyl-3-methyl imidazolium hexafluorophosphate ([bmim][PF6]). *J. Phys. Chem. B* 110, 21357–21364. doi: 10.1021/jp062895t

Volino, F., and Dianoux, A. J. (1980). Neutron incoherent scattering law for diffusion in a potential of spherical symmetry: general formalism and application to diffusion inside a sphere. *Mol. Phys.* 41, 271–279. doi: 10.1080/00268978000102761

Wanderlingh, U., D'Angelo, G., Branca, C., Nibali, V. C., Trimarchi, A., Rifici, S., et al. (2014). Multi-component modeling of quasielastic neutron scattering from phospholipid membranes. *J. Chem. Phys.* 140:174901. doi: 10.1063/1.4872167

Woodka, A. C., Butler, P. D., Porcar, L., Farago, B., and Nagao, M. (2012). Lipid bilayers and membrane dynamics: insight into thickness fluctuations. *Phys. Rev. Lett.* 109:058102. doi: 10.1103/PhysRevLett.109.058102

Yoo, B., Shah, J. K., Zhu, Y., and Maginn, E. J. (2014). Amphiphilic interactions of ionic liquids with lipid biomembranes: a molecular simulation study. *Soft Matter* 10, 8641–8651. doi: 10.1039/C4SM01528B

Conflict of Interest: The authors declare that they have no conflicts of interest with the contents of this article.

frontiers in Chemistry

ORIGINAL RESEARCH
published: 05 January 2021
doi: 10.3389/fchem.2020.613388

Surfactant Monolayer Bending Elasticity in Lipase Containing Bicontinuous Microemulsions

Sandra Engelskirchen[1], Stefan Wellert[2], Olaf Holderer[3], Henrich Frielinghaus[3], Michaela Laupheimer[1], Sven Richter[1], Bettina Nestl[1], Bernd Nebel[1] and Bernhard Hauer[1]*

[1] Department of Chemistry, Universität Stuttgart, Stuttgart, Germany, [2] Department of Chemistry, Technische Universität Berlin, Berlin, Germany, [3] Jülich Centre for Neutron Science (JCNS) at Heinz Maier-Leibnitz Zentrum (MLZ), Forschungszentrum Jülich GmbH, Garching, Germany

Lipase-catalyzed reactions offer many advantages among which a high degree of selectivity combined with the possibility to convert even non-natural substrates are of particular interest. A major drawback in the applicability of lipases in the conversion of synthetically interesting, non-natural substrates is the substantial insolubility of such substrates in water. The conversion of substrates, natural or non-natural, by lipases generally involves the presence of a water–oil interface. In the present paper, we exploit the fact that the presence of lipases, in particular the lipase from *Candida antarctica* B (CalB), changes the bending elastic properties of a surfactant monolayer in a bicontinuous microemulsion consisting of D_2O/NaCl -n-(d)-octane-pentaethylene glycol monodecyl ether ($C_{10}E_5$) in a similar manner as previously observed for amphiphilic block-copolymers. To determine the bending elastic constant, we have used two approaches, small angle neutron scattering (SANS) and neutron spin echo (NSE) spectroscopy. The time-averaged structure from SANS showed a slight decrease in bending elasticity, while on nanosecond time scales as probed with NSE, a stiffening has been observed, which was attributed to adsorption/desorption mechanisms of CalB at the surfactant monolayer. The results allow to derive further information on the influence of CalB on the composition and bending elasticity of the surfactant monolayer itself as well as the underlying adsorption/desorption mechanism.

Keywords: microemulsion, lipase, bending elasticity, neutron scattering, neutron spin echo

OPEN ACCESS

Edited by:
Ramesh L. Gardas, Indian Institute of Technology Madras, India

Reviewed by:
Amiya Kumar Panda, Vidyasagar University, India
Douglas Hayes, The University of Tennessee, United States

****Correspondence:***
Olaf Holderer
o.holderer@fz-juelich.de

Specialty section:
This article was submitted to Physical Chemistry and Chemical Physics, a section of the journal Frontiers in Chemistry

Received: *02 October 2020*
Accepted: *04 November 2020*
Published: *05 January 2021*

Citation:
Engelskirchen S, Wellert S, Holderer O, Frielinghaus H, Laupheimer M, Richter S, Nestl B, Nebel B and Hauer B (2021) Surfactant Monolayer Bending Elasticity in Lipase Containing Bicontinuous Microemulsions. Front. Chem. 8:613388. doi: 10.3389/fchem.2020.613388

1. INTRODUCTION

Lipases belong to the most well-investigated class of enzymes. Lipases show positional, substrate, and stereo-specificity toward their substrates. Whether or not lipases show as well promiscuous activity depends on reaction conditions and the nature of the substrate. Recent research revealed that lipases show great potential in catalyzing standard organic reactions such as: *C-C bond formation, Aldol-addition, Michael-addition, Mannich reaction, C-heteroatom and heteroatom-heteroatom bond formation, perhydrolysis and epoxidation, synthesis of heterocycles, and Hantzsch reactions* (Dwivedee et al., 2018). The non-natural substrates used in these organic reactions are, however, usually poorly water soluble such that a vehicle needs to be found to bring the lipases into contact with these kind of substrates.

Colloidal dispersions, especially microemulsions, have been identified to offer great potential acting as a reaction vehicle for lipase and substrate in providing large interfacial area between water and oil domains. In the present study, we exploit the fact that the influence of the lipase from *Candida antarctica B* (CalB) has already been investigated (Subinya et al., 2014). **Figure 1A** shows the phase diagrams obtained at equal volume fractions of sodium chloride solution (0.4 wt%) and *n*-octane ($\phi = 0.50$) as a function of temperature and $C_{10}E_5$ mass fraction γ for increasing CalB concentrations added to the water phase: 1, 10, 50, and 100 mg/ml. Together with the minimum surfactant concentration needed for complete solubilization of water and oil in the onset of the single-phase region, the phase inversion temperature defines the point X (T_m, γ). In the blank H_2O/NaCl (0.4 wt.%)–*n*-octane–$C_{10}E_5$ system, the location of the X-point had already been well-known (T_m = 38.75°C, γ=0.15). Introducing increasing CalB concentrations to the water phase of the microemulsion revealed that for CalB concentrations of up to 10 mg/ml, the phase boundaries shifted to lower temperatures and the efficiency of the microemulsion increased, hence, less $C_{10}E_5$ was needed to totally solubilize the water and the octane phase. Above this concentration, the temperature trend continued, but the efficiency trend was found to be reversed. The efficiency even decreased below the blank microemulsion. In partitioning studies in Subinya et al. (2014), it has also been shown that the largest part, 80–90%, of CalB is related to the interface. **Figure 1B** shows the development of $\tilde{\gamma}$ as a function of CalB concentration to visualize the trends observed. Furthermore, it was found that the temperature T_m drops continuously with increasing CalB amount. CalB thus obviously induces the surfactant monolayer, which forms the microemulsion membrane, to bend toward the water domain.

To characterize the structural parameters and to access the bending elastic constants of an amphiphilic interface, scattering methods still remain the first choice. In recent years, many studies used light, X-ray, and neutron scattering techniques to explore the manifold of structures that are present in the different phase regions of the large variety of the studied phase systems (Komura, 2007; Gradzielski, 2008; Hoffmann, 2014; Oberdisse and Hellweg, 2017). Beside the influence of composition and thermodynamic variables, the changes in the phase structures due to the presence of additives, for example, enzymes, are accessible by applying these techniques, which improves the understanding of the bio-organic reaction mechanisms inside microemulsions (Hayes et al., 2015). For example, a combination of scattering techniques was used to investigate the effect of the enzyme DFPase, which efficiently hydrolyzes organophosphates, on the structure and dynamics of the host microemulsion with a bicontinuous structure (Wellert et al., 2011). Moreover, enzymes, such as the green fluorescent protein can be used as probes inside the aqueous phase of bicontinuous microemulsions to study fundamentals of diffusion in confinement (Wrede et al., 2019).

In this paper, we combine neutron small angle scattering (SANS) and neutron spin echo spectroscopy (NSE) to measure the effect of the addition of the lipase CalB on the amphiphilic interface inside the investigated bicontinuous microemulsions of the ternary system D_2O/NaCl–n-(d)-octane–$C_{10}E_5$. Changes in the bending elastic constants observed upon the introduction of CalB at different concentrations up to 100 mg/ml provide deep insights into the mechanisms underlying the adsorption/desorption of the lipase to the interfacial layer.

2. THEORY

Unlike emulsions and nanoemulsions, microemulsions are thermodynamically stable, fluid mixtures of at least water, oil, and surfactant (Strey, 1994; Schwarz and Gompper, 2002). Such mixtures may adopt a variety of complex structures depending on

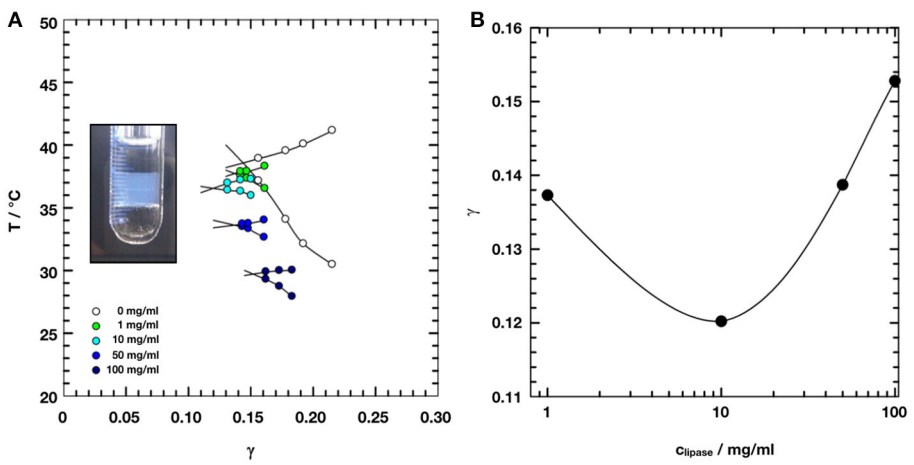

FIGURE 1 | (A) Phase diagrams of microemulsions of type H_2O/NaCl (0.4wt%)– *n*-octane–$C_{10}E_5$–lipase *Candida antarctica B* at equal volume fractions of water and oil $\phi = 0.50$ with increasing concentration of lipase from 0 to 100 mg/ml referred to the water phase. Adapted with permission from Subinya et al. (2014), Copyright 2014 American Chemical Society. **(B)** X-points of the respective microemulsions as a function of lipase concentration. At 10 mg/ml of lipase, the efficiency of the microemulsion runs through a maximum.

the nature of the components, their concentration in the mixture, and on temperature and pressure. The structural properties of the interface depend strongly on the surfactant packing parameter, which measures the ratio of the size of the hydrophilic headgroup and the length of the lipophilic alkyl chain. The topology of the amphiphilic interface is characterized by its curvature and mechanical properties.

The structure of bicontinuous microemulsions can be analyzed either by high-resolution electron microscopy on a freeze fractured microemulsion sample (Davis et al., 1989; Belkoura et al., 2004) or small angle neutron or X-ray scattering (Sottmann et al., 1997; Byelov et al., 2004; Oberdisse and Hellweg, 2017). Characteristic features of the bicontinuous structure are a low degree of ordering and an interconnected, random distribution of oil and water domains of varying size. In a bicontinuous microemulsion, the spontaneous curvature is zero, i.e., the bending of the surfactant film to either side requires the same amount of energy (Schwarz and Gompper, 2002). Cryo TEM images of a very similar bicontinuous microemulsion can be found (e.g., in Belkoura et al., 2004). Typically, such samples show scattering patterns with a broad peak and a steep decay of the scattered intensity at higher scattering angles, respective higher values of the scattering vector Q.

If the sample is prepared in bulk contrast, which provides high scattering contrast between the protonated oil and the deuterated water phase, the scattered intensity can be described by the *Teubner–Strey* (Teubner and Strey, 1987) equation:

$$I_{\mathrm{TS}}(Q) = \frac{8\pi \langle \nu^2 \rangle / \xi_{\mathrm{TS}}}{p^2 - 2Q_{\mathrm{max}}^2 Q^2 + Q^4} \tag{1}$$

In this model, Q is the magnitude of the scattering vector defined as $Q = 4\pi/\lambda \sin(\theta/2)$ with the scattering angle θ and $\langle \nu^2 \rangle$ being the mean square scattering length density fluctuation, which is a measure of the scattering contrast. The quantities $p^2 = (2\pi/D_{\mathrm{TS}})^2 + 1/\xi_{\mathrm{TS}}^2$ and $Q_{\mathrm{max}}^2 = (2\pi/D_{\mathrm{TS}})^2 - 1/\xi_{\mathrm{TS}}^2$ can be used to calculate the mean size of the oil and water domains D_{TS} and the mean correlation length ξ_{TS} of this structure.

The contribution of the elastic properties of the amphiphilic interface of a microemulsion to the free energy can be described by the *Helfrich* Hamiltonian:

$$f_{\mathrm{el}} = \frac{1}{2}\kappa(H - c_0)^2 + \bar{\kappa} K \tag{2}$$

with the total curvature $H = c_1 + c_2$ of the film and $K = c_1 c_2$ being the Gaussian curvature. This equation connects the bending elasticity constant κ and the saddle-splay modulus $\bar{\kappa}$ with the principal curvatures c_1 and c_2 and the mean curvature c_0 of the interfacial surfactant layer in its lowest energetic state (Safran, 1999) taking into account not only elastic but also topological features of the respective structure formed by the amphiphilic interface. Here, the bending elasticity constant κ measures the energy required to deviate the interfacial film from the spontaneous curvature c_0 at the free energy minimum. Similarly, the saddle-splay modulus $\bar{\kappa}$ is a measure of the energy cost for saddle-splay deformations (Safran, 1999). The bending elasticity constant is sensitive to changes in topology and interfacial composition and directly accessible by scattering. Thermally excited undulations lead to a softening of the interfacial film and to a length scale-dependent modification of the bare bending rigidity κ_0, which is called the renormalized bending elasticity constant:

$$\frac{\kappa_{\mathrm{SANS}}}{k_{\mathrm{B}}T} = \frac{\kappa_{0,\mathrm{SANS}}}{k_{\mathrm{B}}T} - \frac{3}{4\pi}\ln\left(\frac{D_{\mathrm{TS}}}{2l_{\mathrm{s}}}\right) \tag{3}$$

It is related to the structural length scales inside the bicontinuous structure by Pieruschka et al. (1995):

$$\frac{\kappa_{\mathrm{SANS}}}{k_{\mathrm{B}}T} = \frac{10\pi\sqrt{3}}{64}\frac{\xi_{\mathrm{TS}}}{D_{\mathrm{TS}}} \tag{4}$$

The saddle-splay modulus can be obtained from phase diagram measurements (Holderer et al., 2013). We denote the bare moduli, which are not affected by renormalization effects, with the subscript 0, and denote the technique also in the subscript (which mainly is relevant for the renormalized moduli and only in the special case of influences of the observation time is also relevant for the bare moduli, as explained later). Monte-Carlo simulations of triangulated surfaces (Peltomäki et al., 2012) and combined phase diagram, SANS, and NSE experiments (Holderer et al., 2013) showed that the bending rigidity measured by SANS is a combination of κ and $\bar{\kappa}$, $\kappa_{0,SANS} = (a_1\kappa_0 + a_2|\bar{\kappa}_0|)$. Also the renormalization term in Equation (3) is slightly modified by a combination of the renormalization terms of κ and $\bar{\kappa}$ and reads $(3a_1 + 10/3|a_2|)/(4\pi)\ln(D_{TS}/2l_s)$ with $a_1 = 0.19$ and $a_2 = -0.84$ (Holderer et al., 2013). These corrections have been applied for the values of the bending rigidity from SANS measurements presented in this paper.

Contributions to dynamic properties in bicontinuous microemulsions result from collective hydrodynamic motions of the sponge-like structure (Holderer et al., 2007) and local thermally excited undulations of the interfacial film (Safran, 1999). The bending elasticity constant κ of the interfacial film and the viscosity η of the surrounding solvent dissipate the undulation energy.

Neutron spin-echo spectroscopy measures the intermediate scattering function $S(Q,\tau_{\mathrm{NSE}})$ normalized by the static structure factor S(Q,0) obtained from an appropriate reference sample. In the low Q-range, at $Q<Q_{\mathrm{max}}$, collective motions are dominant while with increasing Q the amplitude of these motions decreases until at $Q>>Q_{\mathrm{max}}$ the thermal undulations of the interface dominate. Zilman and Granek (1996) derived a stretched exponential form of the normalized intermediate scattering function $S(Q,\tau_{\mathrm{NSE}})/S(Q,0)$ as according to the following equation:

$$\frac{S(Q,\tau_{\mathrm{NSE}})}{S(Q,0)} = \exp\left(-(\Gamma\tau_{\mathrm{NSE}})^{\beta}\right) \tag{5}$$

with a stretching exponent $\beta = 2/3$. The underlying model assumes an ensemble of randomly oriented and independently fluctuating membrane patches dispersed in the viscous solvent.

Within this model, the relaxation rate of the membrane undulations is given by the following equation:

$$\Gamma_u = 0.025\gamma_\kappa \left(\frac{k_B T}{\kappa_{0,\mathrm{NSE}}}\right)^{1/2} \frac{k_B T}{\eta} Q^3 \tag{6}$$

which contains the bare bending elasticity constant $\kappa_{0,\mathrm{NSE}}$ of the interface and the parameter γ_κ given by $\gamma_\kappa \simeq 1 - 3(k_B T/(4\pi\kappa_{0,\mathrm{NSE}})\ln(Q\xi) \simeq 1$ for large enough κ. In a more recent paper, Zilman and Granek refined their analyses of the intermediate scattering function and deduced a more complex formulation including deviations of β from 2/3 depending on the bending elasticity constant (Zilman and Granek, 2002). However, since these effects are rather small, due to limited statistics and measurement time in a typical neutron scattering experiment, we use the previously derived exponent.

3. MATERIALS

Pentaethylene glycol monodecyl ether ($C_{10}E_5$) was obtained in a purity of >97% from Sigma Aldrich, Germany. The lipase *Candida antarctica B* (CalB) was ordered in lyophilized form from Biocatalytics, Pasadena, USA. Purification was performed using ion-exchange chromatography and carried out in the Institute of Technical Biochemistry, Stuttgart, Germany, following the protocol given below. Sodium chloride p.a. was purchased from Merck, Germany, and n-octane in analytical grade was purchased from Fluka, Germany. D_2O and d(18)-octane were obtained from Sigma Aldrich, Germany.

3.1. Purification Protocol

CalB was purified using a cation-exchange chromatography system. A XK 16/20 column (Amersham Biosciences) filled with 7 mL Source 15 S (Amersham Biosciences) was equilibrated with 10 mM sodium formate, 10 mM sodium citrate, and 10 mM sodium acetate, pH 3 (buffer A). A sample volume of 2 mL of the enzyme was loaded onto the column at a volumetric flow rate of 5 mL/min. Afterward, the column was washed with a threefold column volume of buffer A. CalB was eluted with five column volumes of 10 mM sodium formate, 10 mM sodium citrate, and 10 mM sodium acetate, pH 5.5. Chromatography columns and resins were purchased from Amersham Biosciences. All chromatography experiments were carried out at room temperature (20°C) using an ÅKTA explorer chromatography system (Amersham Biosciences) controlled by Unicorn software 3.21.

4. EXPERIMENTAL SECTION

4.1. Microemulsion Sample Preparation

All samples were prepared at a constant oil to water plus oil volume fraction of (ϕ) = 0.50:

$$\phi = \frac{V_{\mathrm{oil}}}{V_{\mathrm{oil}} + V_{\mathrm{buffer}}} \tag{7}$$

A mass fraction ϵ of 0.004 (0.4wt.%) of sodium chloride in D_2O was kept constant for all samples:

$$\epsilon = \frac{m_{\mathrm{NaCl}}}{m_{\mathrm{NaCl}} + m_{\mathrm{buffer}}} \tag{8}$$

Each sample was prepared at a surfactant mass fraction of γ = 0.15 (15 wt.%) irrespective of the CalB concentration.

$$\gamma = \frac{m_{\mathrm{surfactant}}}{m_{\mathrm{surfactant}} + m_{\mathrm{oil}} + m_{\mathrm{buffer}}} \tag{9}$$

This value was chosen from the previously obtained phase diagrams for microemulsions consisting of H_2O/NaCl–n-octane–$C_{10}E_5$–CalB shown in **Figure 1** (Subinya et al., 2014). This value was chosen to ensure that a single phase bicontinuous microemulsion would exist for every CalB concentration, thus taking into account the development of the efficiency of the microemulsion as a function of CalB concentration. In calculating sample compositions, the density differences of H_2O and D_2O as well as n-octane and d-octane were also taken into account.

All samples were prepared on site and phase boundaries were detected via visual inspection as a function of temperature. The respective components were weighed into glass vessels within an accuracy of ±0.0005 g, closed with a polyethylene stopper and sealed with Parafilm. A thermostated water bath setup consisting of thermostat (DC30, Haake, Germany), a precision thermometer (GMH 3750, Greisinger, Germany), a magnetic stirrer (HeiMix L, Heidolph, Germany), and a microscopy lamp (Gerhardt Optik and Feinmechanik, Germany) was used to obtain the phase boundaries. Phase transitions were determined to an accuracy of ±0.05°C.

The lipase CalB was introduced into the microemulsion from a concentrated stock solution of 100 mg/ml enzyme in D_2O/NaCl solution and respective dilutions.

Different contrasts can be applied in neutron scattering by selectively deuterating parts of the sample. In this study, we measured the structure of the microemulsion in so-called "bulk contrast," where H_2O has been replaced by D_2O, the rest being protonated materials. It provides contrast between the major domains water and (surfactant+oil). The SANS experiments have been performed in "bulk contrast." For studying the membrane dynamics with NSE, "film contrast" has been chosen, with deuterated water, deuterated oil, and protonated the surfactant, providing contrast between the surfactant membrane and its environment. The enzyme was protonated in all cases. All experiments have been done close to the X-point of the phase diagram to ensure that temperature shifts due to deuteration are properly taken into account; the phase boundaries for each sample have been determined on site with the actual sample. After the determination of the phase boundaries, the samples were transferred into 2 mm Quartz cuvettes for NSE or 1 mm Quartz cuvettes for SANS measurements. **Table 1** shows the respective sample measurement temperatures that were interpolated from the location of the phase boundaries as determined on site.

TABLE 1 | Temperature conditions of the experiments.

Lipase CalB (mg/ml)	T_{SANS} (°C)	T_{NSE} (°C)
0	35.2	35.5
10	33.3	33.6
50	28.3	30.0
100	24.0	24.5

4.2. Small Angle Neutron Scattering

SANS measurements were performed on the small angle scattering instruments KWS-1 (Feoktystov et al., 2015; Frielinghaus et al., 2015) and KWS-2 (Radulescu et al., 2015) at the high flux neutron source FRM II (Garching, Germany). Scattering curves were determined at three different sample/detector (^{6}Li-Scintillator 1 mm thickness + photomultiplier) distances of 2 m, 8 m, and 20 m accessing the q-range covering the structure peak followed by the Q^{-4} decay. Scattering measurements were performed at a neutron wavelength of $\lambda = 4.7$ Å (Dornier velocity selector, FWHM 10%). Quartz cuvettes of 1 mm in diameter (Hellma, Mülheim/Baden, Germany) were mounted on a thermostated sample holder. This sample thickness ensures that at the used wavelength multiple scattering effects play only a minor role in determining the structural parameters of the microemulsion (Frielinghaus, 2018). The temperature was operated by remote control to allow temperature-dependent measurements. Calibration measurements (empty cell, water, and plexi-glass) were carried out to adjust the spectrometer parameters. The raw data for the two detector distances were joined and the scattering signals were converted to absolute intensity using the supplied on-site software qtiKWS and qtiSAS. The resulting scattering curves were fitted to the *Teubner–Strey* model using Sigma Plot.

4.3. Neutron Spin-Echo Spectroscopy

In neutron spin-echo spectroscopy, the polarization state of a polarized neutron beam after quasi-elastic scattering at a sample is analyzed. The magnetic moment of the neutrons associated with the neutron spin is utilized to control and manipulate their Lamor precession in magnetic guiding fields prior and after the sample. The obtained polarization signal can be related to the Fourier transform of the dynamic structure factor S(Q,ω), which is the intermediate scattering function $S(Q, \tau_{NSE})$. The Fourier time τ_{NSE} is a parameter depending on the neutron wavelength and the integral of the magnetic field along the neutron path. It has the dimension of time. During a measurement, the Fourier time is varied by changing the magnetic field. Experimental details are well-described in the literature and we refer to a series of papers describing method and instrumentation (Hoffmann, 2014; Pasini et al., 2019; Zolnierczuk et al., 2019).

Neutron spin-echo measurements were carried out on the small angle spin-echo spectrometer J-NSE located at the NL2a neutron guide of the high flux neutron source FRMII (Garching, Germany)(Holderer et al., 2008). The normalized intermediate scattering functions $S(Q, \tau_{NSE})/S(Q, 0)$ were measured in a momentum transfer range of $Q = 0.05$–0.2 Å^{-1} using neutron wavelengths of 8, 10, and 12 Å exploring a Fourier time window of $\tau_{NSE} = 0.08$–120 ns. However, here we focus on an analysis of the short time dynamics. Therefore, we restrict the measured data to Fourier times of up to 40 ns. The sample temperature was adjusted in a thermostated bath according to the previously determined phase behavior. The samples were prepared in film contrast and measured in Hellma Quartz cells of 2 mm thickness. The film contrast allows for thicker samples, and multiple scattering plays only a minor effect due to the weaker contrast and due to the circumstance that multiple incoherent scattering quickly depolarizes the beam.

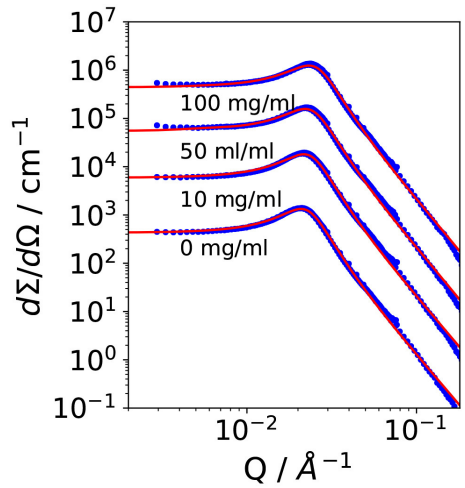

FIGURE 2 | Small angle scattering data of the bicontinuous microemulsions from the ternary system H_2O/NaCl–*n*-octane–pentaethylene glycol monodecylether ($C_{10}E_5$) with different amounts of lipase *Candida antarctica* B (CalB). The data were shifted by a factor of 10 for better visibility.

5. RESULTS

The aim of the presented study is to investigate the influence of the lipase CalB on the bending elasticity of a bicontinuous microemulsion with neutron scattering techniques. The symmetric microemulsion (with the same amounts of water and oil) was always held in the right temperature where it forms a sponge phase. The surfactant concentration was kept constant. Only the concentration of the lipase was varied as the main question, which shall be addressed here.

5.1. Determination of the Bending Elasticity Constant With SANS

Figure 2 shows small angle scattering curves obtained for bicontinuous microemulsion samples containing no enzyme (reference, 0 mg/ml) and 10, 50, or 100 mg/ml of the lipase CalB.

All scattering curves show the characteristic plateau region in the low Q-range followed by the broad structure peak and the steep decay with a Q^{-4} dependence of the scattered intensity in the high *Q*-range. The solid lines are fits to the *Teubner-Strey* model, which describes the scattering around the structure peak.

TABLE 2 | Parameters obtained from small angle neutron scattering (SANS) and phase diagram measurements: Correlation length and domain size determined from SANS experiments and deduced bending rigidity κ_{SANS}, saddle-splay modulus $\bar{\kappa}_{0,Phase}$ from the phase diagram, and $\bar{\kappa}_{0,SANS}$ from SANS as well as $\kappa_{0,SANS|NSE}$ from SANS and neutron spin echo (NSE) measurements as lined out in Holderer et al. (2013).

Lipase CalB (mg/ml)	ξ_{TS} (Å)	D_{TS} (Å)	κ_{SANS} (k_BT)	$\bar{\kappa}_{0,Phase}$ (k_BT)	$\bar{\kappa}_{0,SANS}$ (k_BT)	$\kappa_{0,SANS}$ (k_BT)	$\kappa_{0,NSE}$ (k_BT)
0	146	286	0.43	−0.69	−0.82	0.85	0.87 ± 0.03
10	140	276	0.43	−0.73	−0.79	0.84	0.92 ± 0.03
50	131	270	0.41	−0.69	−0.75	0.82	0.96 ± 0.02
100	124	256	0.41	−0.66	−0.72	0.80	1.03 ± 0.02

The statistical errors from the fits were ≈ 1 Å for d and ξ, and 0.01 kT for the bending rigidities determined from SANS measurements.

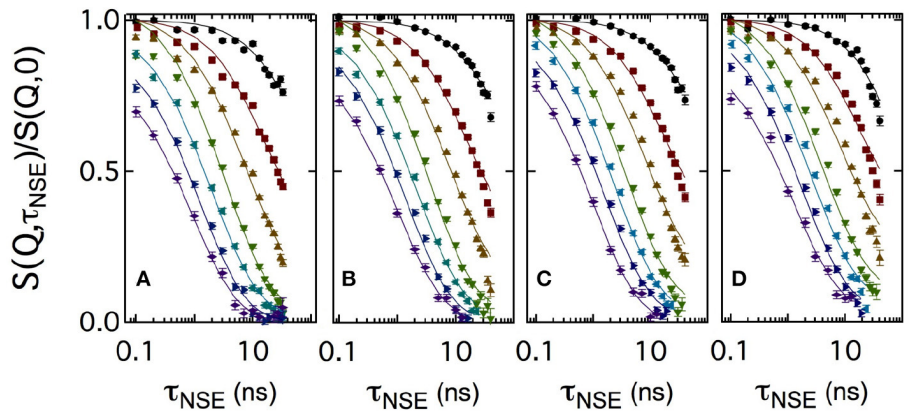

FIGURE 3 | Semi-logarithmic representation of the normalized intermediate scattering functions $S(Q, \tau_{NSE})/S(Q, 0)$ obtained at momentum transfer values $Q = 0.05$, 0.08, 0.12, 0.15, 0.18, 0.21, and 0.24Å^{-1} (from top to bottom). A bicontinuous microemulsion in film contrast with four enzyme concentrations of 0 mg/ml **(A)**, 10 mg/ml **(B)**, 50 mg/ml **(C)**, and 100 mg/ml **(D)** was measured. The solid lines are fits to the data according to Equation (5).

The Porod contribution at high-Q is included into the model (Frank et al., 2007):

$$I(Q) = \left(I_{TS}(Q) + \frac{G\,\mathrm{erf}^{12}(1.06QR_g/\sqrt{6})}{1.5Q^4R_g^4} \right) \exp(-\sigma^2Q^2) + I_{bgr} \tag{10}$$

It is R_g the radius of gyration, σ a surface roughness parameter, and G the amplitude of the Porod scattering contribution. The calculated values of ξ_{TS} and D_{TS} are summarized in **Table 2**. Within the accuracy of the fit routine, no significant dependence of the values was observed when the concentration of CalB was increased up to 100 mg/ml.

Following Safran and Pieruschka, the renormalized bending elastic constant κ_{SANS} can be calculated from D_{TS} and ξ_{TS} by applying Equation (4). Since the addition of CalB did not affect the structural parameters, the calculated values for κ_{SANS} remain constant as a function of CalB concentration.

5.2. Determination of the Bending Elasticity Constant From NSE

Figure 3 shows a set of normalized intermediate scattering functions $S(Q, \tau_{NSE})/S(Q, 0)$ in semi-logarithmic representation. The data were measured with the bicontinuous microemulsions prepared in film contrast where in addition to the deuterated water phase also the oil phase was deuterated. As for the SANS measurements, CalB concentrations of 0 mg/ml (a), 10 mg/ml (b), 50 mg/ml (c), or 100 mg/ml (d) in deuterated sodium chloride solution were used. At low Q values, the curves show a partial decay. At larger Q, the curves fully decay to zero level within the observed Fourier time window. This is the general behavior observed for all measured lipase concentrations.

Usually, intermediate scattering functions measured with bicontinuous microemulsions are fitted with a combination of the stretched exponential accounting for the membrane undulations and a single exponential term including the collective hydrodynamic motions into the analysis. This collective dynamics is measured by dynamic light scattering in an additional independent experiment (Hellweg et al., 2001; Wellert et al., 2010; Klostermann et al., 2012). Here, we choose a different approach. At large Q, the diffusive component from large-scale density fluctuations may be neglected, because the Q^3 dependence of the membrane fluctuations dominates at large Q over the Q^2 dependence of the density fluctuations. A numerical computation routine

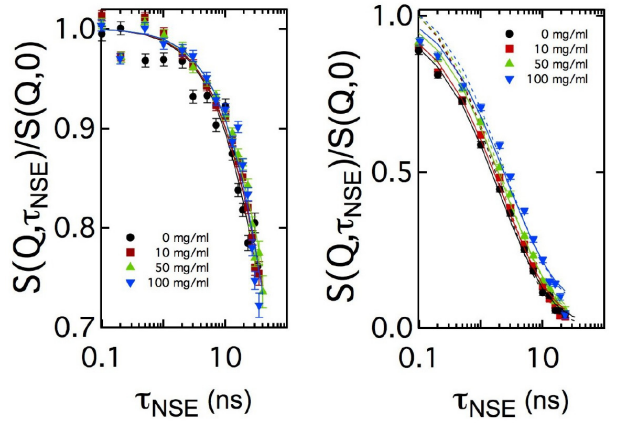

FIGURE 4 | Comparison of the normalized intermediate scattering functions $S(Q, \tau_{NSE})/S(Q, 0)$ measured at $Q = 0.05\text{Å}^{-1}$ and $Q = 0.18\text{Å}^{-1}$ for all enzyme concentrations in semi-logarithmic representation. In the low Q-range, corresponding to length scales close to $2\pi/Q_{max}$, no significant difference in the decay rates is visible while at length scales much smaller than $2\pi/Q_{max}$ the decay of the intermediate scattering function slows down with increasing enzyme concentration. Solid lines are fits according to Equation (5). Additional dashed lines in the right image show fitting results with a fixed amplitude of $S(Q, \tau_{NSE})/S(Q, 0) = 1$, while the solid line uses this amplitude as additional free fitting parameter.

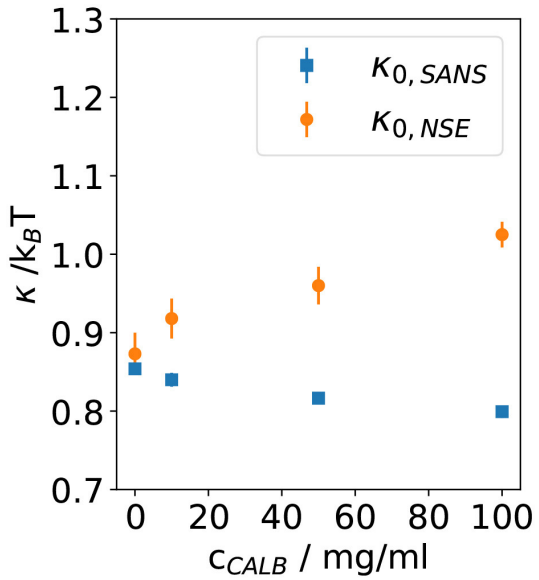

FIGURE 5 | Bending rigidity constant κ_0 obtained from fitting Equation (5) to the normalized intermediate scattering functions shown in **Figure 1** for four samples with different lipase concentrations. Results from neutron spin echo (NSE) measurements are compared with the resulting values from analyzing the small angle neutron scattering (SANS) data.

of $S(Q,\tau_{NSE})$ was previously developed to avoid further approximations and complementary measurements:

$$S(Q, \tau_{NSE}) \propto \int_0^1 d\mu \int_0^R dr\, rJ_0\left(Qr\sqrt{1-\mu^2}\right) \exp\left(-\frac{k_B T}{2\pi\kappa} Q^2\mu^2 \int_{k_{min}}^{k_{max}} \frac{dk}{k^3}\left(1 - J_0(kr)e^{-\omega(k)t}\right)\right) \quad (11)$$

which includes three nested integrals and the Bessel function of order 0 $J_0(kr)$. The integration limits are set by the maximum and minimum values of the system length scales. Here, the lowest wavevector k_{min} is related to the maximum real space value $r_{max} = 2\pi/k_{min}$, with $k_{min} = 2\pi/\xi$ and the upper limit k_{max} is given by $k_{max} \simeq 2\pi/a$. Bending rigidity was used as free parameter and at $Q > 0.18\text{Å}^{-1}$ the amplitude becomes less than one due to background effects. Therefore, the amplitude normally fixed to 1 due to the normalization of $S(Q, \tau_{NSE})/S(Q, 0)$ was also used as free parameter. For a more detailed description of this numerical fitting approach, we refer to the literature (Mihailescu et al., 2001).

For sake of comparison, in **Figure 4** the curves measured at two Q values are plotted for the four CalB concentrations. At $Q = 0.05\text{Å}^{-1}$, no significant difference in the decay of $S(Q, \tau_{NSE})/S(Q, 0)$ is visible. At $Q = 0.18\text{Å}^{-1}$, a splitting occurs indicating a slight slowing down of the relaxation with increasing concentration of CalB.

6. DISCUSSION

In **Figure 5**, the bending rigidities $\kappa_{0,SANS}$ and $\kappa_{0,NSE}$ obtained from the fits to the SANS and NSE data are plotted as a function of the CalB concentration in the deuterated aqueous phase.

These results agree with previous theoretical and experimental work leading to the expectation of $\kappa_0 \approx 1k_BT$ for bicontinuous microemulsions. Without the addition of CalB, for the host microemulsion the SANS and NSE measurement yield $\kappa_{0,SANS} \approx \kappa_{0,NSE}$, which illustrates that the determination of the bending elasticity constants is independent from the method. After the addition of CalB, the values of $\kappa_{0,SANS}$ slightly decrease from 0.85 to 0.8 k_BT when more CalB was added. However, $\kappa_{0,NSE}$ significantly increases from 0.9 to 1.1 k_BT for the same concentrations of CalB.

SANS measurements time-average different configurations of a fluctuating and highly flexible sample structure over a time period of a few minutes. Usually, this counting time is required to achieve a sufficient signal to noise ratio of the recorded 2D scattering pattern.

In contrast to this, in soft matter samples, NSE inherently measures thermal fluctuations in the nanosecond time range at lengths up to a few ten nanometers.

In case of bicontinuous microemulsions, a SANS measurement averages innumerable topological arrangements of the highly flexible amphiphilic interfacial layer while NSE detects undulations and height fluctuations of this interface.

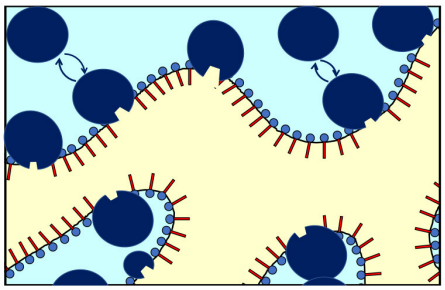

FIGURE 6 | Schematic of the enrichment and exchange of *Candida antarctica* B (CalB) in the amphiphilic interface of a bicontinuous microemulsion with the surfactant layers and the aqueous phase (light blue) and the oil phase (yellow). The lipase CalB is assumed to reside temporarily at the interface. A fraction of the macromolecules is able to detach and return to the aqueous phase (in light blue). At the same time, the opposite process might take place to some extend (sizes of the surfactant and enzymes are not fully to scale).

The lipase CalB consists of hydrophilic and hydrophobic parts. Hence, it is very likely that CalB can reside in the interfacial layer and act as a cosurfactant or amphiphilic block-copolymer. In this case, it is entirely possible that CalB changes the bending elasticity of the interface. Following the preceding argumentation, with SANS the time and space averaged bicontinuous structure was probed where CalB is either solubilized in the aqueous phase or resides as a cosurfactant or block-copolymer inside the amphiphilic interface. Moreover, if there were exchange processes, i.e., adsorption and desorption, between the aqueous phase and the interfacial layer, the SANS measurement includes an averaging of the two states.

The NSE measurement mainly detects fluctuations of the interface in presence of CalB. An effective increase of $\kappa_{0,NSE}$ would result if CalB adsorbed to the interfacial layer causes a stiffening of the interface. However, in light of the phase studies, the local interfacial stiffening may be counterbalanced by an increasing amount of CalB in the water phase of the bicontinuous microemulsion that may induce a counter osmotic pressure as already discussed previously (Kabalnov et al., 1994; Subinya et al., 2014). **Figure 6** sketches the presumed adsorption and desorption process of CalB at the interface.

This argumentation is in line with the previous publication showing that with increasing CalB concentration the concentration of both, the enzyme in the water phase and at the interface, increases (Subinya et al., 2014). Similar effects have also been observed in gradient polymers incorporated into microemulsion membranes, where the anchor point of the polymer may slide through the membrane and hence also lead to a variety of conformations on long length scales while being in one distinct conformation on the nanosecond time scale (Klemmer et al., 2017a,b). The enzyme modifies the bending rigidity and hence the free energy of the membrane, similarly as has been observed with the incorporation of diblock copolymers (Mihailescu et al., 2001) or the above-mentioned gradient polymers.

Contrary, in SANS and NSE measurements on the enzyme DFPase incorporated into the aqueous phase of a sugar surfactant-based microemulsion, there was no different behavior of the two bare bending elasticities. This spherically shaped enzyme shows no amphiphilicity and remains in the aqueous phase (Wellert et al., 2011). In conclusion, the results presented in the present paper in light of the previous phase studies allow for the following interpretation. Adding the lipase CalB to the water phase of a microemulsion of type H_2O/NaCl–n-octane–$C_{10}E_5$ appears to induce two effects. First, the efficiency of the microemulsion runs through a maximum with the efficiency at high CalB concentrations leading to a decrease in efficiency even below the blank microemulsion, i.e., without CalB addition. Second, despite the efficiency running through said maximum value, the values of $\kappa_{0,NSE}$ significantly increase from 0.9 k_BT to 1.1 k_BT for the same concentrations of CalB. While this appears to be counterintuitive at first, it is noted that both phenomena do not necessarily have to correlate as the underlying effects are different. While the observed trend in the efficiency may be attributed to an increase in osmotic pressure as a result of an increasing presence of CalB in the water phase, the significant increase in $\kappa_{0,NSE}$ may be attributed to an increasing presence of CalB in the interfacial layer. Due to presumably fast adsorption and desorption processes, this effect can only be observed by NSE that provides access to the nanosecond time range at lengths up to a few ten nanometers. Consequently, if viewed locally, an increasing concentration of CalB in the water phase may also lead to an increase in bending stiffness, however, on a local scale in the vicinity of the adsorbed enzyme. The effect of CalB on the pure (NSE) bending rigidity seems to be especially pronounced already at low concentrations of CalB, if saturation effects occur and the change in κ is slowed down with increasing CalB concentration remains speculative with the present set of experiments. Keeping these two effects in mind, the application of CalB-catalyzed reactions involving non-natural substrates may thus be determined by a counterbalance between efficiency and interfacial access of the lipase. While solubilization of a non-natural substrate is a matter of efficiency, yield on the other hand may be a matter of interfacial access. Future investigation would need to show as to whether efficiency or interfacial access should be preferred in lipase-catalyzed reactions involving non-natural substrates.

7. CONCLUSION

In this study, we have studied how the introduction of the lipase CalB alters the bending elastic properties of the amphiphilic interface in a bicontinuous microemulsion of the ternary system D_2O/NaCl–n-(d)-octane–pentaethylene glycol monodecyl ether ($C_{10}E_5$). We have determined the renormalized bending elastic constant κ_0 using two scattering techniques. We determined $\kappa_{0,SANS}$ from SANS and $\kappa_{0,NSE}$ from NSE.

The results of both types of measurements show differences when the concentration of CalB is increased up to 100 mg/ml.

While no significant influence of adding CalB to the aqueous phase of the microemulsion is observable for $\kappa_{0,\mathrm{SANS}}$, κ_{NSE} increases when the concentration of CalB rises. This indicates a stiffening of the amphiphilic interface. We attribute this effect to an increasing adsorption of CalB at the amphiphilic interface of the bicontinuous microemulsion. The difference between the structural parameters extracted from SANS on longer times and from NSE, detecting the local short time fluctuations, suggests that the lipase CalB temporarily adsorbs to the interface. We assume the respective residence time to be longer than the typical observation time of NSE of a few 10 ns. The complex situation of this dynamical equilibrium with the lipase being partly adsorbed at the membrane for some time, partly dissolved in the aqueous phase, with the details of the interaction of the lipase with the membrane not exactly known, requires more investigations, for example with molecular dynamics simulations, to shed more light into the lipase-membrane interaction.

The results from NSE experiments are in line with previous results (Klemmer et al., 2017a,b), suggesting that the approach of measuring the elastic constants at different time scales leads to information on the interaction of the additives with the microemulsion membrane. In the case of lipase CalB, the residence time at the membrane at the oil–water interface might be an important parameter for catalytic activities, in particular regarding non-natural substrates.

DATA AVAILABILITY STATEMENT

The raw data supporting the conclusions of this article will be made available by the authors, without undue reservation.

AUTHOR CONTRIBUTIONS

SE and SW: conception and idea. SE, SR, BNes, and BNeb: sample preparation and phase diagram measurements. BH, SE, SW, HF, and OH conducted the neutron scattering experiments. Data evaluation and writing of the paper by SE, SW, and OH. All authors contributed to the article and approved the submitted version.

ACKNOWLEDGMENTS

This work was based upon experiments performed at J-NSE and KWS-1 operated by JCNS at Heinz Maier-Leibnitz Zentrum Garching, Germany. We want to acknowledge Peter Busch (JCNS) for support at the KWS-1 beamline.

SUPPLEMENTARY MATERIAL

The Supplementary Material for this article can be found online at: https://www.frontiersin.org/articles/10.3389/fchem.2020.613388/full#supplementary-material

REFERENCES

Belkoura, L., Stubenrauch, C., and Strey, R. (2004). Freeze fracture direct imaging: a new freeze fracture method for specimen preparation in cryo-transmission electron microscopy. *Langmuir* 20, 4391–4399. doi: 10.1021/la0303411

Byelov, D., Frielinghaus, H., Holderer, O., Allgaier, J., and Richter, D. (2004). Microemulsion efficiency boosting and the complementary effect. 1. Structural properties. *Langmuir* 20, 10433–10443. doi: 10.1021/la049317t

Davis, H., Bodet, J., Scriven, L., and Miller, W. (1989). Microstructure and transport in midrange microemulsions. *Phys. A Stat. Mech. Appl.* 157, 470–481. doi: 10.1016/0378-4371(89)90345-2

Dwivedee, B. P., Soni, S., Sharma, M., Bhaumik, J., Laha, J. K., and Banerjee, U. C. (2018). Promiscuity of lipase-catalyzed reactions for organic synthesis: a recent update. *Chem. Select* 3, 2441–2466. doi: 10.1002/slct.201702954

Feoktystov, A. V., Frielinghaus, H., Di, Z., Jaksch, S., Pipich, V., Appavou, M.-S., et al. (2015). Kws-1 high-resolution small-angle neutron scattering instrument at jcns: current state. *J. Appl. Crystallogr.* 48, 61–70. doi: 10.1107/S1600576714025977

Frank, C., Frielinghaus, H., Allgaier, J., and Prast, H. (2007). Nonionic surfactants with linear and branched hydrocarbon tails: compositional analysis, phase behavior, and film properties in bicontinuous microemulsions. *Langmuir* 23, 6526–6535. doi: 10.1021/la0637115

Frielinghaus, H. (2018). Strategies for removing multiple scattering effects revisited. *Nuclear Instrum. Methods Phys. Res. A* 904, 9–14. doi: 10.1016/j.nima.2018.07.027

Frielinghaus, H., Feoktystov, A., Berts, I., and Mangiapia, G. (2015). Kws-1: Small-angle scattering diffractometer. *J. Large Scale Res. Facilit.* 1:28. doi: 10.17815/jlsrf-1-26

Gradzielski, M. (2008). Recent developments in the characterization of microemulsions. *Curr. Opin. Colloid Interface Sci.* 13, 263–269. doi: 10.1016/j.cocis.2007.10.006

Hayes, D. G., del Rio, J. A. G., Ye, R., Urban, V. S., Pingali, S. V., and OŃeill, H. M. (2015). Effect of protein incorporation on the nanostructure of the bicontinuous microemulsion phase of winsor-III systems: a small angle neutron scattering study. *Langmuir* 31, 1901–1910. doi: 10.1021/la504606x

Hellweg, T., Gradzielski, M., Farago, B., and Langevin, D. (2001). Shape fluctuations of microemulsion droplets: a neutron spin-echo study. *Colloids Surfaces A Physicochem. Eng. Aspects* 183, 159–169. doi: 10.1016/S0927-7757(01)00567-2

Hoffmann, I. (2014). Neutrons for the study of dynamics in soft matter systems. *Colloid Polymer Sci.* 292, 2053–2069. doi: 10.1007/s00396-014-3330-9

Holderer, O., Frielinghaus, H., Monkenbusch, M., Allgaier, J., Richter, D., and Farago, B. (2007). Hydrodynamic effects in bicontinuous microemulsions measured by inelastic neutron scattering. *Eur. Phys. J. E* 22, 157–161. doi: 10.1140/epje/e2007-00021-2

Holderer, O., Frielinghaus, H., Monkenbusch, M., Klostermann, M., Sottmann, T., and Richter, D. (2013). Experimental determination of bending rigidity and saddle splay modulus in bicontinuous microemulsions. *Soft Matter* 9, 2308–2313. doi: 10.1039/c2sm27449c

Holderer, O., Monkenbusch, M., Schätzler, R., Kleines, H., Westerhausen, W., and Richter, D. (2008). The JCNS neutron spin-echo spectrometer J-NSE at the FRM II. *Meas. Sci. Technol.* 19:034022. doi: 10.1088/0957-0233/19/3/034022

Kabalnov, A., Olsson, U., Thuresson, K., and Wennerström, H. (1994). Polymer effects on the phase equilibrium of a balanced microemulsion: adsorbing versus nonadsorbing polymers. *Langmuir* 10, 4509–4513.

Klemmer, H. F., Allgaier, J., Frielinghaus, H., Holderer, O., and Ohl, M. (2017a). Influence of the amphiphilicity profile of copolymers on the formation of liquid crystalline mesophases in microemulsions. *Colloid Polymer Sci.* 295, 911–923. doi: 10.1007/s00396-017-4080-2

Klemmer, H. F., Frielinghaus, H., Allgaier, J., Ohl, M., and Holderer, O. (2017b). The effect of amphiphilic polymers with a continuous amphiphilicity profile on the membrane properties in a bicontinuous microemulsions studied by neutron scattering. *J. Phys. Conf. Ser.* 862, 012014. doi: 10.1088/1742-6596/862/1/012014

Klostermann, M., Strey, R., Sottmann, T., Schweins, R., Lindner, P., Holderer, O., et al. (2012). Structure and dynamics of balanced supercritical co2-microemulsions. *Soft Matter* 8, 797–807. doi: 10.1039/C1SM06533E

Komura, S. (2007). Mesoscale structures in microemulsions. *J. Phys. Condens. Matter* 19:463101. doi: 10.1088/0953-8984/19/46/463101

Mihailescu, M., Monkenbusch, M., Endo, H., Allgaier, J., Gompper, G., Stellbrink, J., et al. (2001). Dynamics of bicontinuous microemulsion phases with and without amphiphilic block-copolymers. *J. Chem. Phys*. 115, 9563–9577. doi: 10.1063/1.1413509

Oberdisse, J., and Hellweg, T. (2017). Structure, interfacial film properties, and thermal fluctuations of microemulsions as seen by scattering experiments. *Adv. Colloid Interf. Sci*. 247, 354–362. doi: 10.1016/j.cis.2017.07.011

Pasini, S., Holderer, O., Kozielewski, T., Richter, D., and Monkenbusch, M. (2019). J-NSE-phoenix, a neutron spin-echo spectrometer with optimized superconducting precession coils at the MLZ in garching. *Rev. Sci. Instrum*. 90:043107. doi: 10.1063/1.5084303

Peltomäki, M., Gompper, G., and Kroll, D. M. (2012). Scattering intensity of bicontinuous microemulsions and sponge phases. *J. Chem. Phys*. 136:134708. doi: 10.1063/1.3701265

Pieruschka, P., Safran, S., and Marcelja, S. (1995). Comment on "fluctuating interfaces in microemulsion and sponge phases". *Phys. Rev. E* 521245. doi: 10.1103/PhysRevE.52.1245

Radulescu, A., Szekely, N. K., and Appavou, M.-S. (2015). Kws-2: small angle scattering diffractometer. *J. Large Scale Res. Facil*. 1:29. doi: 10.17815/jlsrf-1-27

Safran, S. (1999). Curvature elasticity of thin films. *Adv. Phys*. 48, 395–448. doi: 10.1080/000187399243428

Schwarz, U., and Gompper, G. (2002). "Bicontinuous surfaces in self-assembling amphiphilic systems," in *Morphology of Condensed Matter*, ed K. Mecke, and D. Stoyan, Lecture Notes in Physics, Vol. 600 (Berlin; Heidelberg: Springer-Verlag), 107–151.

Sottmann, T., Strey, R., and Chen, S.-H. (1997). A small-angle neutron scattering study of nonionic surfactant molecules at the water-oil interface: area per molecule, microemulsion domain size, rigidity. *J. Chem. Phys*. 106, 6483–6491. doi: 10.1063/1.473638

Strey, R. (1994). Microemulsion microstructure and interfacial curvature. *Colloid Polymer Sci*. 272, 1005–1019. doi: 10.1007/BF00658900

Subinya, M., Steudle, A. K., Nestl, B., Nebel, B., Hauer, B., Stubenrauch, C., et al. (2014). Physicochemical aspects of lipase b from candida antarctica in bicontinuous microemulsions. *Langmuir* 30, 2993–3000. doi: 10.1021/la4042088

Teubner, M., and Strey, R. (1987). Origin of the scattering peak in microemulsions. *J. Chem. Phys*. 87, 3195–3200. doi: 10.1063/1.453006

Wellert, S., Altmann, H.-J., Richardt, A., Lapp, A., Falus, P., Farago, B., et al. (2010). Dynamics of the interfacial film in bicontinuous microemulsions based on a partly ionic surfactant mixture: a neutron spin-echo study. *Eur. Phys. J. E* 33, 243–250. doi: 10.1140/epje/i2010-10668-1

Wellert, S., Tiersch, B., Koetz, J., Richardt, A., Lapp, A., Holderer, O., et al. (2011). The dfpase from loligo vulgaris in sugar surfactant-based bicontinuous microemulsions: structure, dynamics, and enzyme activity. *Eur. Biophys. J*. 40, 761–774. doi: 10.1007/s00249-011-0689-0

Wrede, O., Großkopf, S., Seidel, T., and Hellweg, T. (2019). Dynamics of proteins confined in non-ionic bicontinuous microemulsions: a FCS study. *Phys. Chem. Chem. Phys*. 21, 6725–6731. doi: 10.1039/C8CP06419A

Zilman, A., and Granek, R. (1996). Undulations and dynamic structure factor of membranes. *Phys. Rev. Lett*. 77:4788. doi: 10.1103/PhysRevLett.77.4788

Zilman, A. G., and Granek, R. (2002). Membrane dynamics and structure factor. *Chem. Phys*. 284, 195–204. doi: 10.1016/S0301-0104(02)00548-7

Zolnierczuk, P., Holderer, O., Pasini, S., Kozielewski, T., Stingaciu, L., and Monkenbusch, M. (2019). Efficient data extraction from neutron time-of-flight spin-echo raw data. *J. Appl. Crystallogr*. 52, 1022–1034. doi: 10.1107/S1600576719010847

Conflict of Interest: The authors declare that the research was conducted in the absence of any commercial or financial relationships that could be construed as a potential conflict of interest.

frontiers in Chemistry

PERSPECTIVE
published: 09 February 2021
doi: 10.3389/fchem.2020.619470

Membrane Protein Structures in Lipid Bilayers; Small-Angle Neutron Scattering With Contrast-Matched Bicontinuous Cubic Phases

*Charlotte E. Conn[1], Liliana de Campo[2], Andrew E. Whitten[2], Christopher J. Garvey[2,3,4], Anwen M. Krause-Heuer[5] and Leonie van 't Hag[6]**

[1] School of Science, STEM College, RMIT University, Melbourne, VIC, Australia, [2] Australian Centre for Neutron Scattering, Australian Nuclear Science and Technology Organisation, Lucas Heights, NSW, Australia, [3] Lund Institute for Advanced Neutron and X-Ray Science, Lund, Sweden, [4] Biolfim-Research Center for Biointerfaces and Biomedical Science Department, Faculty of Health and Society, Malmö University, Malmö, Sweden, [5] National Deuteration Facility, Australian Nuclear Science and Technology Organisation, Lucas Heights, NSW, Australia, [6] Department of Chemical Engineering, Monash University, Clayton, VIC, Australia

This perspective describes advances in determining membrane protein structures in lipid bilayers using small-angle neutron scattering (SANS). Differentially labeled detergents with a homogeneous scattering length density facilitate contrast matching of detergent micelles; this has previously been used successfully to obtain the structures of membrane proteins. However, detergent micelles do not mimic the lipid bilayer environment of the cell membrane *in vivo.* Deuterated vesicles can be used to obtain the radius of gyration of membrane proteins, but protein-protein interference effects within the vesicles severely limits this method such that the protein structure cannot be modeled. We show herein that different membrane protein conformations can be distinguished within the lipid bilayer of the bicontinuous cubic phase using contrast-matching. Time-resolved studies performed using SANS illustrate the complex phase behavior in lyotropic liquid crystalline systems and emphasize the importance of this development. We believe that studying membrane protein structures and phase behavior in contrast-matched lipid bilayers will advance both biological and pharmaceutical applications of membrane-associated proteins, biosensors and food science.

Keywords: self-assembly, peptide structure, membrane protein, lipid cubic phase, small-angle scattering

OPEN ACCESS

Edited by:
Ramesh L. Gardas, Indian Institute of Technology Madras, India

Reviewed by:
Sandro Keller, University of Kaiserslautern, Germany
Sarah Rouse, Imperial College London, United Kingdom

****Correspondence:***
Leonie van 't Hag
leonie.vanthag@monash.edu

Specialty section:
This article was submitted to Physical Chemistry and Chemical Physics, a section of the journal Frontiers in Chemistry

Received: *20 October 2020*
Accepted: *02 December 2020*
Published: *09 February 2021*

Citation:
Conn CE, de Campo L, Whitten AE, Garvey CJ, Krause-Heuer AM and van 't Hag L (2021) Membrane Protein Structures in Lipid Bilayers; Small-Angle Neutron Scattering With Contrast-Matched Bicontinuous Cubic Phases. Front. Chem. 8:619470. doi: 10.3389/fchem.2020.619470

INTRODUCTION

Integral and peripheral membrane proteins play an important role in signal transduction, solute transport, energy conversion and charge separation in eukaryotic and prokaryotic cells (Gaur and Natekar, 2010). Such membrane proteins are also important drug targets, with more than half of all pharmaceutical compounds on the market targeting membrane proteins (Service, 2014). There are significant experimental challenges with determining membrane protein structures in their native state due to their limited solubility in water. Membrane protein structures should, therefore, ideally be investigated within a native lipid bilayer environment. Although some studies have used vesicles to investigate membrane proteins in a lipid bilayer environment, most studies to date have focused on using detergent micelles which do not effectively mimic the lipid bilayer. In this perspective we

describe advances in membrane protein structure determination in detergent micelles as well as vesicles. These studies are compared with new data obtained using bicontinuous cubic phases.

Bicontinuous cubic phases, formed via lipid self-assembly, consist of a single lipid bilayer convoluted over three-dimensional space and subdividing space into two interpenetrating aqueous networks. The lipid bilayer adopts the shape of a theoretical surface of zero mean curvature, but with a continually varying Gaussian curvature which is everywhere non-positive (Luzzati et al., 1968). The three known bicontinuous cubic phases are based on the Schoen gyroid (G) minimal surface, the Schwartz primitive (P) minimal surface, and the Schwartz diamond (D) minimal surface, and are denoted Q_{II}^{G}, Q_{II}^{P}, and Q_{II}^{D}, respectively. The bulk bicontinuous cubic phases, which have the form of a viscous sticky gel, may be dispersed into sub-micron particles known as cubosomes, which must be sterically stabilized against flocculation via the addition of a polymer-based stabilizer, such as Pluronic F127 (Barriga et al., 2019; Fornasier et al., 2020). The elegant, bilayer-based, amphiphilic nanostructure of the cubic phase provides an ideal matrix for the encapsulation of transmembrane and membrane-associated proteins and peptides with a wide range of molecular masses (Conn and Drummond, 2013). Water-soluble proteins may also be encapsulated within the aqueous networks. The main applications of the bicontinuous cubic phases, including as drug delivery vehicles (Zhai et al., 2019), biosensors (Vallooran et al., 2016) and matrices for membrane protein crystallization (Caffrey, 2009), depend on their properties, such as the ability to encapsulate hydrophobic and hydrophilic moieties, large surface-area, biocompatibility, and retention of functionality for encapsulated proteins.

Encapsulation of a specific protein can impact the underlying cubic nanostructure depending on a range of factors including the charge on the protein and geometric mismatch between the protein and the aqueous channel diameter (for water soluble proteins) or bilayer thickness (for membrane-associated proteins) (Angelova et al., 2012; van 't Hag et al., 2016b, 2017b; Meikle et al., 2017). For water-soluble proteins or peptides, encapsulation may be quantified by separating the bulk cubic phase, or cubosomes, from the surrounding aqueous phase via centrifugal filtration. Loading efficiency may be calculated by using UV absorption to determine the peptide or protein concentration in the filtrate. For poorly water-soluble peptides, either the insoluble precipitate, or the loaded cubosomes, may be analyzed to determine the peptide loading. Encapsulation efficiencies of up to 90 mol% have been measured for smaller peptides, such as some antimicrobial peptides (Conn et al., 2011; Boge et al., 2019). In contrast, for larger proteins, such as GPCRs, the underlying cubic nanostructure may be completely disrupted at low protein concentrations of <3 mol% (Conn et al., 2010).

The lipid bilayer structure of the bicontinuous cubic phase can provide an ideal matrix for structure determination in a more biomimetic environment compared to detergent micelles. Neutron scattering with contrast-variation allows for the isolation of scattering from individual components within a complex system of protein, lipid(s), and solvent (water or buffer). The neutron scattering contrast can be varied over a wide range using the difference in neutron scattering length density (SLD) between hydrogen and deuterium. Isotopic substitution of this type usually has small but volume fraction defined effects on the phase diagram of lipid mesophases in water (Vandoolaeghe et al., 2009b; Bremer et al., 2017; Bryant et al., 2019). The effects for hydrogens which take part in hydrogen bonding, e.g., water (Takahashi and Jojiki, 2017) are more complex (Bryant et al., 2019) but may also account for small shifts in the phase boundaries. We describe how this has been used to study proteins in detergent micelles and vesicles and show that this has now been successfully applied to study peptide structures in contrast-matched lipid cubic phases. Advances in using SANS for time-resolved studies will also be discussed.

MEMBRANE PROTEIN STRUCTURES IN LIPID MEMBRANES

Detergents

Early attempts to study membrane proteins with contrast-matched detergent micelles were performed on rhodopsin in the 1970s (Osborne et al., 1978). Since that time, this approach has been used to study the structure of other membrane proteins (Breyton et al., 2013; Naing et al., 2018), however, these studies tended to focus on the radius of gyration and oligomeric state of the proteins. More recently, structural work on membrane proteins showed how the use of differentially labeled detergents with a homogeneous scattering length density allowed for superior contrast-matching of the detergent micelle; consequently, the scattering curves were a more faithful representation of the isolated membrane protein (Midtgaard et al., 2018). At the same time, approaches are being developed to model the protein structure and the detergent micelles from SANS or SAXS (Pérez and Koutsioubas, 2015; Koutsioubas, 2017), but the impact remains modest, largely due to the difficulties involved in working with membrane proteins. Additionally, as detergent micelles do not mimic the lipid bilayer environment of the cell membrane *in vivo,* the structure and function of membrane proteins can be significantly affected in a detergent environment (Bayburt and Sligar, 2010; Breyton et al., 2013).

Vesicles

SANS has also been used to study membrane protein assemblies and, in particular, oligomerization in liposomes (Hunt et al., 1997). In this case, liposome polydispersity must be accounted for which is a significant challenge. Fitting of a membrane associated protein with vesicles was, for example, modeled using five parameters: liposome radius, lipid thickness, lipid bilayer SLD, protein thickness and protein SLD. Relative differences in conformation could be detected using this method (Satsoura et al., 2012; Heberle et al., 2013). In another study, results were mainly focused on changes in the lipid bilayer thickness and not the protein structures (Gilbert et al., 1999). In recent years there has been significant progress in modeling complex phase-behavior, such as the formation of lipid rafts in lipid-only vesicles

using SAXS and SANS (Marquardt et al., 2015; Heberle and Pabst, 2017).

Protein-protein interference effects due to the structure factor caused by the large number of protein monomers per vesicle are a significant limitation when studying membrane proteins reconstituted in vesicles. For bacteriorhodopsin the radius of gyration was obtained in contrast-matched vesicles of dimyristoylphosphatidylcholine (DMPC-d_{67}-h_5). However, the study indicated that only a limited q-region (0.01–0.05 $Å^{-1}$) was free from interference effects (Hunt et al., 1997). While the limited q-range allowed for determination of the radius of gyration, it was not possible to obtain the detailed protein conformation which relates to its function. *Ab initio* modeling of membrane protein structures in a lipid bilayer membrane has had limited success to date (Breyton et al., 2013; Skar-Gislinge et al., 2015).

Cubic Phases

Membrane protein encapsulation can also be studied using the lipid self-assembly bulk bicontinuous cubic phase, which has a significantly higher surface area to volume ratio compared to vesicles. This affords the significant advantage that large amounts of protein can be encapsulated, increasing the neutron scattering signal. To prepare the bicontinuous cubic phases, lipid (50–80% v/v) is typically mixed with membrane protein solution (50–20% v/v) in detergent. For this preparation method, there is no point where the protein is completely separated from the detergent micelle or lipid bilayer (van 't Hag et al., 2017a).

Herein, we present new data where hydrophobic peptides are directly mixed with lipid without the need to use detergents. We have recently shown that deuterated lipids can be used to contrast match the lipid membrane to D_2O, in order to isolate the scattering from the peptides. This can be used to retrieve the Bragg peaks from the cubic phase geometry due to the scattering of the homogeneously encapsulated peptides in the contrast-matched membrane (van 't Hag et al., 2016a, 2019). For gramicidin A in the lipid cubic phase of monoolein (MO), an increase in Bragg peak intensity was found with increasing peptide concentration (van 't Hag et al., 2019). In contrast, the cubic phase formed by the branched chain lipid phytanoyl monoethanolamine (PE) showed Bragg peaks at low peptide concentrations, but limited WALP21 and WALPS53 encapsulation at high concentrations (van 't Hag et al., 2016a,b). This can be explained by the significantly higher lateral bilayer pressure in the case of PE bilayers and illustrates the importance of the physicochemical properties of the membrane.

Herein, we extend this work by investigating the peptide structures of Gramicidin A (gA) and WALPS53 in the contrast-matched cubic Q_{II} phase of MO (M-MO) (**Figure 1**). gA can appear in two different conformations in a lipid bilayer: as a helical dimer (PDF ID: 1MAG, **Figure 1D**) and/or as a double helix (PDB ID: 1BDW, **Figure 1E**). The time-of-flight SANS data, as collected during a single measurement of each sample and scaled to peptide concentration, was in excellent quantitative agreement with the gA form factor of a mixture of helical dimer and double helix (**Figures 1A,B**). An approximately equal contribution of each structure is in agreement with what was found using circular dichroism spectroscopy of gA in the diamond cubic Q_{II}^{D} phase of MO (Meikle et al., 2017). The simulated form factor data was obtained using CRYSON (v 2.7) (Svergun et al., 1998), using the gA structures (PDB ID: 1MAG and PDB ID: 1BSW), assuming a D_2O solvent concentration of 100%, and setting the contrast of the solvation shell to 0. The form factors from CRYSON were multiplied by $N_A/M_w \times 10^{-24}$, permitting direct comparison with SANS data on an absolute scale normalized by peptide concentration.

The model peptide WALPS53 consists of two transmembrane α-helices [amino acid sequence GWW-$(LA)_7$L-WWA] bound by a short hydrophilic domain [amino acid sequence $S(RS)_5$]. In the cubic phase of MO with a water channel diameter of ∼50 Å, the WALPS53 hydrophilic domain, with a length of ∼46 Å (based on a distance of 3.5 Å between α-carbons) (van 't Hag et al., 2016b), would be able to bridge the water channels based on geometrical considerations. The two peptide conformations investigated are therefore (i) one where the transmembrane α-helices are present as a dimer (**Figure 1F**) and (ii) another where the structure is fully extended (**Figure 1G**). A model structure of the WALPS53 dimer was generated using the iTasser server (Yang et al., 2015), while the extended structure was generated from that dimer by manually rotating the C-terminal helix (S30-A53) around residue R29 by an angle of ∼180° using PyMol (Version 1.2r3pre, Schrödinger, LLC). This simple two state model allows for comparison of the two extreme conformations: extended vs. compact. We note, however, that in the extended conformation the two helices are expected to be able to move freely around the linker region. The form factors for the fully extended and compact structures were calculated for each structure as described above for gA. The SANS data with two different peptide concentrations showed that the peptide is present as a dimer in the gyroid cubic Q_{II}^{G} phase at 0.2 and 0.4 mol% and 35% v/v D_2O. The data for WALPS53 are noisier than data for gA due to the significantly lower peptide concentrations which also resulted in a narrower available q-range after subtraction. Nevertheless, the SANS data shows good quantitative agreement with the simulated form factor of the dimeric form of the peptide as predicted by the iTasser server.

DISPERSED CUBIC PHASES FOR THERAPEUTIC PROTEIN DELIVERY

It was recently shown that the internal structure of cubosomes (dispersed cubic phases) can also be contrast-matched (Yepuri et al., 2019). These nanoparticles can be used for the delivery of therapeutic and antimicrobial peptides, imaging agents and hydrophobic drugs (Mulet et al., 2013; Zhai et al., 2015). Polymeric stabilizers, such as Pluronic F127 and Tween 80, used to prevent aggregation of the cubosomes are known to affect the internal cubic phase nanostructure. For phytantriol cubosomes, deuterated phytantriol was used to prove that Tween 80 was distributed throughout the internal lipid bilayer network and not just on the surface, which led to a phase transition to the more swollen and less curved primitive cubic Q_{II}^{P} phase (Yepuri et al., 2019). This demonstrates that SANS with contrast-matched cubic

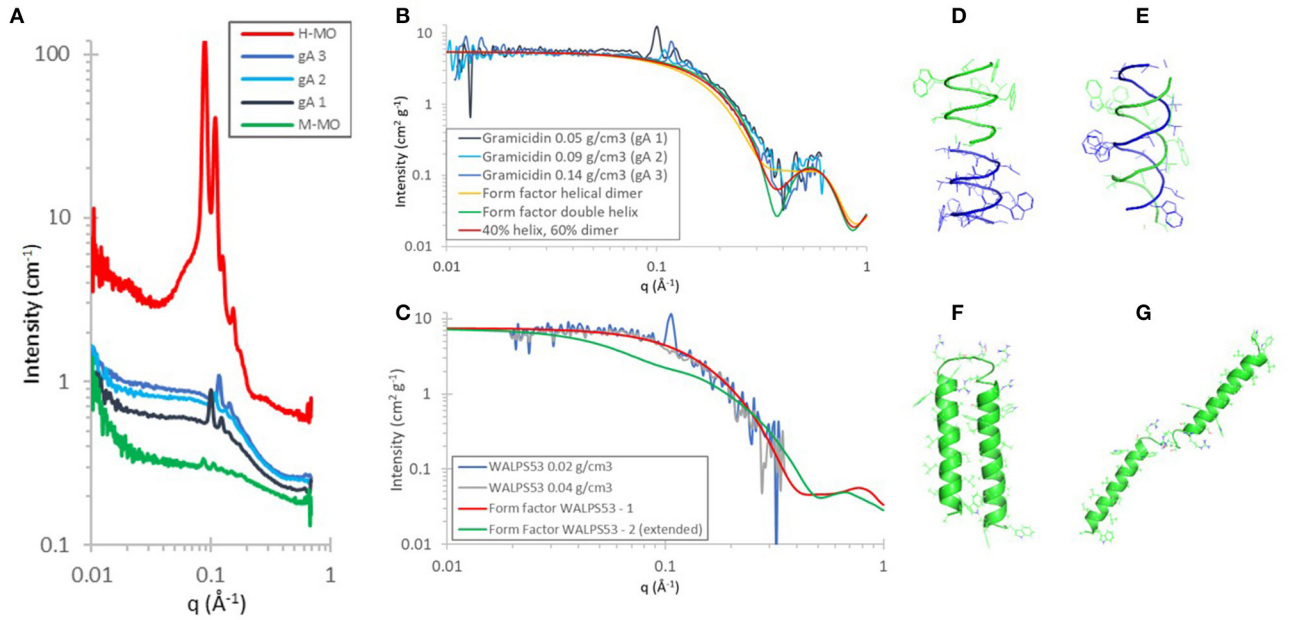

FIGURE 1 | (A–C) SANS data showing H-MO and peptide encapsulation in 92% D-MO/8% H-MO (M-MO) at a range of peptide concentrations at 20°C in D_2O. **(A,B)** Gramicidin A (1.9 kDa) concentrations reflect 1.6, 3.1, and 5.3 mol% with respect to MO and at 40% v/v D_2O: diamond cubic Q_{II}^D phase. **(C)** WALPS53 (5.9 kDa) at 0.2 and 0.4 mol% with respect to MO and at 35% v/v D_2O: gyroid cubic Q_{II}^G phase. The SANS data was treated by first subtracting the MO cubic phase as background, then scaled to peptide concentration, and then a further incoherent background was subtracted. The calculated form factors were obtained using CRYSON. **(D–G)** were created using PyMOL and show cartoon representations of the secondary structures with side-chains shown as lines. They were obtained using PDB ID **(D)** 1MAG: helical dimer and **(E)** 1BDW: double helix. **(F)** WALPS53–1 dimer as generated using the iTasser server (Yang et al., 2015) and **(G)** WALPS53–2 (extended version of WALPS53–1).

phases can also be used to study dispersed cubic phase systems, and opens up the possibility to study release of bioactives from cubosome nanoparticles using this technique.

TIME-RESOLVED STUDIES ON MULTI-COMPONENT SYSTEMS USING SANS

The non-destructive nature of the neutron beam makes SANS suitable for *in situ* kinetic studies. We describe how this has been used to study lyotropic liquid crystalline systems to date, and could be used in the future, to study the kinetics of hybrid protein-lipid materials. Kinetic studies are of fundamental importance for understanding what happens during delivery and digestion of therapeutic proteins (Conn and Drummond, 2013; Mulet et al., 2013), enzymatic reactions in lipid phases for use as biosensors and biofuel cells (Nazaruk et al., 2008; Vallooran et al., 2016), and during *in meso* crystallization of membrane proteins for high-resolution structure determination (Cherezov, 2011; van 't Hag et al., 2014; van 't Hag et al., 2019; Caffrey, 2015; Zabara et al., 2017).

SAXS and SANS have commonly been used to study the phase transitions and geometric pathways between lyotropic liquid crystalline phases formed by a single amphiphile/surfactant in water (Hamley et al., 1998; Angelov et al., 2007; Vandoolaeghe et al., 2009a; Squires et al., 2015; van 't Hag et al., 2017b), whereby X-ray studies have a much higher time resolution but are limited by radiation damage and a single contrast. In 2000 it was reported that a significant increase in the neutron flux and detector size enabled time-resolved studies of relatively fast surfactant phase transitions in solution, elucidating the transition from micelles to vesicles as well as nucleation and growth of oil droplets with measurement times of 30 s (Egelhaaf et al., 2000). Additionally, hydrogels, polymer systems, emulsions, and surfactant lamellar phases are examples of systems that have been studied under flow, using Rheo-SANS. Bulk surfactant lamellar phases were suggested to form multi-lamellar vesicles under shear via intermediate cylinders or buckling. Currently most Rheo-SANS measurements focus on a time average and the ensemble structure formed by a single amphiphile (Eberle and Porcar, 2012). It was suggested that studying transient structural reorientation of complex fluids requires powerful neutron sources and techniques, but that multicomponent systems and contrast-matching will become invaluable for understanding the relation between the rheological properties and membrane structure by using new sources, such as the European Spallation Source and new techniques including examination of steady perturbed states (Glinka et al., 2020).

Angelov et al. used a combination of SANS and SAXS to show that the cubic phase behavior of the ternary system consisting of MO, water and octyl glucoside (OG) undergoes phase separation. At low temperatures the swollen cubic phases were found to have OG encapsulated within the lipid bilayer. In contrast, when

heated to higher temperatures the OG molecules were suggested to be released into the aqueous water channels (Angelov et al., 2007; Angelova et al., 2011). Additionally, using SAXS the protein neurotrophin was found to impact the curvature of MO-eicosapentaenoic-water cubic phases within milliseconds, leading to a hydrated mixed Q_{II}^{D}/Q_{II}^{G} shell connected to a lamellar core phase (Angelov et al., 2014). Multi-phase liquid-crystalline nanoparticles with the cubic phase forming lipid MO have also been observed in a ternary mixture with capric acid and water (Killian, 2003). Recently, the complex phase behavior resulting from the interactions of silica nanoparticles with a ternary water-oil system was extensively studied using SANS with contrast-variation. Nanoparticles were found to aggregate at domain boundaries which led to a change in the liquid crystalline domain size (Marlow et al., 2019). In the case of triphilic star-polyphiles, hybrid double chain surfactants with a hydrocarbon and fluorocarbon chain, contrast-variation SANS was successfully used to show that the membrane was fully de-mixed into hydrocarbon and fluorocarbon domains in the hexagonal phase, demonstrating more complex phase behavior than that found in amphiphiles (de Campo et al., 2011).

Using the contrast-matched MO cubic phase we were able to follow the *in meso* crystallization of the biologically relevant transmembrane peptides glycophorin A (GpA) (Trenker et al., 2015) and DAP12 (Knoblich et al., 2015) using SANS. Peptide crystal growth was directly related to a significant decrease in form factor scattering intensity of the peptides. For DAP12 a transient fluid lamellar L_α phase was observed. In contrast, for GpA the lamellar crystalline L_c phase of the peptide single crystals was observed. This suggested that the specific mechanism is peptide and protein dependent (van 't Hag et al., 2019). This was the first time *in meso* crystallization was studied from the protein-eye perspective as previous studies using SAXS and SANS without contrast-matching focused, by necessity, on the lipid phase (Efremov et al., 2005; van 't Hag et al., 2016c; Zabara et al., 2017).

DISCUSSION

We have described current progress on the use of detergent micelles and vesicles to determine membrane protein structures. To date, neither of these environments have proved wholly successful in determining membrane protein conformations in a lipid bilayer environment. While membrane protein studies with phospholipid nanodiscs have recently gained a lot of attention (Bayburt and Sligar, 2010; Skar-Gislinge and Arleth, 2011) we note that they face significant challenges with regards to contrast-matching, mainly due to the use of an encircling helical protein belt that keeps the nanodiscs together. The new data presented herein, to the best of our knowledge, represents the first time that specific membrane protein conformations were determined in contrast-matched bicontinuous cubic phases using SANS. This is a promising approach for studying membrane proteins that are too small for structural studies with Cryo-EM (<100 kDa) (Cheng, 2018) and too large for NMR (>25 kDa) (Liang and Tamm, 2016).

We suggest that the use of contrast-matched cubic phases, as presented herein, is also suitable for investigating the structures of large and complex membrane proteins. Membrane proteins may be reconstituted directly into the cubic phase from a solution with deuterated detergents. Alternatively, the use of 100% D-MO (rather than 92% D-MO and 8% H-MO as presented herein) and H-detergent will also lead to contrast-matched cubic phases. Furthermore, swollen cubic phases could be employed for membrane proteins with a large hydrophilic domain (Zhai et al., 2020). The complex phase behavior in lyotropic liquid crystalline systems is evident in time-resolved studies and emphasize the importance of this development.

The use of SANS with contrast-matching has the potential to further advance our understanding of encapsulated proteins and other additives in lyotropic lipid cubic phases. Many questions remain, such as do large amphiphilic proteins encapsulate within the cubic phase water channels or in the cubic phase domain boundaries? How do protein molecules from several cubic phase domains feed the protein crystals during *in meso* crystallization? How do the lipid bilayer physicochemical properties affect protein structures (Frewein et al., 2016)? How can we improve the use of lipid nanoparticles with therapeutic peptides for oral delivery by studying digestion of the protein-lipid materials? Therapeutic peptides have shown to be a promising treatment for cancer, viral infections as well as multi-drug resistant bacterial infections (Walsh, 2014). However, their effective delivery remains a challenge.

Additionally, protein and peptide interactions with the cell membrane are of significant importance for pharmaceutical applications with more than half of all drugs on the market targeting membrane proteins (Service, 2014). Biological cell membranes consist of hundreds of different lipids and display complex phase behavior (Sarkar et al., 2019). We believe that studying membrane protein structures and phase behavior in contrast-matched lipid bilayers will advance biological and pharmaceutical applications, biosensors and food science. Combined with recent advances in chemical and biological deuteration, neutron scattering technology and instrumentation we expect a bright future for this research field.

MATERIALS AND METHODS

Materials

H-MO, gramicidin from *Bacillus aneurinolyticus*, hexafluoroisopropanol (HFIP) and methanol-d1 (MeOD) was purchased from Sigma Aldrich (St Louis, MO). Hamilton syringes were obtained from Hamilton Company (Reno, NV) and syringe couplers from TTP Labtech (Cambridge, MA). WALPS53 with >95% purify was purchased from CS Bio, Inc. (Menlo Park, CA, USA) and mass and purity were confirmed (van 't Hag et al., 2016b). The synthesis of D-MO was described in a previous publication (van 't Hag et al., 2019).

Sample Preparation

Initially, the exchangeable hydrogens of H-MO and D-MO were exchanged for deuterium using MeOD. Homogeneous peptide/lipid mixtures were obtained by co-dissolving the peptide with the appropriate H/D-MO mixture: gA with H/D-MO was dissolved in 260 μL MeOD or WALPS53 was dissolved in 100 μL HFIP, and then mixed with H/D-MO in 160 μL MeOD. While in the gA samples the hydrogens remained fully exchanged, the co-solvation process for WALP53 led to an exchangeable H/D ratio of ∼1:4. Most of the solvent was evaporated using a stream of N_2, followed by freezing in liquid N_2 followed by lyophilizing overnight. D_2O was loaded into the first 100 μL Hamilton syringe, the second syringe was loaded with the peptide/lipid mixture after it was molten at 40°C. Samples were mixed at 35% v/v or 40% v/v D_2O.

Small-Angle Neutron Scattering (SANS)

SANS measurements were performed on BILBY at the ANSTO OPAL reactor in time-of-flight mode using neutrons with wavelengths between 3 and 12 Å (Sokolova et al., 2019; van 't Hag et al., 2019). The sample detector distances were 1.8 m (horizontal curtains), 2.8 m (vertical curtains) and 6.0 m (rear). The collimation length was 6.7 mm and a sample aperture of 7.5 mm was used. Using the Mantid software (Arnold et al., 2014) the data was put on absolute scale using a direct beam measurement and corrected for scattering contributions from the background.

DATA AVAILABILITY STATEMENT

The raw data supporting the conclusions of this article will be made available by the authors, without undue reservation.

AUTHOR CONTRIBUTIONS

CC performed SANS measurements, assisted with design of the study, and drafting the manuscript. LC developed and facilitated TOF-SANS measurements and data analysis protocols. AW performed the peptide structure modeling and form factor simulations. CG provided the critical commentary on the results and manuscript. AK-H performed the synthesis and characterization of deuterated MO. LH designed the study, analyzed the data, and drafted the manuscript. All authors contributed to editing the paper and gave final approval for publication.

ACKNOWLEDGMENTS

We acknowledge the Australian Center for Neutron Scattering (ACNS), Australian Nuclear Science and Technology Organization (ANSTO) for providing neutron research facilities, and the Australian National Deuteration facility [supported by the National Collaborative Research Infrastructure Strategy (NCRIS), an initiative of the Australian Government], for providing chemical deuteration facilities. We thank Nhiem Tran and Thomas G. Meikle for their support during SANS beamtime over the years, and Anna E. Leung and Tamim A. Darwish for their contributions to the deuteration of MO. CC was the recipient of an RMIT Vice Chancellor's Senior Research Fellowship. We acknowledge AINSE, Ltd. for providing a Post-Graduate Research Award (PGRA) and Early Career Researcher Grant (ECRG) to LH.

REFERENCES

Angelov, B., Angelova, A., Filippov, S. K., Drechsler, M., Štěpánek, P., and Lesieur, S. (2014). Multicompartment lipid cubic nanoparticles with high protein upload: millisecond dynamics of formation. *ACS Nano* 8, 5216–5226. doi: 10.1021/nn5012946

Angelov, B., Angelova, A., Garamus, V. M., Lebas, G., Lesieur, S., Ollivon, M., et al. (2007). Small-angle neutron and X-ray scattering from amphiphilic stimuli-responsive diamond-type bicontinuous cubic phase. *J. Am. Chem. Soc.* 129, 13474–13479. doi: 10.1021/ja072725+

Angelova, A., Angelov, B., Garamus, V. M., Couvreur, P., and Lesieur, S. (2012). Small-angle X-ray scattering investigations of biomolecular confinement, loading, and release from liquid-crystalline nanochannel assemblies. *J. Phys. Chem. Lett.* 3, 445–457. doi: 10.1021/jz2014727

Angelova, A., Angelov, B., Mutafchieva, R., Garamus, V. M., Lesieur, S., Funari, S. S., et al. (2011). "Swelling of a sponge lipid phase via incorporation of a nonionic amphiphile: SANS and SAXS studies," in *BT–Trends in Colloid and Interface Science XXIV*, eds V. Starov and K. Procházka (Berlin; Heidelberg: Springer), 1–6.

Arnold, O., Bilheux, J. C., Borreguero, J. M., Buts, A., Campbell, S. I., Chapon, L., et al. (2014). Mantid—Data analysis and visualization package for neutron scattering and μ SR experiments. *Nucl. Instruments Methods Phys. Res. A Accel. Spectrom. Detect. Assoc. Equip.* 764, 156–166. doi: 10.1016/j.nima.2014.07.029

Barriga, H. M. G., Holme, M. N., and Stevens, M. M. (2019). Cubosomes: the next generation of smart lipid nanoparticles? *Angew. Chemie Int. Ed.* 58, 2958–2978. doi: 10.1002/anie.201804067

Bayburt, T. H., and Sligar, S. G. (2010). Membrane protein assembly into Nanodiscs. *FEBS Lett.* 584, 1721–1727. doi: 10.1016/j.febslet.2009.10.024

Boge, L., Browning, K. L., Nordström, R., Campana, M., Damgaard, L. S. E., Seth Caous, J., et al. (2019). Peptide-loaded cubosomes functioning as an antimicrobial unit against *Escherichia coli*. *ACS Appl. Mater. Interfaces* 11, 21314–21322. doi: 10.1021/acsami.9b01826

Bremer, A., Kent, B., Hauß, T., Thalhammer, A., Yepuri, N. R., Darwish, T. A., et al. (2017). Intrinsically disordered stress protein COR15A resides at the membrane surface during dehydration. *Biophys. J.* 113, 572–579. doi: 10.1016/j.bpj.2017.06.027

Breyton, C., Gabel, F., Lethier, M., Flayhan, A., Durand, G., Jault, J.-M., et al. (2013). Small angle neutron scattering for the study of solubilised membrane proteins. *Eur. Phys. J. E* 36:71. doi: 10.1140/epje/i2013-13071-6

Bryant, G., Taylor, M. B., Darwish, T. A., Krause-Heuer, A. M., Kent, B., and Garvey, C. J. (2019). Effect of deuteration on the phase behaviour and structure of lamellar phases of phosphatidylcholines–deuterated lipids as proxies for the physical properties of native bilayers. *Colloids Surf. B Biointerfaces* 177, 196–203. doi: 10.1016/j.colsurfb.2019.01.040

Caffrey, M. (2009). Crystallizing membrane proteins for structure determination: use of lipidic mesophases. *Annu. Rev. Biophys.* 38, 29–51. doi: 10.1146/annurev.biophys.050708.133655

Caffrey, M. (2015). A comprehensive review of the lipid cubic phase or *in meso* method for crystallizing membrane and soluble proteins and complexes. *Acta Crystallogr. F* 71, 3–18. doi: 10.1107/S2053230X14026843

Cheng, Y. (2018). Membrane protein structural biology in the era of single particle cryo-EM. *Curr. Opin. Struct. Biol.* 52, 58–63. doi: 10.1016/j.sbi.2018.08.008

Cherezov, V. (2011). Lipidic cubic phase technologies for membrane protein structural studies. *Curr. Opin. Struct. Biol.* 21, 559–566. doi: 10.1016/j.sbi.2011.06.007

Conn, C. E., Darmanin, C., Sagnella, S. M., Mulet, X., Greaves, T. L., Varghese, J. N., et al. (2010). Incorporation of the dopamine D2L receptor and bacteriorhodopsin within bicontinuous cubic lipid phases. 2. Relevance to *in meso* crystallization of integral membrane proteins in novel lipid systems. *Soft Matter* 6, 4838–4846. doi: 10.1039/C0SM00464B

Conn, C. E., and Drummond, C. J. (2013). Nanostructured bicontinuous cubic lipid self-assembly materials as matrices for protein encapsulation. *Soft Matter* 9, 3449–3464. doi: 10.1039/C3SM27743G

Conn, C. E., Mulet, X., Moghaddam, M. J., Darmanin, C., Waddington, L. J., Sagnella, S. M., et al. (2011). Enhanced uptake of an integral membrane protein, the dopamine D2L receptor, by cubic nanostructured lipid nanoparticles doped with Ni(ii) chelated EDTA amphiphiles. *Soft Matter* 7, 567–578. doi: 10.1039/C0SM00790K

de Campo, L., Varslot, T., Moghaddam, M. J., Kirkensgaard, J. J. K., Mortensen, K., and Hyde, S. T. (2011). A novel lyotropic liquid crystal formed by triphilic star-polyphiles: hydrophilic/oleophilic/fluorophilic rods arranged in a 12.6.4. tiling. *Phys. Chem. Chem. Phys.* 13, 3139–3152. doi: 10.1039/C0CP01201G

Eberle, A. P. R., and Porcar, L. (2012). Flow-SANS and Rheo-SANS applied to soft matter. *Curr. Opin. Colloid Interface Sci.* 17, 33–43. doi: 10.1016/j.cocis.2011.12.001

Efremov, R., Shiryaeva, G., Bueldt, G., Islamov, A., Kuklin, A., Yaguzhinsky, L., et al. (2005). SANS investigations of the lipidic cubic phase behaviour in course of bacteriorhodopsin crystallization. *J. Cryst. Growth* 275, e1453–e1459. doi: 10.1016/j.jcrysgro.2004.11.235

Egelhaaf, S. U., Olsson, U., and Schurtenberger, P. (2000). Time-resolved SANS for surfactant phase transitions. *Phys. B Condens. Matter* 276–278, 326–329. doi: 10.1016/S0921-4526(99)01527-6

Fornasier, M., Biffi, S., Bortot, B., Macor, P., Manhart, A., Wurm, F. R., et al. (2020). Cubosomes stabilized by a polyphosphoester-analog of pluronic F127 with reduced cytotoxicity. *J. Colloid Interface Sci.* 580, 286–297. doi: 10.1016/j.jcis.2020.07.038

Frewein, M., Kollmitzer, B., Heftberger, P., and Pabst, G. (2016). Lateral pressure-mediated protein partitioning into liquid-ordered/liquid-disordered domains. *Soft Matter* 12, 3189–3195. doi: 10.1039/C6SM00042H

Gaur, R. K., and Natekar, G. A. (2010). Prokaryotic and eukaryotic integral membrane proteins have similar architecture. *Mol. Biol. Rep.* 37, 1247–1251. doi: 10.1007/s11033-009-9497-3

Gilbert, R. J. C., Heenan, R. K., Timmins, P. A., Gingles, N. A., Mitchell, T. J., Rowe, A. J., et al. (1999). Studies on the structure and mechanism of a bacterial protein toxin by analytical ultracentrifugation and small-angle neutron scattering. *J. Mol. Biol.* 293, 1145–1160. doi: 10.1006/jmbi.1999.3210

Glinka, C., Bleuel, M., Tsai, P., Zákutná, D., Honecker, D., Dresen, D., et al. (2020). Sub-millisecond time-resolved small-angle neutron scattering measurements at NIST. *J. Appl. Crystallogr.* 53, 598–604. doi: 10.1107/S1600576720004367

Hamley, I. W., Pople, J. A., Booth, C., Yang, Y.-W., and King, S. M. (1998). A small-angle neutron-scattering study of shear-induced ordering in the cubic phase of a block copolymer gel. *Langmuir* 14, 3182–3186. doi: 10.1021/la971191v

Heberle, F. A., and Pabst, G. (2017). Complex biomembrane mimetics on the sub-nanometer scale. *Biophys. Rev.* 9, 353–373. doi: 10.1007/s12551-017-0275-5

Heberle, F. A., Petruzielo, R. S., Pan, J., Drazba, P., Kučerka, N., Standaert, R. F., et al. (2013). Bilayer thickness mismatch controls domain size in model membranes. *J. Am. Chem. Soc.* 135, 6853–6859. doi: 10.1021/ja3113615

Hunt, J. F., McCrea, P. D., Zaccai, G., and Engelman, D. M. (1997). Assessment of the aggregation state of integral membrane proteins in reconstituted phospholipid vesicles using small angle neutron scattering. *J. Mol. Biol.* 273, 1004–1019. doi: 10.1006/jmbi.1997.1330

Killian, J. A. (2003). Synthetic peptides as models for intrinsic membrane proteins. *FEBS Lett.* 555, 134–138. doi: 10.1016/S0014-5793(03)01154-2

Knoblich, K., Park, S., Lutfi, M., van 't Hag, L., Conn, C. E., Seabrook, S. A., et al. (2015). Transmembrane complexes of DAP12 crystallized in lipid membranes provide insights into control of oligomerization in immunoreceptor assembly. *Cell Rep.* 11, 1184–1192. doi: 10.1016/j.celrep.2015.04.045

Koutsioubas, A. (2017). Low-resolution structure of detergent-solubilized membrane proteins from small-angle scattering data. *Biophys. J.* 113, 2373–2382. doi: 10.1016/j.bpj.2017.10.003

Liang, B., and Tamm, L. K. (2016). NMR as a tool to investigate the structure, dynamics and function of membrane proteins. *Nat. Struct. Mol. Biol.* 23, 468–474. doi: 10.1038/nsmb.3226

Luzzati, V., Tardieu, A., Gulik-Krzywicki, T., Rivas, E., Reiss-Husson, and F (1968). Structure of the cubic phases of lipid-water systems. *Nature* 220, 485–488. doi: 10.1038/220485a0

Marlow, J. B., McCoy, T. M., Ho, C. Q., de Campo, L., Knott, R., Bell, T. D. M., et al. (2019). Tuning the structure, thermal stability and rheological properties of liquid crystal phases via the addition of silica nanoparticles. *Phys. Chem. Chem. Phys.* 21, 25649–25657. doi: 10.1039/C9CP04908H

Marquardt, D., Heberle, F. A., Nickels, J. D., Pabst, G., and Katsaras, J. (2015). On scattered waves and lipid domains: detecting membrane rafts with X-rays and neutrons. *Soft Matter* 11, 9055–9072. doi: 10.1039/C5SM01807B

Meikle, T. G., Zabara, A., Waddington, L. J., Separovic, F., Drummond, C. J., and Conn, C. E. (2017). Incorporation of antimicrobial peptides in nanostructured lipid membrane mimetic bilayer cubosomes. *Colloids Surf. B Biointerfaces* 152, 143–151. doi: 10.1016/j.colsurfb.2017.01.004

Midtgaard, S. R., Darwish, T. A., Pedersen, M. C., Huda, P., Larsen, A. H., Jensen, G. V., et al. (2018). Invisible detergents for structure determination of membrane proteins by small-angle neutron scattering. *FEBS J.* 285, 357–371. doi: 10.1111/febs.14345

Mulet, X., Boyd, B. J., and Drummond, C. J. (2013). Advances in drug delivery and medical imaging using colloidal lyotropic liquid crystalline dispersions. *J. Colloid Interface Sci.* 393, 1–20. doi: 10.1016/j.jcis.2012.10.014

Naing, S.-H., Oliver, R. C., Weiss, K. L., Urban, V. S., and Lieberman, R. L. (2018). Solution structure of an intramembrane aspartyl protease via small angle neutron scattering. *Biophys. J.* 114, 602–608. doi: 10.1016/j.bpj.2017.12.017

Nazaruk, E., Smoliński, S., Swatko-Ossor, M., Ginalska, G., Fiedurek, J., Rogalski, J., et al. (2008). Enzymatic biofuel cell based on electrodes modified with lipid liquid-crystalline cubic phases. *J. Power Sources* 183, 533–538. doi: 10.1016/j.jpowsour.2008.05.061

Osborne, H. B., Sardet, C., Michel-Villaz, M., and Chabre, M. (1978). Structural study of rhodopsin in detergent micelles by small-angle neutron scattering. *J. Mol. Biol.* 123, 177–206. doi: 10.1016/0022-2836(78)90320-0

Pérez, J., and Koutsioubas, A. (2015). *Memprot*: a program to model the detergent corona around a membrane protein based on SEC–SAXS data. *Acta Crystallogr. D* 71, 86–93. doi: 10.1107/S1399004714016678

Sarkar, S., Tran, N., Rashid, M. H., Le, T. C., Yarovsky, I., Conn, C. E., et al. (2019). Toward cell membrane biomimetic lipidic cubic phases: a high-throughput exploration of lipid compositional space. *ACS Appl. Bio Mater.* 2, 182–195. doi: 10.1021/acsabm.8b00539

Satsoura, D., Kučerka, N., Shivakumar, S., Pencer, J., Griffiths, C., Leber, B., et al. (2012). Interaction of the full-length Bax protein with biomimetic mitochondrial liposomes: a small-angle neutron scattering and fluorescence study. *Biochim. Biophys. Acta* 1818, 384–401. doi: 10.1016/j.bbamem.2011.10.007

Service, R. F. (2014). Gently does it. *Science* 343, 1094–1097. doi: 10.1126/science.343.6175.1094

Skar-Gislinge, N., and Arleth, L. (2011). Small-angle scattering from phospholipid nanodiscs: derivation and refinement of a molecular constrained analytical model form factor. *Phys. Chem. Chem. Phys.* 13, 3161–3170. doi: 10.1039/C0CP01074J

Skar-Gislinge, N., Kynde, S. A. R., Denisov, I. G., Ye, X., Lenov, I., Sligar, S. G., et al. (2015). Small-angle scattering determination of the shape and localization of human cytochrome P450 embedded in a phospholipid nanodisc environment. *Acta Crystallogr. D. Biol. Crystallogr.* 71, 2412–2421. doi: 10.1107/S1399004715018702

Sokolova, A., Whitten, A. E., de Campo, L., Christoforidis, J., Eltobaji, A., Barnes, J., et al. (2019). Performance and characteristics of the BILBY time-of-flight small-angle neutron scattering instrument. *J. Appl. Crystallogr.* 52, 1–12. doi: 10.1107/S1600576718018009

Squires, A. M., Akbar, S., Tousley, M. E., Rokhlenko, Y., Singer, J. P., and Osuji, C. O. (2015). Experimental evidence for proposed transformation pathway from the inverse hexagonal to inverse diamond cubic phase from oriented lipid samples. *Langmuir* 31, 7707–7711. doi: 10.1021/acs.langmuir.5b01676

Svergun, D. I., Richard, S., Koch, M. H. J., Sayers, Z., Kuprin, S., and Zaccai, G. (1998). Protein hydration in solution: experimental observation by x-ray and neutron scattering. *Proc. Natl. Acad. Sci. U.S.A.* 95, 2267–2272. doi: 10.1073/pnas.95.5.2267

Takahashi, H., and Jojiki, K. (2017). Water isotope effect on the lipidic cubic phase: heavy water-Induced interfacial area reduction of monoolein-water system. *Chem. Phys. Lipids* 208, 52–57. doi: 10.1016/j.chemphyslip.2017.09.001

Trenker, R., Call, M. E., and Call, M. J. (2015). Crystal structure of the glycophorin A Transmembrane dimer in lipidic cubic phase. *J. Am. Chem. Soc.* 137, 15676–15679. doi: 10.1021/jacs.5b11354

Vallooran, J. J., Handschin, S., Pillai, S. M., Vetter, B. N., Rusch, S., Beck, H. P., et al. (2016). Lipidic cubic phases as a versatile platform for the rapid detection of biomarkers, viruses, bacteria, and parasites. *Adv. Funct. Mater.* 26, 181–190. doi: 10.1002/adfm.201503428

van 't Hag, L., Anandan, A., Seabrook, S. A., Gras, S. L., Drummond, C. J., Vrielink, A., et al. (2017a). Direct demonstration of lipid phosphorylation in the lipid bilayer of the biomimetic bicontinuous cubic phase using the confined enzyme lipid A phosphoethanolamine transferase. *Soft Matter* 13, 1493–1504. doi: 10.1039/C6SM02487D

van 't Hag, L., Darmanin, C., Le, T. C., Mudie, S., Conn, C. E., and Drummond, C. J. (2014). *In meso* crystallization: compatibility of different lipid bicontinuous cubic mesophases with the cubic crystallization screen in aqueous solution. *Cryst. Growth Des.* 14, 1771–1781. doi: 10.1021/cg4018954

van 't Hag, L., de Campo, L., Garvey, C. J., Feast, G. C., Leung, A. E., Yepuri, N. R., et al. (2016a). Using SANS with contrast-matched lipid bicontinuous cubic phases to determine the location of encapsulated peptides, proteins, and other biomolecules. *J. Phys. Chem. Lett.* 7, 2862–2866. doi: 10.1021/acs.jpclett.6b01173

van 't Hag, L., de Campo, L., Tran, N., Sokolova, A., Trenker, R., Call, M. E., et al. (2019). Protein-eye view of the *in meso* crystallization mechanism. *Langmuir* 35, 8344–8356. doi: 10.1021/acs.langmuir.9b00647

van 't Hag, L., Gras, S. L., Conn, C. E., and Drummond, C. J. (2017b). Lyotropic liquid crystal engineering moving beyond binary compositional space–ordered nanostructured amphiphile self-assembly materials by design. *Chem. Soc. Rev.* 46, 2705–2731. doi: 10.1039/C6CS00663A

van 't Hag, L., Knoblich, K., Seabrook, S. A., Kirby, N. M., Mudie, S. T., Lau, D., et al. (2016c). Exploring the *in meso* crystallization mechanism by characterizing the lipid mesophase microenvironment during the growth of single transmembrane α-helical peptide crystals. *Philos. Trans. R. Soc. A Math. Phys. Eng. Sci.* 374:20150125. doi: 10.1098/rsta.2015.0125

van 't Hag, L., Li, X., Meikle, T. G., Hoffmann, S. V, Jones, N. C., Pedersen, J. S., et al. (2016b). How peptide molecular structure and charge influence the nanostructure of lipid bicontinuous cubic mesophases: model synthetic WALP peptides provide insights. *Langmuir* 32, 6882–6894. doi: 10.1021/acs.langmuir.6b01058

Vandoolaeghe, P., Barauskas, J., Johnsson, M., Tiberg, F., and Nylander, T. (2009a). Interaction between lamellar (vesicles) and nonlamellar lipid liquid-crystalline nanoparticles as studied by time-resolved small-angle X-ray diffraction. *Langmuir* 25, 3999–4008. doi: 10.1021/la802768q

Vandoolaeghe, P., Rennie, A. R., Campbell, R. A., and Nylander, T. (2009b). Neutron reflectivity studies of the interaction of cubic-phase nanoparticles with phospholipid bilayers of different coverage. *Langmuir* 25, 4009–4020. doi: 10.1021/la802766n

Walsh, G. (2014). Biopharmaceutical benchmarks 2014. *Nat. Biotechnol.* 32:992. doi: 10.1038/nbt.3040

Yang, J., Yan, R., Roy, A., Xu, D., Poisson, J., and Zhang, Y. (2015). The I-TASSER suite: protein structure and function prediction. *Nat. Methods* 12, 7–8. doi: 10.1038/nmeth.3213

Yepuri, N. R., Clulow, A. J., Prentice, R. N., Gilbert, E. P., Hawley, A., Rizwan, S. B., et al. (2019). Deuterated phytantriol–a versatile compound for probing material distribution in liquid crystalline lipid phases using neutron scattering. *J. Colloid Interface Sci.* 534, 399–407. doi: 10.1016/j.jcis.2018.09.022

Zabara, A., Meikle, T. G., Newman, J., Peat, T. S., Conn, C. E., and Drummond, C. J. (2017). The nanoscience behind the art of in-meso crystallization of membrane proteins. *Nanoscale* 9, 754–763. doi: 10.1039/C6NR07634C

Zhai, J., Fong, C., Tran, N., and Drummond, C. J. (2019). Non-lamellar lyotropic liquid crystalline lipid nanoparticles for the next generation of nanomedicine. *ACS Nano* 13, 6178–6206. doi: 10.1021/acsnano.8b07961

Zhai, J., Sarkar, S., Conn, C. E., and Drummond, C. J. (2020). Molecular engineering of super-swollen inverse bicontinuous cubic and sponge lipid phases for biomedical applications. *Mol. Syst. Des. Eng.* 5, 1354–1375. doi: 10.1039/D0ME00076K

Zhai, J., Scoble, J. A., Li, N., Lovrecz, G., Waddington, L. J., Tran, N., et al. (2015). Epidermal growth factor receptor-targeted lipid nanoparticles retain self-assembled nanostructures and provide high specificity. *Nanoscale* 7, 2905–2913. doi: 10.1039/C4NR05200E

Conflict of Interest: The authors declare that the research was conducted in the absence of any commercial or financial relationships that could be construed as a potential conflict of interest.

frontiers in Physics

ORIGINAL RESEARCH
published: 10 February 2021
doi: 10.3389/fphy.2020.620082

Data Analysis and Background Subtraction in Neutron Spin Echo Spectroscopy

Ingo Hoffmann *

Institut Laue-Langevin, Grenoble, France

With the constantly improving performance of neutron spin echo (NSE) spectrometers it becomes possible to perform measurements on increasingly complex samples and to study more and more delicate effects. To properly study such effects, proper background correction becomes increasingly important. In this paper, we will review different methods to subtract the buffer from NSE measurements and study the effect of small errors in the subtraction of the background. In the large dynamic range of modern neutron spin-echo spectrometers multiple effects become visible in a single measurement. Specifically, for vesicles both membrane undulations and translational diffusion have an effect on the intermediate scattering function in the NSE time window and here, we will investigate how taking this into account differently affects the results obtained from data analysis.

Keywords: neutron spin echo, membrane dynamics, phospholipid, neutron scattering, quasielastic scattering, vesicles

OPEN ACCESS

Edited by:
Alexandros Koutsioumpas, Helmholtz Association of German Research Centers (HZ), Germany

Reviewed by:
Elizabeth Kelley, National Institute of Standards and Technology (NIST), United States
Piotr Adam Zolnierczuk, Oak Ridge National Laboratory (DOE), United States

***Correspondence:**
Ingo Hoffmann
hoffmann@ill.fr

Specialty section:
This article was submitted to Physical Chemistry and Chemical Physics, a section of the journal Frontiers in Physics

Received: *21 October 2020*
Accepted: *23 November 2020*
Published: *10 February 2021*

Citation:
Hoffmann I (2021) Data Analysis and Background Subtraction in Neutron Spin Echo Spectroscopy. Front. Phys. 8:620082. doi: 10.3389/fphy.2020.620082

1 INTRODUCTION

After the invention of neutron spin echo (NSE) spectroscopy by Mezei [1] in 1972 it took more than another decade before the technique was used to study membrane dynamics, at first using droplet microemulsions [2]. Later, bicontinuous microemulsions [3] and lipid bilayers [4] were studied. The development of the Zilman-Granek model [5], adapting a model for semi-flexible polymers by Farge and Maggs [6] for the two dimensional case of bilayers and starting from a Helfrich bending Hamiltonian [7] meant a major breakthrough for the field as it managed to explain the anomalous scaling of the relaxation rate $\Gamma \propto \kappa^{-1/2}$ and the stretched exponential shape of the intermediate scattering function with a stretch exponent of 2/3 that was found soon after the publication of the paper in many membrane systems by NSE and dynamic light scattering (DLS) [8–10]. The expression for the normalized intermediate scattering function reads

$$S_{ZG}(q,t) = \exp\left(-\left(\Gamma_{ZG} q^3 t\right)^{2/3}\right) \tag{1}$$

with the modulus of the scattering vector q, Fourier time t and

$$\Gamma_{ZG} = 0.025\gamma\sqrt{\frac{k_B T}{\kappa}}\,\frac{k_B T}{\eta}, \tag{2}$$

where k_B is the Boltzmann constant, T is the temperature, η is the viscosity, κ is the bending rigidity and $\gamma \approx 1$ for $\kappa/k_B T >> 1$.

Since then, membrane dynamics have become one of the major subjects studied by NSE. As an admittedly somewhat random example, in the last proposal round 2019, a little less than 40% of all proposals submitted for the NSE spectrometer IN15 [11] at the Institut Laue-Langevin were related

to the study of membrane dynamics. Another (less random) example is the number of citations of papers mentioning NSE and membrane dynamics from the Web of Science core collection (November 2020) which has increased by almost a factor 30 between 2000 and 2020, accounting for more than 15% of all the citations of papers mentioning NSE compared to less than 2% in 2000.

It was realized early on that bending rigidities obtained from fitting the Zilman-Granek model to NSE data are usually too high by about a factor 10 [12, 13] while values obtained from DLS give reasonable values [8]. The simplest remedy for this problem is to use a higher effective viscosity (typically $\eta_{eff} = 3\eta$) and attribute the discrepancies to internal dissipation in the membrane. Seifert and Langer [14] found that at the length and time scale of NSE it is not a simple bending mode but a combined bending-stretching mode that is observed with an effective bendig rigidity

$$\tilde{\kappa} = \kappa + 2d^2k, \tag{3}$$

with the monlayer elastic area compressibility modulus k and the height of the monolayer neutral surface from the bilayer midsurface d. Fortunately, the compressibility modulus of the bilayer K_a is proportional to the bending rigidity [15].

$$K_a = \frac{24\kappa}{d_{bilayer}^2}, \tag{4}$$

which is related to k for a symmetric bilayer by $K_a = 2k$ [16] even though others claim to have found $K_a = k$ [17]. The factor 24 in **Eq. 4** stems from treating the chain entropy of the lipids as short polymers in non-coupling monolayers ignoring van der Waals interactions or effects from the headgroup. This yields excellent results in treating data from micropipette suction [15] but different theoretical treatments can lead to factors between 4 and 48 [18] instead of 24 in **Eq. 4** depending on the level of coupling between the monolayers and the distribution of lateral pressure across the membrane. The remaining parameter in **Eq. 4** d_{bilayer} is the mechanical thickness of the bilayer. For saturated and monounsaturated it can be replaced by the thickness of the hydrophobic part of the bilayer, but deviations are observed for more complicated bilayers such as systems with polyunsaturated lipids [15] or bilayers with cholesterol [19]. Inserting **Eq. 4** in **Eq. 3** with $K_a = 2k$ gives

$$\tilde{\kappa} = \kappa + 24\left(d/\mathrm{d}_{\mathrm{bilayer}}\right)^2, \tag{5}$$

where the exact value of d is not known but is commonly assumed to be between 0.5 and 1 times the monolayer thickness [20, 21]. Watson and Brown [20] have shown that **Eq. 5** can simply be used in the framework of the Zilman Granek model replacing κ by $\tilde{\kappa}$ which simply leads to a different prefactor in **Eq. 2**. The current consensus is to use a value of 0.0069 instead of 0.025 [22] which is close to the commonly used three times higher effective viscosity and corresponds to setting d at $\sqrt{(0.025/0.0069 - 1)/24} \cdot 2 = 0.66$ times the hydrophobic monolayer thickness. Different prefactors were used in different papers and Table 1 in the review by Gupta et al. [23] gives a comprehensive overview. However, it should be kept in mind that these prefactors are merely the result of matching values obtained from NSE measurements by fitting **Eq. 1** with values from other methods.

Another complication comes from the fact that in the derivation of the approximate form of the Zilman-Granek model in **Eq. 1** an averaging over the wavelengths of the undulations has to be performed. Monkenbusch et al. [13] have shown for length and time scales relevant for microemulsions that the explicit length scale influences the result when explicitly evaluating the nested integrals that are otherwise approximated to give **Eq. 1**.

Given these uncertainties in the theoretical treatment, the prefactor in **Eq. 2** should be considered as a simple fudge factor and for a relative comparison between data from structurally similar vesicles **Eq. 1** is perfectly sufficient as long as care is taken not to over interpret absolute values of κ.

This paper can not and will not try to resolve all the aforementioned theoretical uncertainties but focus on the effect of the exact fitting procedure of the data. While many publications simply fit data with **Eq. 1**, diffusion of vesicles certainly has an influence on the intermediate scattering function and in **Section 2** we will investigate how values of κ are influenced by different methods of taking into account translational diffusion. In addition it will be investigated how the use of the explicit form of the Zilman-Granek model as in Monkenbusch et al. [13] influences the obtained results on length scales relevant to lipid vesicles.

In **Section 3** the effect of the background subtraction will be examined in detail. While the details of the procedure for the subtraction of the background are comparably unimportant as long as the data is simply analyzed by fitting a single stretched exponential it becomes increasingly important as more subtle effects are investigated as for example thickness fluctuations [22, 24, 25] or short range motions of the lipids in the membrane [26, 27].

All of this is done in the hope that it will allow to extract more robust information from NSE experiments, which may in turn help to further develop the underlying theory.

2 DATA ANALYSIS

A closer look at **Eq. 1** reveals that the q^3 dependence of the undulation mode is merely the result of keeping the q dependence of the relaxation rate in the parentheses with the 2/3 exponent and **Eq. 1** could equally well be rewritten as $S_{ZG} = \exp\left(-\Gamma_{ZG}^{2/3} q^2 t^{2/3}\right)$ which shows a q^2 dependence just like simple diffusion. Therefore, observing a q^3 dependence when fitting **Eq. 1** does not unambiguously verify the validity of the Zilman-Granek model and the telltale sign is in fact the stretched exponential shape of the curve. Looking at the first derivative of **Eq. 1**

$$S'_{ZG}(q,t) = -\frac{2/3 \exp\left(-\left(\Gamma_{ZG} q^3 t\right)^{2/3}\right)^{2/3} \left(\Gamma_{ZG} q^3\right)^{2/3}}{t^{1/3}} \tag{6}$$

and comparing it to the derivative of the simple exponential describing diffusion $\left(S_{diff}(q,t)\right)' = -Dq^2 \exp\left(-Dq^2 t\right)$, with diffusion coefficient D) it is clear that at short times the decay is much steeper for a stretched exponential contribution following the Zilman-Granek model than for simple diffusion because of the $t^{1/3}$ term in the denominator of **Eq. 6** which also ensures that at long times the simple exponential will eventually decay faster. **Figure 1**) shows the ratio between the slopes of the

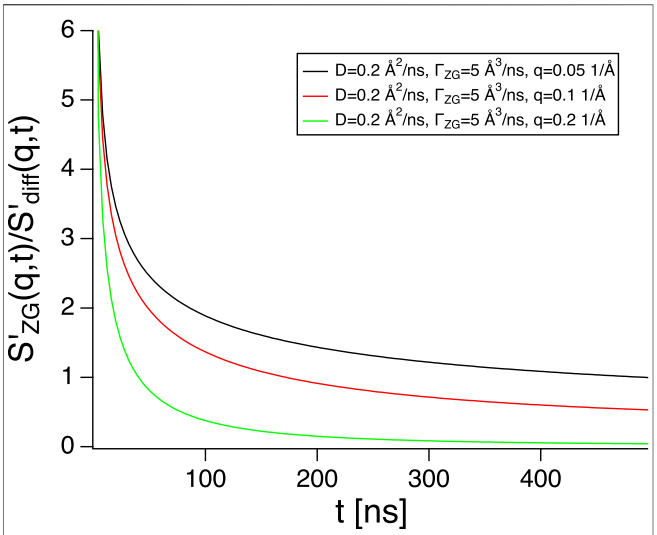

FIGURE 1 | Ratio between the slope of the Zilman-Granek stretched exponential (see **Eq. 6**) and the derivative of simple exponential for diffusion with parameters typical for fluid phase lipid vesicles. Only at short times the contribution from diffusion is negligible.

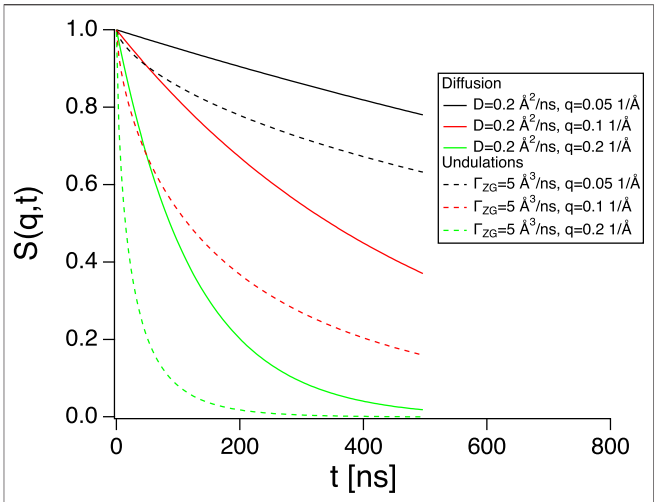

FIGURE 2 | Intermediate scattering functions for diffusion ($S_{diff}(q, t)$, full lines) and membrane undulations ($S_{ZG}(q, t)$, dashed lines) using parameters indicated in the graph. Diffusion gives a non-negligible contribution.

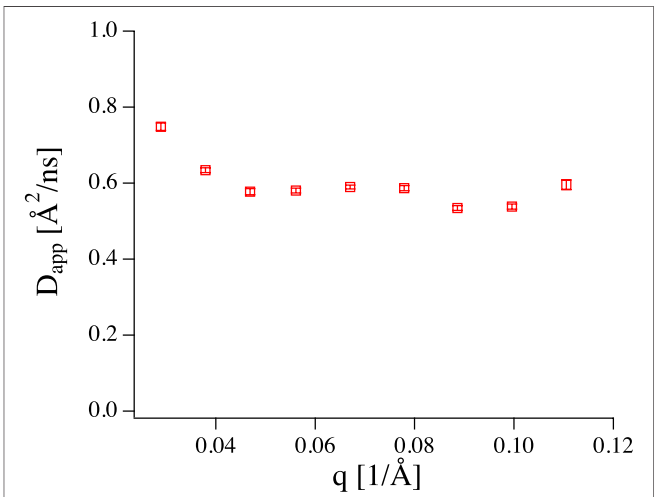

FIGURE 3 | Apparent diffusion coefficient obtained from fitting NSE data of 100 nm vesicles (2 mg/ml) with a simple exponential. The value is too large for simple diffusion, but no q^3 dependence is present.

Zilman-Granek stretched exponential and the simple exponential of translational diffusion using typical values both for D and Γ_{ZG}. A diffusion coefficient of 0.2 Å^2/ns corresponds to a hydrodynamic radius $R_H = k_BT/(6\pi\eta D) = 100$ nm at room temperature in D^{2}O and $\Gamma_{ZG} = 5$ Å^3/ns, using the usual prefactor 0.0069 corresponds to a bending rigidity of 26 k_BT which is a reasonable value for a phospholipid bilayer. It can be seen that the ratio quickly drops to values on the order of two or less already below 100 ns. In practice, on IN15 a q value of 0.05 could be measured with a neutron wavelength of 13.5 Å, which would allow to reach almost 500 ns, 0.1 1/Å could be measured at a wavelength of 10 Å which would allow to reach fourier times up to almost 200 ns and $q = 0.2$ 1/Å has to be measured using 6 Å neutrons, which would allow to measure Fourier times up to almost 50 ns. In any case, while the initial decay is dominated by the Zilman-Granek contribution, near the end of the Fourier time range the ratio of decays has dropped to values close to one and it is clear that the contribution from translational diffusion can not be neglected in the analysis of the data. From **Figure 1** it might seem as if the Zilman-Granek contribution would be the least visible at high q. However, at higher q, the intermediate scattering function has already mostly decayed during the initial fast decay as can be seen in **Figure 2**. With the values used here, S_{ZG} has already decayed to about 0.2 while $S_{diff} \sim 0.8$, still. In practice such a high q value can result in somewhat lengthy acquisition times, since the formfactor of the vesicle has mostly decayed.

Let us now turn our attention to a practical example. Fluid phase phosphatidylcholine (PC) vesicles with a radius of about 100 nm at a lipid concentration of 2 mg/ml have been measured at IN15. Fitting a simple exponential to determine an apparent diffusion coefficient ($S(q,t) = A\exp(-D_{app}q^2t)$) (equivalent of fitting a simple Lorentzian to determine a linewidth in $S(q,\omega)$) gives fairly constant values of D_{app} (see **Figure 3**) and does not give a q^3 dependence. In fact values slightly decrease with increasing q as the dynamic window of the measurement increasingly covers the long t part of the curve with its slow decay. Upon closer inspection, a small dip can be seen at 0.09 1/Å which might stem from correlations between membranes resulting in de Gennes narrowing [28] ($D(q) = D_0/S(q)$, with the static structure factor $S(q)$)), which would imply that a few vesicles are not entirely unilamellar. At the lowest q, a slight increase in D_{app} can be seen. This behavior can be observed quite frequently in NSE data, when only a relatively weak decay of $S(q, t)$ takes place in the NSE time window and the curves are not perfectly normalized to 1. Here, the curve for 0.029 1/Å does not decay below 0.8 and only has a value of 0.98 at the shortest times (see **Figure 4**). This effect is mostly taken into account by applying

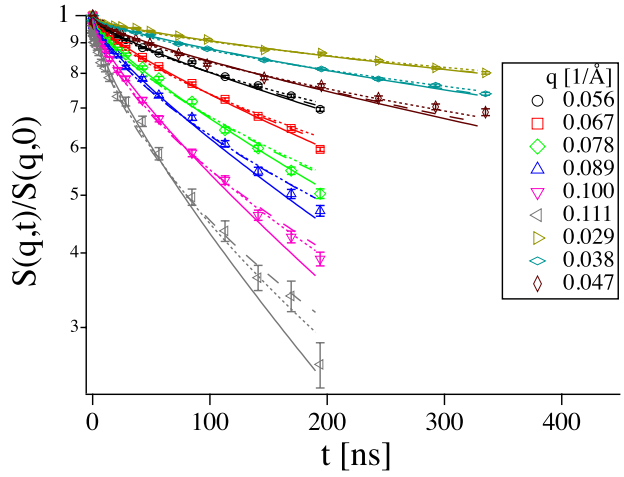

FIGURE 4 | Intermediate scattering function of the same vesicles as in **Figure 3** with different fits: Dashed lines: **Eq. 8,** full lines: **Eq. 7,** dotted lines: **Eq. 1.** All fit functions yield reasonable fits.

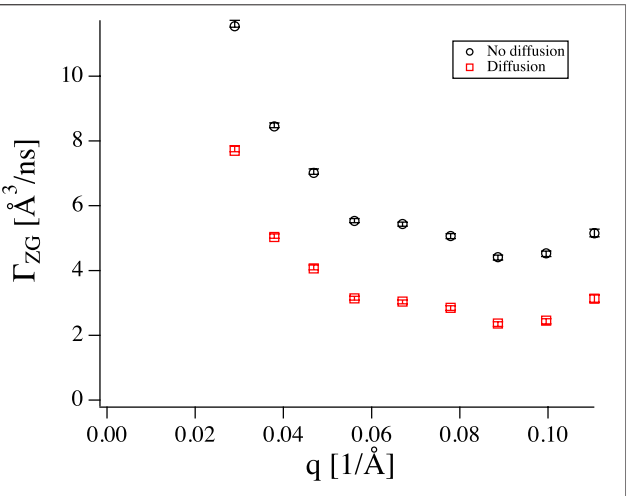

FIGURE 5 | Γ_ZG obtained from fitting **Eq. 1** (black circles) and **Eq. 7** (red squares) to the vesicle data. Including diffusion leads to systematically lower values.

a prefactor to the exponential as additional fit parameter as has been the case for the determination of D_{app} but becomes more severe without as can be seen in **Figures 5** and **6**. Looking at the curves in **Figure 4** it is clear that $S(q, t)$ is not a simple exponential and the values for D_{app} in **Figure 3** are too large for the simple diffusion of a vesicle with a 100 nm radius, so it can be concluded that we are in fact observing membrane dynamics. Fitting **Eq. 1** to the data yields values of Γ_{ZG} on the order of 5 Å^3/ns (see **Figure 5**), realistic values of the bending rigidity, which is however no surprise at all, since the prefactors were chosen such that they give reasonable values.

The simplest way to include diffusion in the fit is by multiplication of the diffusion term with the Zilman-Granek expression:

$$S(q,t) = \exp(-Dq^2t)\exp\left(-(\Gamma_{ZG}q^3t)^{2/3}\right). \tag{7}$$

Fitting two fairly similar relaxation rates which only differ in the exact shape of the curve is fairly difficult. Therefore, D should be known from an independent measurement such as DLS. Using $D = 0.208$ Å^2/ns a value of $\Gamma_{ZG} = 3$ Å^3/ns is obtained which would correspond to a fairly high $\kappa = 73\ k_BT$, which again is by no means surprising since the prefactor was chosen such that it would yield reasonable values of κ in fits without diffusion and adding a second dynamic contribution obviously leads to a decrease of the relaxation rate of the other.

The undulation motion of the membrane has a limited amplitude and consequently its visibility depends on q. Therefore, it is in principle necessary to include an amplitude $a(q)$:

$$S(q,t) = \exp(-Dq^2t)\left((1-a(q)) + a(q)\exp\left(-(\Gamma_{ZG}q^3t)^{2/3}\right)\right), \tag{8}$$

where **Eq. 7** is the special case where $a = 1$. Unfortunately, **Eq. 8** inflates the number of fit parameters but conceptionally κ should be q independent and using a single κ for all q values reduces the number of fit parameter to a reasonable value. Performing the fit on the data in **Figure 4** results in the amplitudes shown in **Figure 6** and $\Gamma_{ZG} = 12$ Å^3/ns, which is much higher than the value obtained by simply fitting **Eq. 1** due to the reduced contribution of the Zilman-Granek term.

The Milner-Safran model [29] describes membrane fluctuations for small microemulsion droplets [30] and provides an explicit expression for the amplitude. Mell et al. [31] have tried to apply Zilman-Granek model but using the amplitudes from the Milner-Safran model. They found rather mediocre agreement between theory and data. The problem might result from the fact that in the Millner-Safran theory a sphere is expanded in spherical harmonics to describe the fluctuations. This requires some excess area, relative to a perfect sphere, which minimizes the surface to volume ratio and the volume is conserved since the material can not be exchanged on the nanosecond time scale of the undulations. The longest undulation wavelength corresponds to half the circumference of the sphere and with equipartition the amplitude of that mode ($n = 2$) is given by **Eq. 6** of Schneider et al. [32].

$$\langle U^2 \rangle = \frac{k_BT}{16\kappa}R^2 \tag{9}$$

which gives $\sqrt{\langle U^2 \rangle} = 5.6$ nm for $\kappa = 20\ k_BT$ and $R = 100$ nm which in turn would result in unreasonably large excess areas and therefore, it is safe to assume that long wavelength undulations are not present in a real phospholipid vesicle system as predicted by the Milner-Safran theory.

This raises another interesting question. What is the range of undulation wavelengths that is actually relevant for NSE measurements of lipid vesicles? Half the vesicles circumference is an upper limit which is most likely not reached due to the lack of excess area in the vesicles. To satisfy equipartition, long wavelength undulations need rather large amplitudes, which

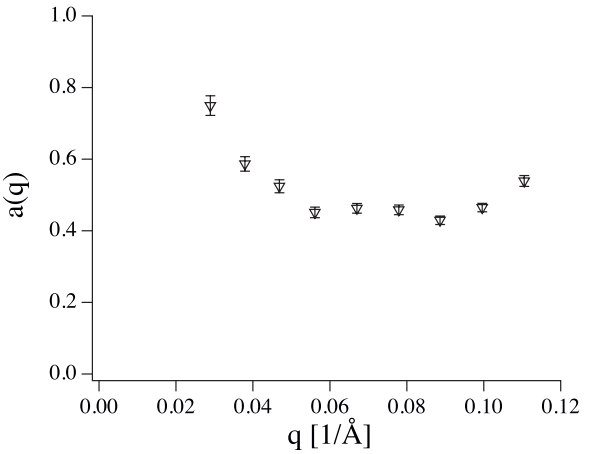

FIGURE 6 | Amplitude $a(q)$ obtained from fitting data shown in **Figure 4** to **Eq. 8** with Γ_{ZG} as shared parameter (dashed lines). Leaving $a(q)$ free it takes values significantly smaller than 1.

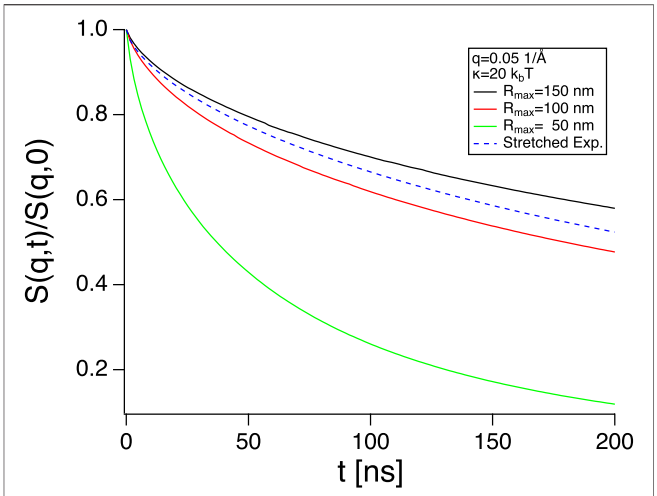

FIGURE 7 | $S(q, t)$ calculated using **Eq. 10** with different R_{max} (full lines) and **Eq. 1** (dashed blue line, using κ not $\tilde{\kappa}$) using parameters indicated in the graph. The maximum length scale clearly has an effect on $S(q, t)$.

results in a strong deformation of the vesicles from their ideal spherical shape and increases the surface to volume ratio. Since the volume of the vesicles is conserved over the nanosecond timescale of the undulations some excess surface are is needed to perform undulation motions [29] and the amount of excess area that would be needed for the long wavelength undulations with their large amplitudes may not be available in practice. Monkenbusch et al. [13] mapped the parameter space but in a range more relevant to microemulsions by evaluating the complete expression of the Zilman-Granek expression:

$$s(q,t) \sim \int_0^1 \mathrm{d}\mu \int_0^{R_{max}} \mathrm{d}r J_0\left(qr\sqrt{1-\mu^2}\right) \times \exp\left(\frac{-k_B T}{2\pi\kappa} q^2 \mu^2 \int_{k_{min}}^{k_{max}} \mathrm{d}k \frac{1 - J_0(kr)\exp\left(-\kappa/(4\eta)k^3 t\right)}{k^3}\right) \quad (10)$$

where J_0 is the 0 order Bessel function, $R_{\max}$ is the maximum length scale, related to the minimum undulation wavevector $k_{min} = 2\pi/R_{max}$ and the maximum wavevector is given by a cut-off length on the order of the molecular length which has relatively little influence on the result. **Figure 7** compares the result for **Eq. 1** and 10 for $q = 0.05$ 1/Å, $\kappa = 20\ k_B T$ with different $R_{\max}$. It can be seen that $R_{\max}$ does have an influence on the intermediate scattering function. The result from **Eq. 1** falls right between $R_{\max} = 100$ and $R_{\max} = 150$ which is not too far from the maximum length πR in typical vesicles, which are usually between 50 and 100 nm in radius. In the future, it might be interesting to investigate vesicles of different sizes. However this might be challenging since smaller vesicles are difficult to produce and larger vesicles tend to be unstable. While **Eq. 10** is still computationally expensive due to the nested integrals, with modern computers it is possible to use **Eq. 10** as a fit function. For example, the curves in **Figure 7** were calculated with 128 points on a 2016 MacBook Pro in about 30, 9 and 2 s for $R_{\max}$ 150, 100 and 50 nm using not particularly optimized C code.

A more a fundamental problem is that either κ or $R_{\max}$ should be known to fit the other.

3 BACKGROUND SUBTRACTION

As new experiments are looking for increasingly subtle effects in membranes using NSE, such as thickness fluctuations of the membrane [22, 25] or short scale motions of lipids [26] a careful background subtraction becomes increasingly important.

Background correction in NSE [33] is greatly complicated by the fact that the incoherent scattering process changes the polarisation of the beam to -1/3 of its initial value [34]. As a result the shape of the background can be a rather complicated combination of coherent and incoherent dynamics with an amplitude of opposite sign (see **Figure 8**).

In addition scattering from the instrument itself contributes a mostly elastic signal. This complicated shape of the background sets a high-q limit for the measurement of coherent dynamics in aqueous solution by NSE. The form factor typically decays as q^{-4} at high q while the incoherent scattering coming mostly from the background has a constant intensity with q and the subtraction of a background with a complicated shape from a weak signal quickly starts requiring a level of precision which would make acquisition times prohibitively long. As a rule of thumb, the coherent signal should ideally be noticeably higher than the incoherent signal. As long as it is on the same order of magnitude, measurements start becoming lengthy but are still feasible. With the intensity of deuterated buffer, and typical concentrations of lipid vesicles, this means that anything above 0.2 1/Å becomes extremely lengthy to measure.

After correcting for resolution effects [35] the non-normalized intermediate scattering function of a sample with coherent intensity I_{coh} and incoherent intensity I_{inc} will give

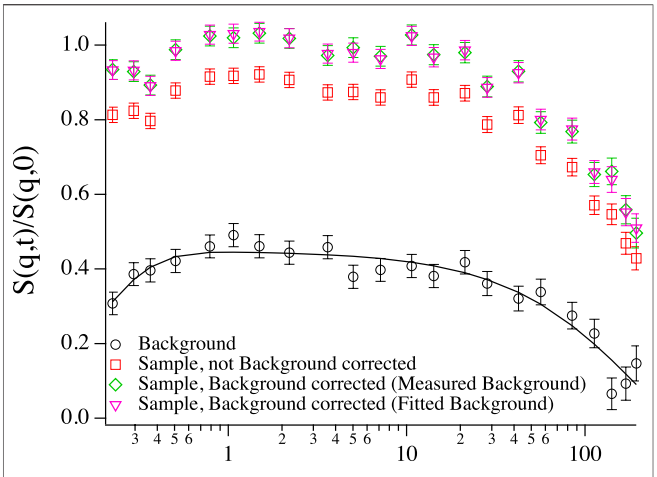

FIGURE 8 | Intermediate scattering function of vesicles at low concentration (~1 mg/ml) at q = 0.1 1/Å, background corrected with directly subtracted background (green diamonds), background corrected with fitted background (purple triangles), without background correction (red squares) and the corresponding background that was subtracted from the sample to give the background subtracted data sets (black circles, black line: double exponential fit) with fast incoherent dynamics at short times, which are still visible in the background corrected sample and background correction could not fully account for it.

$$s(q,t) = I_{coh} f_{coh}(t) - 1/3 I_{inc} f_{inc}(t), \tag{11}$$

where $f = 1$ at $t = 0$. This signal is normalized by the difference of the polarized intensity in up and down direction with $I_{up} = I_{coh} + 1/3I_{inc}$ and $I_{down} = 2/3I_{inc}$ so that the normalized intermediate scattering function reads

$$S(q,t) = \frac{I_{coh} f_{coh}(t) - 1/3 I_{inc} f_{inc}(t)}{I_{coh} - 1/3 I_{inc}}. \tag{12}$$

A few remarks on **Eq. 12** are in order. If the decay rate of f_{inc} is higher than that of f_{coh} and I_{inc} is sufficiently large relative to I_{coh}, $S(q, t)$ can have values larger than 1. If both the nominator and denominator in **Eq. 12** are negative, their negative signs will cancel out and incoherent scattering will appear as a relaxation with a positive amplitude. There can be fast dynamics, mostly in the background, which prevent the curve from tending to one within the dynamic window of the measurement.

While it is possible to directly subtract the transmission weighted background measurement directly from the individual detector images that are afterward used to calculate the echo, this requires the phase of the echo to be extremely stable [36]. Therefore, the standard procedure on IN15 is to calculate $s(q, t)$ for sample and background individually and subtract the background echo from the sample echo to obtain the background corrected non-normalized intermediate scattering function

$$s_{cor}(q,t) = s_{sample}(q,t) - T_{sb} s_{bkg}(q,t), \tag{13}$$

where T_{sb} is the transmission of the sample relative to the background. For normalization the transmission weighted up and down intensities of the background measurement are subtracted from the up and down intensities of the sample

$$S_{cor}(q,t) = \frac{s_{cor}(q,t)}{I_{coh,sample} - 1/3 I_{inc,sample} - T_{sb} I_{coh,bkg} + 1/3 T_{sb} I_{inc,bkg}}. \tag{14}$$

Assuming that $s_{sample}(q,t)$ contains coherent and incoherent contributions from the background (solvent and instrument) and from the part we are interested (e.g., vesicles), then

$$s_{sample}(q,t) = I_{coh,ves} f_{coh,ves}(t) - 1/3 I_{inc,ves} f_{inc,ves}(t) + T_{sb}\left(I_{coh,bkg} f_{coh,bkg}(t) - 1/3 I_{inc,bkg} f_{inc,bkg}(t)\right), \tag{15}$$

and the subtraction according to **Eq. 13** eliminates all background contributions but leaves both $f_{coh,ves}(t)$ and $f_{inc,ves}(t)$ untouched. However, assuming that both show the same time dependence, which should be valid at large q, the incoherent contribution from the relevant part of the sample manifests simply as a reduction of the amplitude of the signal, which normalization according to **Eq. 14** should take care of as long as the condition $I_{coh,ves} - 1/3 I_{inc,ves} \neq 0$ is fulfilled. Otherwise no signal can be detected. This procedure is generally quite robust but has its limitations as soon as the background contains several contributions with different phase, in which case the background should be subtracted detector image by detector image. This background subtraction procedure also delicately depends on both correct values of the transmission and the ratio of coherent to incoherent scattering. With aqueous samples, this can easily lead to some small inaccuracies since it is almost inevitable that the D_2O of the solvent exchanges with H_2O in the surrounding air. The degree of exchange can easily be slightly different between sample and background, for example because the background sample was prepared in a larger container than the other samples and standing open for longer during the preparation of the other samples using solvent from that container. If the sample compound itself contains a large number of exchangeable hydrogen atoms, it can even be advantageous to deliberately add H_2O to the background sample to match the coherent to incoherent ratio in the solvent of the sample [37]. Even if the samples and their background have been prepared with greatest care, there can still be small effects from multiple scattering which lead to a slightly increased apparent incoherent background. Following Eq. 33 from Shibayama et al. [38] with 2 mm sample thickness and assuming a relatively high concentration of 1 v% hydrogenated material (for which for simplicity we take the cross section of H_2O) results in a correction on the order of 0.005, which may still be important but typically, imperfections in the normalization stemming from sample preparation are on the order of a few percent.

Instead of subtracting a completely measured curve $s_{bkg}(q, t)$ in **Eq. 13,** in some situations it can be advantageous to subtract a curve that is the result of a fit to $s_{bkg}(q, t)$. If the shape is known and simple enough, it can save quite some time to only measure a few Fourier time points of $s_{bkg}(q, t)$ and fit the rest of the expression. To give an example, fully deuterated polymer melts show an essentially flat background with fast dynamics

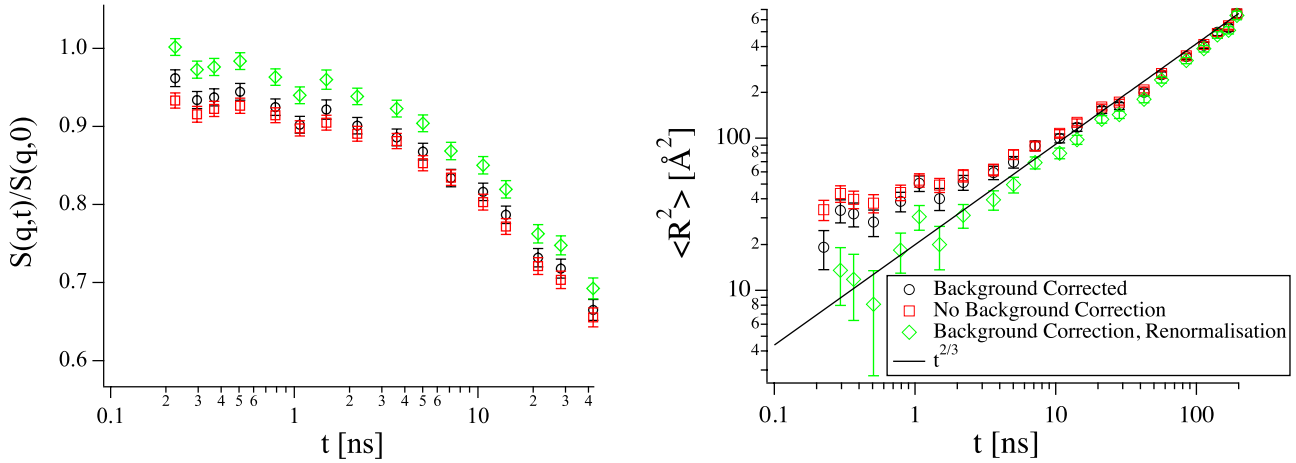

FIGURE 9 | Left: Short time range of $S(q, t)$ from the same vesicle sample as in **Figure 4** at $q = 0.11$ 1/Å with logarithmic x-axis, the same color code as in the right hand panel applies. Right: Mean square displacement calculated from the curves on the left. The black line shows scaling with $t^{2/3}$ as expected for the Zilman-Granek model. The Background corrected sample does not exactly go up to one at short times **(left)**. As a result a scaling with low scaling exponent x appears at short times in $\langle R^2 \rangle$ **(right)**. This behavior disappears when brute force renormalizing the curve with a factor 1/0.96 which ensures that the curve starts at 1 **(left)** and $\langle R^2 \rangle$ scales as $t^{2/3}$ even at the shortest time **(right)**.

that are not in the time window of NSE. Even if the full curve has been measured, it can be preferable to use a fitted background to avoid extra noise from a noisy background measurement. On the other hand, one runs the risk of introducing artifacts by using an oversimplified fit function for the background. Sometimes, even a double exponential fit can fail to capture all subtleties of the background. To the author's experience, it is generally preferable to measure the full background curve, whenever possible. After all, a fitted background can still be used after measuring the full curve, while the opposite case is more difficult. In **Figure 8** both versions of background subtraction are shown. Since the double exponential fit (black line) nicely describes the measured background, there is not much of a difference between the two versions of background correction, except for the third to last point, which is artificially high in the green curve where the background was directly subtracted, since the same point seems somewhat low in the measured background and the background fit straightens out this artifact.

The intricate details of background subtraction do not matter too much as long as the signal from the sample is large compared to the background. Unfortunately, some of the most interesting phenomena are best seen where the intensity is weak. Both shape fluctuations of microemulsion droplets [30, 39] and thickness fluctuations of membranes [22, 24, 25, 40] are best seen in their respective form factor minima. The result of an imperfect background subtraction usually is a curve that does not have an amplitude of exactly one together with a slight increase or flattening of $S(q, t)$ at short times, which is the result of a not perfectly subtracted incoherent contribution. Fitting such a curve with an amplitude fixed at 1, can lead to too high relaxation rates (see **Figures 5** and **6**), while leaving the amplitude as a free fit parameter leads to larger error bars and can potentially result in too low fitted relaxation rates.

Another kind of phenomenon where careful background subtraction is crucial are the short length scale motions observed by Gupta et al. [26], where a different exponent x in the evolution of the mean square displacement $\langle R^2 \rangle = -6 \ln(S(q,t))/q^2 \sim t^x$ at short times is attributed to an anomalous local motion of the head groups. Instead of $x = 1$ for diffusion or $x = 2/3$ for undulations a smaller value of 0.26 is found. This is an extremely subtle effect that prevails up to about $\langle R^2 \rangle = 10$ Å^2 which implies a decay of $S(q, t)$ at 0.15 1/Å from one to about 0.96. To complicate things more, imperfect background subtraction would have the exact same effect on the $\langle R^2 \rangle$ with an intercept that is not exactly one and some residual incoherent contribution from the background, which slows down the decay of $S(q, t)$ at short times. The curve in **Figure 9** (left) is not brought up to exactly one at short times but only to about 0.95, converting to $\langle R^2 \rangle$ shows a small scaling exponent x at short times even after background subtraction. However, the contribution has almost disappeared when brute force renormalising $S(q, t)$ with a factor 1/0.96. This shows that it is extremely difficult to differentiate such effects from an imperfect background subtraction.

4 CONCLUSION

In this paper the effect of background subtraction and data treatment on the information that can be gained from neutron spin echo (NSE) experiments on bilayers was discussed. The diffusion of typical lipid vesicles with radii between 50 and 100 nm as they are used in NSE experiments to investigate membrane dynamics does have an effect on the time and length scale covered by modern NSE spectrometers.

As long as vesicles of the same size and therefore same diffusion coefficient are compared, it is not strictly necessary to include translational diffusion in the analysis but it should be kept in mind that the absolute values of the bending rigidity that are obtained from the data without taking into account diffusion have only a limited significance. Unfortunately, the renormalization factors that are currently in use are based on data that was analyzed without diffusion to give values of the bending rigidity that agree with values obtained from other methods. If diffusion is taken into account when fitting data, there is still uncertainty concerning the value of the amplitude $a(a)$ in **Eq. 8**. Depending on whether it is fixed at one or left as a free parameter in the fit, the apparent value of the bending rigidity can change in either direction compared to the case without contribution from diffusion.

Nevertheless, as soon as bending rigidities from vesicles with different radii are compared it is advised to include a contribution from diffusion. Given the similar time scales, the diffusion coefficient should be obtained from an independent measurement such as DLS, which has its intricacies as well, since in the relatively concentrated samples used in NSE, the diffusion coefficient obtained at low q by DLS is most likely affected by de Gennes narrowing [28] ($D(q) = D_0/S(q)$, with the static structure factor $S(q)$) while it is (almost) not in the NSE q range. Therefore, the diffusion coefficient should ideally be determined in a dilute sample. If this is not possible, the effect of de Gennes narrowing can either be calculated from a measured structure factor (e.g., by SANS), simply be estimated from a suitable model or D can be calculated via the Stokes-Einstein equation from a size measured by SANS or another suitable technique. While this helps in making values obtained from vesicles with different sizes comparable, it still does not prevent the obtained values from being unreliable as far as their absolute values are concerned and given both the experimental uncertainties concerning the exact fitting procedure and the theoretical uncertainties concerning exact prefactors in the equations used for fitting, we will probably have to accept that we can only have a reliable relative comparison. What would put NSE in a position to provide reliable absolute values would be an expression for $a(q)$, which would allow to refine parameters from theory such as the height of the neutral surface in **Eq. 3**.

While usually background subtraction is not discussed in too much detail in NSE, it becomes increasingly important as more subtle effects are being studied and incorrect background subtraction and it was shown how imperfect background subtraction can lead to artifacts.

All of this shows that there are some challenges ahead on the way to gaining even more detailed information on membrane dynamics from NSE measurements.

DATA AVAILABILITY STATEMENT

The datasets presented in this study can be found in online repositories. The names of the repository/repositories and accession number(s) can be found below: dx.doi.org/10.5291/ILL-DATA.TEST-2861 dx.doi.org/10.5291/ILL-DATA.TEST-2712.

AUTHOR CONTRIBUTIONS

The author confirms being the sole contributor of this work and has approved it for publication.

ACKNOWLEDGMENTS

Raw data of the NSE curves shown here are available under dx.doi.org/10.5291/ILL-DATA.TEST-2861 and dx.doi.org/10.5291/ILL-DATA.TEST-2712. The author would like to thank Andrew Dennison, Andrew Parnell and Michael Gradzielski for letting him use their data in this paper as much as Olaf Holderer for sharing his *Python* code for **Eq. 10**. Financial support from the BMBF Project No. 05K13KT1 is gratefully acknowledged.

REFERENCES

1. Mezei F. Neutron spin echo: a new concept in polarized thermal neutron techniques. *Z Phys A Hadrons Nuclei* (1972) 255:146–60. doi:10.1007/BF01394523
2. Huang JS, Milner ST, Farago B, Richter D. Study of dynamics of microemulsion droplets by neutron spin-echo spectroscopy. *Phys Rev Lett* (1987) 59:2600–3. doi:10.1103/PhysRevLett.59.2600
3. Farago B, Monkenbusch M, Goecking K, Richter D, Huang J. Dynamics of microemulsions as seen by neutron spin echo. *Physica B* (1995) 213–214:712–7. doi:10.1016/0921-4526(95)00257-A
4. Pfeiffer W, König S, Legrand JF, Bayerl T, Richter D, Sackmann E. Neutron spin echo study of membrane undulations in lipid multibilayers. *Europhys Lett* (1993) 23:457. doi:10.1209/0295-5075/23/6/013
5. Zilman AG, Granek R. Undulations and dynamic structure factor of membranes. *Phys Rev Lett* (1996) 77:4788–91. doi:10.1103/PhysRevLett.77.4788
6. Farge E, Maggs AC. Dynamic scattering from semiflexible polymers. *Macromolecules* (1993) 26:5041–4. doi:10.1021/ma00071a009
7. Helfrich W. Elastic properties of lipid bilayers - theory and possible experiments. *Z Naturforsch C Biosci: J Biosci* (1973) 28:693–703. doi:10.1515/znc-1973-11-1209
8. Freyssingeas E, Roux D, Nallet F. Quasi-elastic light scattering study of highly swollen lamellar and sponge phases. *J Phys II* (1997) 7:913–29. doi:10.1051/jp2:1997162
9. Nagao M, Seto H, Kawabata Y, Takeda T. Temperature and pressure effects on structural formations in a ternary microemulsion. *J Appl Crystallogr* (2000) 33:653–6. doi:10.1107/S0021889899013679
10. Mihailescu M, Monkenbusch M, Endo H, Allgaier J, Gompper G, Stellbrink J, et al. Dynamics of bicontinuous microemulsion phases with and without amphiphilic block-copolymers. *J Chem Phys* (2001) 115:9563–77. doi:10.1063/1.1413509
11. Farago B, Falus P, Hoffmann I, Gradzielski M, Thomas F, Gomez C. The IN15 upgrade. *Neutron News* (2015) 26:15–7. doi:10.1080/10448632.2015.1057052
12. Komura S, Takeda T, Kawabata Y, Ghosh SK, Seto H, Nagao M. Dynamical fluctuation of the mesoscopic structure in ternary -water-n-octane amphiphilic systems. *Phys Rev E* (2001) 63:041402. doi:10.1103/PhysRevE.63.041402
13. Monkenbusch M, Holderer O, Frielinghaus H, Byelov D, Allgaier J, Richter D. Bending moduli of microemulsions; comparison of results from small angle neutron scattering and neutron spin-echo spectroscopy. *J Phys Condens Matter* (2005) 17:S2903–9. doi:10.1088/0953-8984/17/31/017
14. Seifert U, Langer SA. Viscous modes of fluid bilayer membranes. *Europhys Lett* (1993) 23:71–6. doi:10.1209/0295-5075/23/1/012

15. Rawicz W, Olbrich K, McIntosh T, Needham D, Evans E. Effect of chain length and unsaturation on elasticity of lipid bilayers. *Biophys J* (2000) 79:328–39. doi:10.1016/j.bpj.2009.11.026
16. Nagle JF. Area compressibility moduli of the monolayer leaflets of asymmetric bilayers from simulations. *Biophys J* (2019) 117:1051–6. doi:10.1016/j.bpj.2019.08.016
17. Doktorova M, Levine MV, Khelashvili G, Weinstein H. A new computational method for membrane compressibility: bilayer mechanical thickness revisited. *Biophys J* (2019) 116:487–502. doi:10.1016/j.bpj.2018.12.016
18. Bloom M, Evans E, Mouritsen OG. Physical properties of the fluid lipid-bilayer component of cell membranes: a perspective. *Q Rev Biophys* (1991) 24:293–397. doi:10.1017/S0033583500003735
19. Pan JJ, Tristram-Nagle S, Nagle JF. Effect of cholesterol on structural and mechanical properties of membranes depends on lipid chain saturation. *Phys Rev E* (2009) 80:021931. doi:10.1103/PhysRevE.80.021931
20. Watson MC, Brown FLH. Interpreting membrane scattering experiments at the mesoscale: the contribution of dissipation within the bilayer. *Biophys J* (2010) 98:L9–11. doi:10.1016/j.bpj.2009.11.026
21. Lee J, Choi S, Doe C, Faraone A, Pincus PA, Kline SR. Thermal fluctuation and elasticity of lipid vesicles interacting with pore-forming peptides. *Phys Rev Lett* (2010) 105:038101. doi:10.1103/PhysRevLett.105.038101
22. Nagao M, Kelley EG, Ashkar R, Bradbury R, Butler PD. Probing elastic and viscous properties of phospholipid bilayers using neutron spin echo spectroscopy. *J Phys Chem Lett* (2017) 8:4679–84. doi:10.1021/acs.jpclett.7b01830
23. Gupta S, de Mel JU, Schneider GJ. Dynamics of liposomes in the fluid phase. *Curr Opin Colloid Interface Sci* (2019) 42:121–36. doi:10.1016/j.cocis.2019.05.003
24. Nagao M, Chawang S, Hawa T. Interlayer distance dependence of thickness fluctuations in a swollen lamellar phase. *Soft Matter* (2011) 7:6598–605. doi:10.1039/C1SM05477E
25. Woodka AC, Butler PD, Porcar L, Farago B, Nagao M. Lipid bilayers and membrane dynamics: insight into thickness fluctuations. *Phys Rev Lett* (2012) 109:058102. doi:10.1103/PhysRevLett.109.058102
26. Gupta S, de Mel JU, Perera RM, Zolnierczuk P, Bleuel M, Faraone A, et al. Dynamics of phospholipid membranes beyond thermal undulations. *J Phys Chem Lett* (2018) 9:2956–60. doi:10.1021/acs.jpclett.8b01008
27. Gupta S, Schneider GJ. Modeling the dynamics of phospholipids in the fluid phase of liposomes. *Soft Matter* (2020) 16:3245–56. doi:10.1039/C9SM02111F
28. de Gennes PG. Liquid dynamics and inelastic scattering of neutrons. *Physica* (1959) 25:825–39. doi:10.1016/0031-8914(59)90006-0
29. Milner ST, Safran SA. Dynamical fluctuations of droplet microemulsions and vesicles. *Phys Rev A* (1987) 36:4371–9. doi:10.1103/PhysRevA.36.4371
30. Farago B, Gradzielski M. The effect of the charge density of microemulsion droplets on the bending elasticity of their amphiphilic film. *J Chem Phys* (2001) 114:10105–22. doi:10.1063/1.1362690
31. Mell M, Moleiro L, Hertle Y, Fouquet P, Schweins R, López-Montero I, et al. Bending stiffness of biological membranes: what can be measured by neutron spin echo? *Eur Phys J E* (2013) 36:1–13. doi:10.1140/epje/i2013-13075-2
32. Schneider M, Jenkins J, Webb W. Thermal fluctuations of large quasi-spherical bimolecular phospholipid vesicles. *J Phys France* (1984) 45:1457–72. doi:10.1051/jphys:019840045090145700
33. Farago B. The basics of neutron spin-echo (2003). Available at: https://www.osti.gov/etdeweb/servlets/purl/20009251.
34. Mezei F. The principles of neutron spin echo. In: F Mezei, editor *Neutron spin echo spectroscopy: basics, trends and applications*. Berlin, Heidelberg: Springer Berlin Heidelberg (1980). p. 1–26.
35. Mezei F. Fundamentals of neutron spin echo spectroscopy. In: *Neutron spin echo spectroscopy: basics, trends and applications*. Berlin, Heidelberg: Springer Berlin Heidelberg (2003). p. 5–14.
36. Farago B. in preparation (2020).
37. Farago B. Private communication (2020).
38. Shibayama M, Nagao M, Okabe S, Karino T. Evaluation of incoherent neutron scattering from softmatter. *J Phys Soc Jpn* (2005) 74:2728–36. doi:10.1143/JPSJ.74.2728
39. Nagao M, Seto H. Concentration dependence of shape and structure fluctuations of droplet microemulsions investigated by neutron spin echo spectroscopy. *Phys Rev E* (2008) 78:011507. doi:10.1103/PhysRevE.78.011507
40. Nagao M. Observation of local thickness fluctuations in surfactant membranes using neutron spin echo. *Phys Rev E* (2009) 80:031606. doi:10.1103/PhysRevE.80.031606

Conflict of Interest : The author declares that the research was conducted in the absence of any commercial or financial relationships that could be construed as a potential conflict of interest.

frontiers in Chemistry

ORIGINAL RESEARCH
published: 18 March 2021
doi: 10.3389/fchem.2021.628186

Structural Characterization of Natural Yeast Phosphatidylcholine and Bacterial Phosphatidylglycerol Lipid Multilayers by Neutron Diffraction

Alessandra Luchini[1], Giacomo Corucci[2,3], Krishna Chaithanya Batchu[2], Valerie Laux[2], Michael Haertlein[2], Viviana Cristiglio[2] and Giovanna Fragneto[2,3]*

[1]Niels Bohr Institute, University of Copenhagen, Copenhagen, Denmark, [2]Institut Laue Langevin, Grenoble, France, [3]Université Grenoble Alpes, Ecole Doctorale de Physique, Saint-Martin-d'Héres, France

Eukaryotic and prokaryotic cell membranes are difficult to characterize directly with biophysical methods. Membrane model systems, that include fewer molecular species, are therefore often used to reproduce their fundamental chemical and physical properties. In this context, natural lipid mixtures directly extracted from cells are a valuable resource to produce advanced models of biological membranes for biophysical investigations and for the development of drug testing platforms. In this study we focused on single phospholipid classes, i.e. *Pichia pastoris* phosphatidylcholine (PC) and *Escherichia coli* phosphatidylglycerol (PG) lipids. These lipids were characterized by a different distribution of their respective acyl chain lengths and number of unsaturations. We produced both hydrogenous and deuterated lipid mixtures. Neutron diffraction experiments at different relative humidities were performed to characterize multilayers from these lipids and investigate the impact of the acyl chain composition on the structural organization. The novelty of this work resides in the use of natural extracts with a single class head-group and a mixture of chain compositions coming from yeast or bacterial cells. The characterization of the PC and PG multilayers showed that, as a consequence of the heterogeneity of their acyl chain composition, different lamellar phases are formed.

Keywords: natural lipids, lipid multilayers, neutron diffraction, Pichia pastoris, *Escherichia coli*, deuterated lipids

OPEN ACCESS

Edited by:
Tommy Nylander, Lund University, Sweden

Reviewed by:
Amiya Kumar Panda, Vidyasagar University, India
Carmelo Corsaro, University of Messina, Italy

****Correspondence:***
Alessandra Luchini
a.luchini@nbi.ku.dk

Specialty section:
This article was submitted to Physical Chemistry and Chemical Physics, a section of the journal Frontiers in Chemistry

Received: *11 November 2020*
Accepted: *01 February 2021*
Published: *18 March 2021*

Citation:
Luchini A, Corucci G, Chaithanya Batchu K, Laux V, Haertlein M, Cristiglio V and Fragneto G (2021) Structural Characterization of Natural Yeast Phosphatidylcholine and Bacterial Phosphatidylglycerol Lipid Multilayers by Neutron Diffraction. Front. Chem. 9:628186. doi: 10.3389/fchem.2021.628186

INTRODUCTION

In cell membranes, lipids are organized in a bilayer-like structure with their hydrophobic acyl chains pointing towards each other and the polar headgroups exposed to the extracellular and cytoplasmic aqueous media. Whereas both eukaryotic and prokaryotic cells are delimited by a cytoplasmic membrane, their lipid composition is significantly different (van Meer and Voelker, 2008; Harayama and Riezman, 2018). In the eukaryotic plasma membrane, phospholipids and sterols are the main membrane components (Maxfiled and van Meer, 2010), and among the phospholipids, phosphatidylcholine (PC) is the most abundant (Harayama and Riezman, 2018). Among the prokaryotic cells, most of the bacteria have only phospholipids as lipid components of their cytoplasmic membrane (Strahl and Errington, 2017) and more specifically phosphatidylethanolamine (PE) and phosphatidylglycerol (PG) are the most abundant (Romantsov and Wood, 2016).

The direct investigation of cell membranes has been limited by their high level of complexity, which makes their isolation difficult and prevents the implementation of the most common biophysical methods (Seddon et al., 2004). For this reason, most of the information available on the structure, dynamics and function of biological membranes have been obtained so far by using model systems that are characterised by a considerably simpler lipid composition, typically 1–3 synthetic phospholipid species, and, therefore, are easy to produce (Bagatolli et al., 2010; Mouritsen, 2011). In particular, liposomes, supported lipid bilayers, lipid monolayers and lipid multilayers are among the most common model systems for studying lipid membranes in solution or at solid/liquid and liquid/air interfaces (Katsaras and Gutberlet, 2001; Hardy et al., 2013). They are also often used as platforms to investigate the structure and function of membrane proteins (Retel et al., 2017; Luchini et al., 2019) and to test the activity of drugs (Seddon et al., 2009; Vitiello et al., 2015). These applications prompted the design of more advanced model membrane systems that better resemble the lipid composition of real cell membranes, while still preserving the compatibility with biophysical methods for their structural and dynamical characterization. In particular, the extraction of lipids from eukaryotic or bacterial cells, resulted to be a successful strategy to produce membrane systems closer to real cell membranes compared to the ones composed by the simpler synthetic lipid mixtures (Lind et al., 2015; Himbert et al., 2017; Fragneto et al., 2018).

In this context, we recently reported the production and characterization of natural membranes composed of lipid mixtures extracted from the yeast *Pichia pastoris* (de Ghellinck et al., 2014; Gerelli et al., 2014; de Ghellinck et al., 2015; Luchini et al., 2018; Luchini et al., 2020). The study of these lipid mixtures is relevant for the general understanding of eukaryotic membranes as well as for the development of lipid platforms to investigate the activity of antifungal drugs (de Ghellinck et al., 2015). More specifically, in one of our previous studies we investigated the structure of lipid multilayers composed of the total *P.pastoris* lipid extract by means neutron diffraction measurements (Luchini et al., 2018). The *P.pastoris* total lipid extract is a complex lipid mixture, including different phospholipid species, *i.e.* different headgroup and acyl chain composition, as well as sterols, *i.e.* ergosterol, steryl-esters, free fatty acids and triglycerides. We compared the structure of the multilayers prepared with the total lipid extract with that of multilayers prepared with only the phospholipid extract from *P.pastoris* (Luchini et al., 2018). The phospholipid extract still contains several phospholipid species with different headgroup and acyl chain composition. The collected neutron diffraction data showed self-segregation of the lipids in regions of the multilayers with different d-spacing, *i.e.* the characteristic repetitive distance within the multilayer. This observation suggested the coexistance of different lipid phases in both the multilayer prepared with the total lipid extract and the phospholipid extract. However, being these lipid extracts characterized by both an heterogeneous composition of the lipid headgroups and acyl chains, we were unable to identify if both the headgroups and the acyl chains could induce the observed lipid self-segregation. In these previous studies, neutron diffraction experiments were performed on lipid multilayers prepared with both hydrogenous and deuterated lipid extracts. Indeed, we previously described the production of natural deuterated lipids by growing *P.pastoris* cells in a deuterated culture media (de Ghellinck et al., 2014). Deuterated lipids are valuable for the investigation of biological membranes with neutron scattering methods but also NMR and infrared spectroscopy. Indeed, deuterated lipids can be used in mixtures with hydrogenous compounds and exploit the contrast variation method that allows highlighting the parts of interest of the system under study. They can also be used instead of hydrogenous lipids to improve signal to noise ratio.

TABLE 1 | Composition of different *P.pastoris* lipid extracts expressed as % mol of the total lipids. The h-phospholipid and d-phospholipid extracts contain all the phospholipids composing the total lipid extract. Their characterization and composition analysis was previously reported (Luchini et al., 2018). In the *E.coli* extracts, cyclo C17 and cyclo C19 acyl chains exhibit a cyclopropane ring in their chemical structure.

P.Pastoris Extracts	**C16:0**	**C16:1**	**C16:2**	**C16:3**	**C18:0**	**C18:1**	**C18:2**	**C18:3**
h-phospholipids	15.9	3.8	1.1	1.9	4.2	41.8	26.4	4.9
d-phospholipids	16.7	2.7	0.7	1.3	1.8	72.0	3.6	1.1
HPC	10.3	6.3	-	-	20.4	32.1	24.1	6.8
DPC	9.4	17.3	-	-	0.9	49.3	19.2	3.8
E. Coli Extracts	**C14:0**	**C16:0**	**C16:1**	**C16:2**	**cyclo C17:0**	**C18:0**	**C18:1**	**cyclo C19:0**
HPG	5.1	39.7	3.5	2.4	18.7	1.9	6.2	22.4
DPG	6.1	45.7	4.1	1.2	25.8	0.9	7.1	8.9

In the present study, we continued our characterization of lipid extracts from *P. pastoris* and more specifically we focused on phosphatidylcholine (PC) lipid extracts. PC lipids are the most abundant lipids in *P.pastoris* as well as in mammalian membranes. The structure of multilayers prepared with these PC extracts are presented here for the first time. The interest of the study is that such extracts have a complex composition in terms of acyl chains (**Table 1** and **Supplementary Material**) which enabled us to investigate the impact of the heterogeneous acyl chain composition on the lipid self-segregation within a multilayer. Neutron diffraction was used also in the present study as characterization method for the investigation of multilayers prepared with with hydrogenous or deuterated PC lipid extracts. Drop casting of lipid solutions both in organic solvents or water are the most common protocols for the preparation of lipid multilayers for both X-ray or neutron diffraction studies (Tristram-Nagle, 2007; Sironi et al., 2016). Indeed, they allow lipid multilayers composed of 10–100 stacked bilayers to be produced, which are the ideal samples for neutron diffraction experiments in controlled humidty chambers. We tested and compared these two preparation methods for the production of lipid multilayers with PC-lipids. The collected data suggests that the deposition of lipid vesicle suspension in water allowed for the production of lipid multilayers that better resembled the spontaneous lipid organization in aqueous solution.

Recently, we also reported a protocol for producing hydrogenous and deuterated lipid extracts from the bacterium *E.coli* (Haertlein et al., 2016). Lipid extracts from *E.Coli* also present a heterogeneous composition of the headgroups and acyl chains. In the present study, we show for the first time the preparation and characterization of the PG lipid extract from *E.Coli*. PG lipids are among the most abundant lipids in the bacterial cytoplasmic membrane. PG lipids have a different acyl chain composition compared to the PC lipids extract from *P.pastoris* and the investigation of the PG multilayer with neutron diffraction allowed us to assess if also in this case lipid self-segregation occurs. As for the PC-lipids, also the PG lipids were produced and characterized in their hydrogenous and deuterated version.

As a result, the hydrogenous and deuterated PC mixtures (hPC and dPC) as well as the hydrogenous and deuterated PG mixtures (dPG and hPG) were characterized by the coexistence of different lipid phases within the multilayer. We hypothesise that, because of the hydrophobic mismatch, the PC and PG lipids with short and long acyl chains tend to separate into different regions of the multilayer, thus originating different sets of diffraction peaks. The PG multilayers exhibited larger *d*-spacing values than the PC multilayers. We propose that such difference is associated both to the different acyl chain composition of the PC and PG mixtures as well as to the electrostatic repulsion between the PG headgroups of consecutive bilayers. Interestingly, both PC and PG extracts showed a slightly different acyl chain composition in the deuterated lipid mixtures compared to the hydrogenous ones. As a consequence, both the dPC and dPG multilayers exhibited some structural differences compared to the hPC and hPG multilayers, respectively. Altogether, we provide valuable information for future application of the hydrogenous and deuterated *P.pastoris* - PC and *E.coli* - PG lipid mixtures, for the development of advanced models of biological membranes and potential drug testing platforms.

MATERIALS AND METHODS

Chemicals

Cell culture reagents were purchased from Sigma Aldrich, France. D_8-glycerol was from Euriso-Top, France while dio-modified silica column and thin layer chromatography plates (TLC) were purchased from Macherey-Nagel, France. Organic solvents were all HPLC grade, i.e. chloroform ($CHCl_3$, ≥ 99.8% purity), ethanol (CH_3CH_2OH ≥ 99.8% purity), acetone ($(CH_3)_2O$, ≥ 99.9% purity), methanol (CH_3OH, ≥ 99.9% purity) (hexane, ≥99.8% purity) and deuterated water (D_2O, ≥ 99.9% purity) were all purchased from Sigma Aldrich and used without further purification.

Cell Culture

Hydrogenous and deuterated PC mixtures were extracted from the methylotropic yeast *P.pastoris*, grown either in a hydrogenated or a deuterated culture media, respectively while hydrogenous and deuterated PG mixtures were extracted from *E.coli* cells grown into a hydrogenated and deuterated culture media, respectively. The culture conditions for *P.pastoris* and *E.coli* are extensively described below.

Pichia pastoris cell culture - Cells cultures were carried out as done previously by de Ghellinck et al. (2014), de Ghellinck et al. (2015). Hydrogenated and deuterated *P.pastoris* were cultured in flasks at 30°C using a basal salts medium (BSM) as the minimal medium at pH 6.0 (*Pichia pastoris* fermentation process guidelines, Invitrogen, United States) containing either 20 gL–1 of hydrogenous glycerol in H_2O or deuterated glycerol (Euriso-Top, France) in D_2O. Cells upon entering the exponential phase at an OD of 600 were harvested by centrifugation and frozen at −80°C.

Escherichia coli cell culture - Cells were grown on both hydrogenated and deuterated minimal medium at pH 6.0 in flask cultures at 30°C (Haertlein et al., 2016). The composition of the Enfors medium employed was: 6.86 g L-1 $(NH_4)_2SO_4$, 1.56 g L-1 KH_2PO_4, 6.48 g L-1 $Na_2HPO_2.2H_2O$, 0.49 g L-1 $(NH_4)_2HC_6H_5O_7$ (di-ammonium hydrogen citrate), 0.25 g L-1 $MgSO_4.7H_2O$, with 1.0 ml L-1 of trace metal stock solution (0.5 g L-1$CaCl_2.2H_2O$, 16.7 g L-1 $FeCl_3$. $6H_2O$, 0.18 g L-1$ZnSO_4.7H_2O$, 0.16 g L-1$CuSO_4.5H_2O$, 0.15 g L-1$MnSO_4.H_2O$, 0.18 g L-1 $CoCl_2.6H_2O$, 20.1 g L-1 EDTA), 5 g L-1 glycerol. For the preparation of the fully deuterated medium only anhydrous forms of these components were used and diluted into D_2O. D_8-glycerol was used as the carbon source. Cells were harvested by centrifugation at their exponential phase (OD 600), and frozen at −80°C.

Lipid Extraction and Purification

Harvested cells were resuspended into 10 ml deionised water and lysed by probe sonication for 3×5 min with 30 s intervals, 25% duty cycle. The resulting cell lysate was poured into boiling ethanol containing 1% butylated hydroxytoluene (BHT) followed by vigorous stirring in order to denature lipases that have the ability to hydrolyse phospholipids. Lipids were then extracted according to the method of Folch et al. (1957), followed by evaporation of the organic phase under a N_2 stream and reconstitution of the film was done in $CHCl_3$. Purification of various classes of phospholipids containing species of mixed acyl chain lengths was achieved, for both hydrogenated and deuterated mixtures through a diol-modified silica stationary phase column coupled to a High-performance liquid chromatography-Evaporative light scattering detector (HPLC-ELSD) system. The mobile phase employed was a gradient of solvent A ($CHCl_3$/MeOH/NH_4OH, 80:20.5:0.5, v/v) and solvent B ($CHCl_3$/MeOH/H_2O/NH_4OH, 60:35:5.5:0.5, v/v) (Boselli et al., 2012). TLC analysis was carried out on a High-Performance Thin-Layer Chromatography (HPTLC) system (CAMAG, Muttenz, Switzerland) to assess the identity and purity of each of the purified classes.

Gas Chromatography

The fatty acid composition of the purified PC and PG natural mixtures was determined by capillary gas chromatography after derivatizing them into their respective fatty acid methyl esters) (FAMEs). About 3 ml of methanolic HCl was added to a glass vial containing 2 mg of purified polar fraction. The vial tube was vortexed, bubbled with Argon, and sealed tightly with a Teflon-lined cap. The solution was incubated at 85°C for 1 h. Once cooled

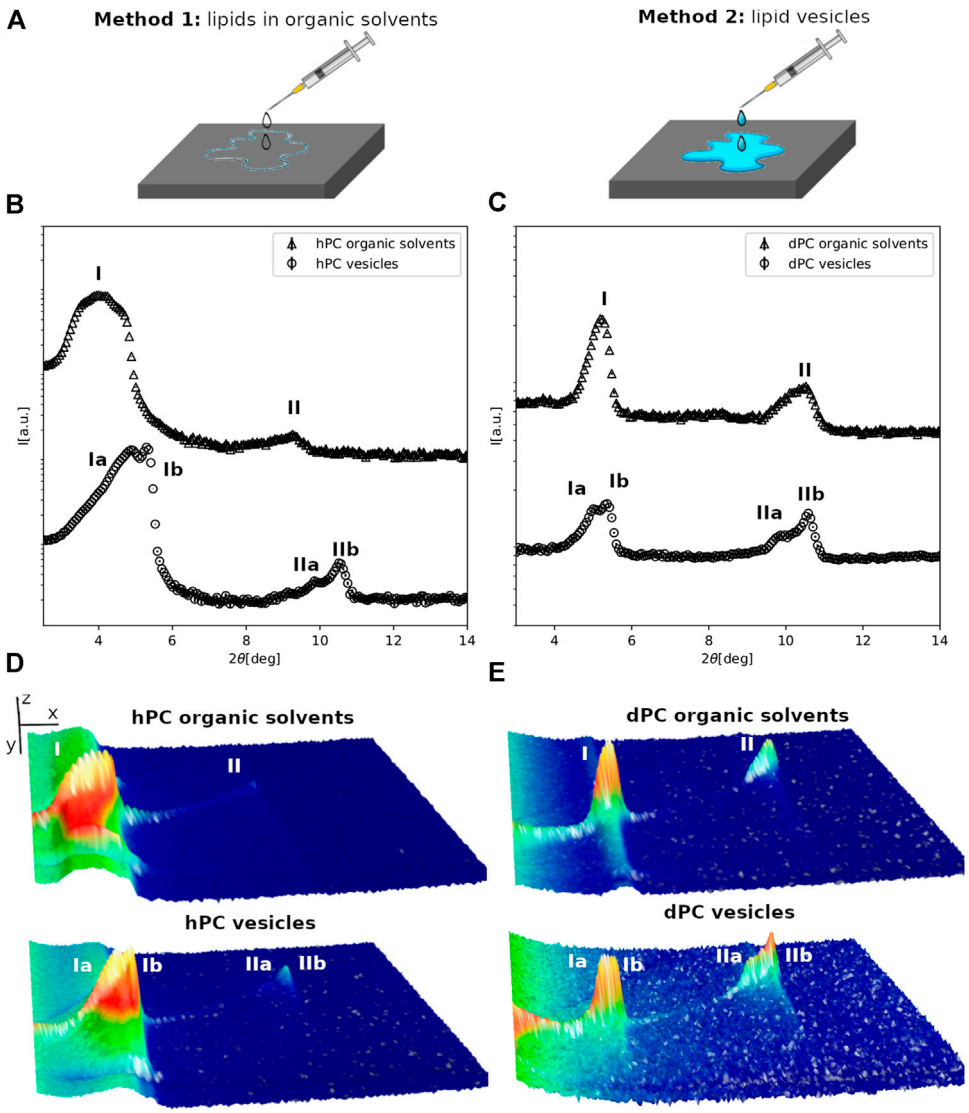

FIGURE 1 | (A) Schematic representation of the multilayer preparation methods. **(B,C)** Neutron diffraction data collected for hPC **(A)** and dPC **(B)** multilayers at 57%RH prepared with either method 1, i.e. deposition of lipids dissolved in an organic solvent solution or method 2, i.e. deposition of an aqueous vesicle suspension. **(D,E)** 3D representation of the detector images corresponding to the diffraction profiles reported in **(A,B)**. In **(D,E)** the sample angle (ω) and the angle at the detector (2θ) are reported on the *x* and *y* direction respectively, while the intensity of the peak is reported on z direction. In **(B–E)** the different diffraction peaks are identified with Roman numbers, while the letters *a* and *b* are used to distinguish the different lipid phases.

to room temperature (~10 min), 3 ml of H_2O was added and the solution vortexed following which 3 ml of hexane was added and vortexed vigorously to create an emulsion. Slow centrifugation at ~500 g for 5 min at room temperature was carried out to break the emulsion and produce an upper hexane-rich phase containing the FAMEs. This supernatant phase (2.8 ml) was then transferred into a fresh vial, evaporated under a stream of N_2 and the resulting dried film was reconstituted in 50 µl hexane and transferred into a GC auto sampler vial that was then loaded into the GC's automatic liquid sampler. The GC instrument (GC 2010 Plus, Shimadzu) was equipped with a split/splitless injector and a SGE BPX70-Cyanopropyl Polysilphenylene-siloxane column (25 m by 0.22 mm ID and 0.25 µm film thickness). Helium was used as a carrier gas at a flow rate of 1.04 ml/min with a linear velocity of 35 cm/s and a purge flow rate of 1 ml/min. The column was allowed to equilibrate for 3 min at 155°C before injection and then the temperature was ramped up to 180°C at a rate of 2°C/min and then to 220°C at a rate of 4°C/min and finally held at 220°C for 5 min resulting in a 27.5 min total run time. Samples (5 µL) were injected into the column at 250°C using an AOC-20i auto injector. Detection was done using a Flame Ionization detector (FID) operating at 260°C with 40 ml/min H_2, 400 ml/min compressed air and 30 ml/min Helium make-up flow. LabSolutions software (Shimadzu) was used to assign and integrate the total ion chromatogram peaks from which the total mole fraction amounts of individual fatty acids were obtained.

Lipid Multilayer Preparation

Lipid multilayers were prepared by drying a lipid film on a freshly cleaned quartz support followed by re-hydration in controlled humidity conditions. 50×25×1 mm quartz support were cleaned by sequential sonication in chloroform, acetone, ethanol, ~15 min each, followed by treatment with UV-ozone lamp for ~20 min. Lipid multilayers corresponding to 2 mg of hydrogenous or deuterated lipids were prepared with two different methods (**Figure 1C**). In method 1, a proper amount of a 1:4 chloroform: methanol lipid solution was deposited by drop casting and dried on the cleaned quartz support. In method 2, the same amount of the 1:4 chloroform: methanol lipid solution was first dried on the bottom of a glass vial under nitrogen. Subsequently, the film was re-dissolved with 600 µl of ultra-pure water and sonicated for ~5 min with a tip sonicator in order to obtain a homogeneous vesicle suspension. The vesicle suspension was deposited by drop casting on a freshly cleaned quartz support and dried. All lipid multilayers, prepared by either method 1 or 2, were stored under vacuum at 45°C for ~12 h. We also tested shorter annealing time, i.e. 4 h, which did not produce any significant difference in the multilayer structure. The multilayers were subsequently equilibrated at 97% relative humidity (RH) for 24 h and then placed in humidity controlled chamber used as sample environment for the neutron measurements. The reservoir of the humidity chamber was filled with H_2O for the deuterated multilayers and D_2O for the hydrogenated multilayers in order to achieve the largest contrast between the lipids and the hydration water (see below).

Neutron Diffraction

Neutron diffraction data were collected on the cold neutron diffractometer 16D (Cristiglio et al., 2015) at the Institut Laue-Langevin, located in Grenoble, France. Neutrons with 4.5 *Å* wavelength (λ) were produced by reflection of the beam from a highly ordered pyrolytic graphite (HOPG) focusing monochromator. The sample to detector distance was 0.95 m and all samples were measured in reflection mode. The lipid coated quartz supports were mounted vertically on a goniometer head placed in the top compartment of a humidity chamber (Gonthier et al., 2019). The temperature of the sample was maintained at 30.0 ± 0.1°C throughout the measurements while the temperature of the bottom compartment, corresponding to the aqueous reservoir, was adjusted according to the required relative humidity.

Diffraction data were collected at a detector angle (γ) of 12 , by scanning the sample angle (ω) in the range −1 to 10, with a step of 0.05 and acquisition time of 40 s. The neutron scattering intensity was recorded by a position sensitive two-dimensional ^{3}He detector (320×320 mm^2 area with a spatial resolution of (1×1 mm^2. Samples were first measured at 57% RH and subsequently the RH was increased up to 98% RH. Effective equilibration at 98% RH was monitored by collecting ω-2θ scans until no changes were observed in the diffraction pattern. The equilibration at 98% RH required at least 12 h.

Data reduction was carried out with the ILL software LAMP (Large Array Manipulation Program, http:/www.ill.fr/data_treat/lamp/lamp.html). Background subtraction was carried out with a measurement of the empty humidity chamber scattering. The uniformity of the detector efficiency was calibrated with an H_2O scattering calibration file in LAMP. The reduced 2D images were integrated in the ω range corresponding to the observed diffraction peaks in order to obtain intensity vs 2θ plots. The positions of the Bragg peaks in the plots were determined by fitting the peaks with a Gaussian function. The angular position 2θ of a Bragg peak is related to the scattering vector (q) value by **Eq. (1)**.

$$q = \frac{4\pi \sin(\theta)}{\lambda} \tag{1}$$

The diffraction pattern produced by a lamellar phase composed of lipid bilayers alternating with water layers is characterized by Bragg peaks whose q-positions correspond to the characteristic ratio h/d, where h is the diffraction order and d is the lamellar spacing. Hence, from the q_1 and q_2 position of the first and second order Bragg peaks in the collected data, the characteristic lamellar d-spacing can be calculated according to **Eq. (2)**.

$$d = \frac{2\pi}{(q_2 - q_1)} \tag{2}$$

The d-spacing corresponds to the unit cell thickness (one lipid bilayer and water layer). The errors reported for the d-values were obtained by propagation from the uncertainty in the q-positions estimated from the fit of the Bragg peaks. Diffraction data collected for samples hydrated with different H_2O/D_2O mixtures as well as pure D_2O and H_2O can be used to extrapolate the phases of the diffracted waves and hence to calculate the scattering length density distribution across the bilayers. The scattering length density distribution can provide information on how the molecules contained in the sample (in the present case phospholipids) are distributed in the direction perpendicular to the substrate surface. However, this approach can only be applied when a sufficient number of diffraction orders (minimum 3) are observed. Because of the limited number of diffraction peaks produced by the PC and PG multilayers, data were collected in only one contrast (i.e. H_2O or D_2O) and this work deals exclusively with the determination of the d-spacing. Although a molecular description of the lipid membranes cannot be directly extracted from the collected data, the d-spacing evaluation still allowed us the comparison between the overall structure, e.g. membrane thickness or number of lipid phases, of the multilayers prepared with different lipid composition. Further details on the contrast variation method as well as some applications can be found elsewhere (Foglia et al., 2015).

RESULTS

Effect of Sample Preparation Method on Multilayer Structure

The hPC and dPC lipid extracts are composed by a single phospholipid headgroup class, i.e. PC, and acyl chains with different length and unsaturation as reported in **Table 1** and

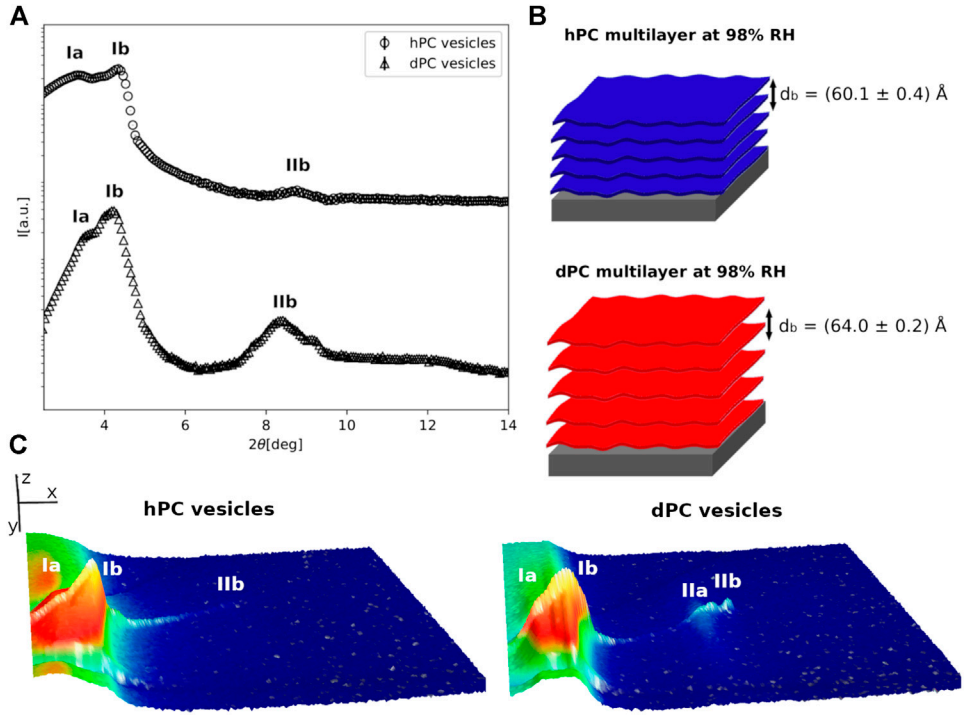

FIGURE 2 | (A) Neutron diffraction data collected for hPC and dPC multilayers at 98%RH prepared by deposition of an aqueous vesicle suspension. **(B)** Cartoon representation of the two multilayers with their characteristic *d*-spacing. **(C)** 3D representation of the detector images corresponding to the diffraction profiles reported in **(A)**. In **(C)** the sample angle (ω) and the angle at the detector (2θ) are reported on the *x* and *y* direction respectively, while the intensity of the peak is reported on *z* direction. In **(A,C)**, the different diffraction peaks are identified with Roman numbers, while the letters *a* and *b* are used to distinguish the different lipid phases.

in **Supplementary Material**. **Figure 1** shows the diffraction data collected for the hPC (1B) and dPC (1C) multilayers at 57% RH. Initially, we characterized the multilayers prepared with method 1 (**Figure 1A**). As detailed in the materials and method section, the analysis of the diffraction data consists in evaluating the number of Bragg peaks and their relative position. Both in the case of hPC and dPC, two diffraction peaks were detected. In both datasets, the second diffraction order peak, *i.e.* $2\theta \sim 9$ for hPC and $2\theta \sim 10.6$ for dPC, is positioned at twice the 2θ value of the first diffraction order peak, *i.e.* $2\theta \sim 4.5$ for hPC and $2\theta \sim 5.3$. Therefore, the 2θ spacing between the first and the second diffraction order is compatible with the arrangement of both the hPC and dPC lipids into a lamellar phase. From the 2θ peak positions, and according to **Eq. (2)**, we estimated a *d*-spacing of $(49.7 \pm 0.3)\AA$ for hPC and of $(50.4 \pm 0.3)\AA$ for dPC.

hPC and dPC multilayers prepared with method 2 produced considerably different diffraction profiles, showing additional diffraction peaks compared to the data for the multilayers prepared with method 1. In that case, suspensions of either hPC or dPC vesicles with hydrodynamic radius ~200 nm, as estimated from dynamic light scattering measurements, were deposited on the quartz support (**Figure 1C**). **Figures 1A,B** clearly show that the diffraction profiles are more complex. In fact, based on the 2θ position of the diffraction peaks, both the hPC and dPC multilayers produced two different sets of diffraction peaks suggesting that the multilayers are composed of at least two different lipid phases (named phase *a* and phase *b*). Indeed, the coexistence of different lipid phases characterized by different d-spacing, and therefore producing different sets of diffraction peaks, was already reported for other lipid mixtures produced from *P.pastoris* (Luchini et al., 2018; Luchini et al., 2020) as well as other synthetic lipid mixtures (Mills et al., 2008; Tayebi et al., 2012). The position of the diffraction orders indicates that both phase *a* and *b* are potentially lamellar and the corresponding *d*-spacing values for hPC are $d_a = (51.9 \pm 0.4)\AA$ and $d_b = (49.5 \pm 0.1)\AA$, while for dPC are $d_a = (51.3 \pm 0.7)\AA$ and $d_b = (49.8 \pm 0.2)\AA$.

Diffraction data were also collected for the multilayers prepared with the two different methods at 98% RH (**Figure 2**, and SM **Figure 1**). Indeed, both for hPC and dPC, the multilayers prepared with the two methods exhibited two different sets of diffraction peaks, although not in all datasets two different diffraction orders were resolved.

At 98% RH, in the case of the hPC multilayer prepared with method 1, we were able to identify two lamellar phases with *d*-spacing $d_a = (51 \pm 1)\AA$ and $d_b = (53.0 \pm 0.1)\AA$ (SM-**Figure1**). The same multilayer prepared with method 2 also produced 2 different sets of diffraction peaks; however, only one lamellar phase (phase *b*) with *d*-spacing $d_b = (60.1 \pm 0.4)\AA$ was identified (**Figure 2**, SM-**Figure 1**). Indeed, the other lipid phase (phase *a*) produced a single diffraction peak. Because of the lack of a second diffraction order we were not able to calculate with confidence a corresponding *d*-spacing. Although at 98% RH both method one and 2 produced a similar number of lipid phases within the hPC

multilayer, the corresponding *d*-spacing values are considerably different. This indicates that the bilayer thickness and the thickness of the water layers between consecutive bilayers is different in the hPC multilayer prepared with method 1 compared to method 2.

In the case of the dPC multilayers at 98% RH, a lamellar phase with *d*-spacing $d_b = (61.8 \pm 0.4)\AA$ and $d_b = (64.0 \pm 0.2)\AA$ was detected in both the diffraction profiles of the multilayer prepared with method 1 and method 2, respectively (**Figure 2**, SM-**Figure 1**). A first diffraction order of an additional lipid phase is also present in the collected data. However, since the peak for the second order is not well-resolved, we were not able to calculate the corresponding *d*-spacing. Interestingly, also in the case of the dPC multilayer, the *d*-spacing calculated for the multilayer prepared by method 1 is smaller than the *d*-spacing calculated for the multilayer prepared by method 2. This observation further supports the hypothesis that the sample preparation method might influence the structure of the produced multilayer.

Altogether, while method 1 produces multilayers with different structure at 57% and 98% RH, a similar arrangement of the multilayers, in terms of number of co-existing lipid phases, is observed at both RH values in case of method 2. The multilayer formation by deposition of the lipid solution in the organic solvents produces multilayers at 57% RH characterized by a single lamellar lipid phase. When the humidity is increased to 98% RH, the fluidity of the bilayers within the multilayers is increased and the lipids can diffuse and eventually self-segregate into domains characterized by a different *d*-spacing. Since all the lipids in the multilayers have the same headgroup, the heterogeneous composition of the acyl chains must drive the observed lipid segregation. In particular, it is reasonable to hypothesise that the PC lipids with shorter acyl chain (*i.e.* C16:0 and C16:1) tend to separate from those with longer acyl chains (*i.e.* C18:0, C18:1 and C18:2) because of hydrophobic mismatch and form slightly thinner bilayer regions within the multilayer compared to the regions formed by lipids with longer acyl chains. Difference in the acyl chain unsaturation level can also favour the lipid self-segregation. As an example, mixtures of DPPC and POPC exhibit the coexistence of fluid and condensed phases (Svetlovics et al., 2012; Åkesson et al., 2012). Indeed in our PC mixtures C18 acyl chains exhibit a higher concentration of single or double unsaturated acyl chains compared to the C16 acyl chains (**Table 1**). When the multilayers are prepared by deposition of the vesicle suspension, lipids might be already organized into separate domains within the vesicles and are well-hydrated during the formation of the multilayer at the support surface. Therefore, the multilayer appears to be organized into different phases already at 57% RH. We cannot exclude that the observed different structure of the multilayers prepared with method 1 compared to method 2, both in terms of number of lipid phases and the corresponding *d*-spacing values, is also caused by traces of organic solvent molecules among the lipids within the multilayers prepared with method 1.

The collected data suggest that the multilayers prepared with method 2 better resemble the spontaneous organization of the lipids in aqueous solution at the two explored humidity conditions. In addition, method 2 allowed us to mimic physiological conditions during both sample preparation and characterization. Therefore, we decided to adopt method 2 for the comparison of the structure of the yeast and bacterial lipid multilayers.

Structure of Natural Phosphatidylcholine Multilayers

Figure 2 shows a comparison of the diffraction data collected for the hPC and dPC multilayers at 98% RH. As previously described, at least 2 different lipid phases are present in both multilayers, although for only one of them (phase *b*) two diffraction orders were observed. The 2θ position of these latter suggests a lamellar phase with corresponding characteristic *d*-spacing $d_b = (60.1 \pm 0.4)\AA$ for hPC and $d_b = (64.0 \pm 0.2)\AA$ for dPC. As expected, in both cases, the calculated *d*-spacing resulted to be larger than the corresponding value at 57% RH (**Figure 1**). Indeed, the increased humidity affects both the lipid organization and therefore the thickness of the bilayers composing the multilayer as well as the amount of water between two consecutive bilayers.

Interestingly, while at 57% RH hPC and dPC multilayers showed a comparable *d*-spacing, at 98% RH the dPC multilayer exhibited a *d*-spacing ~4Å larger than the hPC multilayer. A difference between multilayers prepared with *P.pastoris* hydrogenous and deuterated lipids was already reported in case of multilayers prepared with either the *P.pastoris* total lipid extract or the *P.pastoris* phospholipid extract, both of which contain phospholipids with different headgroups and acyl chains (Luchini et al., 2018; Luchini et al., 2019). In these previous studies, we attributed the different structure of the hydrogenous and deuterated multilayers to the slightly different composition of the headgroups and acyl chains in the hydrogenous and deuterated lipid mixtures. **Table 1** shows a comparison of the acyl chain composition analysis for the hydrogenous and deuterated phospholipids, i.e. h-phospholipids and d-phospholipids, which was also previously reported (Luchini et al., 2018), and the one obtained for the hPC and dPC extracts (SM-2). The h-phospholipid and d-phospholipid extract differ from the hPC and dPC extracts both for the composition of the lipid headgroups, different headgroup species are present instead of just PC, as well as for the composition and relative concentration of the lipid acyl chains. In both the d-phospholipid and the dPC extract, the main acyl chain components are C16:0 and C18:1. On the other hand, in the h-phospholipid and the hPC extracts the amount of the different acyl chains is more homogeneously distributed with C16:0, C18:0, C18:1 and C18:2 being the most abundant. Both the phospholipid and PC extracts exhibit different acyl chain composition when produced in their hydrogenous and deuterated versions. However, in the case of h-phospholipid and d-phospholipid extracts the difference in the C18:1 content is more remarkable than in the case of hPC vs. dPC. As a consequence, we reported a difference in *d*-spacing for the h-phospholipid and d-phospholipid multilayers of ~10Å (Luchini et al., 2018), while in the case of the hPC and dPC

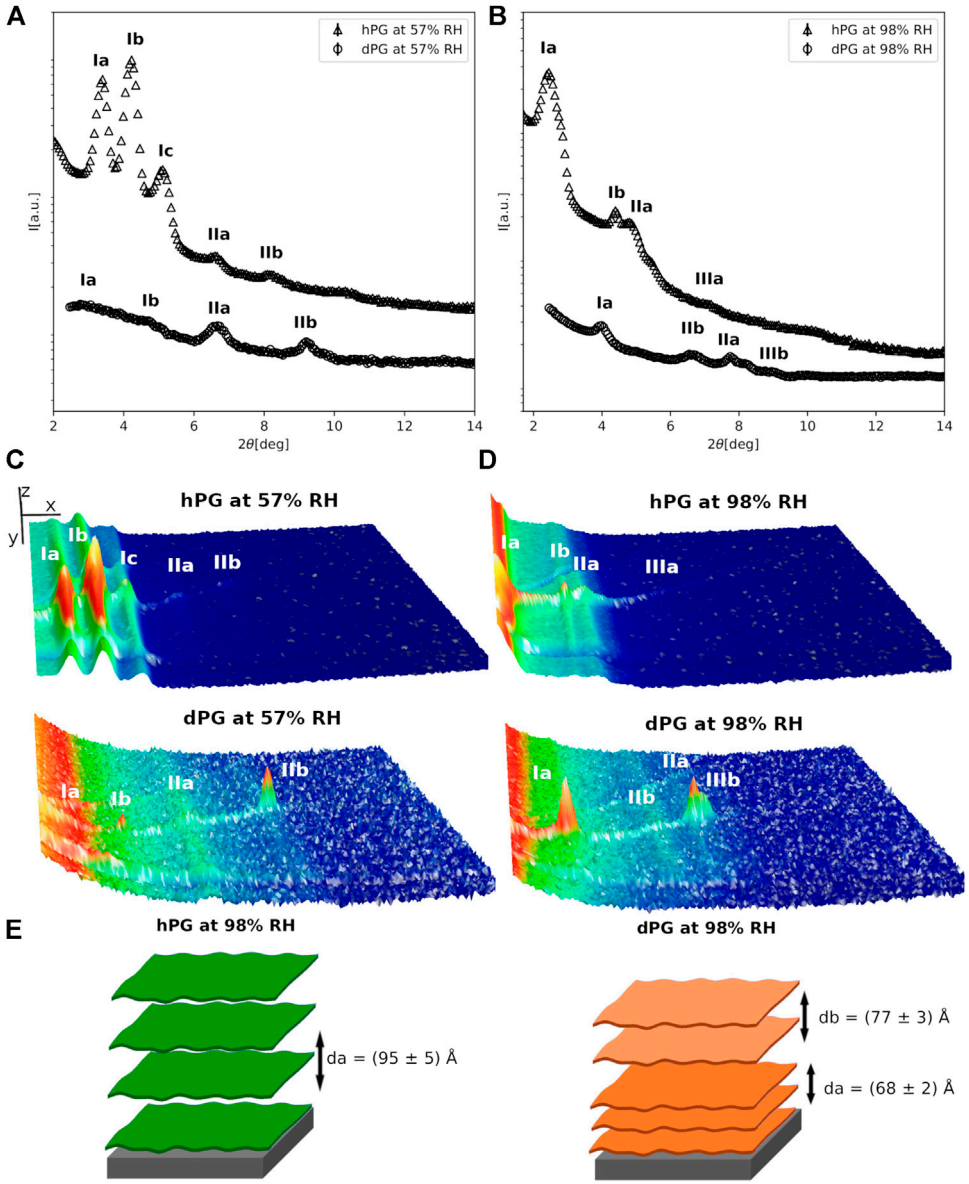

FIGURE 3 | (A,B) Neutron diffraction data collected for hPG and dPG multilayers at 57%RH **(A)** and 98%RH **(B)** prepared by deposition of an aqueous vesicle suspension. **(C,D)** 3D representation of the detector images corresponding to the diffraction profiles reported in **(A)**. In **(C,D)** the sample angle (ω) and the angle at the detector (2θ) are reported on the *x* and *y* direction respectively, while the intensity of the peak is reported on z direction. In **(A–D)** the different diffraction peaks are identified with Roman numbers, while the letters *a* and *b* are used to distinguish the different lipid phases. The data collected for the hPG multilayer are scaled for visualization. **(E)** Cartoon representation of the two multilayers with their characteristic *d*-spacing.

the difference in *d*-spacing is only ~4Å. Altogether, **Table 1** shows that the acyl chain composition is likely to differ depending on the specific lipid headgroup composition.

Structure of Natural Phosphatidylglycerol Multilayers

Figure 3 shows diffraction data collected for the *E.coli* hPG and dPG multilayers at 57% and 98% RH. For both hPG and dPG mixtures, lipid multilayers were prepared by method 2, i.e. suspensions of vesicles with hydrodynamic radius ~120 nm, as estimated from dynamic light scattering measurements, were deposited on the support. Different diffraction orders belonging to different lipid phases were detected for both the hPG and dPG multilayers at 57%RH. In case of the hPG multilayer, 5 diffraction peaks were detected. By evaluating the position of each of these peaks, we were able to exclude the presence of non-lamellar phases, such as cubic or hexagonal phase, as also expected being the multilayer composed by PG lipids that are known to form lamellar phases (Krumova et al.,

2008). Furthermore, the position of the peaks in the 2θ range 6–9 *deg* corresponds to twice the 2θ position of the first two diffraction peaks at 2θ~3.4 and ~4.2. Therefore, we interpreted the diffraction profile as composed by the first and the second diffraction orders of two separate lipid phases named *a* and *b* (**Figure 3A**). The *d*-spacing associated to the two lipid phases resulted to be $d_a = (80.2 \pm 0.5)\AA$ and $d_b = (65.3 \pm 0.3)\AA$. An additional diffraction peak is also observed at 2θ~5. This latter most likely belongs to another lipid phase (named *c*), which could not be fully characterized because of the lack of higher order diffraction peaks. At 57% RH, the dPG multilayer also exhibited two different lipid phases. The position of the diffraction peaks suggests two different lamellar phases with *d*-spacing $d_a = (76 \pm 4)\AA$ and $d_b = (55 \pm 1)\AA$.

When humidity is increased to 98% RH the diffraction peaks collected for both hPG and dPG multilayers showed a lower intensity due to the more disordered structural organization of the multilayers promoted by high humidity. The two lipid phases (i.e. *a* and *b*) in the diffraction data collected at 57%RH, are also observed in both the hPG and dPG multilayers at 98%RH. However, for the hPG multilayer, only in the case of phase *a* two diffraction orders were detectable with associated *d*-spacing $d_a = (95 \pm 5)\AA$. In the case of the dPG multilayer, the diffraction profile included a sufficient number of diffraction orders to allow us to calculate the *d*-spacing for both lamellar lipid phases $d_a = (77 \pm 3)\AA$ and $d_b = (68 \pm 2)\AA$. **Table 1** shows the acyl chain composition of the hPG and dPG extracts. In both cases, C16:0, cyclo C17:0 and clyclo C19:0 resulted to be the most abundant species. As for the PC mixtures, we hypothesise that acyl chains with the similar length tend to self-segregated into different regions of the multilayer therefore producing at least two observable d-spacings.

Finally, for both hPG and dPG multilayers, increasing the humidity to 98%RH produced a structural rearrangement of the multilayers and more specifically increased the thickness of the two lipid phases observed in the two lipid systems. While at 57% RH the *d*-spacing values estimated for the hPG and dPG multilayer are comparable and within the corresponding errors, at 98%RH the hPG multilayer is evidently characterized by a considerably larger *d*-spacing than the dPG multilayer. The analysis of the acyl chain composition (**Table1**) indicates that the hPG lipids have a slightly smaller content of short acyl chains (i.e. C14 and C16), but contain double the amount of the long acyl chains (i.e. cyclo C19, see below) compared to the dPG lipids. This difference in the acyl chain composition can contribute to the overall larger *d*-spacing associated to the hPG multilayer compared to the dPG multilayer.

TABLE 2 | *d*-spacing values calculated for the hPC, dPC and hPG, dPG multilayers at 57% and 98% RH.

Extracts	57% RH	98% RH
hPC	$d_a = (51.9 \pm 0.4)$; $d_b = (49.5 \pm 0.1)$	$d_a = (60.1 \pm 0.4)$
dPC	$d_a = (51.3 \pm 0.7)$; $d_b = (49.8 \pm 0.2)$	$d_a = (64.0 \pm 0.2)$
hPG	$d_a = (76 \pm 4)$; $d_b = (55 \pm 1)$	$d_a = (77 \pm 3) d_b = (68 \pm 2)$
dPG	$d_a = (80.2 \pm 0.5)$; $d_b = (65.3 \pm 0.3)$	$d_a = (95 \pm 5)$

DISCUSSION

Natural lipids directly extracted from eukaryotic or prokaryotic cells are valuable compounds to produce advanced models of biological membranes. Indeed, they can be characterized by biophysical methods and are pivotal for understanding the physico-chemical properties of real cell membranes as well as to develop lipid platforms for drug-testing. Indeed, more than 60% of the currently marketed drugs target components of cell membranes (Overington et al., 2006). Therefore the development of membrane models close to real biological membranes is of great relevance in the investigation of drug-membrane interactions. A detailed characterization of such interactions can potentially prompt the design of new and more efficient drugs.

In this study, we discussed for the first time the characterization by means of neutron diffraction of hydrogenous and deuterated lipid multilayers prepared with the phosphatidylcholine extract from the yeast *P.pastoris* and the phosphatidylglycerol extract from the bacterium *E.coli*. Specifically, we investigated the impact of sample preparation method and acyl chain composition on the structural organization of the two different kinds of multilayers. The obtained results are summarised in **Table 2**.

The drop-casting of a lipid solution followed by annealing under vacuum and subsequent re-hydration is one of the common approaches to produce lipid multilayers (Nagle and Tristram-Nagle, 2000; Tristram-Nagle, 2007; Sironi et al., 2016). In the case of the hPC and dPC mixtures, we tested two different sample preparation methods. In method one lipids were dissolved in a chloroform/methanol solution, while in method 2 a lipid vesicle suspension was used. Different multilayer structures were induced by these two methods, similarly to previous findings (Luchini et al., 2020). However, in this previous work, we compared different lipid mixtures prepared with either method 1 or 2. Here, we performed a more systematic characterization and used the exact same lipid mixtures, *i.e.* hPC and dPC, for the comparison of the two sample preparation methods. Altogether, the collected data indicates that the multilayers produced by method 2 show already at 57%RH a structural organization similar to 98%RH, which might be favoured by the spontaneous organization of the lipids into separate domains within the vesicle suspension, compared to the more homogeneous solubilization of the lipids in the organic solvents. In addition, method 2 allowed us to keep the experimental conditions for sample preparation and characterization closer to physiological conditions. Therefore we chose method 2 for the preparation of the samples in the rest of the study.

Both hPC and dPC multilayers exhibited the co-existence of two different lipid phases at both 57% and 98% RH, in case of samples prepared with method 2. Evidence of the coexistence of two lipid phases is the presence of two sets of diffraction peaks in the collected neutron diffraction data, as also previously observed for other lipid mixtures produced from *P.pastoris* (Luchini et al., 2018;

Luchini et al., 2020) as well as other synthetic lipid mixtures (Tayebi et al., 2012; Mills et al., 2008). Inspection of **Table 1**, reporting the acyl chain composition of hPC and dPC extracts, shows that acyl chains are composed by 16 and 18 C atoms and different unsaturations. We suggest that, because of hydrophobic mismatch, the short acyl chains tend to separate from the long acyl chain and form domains within the bilayers, characterized by different *d*-spacing (**Table 2**). Differences in the acyl chain unsaturation level can also favour lipid self-segregation. Indeed, in both hPC and dPC mixtures, C18 acyl chains exhibit a higher concentration of single or double unsaturations compared to the C16 acyl chains (**Table 1**). As previously observed for other lipid extracts from *P.pastoris* (Luchini et al., 2018; Luchini et al., 2020), we report differences in the structure of the hPC compared to the dPC multilayers. Such structural differences are related to the different acyl chain composition of the two lipid mixtures and in particular to the higher content of the acyl chain C18:1 in the dPC compared to the hPC.

We also discussed the characterization of lipid multilayers prepared with the bacterial PG extracts produced by *E.coli* cells grown in either a hydrogenous or deuterated culture medium. Interestingly, also in this case the heterogeneity of the lipid acyl chain composition is responsible for the presence of different sets of diffraction peaks belonging to different lamellar lipid phases (**Table 2**). Indeed, **Table 1** shows that acyl chains are mainly saturated and that the most abundant species are C16:0, cyclo C17:0 and clyclo C19:0. As for the PC mixtures, we suggest that acyl chains with similar length tend to self-segregated into different regions of the multilayer therefore producing at least two observable d-spacings. In addition, also the hPG and dPG lipid mixtures exhibited a slightly different acyl chain composition, with C19 acyl chains being more abundant in hPG compared to dPG extracts. This difference in composition is most likely responsible for the larger *d*-spacing measured in the case of hPG multilayers.

Interestingly, at both the two explored humidity conditions, the PG multilayers exhibited a larger *d*-spacing than the PC multilayers. PG lipid extracts have a large content of short acyl chains, *i.e.* C14 and C16 compared to the PC extracts, where the C18 acyl chain is the most abundant (**Table 1**). However, they also contain a considerable fraction of C19 acyl chains, which are completely absent in the PC extracts. This difference in composition might produce thicker bilayers in the case of the PG extracts compared to the PC. The calculated *d*-spacing depends on both the bilayer thickness and the thickness associated to the water layer separating two consecutive bilayers in the multilayer. Whereas PC lipids have a zwitterionic headgroup, *i.e.* no net charge, the PG lipids are instead negatively charged. Hence, the observed different *d*-spacing in the PG and PC multilayers might also be affected by the electrostatic repulsion between the PG headgroups belonging to two consecutive bilayers, which makes the thickness of the water layers larger in the PG multilayers compared to the PC multilayers.

In conclusion, neutron diffraction allowed us to investigate complex lipid mixtures, such as yeast or bacterial lipid extracts, highlighting their structural organization into different lipid phases. While the co-existence of different lipid phases was previously reported for other yeast lipid mixtures, the current data confirms this behaviour for the case of *P.pastoris* PC and *E.coli* PG multilayers. In particular, we showed that the acyl chain composition of both yeast and bacterial lipid mixtures determines the organization of the multilayers in domains with different *d*-spacing. The novelty of this work resides in the use of natural extracts with a single species headgroup (either PC or PG) and a mixture of chain compositions coming from yeast or bacterial cells. These lipids assemble in lamellar structures of great bio-relevance while the possibility to use fully deuterated material allows a fine characterisation by neutron scattering.

DATA AVAILABILITY STATEMENT

The dataset presented in this study are stored in the online repository of Institut Laue Langevin (data@ill.eu).

AUTHOR CONTRIBUTIONS

AL and GF designed the experiment. KB extracted and analysed the lipids. AL, GC, VC and GF carried out the experiment. AL analysed the data and wrote the manuscript. VL prepared the hydrogenous and deuterated yeast cells. GF, GC, KB, VC, VL, MH proofread the manuscript.

FUNDING

This research was funded by SINE2020, an European Union project awarded to the Institut Laue-Langevin within the European Commission's Horizon 2020 Research and Innovation program under grant agreements N°64500. The open access fee was covered by the ANR/NSF-PIRE project REACT (Research and Education in Active Coatings Technologies for Human Health).

ACKNOWLEDGMENTS

The authors thank the Institut Laue-Langevin (DOI: 10.5291/ILL-DATA.8–02–874) for the allocation of beamtime, the Deuteration lab for the preparation of the hydrogenous and natural yeast cells and the Partnership for Soft Condensed Matter (PSCM) for the lab support during the neutron diffraction experiments.

SUPPLEMENTARY MATERIAL

The Supplementary Material for this article can be found online at: https://www.frontiersin.org/articles/10.3389/fchem.2021.628186/full#supplementary-material.

REFERENCES

Åkesson, A., Lind, T., Ehrlich, N., Stamou, D., Wacklin, H., and Cárdenas, M. (2012). Composition and structure of mixed phospholipid supported bilayers formed by popc and dppc. *Soft Matter* 8, 5658–5665. doi:10.1039/C2SM00013J

Bagatolli, L., Ipsen, J., Simonsen, A., and Mouritsen, O. (2010). An outlook on organization of lipids in membranes: searching for a realistic connection with the organization of biological membranes. *Prog. Lipid Res* 49, 378–389. doi:10.1016/j.plipres.2010.05.001

Boselli, E., Pacetti, D., Lucci, P., and Frega, N. G. (2012). Characterization of phospholipid molecular species in the edible parts of bony fish and shellfish. *J. Agric. Food Chem* 60, 3234–3245. doi:10.1021/jf205159a

Cristiglio, V., Giroud, B., Didier, L., and Demé, B. (2015). D16 is back to business: more neutrons, more space, more fun. *Neutron News* 26, 22–24. doi:10.1080/10448632.2015.1057051

de Ghellinck, A., Fragneto, G., Laux, V., Haertlein, M., Jouhet, J., Sferrazza, M., et al. (2015). Lipid polyunsaturation determines the extent of membrane structural changes induced by amphotericin b in pichia pastoris yeast. *Biochim. Biophys. Acta* 1848, 2317–2325. doi:10.1016/j.bbamem.2015.06.006

de Ghellinck, A., Schaller, H., Laux, V., Haertlein, M., Sferrazza, M., Maréchal, E., et al. (2014). Production and analysis of perdeuterated lipids from pichia pastoris cells. *PLoS One* 9, e92999. doi:10.1371/journal.pone.0092999

Fogila, F., Lawrence, M. J., and Barlow, D. J. (2015). Studies of model biological and bio-mimetic membrane structure: reflectivity vs diffraction, a critical comparison. *Curr. Opin. Colloid Interf. Sci* 20, 235–243. doi:10.1016/j.cocis.2015.08.001

Folch, J., Lees, M., and Sloane Stanley, G. H. (1957). A simple method for the isolation and purification of total lipides from animal tissues. *J. Biol. Chem* 226, 497–509. doi:10.1016/s0021-9258(18)64849-5

Fragneto, G., Delhom, R., Joly, L., and Scoppola, E. (2018). Neutrons and model membranes: moving towards complexity. *Curr. Opin. Colloid Interf. Sci* 38, 108–121. doi:10.1016/j.cocis.2018.10.003

Gerelli, Y., de Ghellinck, A., Jouhet, J., Laux, V., Haertlein, M., and Fragneto, G. (2014). Multi-lamellar organization of fully deuterated lipid extracts of yeast membranes. *Acta Crystallogr. D Biol. Crystallogr* 70, 3167–3176. doi:10.1107/S1399004714022913

Gonthier, J., Barrett, M. A., Aguettaz, O., Baudoin, S., Bourgeat-Lami, E., Demé, B., et al. (2019). Berill: the ultimate humidity chamber for neutron scattering. *JNR* 21, 65–76. doi:10.3233/JNR-190109

Haertlain, M., Moulin, M., Devos, J., Laux, V., Dunne, O., and Forsyth, V. (2016). Biomolecular deuteration for neutron structural biology and dynamics. *Meth Enzymol* 566, 113–157. doi:10.1016/bs.mie.2015.11.001

Harayama, T., and Riezman, H. (2018). Understanding the diversity of membrane lipid composition. *Nat. Rev. Mol. Cell Biol* 19, 281–296. doi:10.1038/nrm.2017.138

Hardy, G. J., Nayak, R., and Zauscher, S. (2013). Model cell membranes: techniques to form complex biomimetic supported lipid bilayers via vesicle fusion. *Curr. Opin. Colloid Interf. Sci* 18, 448–458. doi:10.1016/j.cocis.2013.06.004

Himbert, S., Alsop, R., Rose, M., Hertz, L., Dhaliwal, A., RoseMoran-Mirabal, J. M., et al. (2017). The molecular structure of human red blood cell membranes from highly oriented, solid supported multi-lamellar membranes. *Sci. Rep* 7, 39661. doi:10.1038/srep39661

Katsaras, J., and Gutberlet, T. (2001). *Lipid bilayers: structure and interactions*. Berlin Heidelberg: Springer-Verlag. doi:10.1007/978-3-662-04496-4

Krumova, S. B., Dijkema, C., de Waard, P., Van As, H., Garab, G., and van Amerongen, H. (2008). Phase behavior of phosphatidylglycerol in spinach thylakoid membranes as revealed by 31p-nmr. *Biochim. Biophys. Acta* 1778, 997–1003. doi:10.1016/j.bbamem.2008.01.004

Lind, T. K., Wacklin, H., Schiller, J., Moulin, M., Haertlein, M., Pomorski, T. G., et al. (2015). Formation and characterization of supported lipid bilayers composed of hydrogenated and deuterated escherichia coli lipids. *PLoS One* 10, e0144671. doi:10.1371/journal.pone.0144671

Luchini, A., Delhom, R., Cristiglio, V., Knecht, W., Wacklin-Knecht, H., and Fragneto, G. (2020). Effect of ergosterol on the interlamellar spacing of deuterated yeast phospholipid multilayers. *Chem. Phys. Lipids* 227, 104873. doi:10.1016/j.chemphyslip.2020.104873

Luchini, A., Delhom, R.Demé, B.Laux, V.Moulin, M.Haertlein, M., et al. (2018). The impact of deuteration on natural and synthetic lipids a neutron diffraction study. *Colloids and Surfaces B Biointerfaces* 168, 126–133. doi:10.1016/j.colsurfb.2018.02.009

Luchini, A., Nzulumike, A. N. O., Lind, T. K., Nylander, T., Barker, R., Arleth, L., et al. (2019). Towards biomimics of cell membranes: structural effect of phosphatidylinositol triphosphate (pip3) on a lipid bilayer. *Colloids Surf. B Biointerfaces* 173, 202–209. doi:10.1016/j.colsurfb.2018.09.031

Maxfiled, F. R., and van Meer, G. (2010). Cholesterol, the central lipid of mammalian cells. *Curr. Opin. cell Biol* 22, 422–431. doi:10.1016/j.ceb.2010.05.004

Mills, T., Tristram-Nagle, S., Heberle, F., Morales, N., Zhao, J., Wu, J., et al. (2008). Liquid-liquid domains in bilayers detected by wide angle x-ray scattering. *Biophys. J* 95, 682–690. doi:10.1529/biophysj.107.127910

Mouritsen, O. (2011). Model answers to lipid membrane questions. *Cold Spring Harb Perspect. Biol* 3, a004622. doi:10.1101/cshperspect.a004622

Nagle, J., and Tristram-Nagle, S. (2000). Structure of lipid bilayers. *Biochim. Biophys. Acta* 1469 (3), 159–195. doi:10.1016/s0304-4157(00)00016-2

Overington, J., Al-Lazikani, B., and Hopkins, A. L. (2006). How many drug targets are there?. *Nat. Rev. Drug Discov* 5, 993–996. doi:10.1038/nrd2199

Retel, J., Nieuwkoop, A., Hiller, M., Higman, V., Barbet-Massin, E., Stanek, J., et al. (2017). Structure of outer membrane protein g in lipid bilayers. *Nat. Commun* 8, 2073. doi:10.2210/pdb5mwv/pdb

Romantsov, T., and Wood, J. M. (2016). *Contributions of membrane lipids to bacterial cell homeostasis upon osmotic challenge*. New York: Springer International Publishing. doi:10.1007/978-3-319-43676-0_58-1

Seddon, A., Casey, D., Law, R., Gee, A., Templer, R., and Ces, O. (2009). Drug interactions with lipid membranes. *Chem. Soc. Rev* 38, 2509–2519. doi:10.1039/b813853m

Seddon, A., Curnow, P., and Booth, P. (2004). Membrane proteins, lipids and detergents: not just a soap opera. *Biochim. Biophys. Acta* 1666, 105–117. doi:10.1016/j.bbamem.2004.04.011

Sironi, B., Snow, T., Redeker, C., Slastanova, A., Bikondoa, O., Arnold, T., et al. (2016). Structure of lipid multilayers via drop casting of aqueous liposome dispersions. *Soft Matter* 12, 3877–3887. doi:10.1039/C6SM00369A

Strahl, H., and Errington, J. (2017). Bacterial membranes: structure, domains, and function. *Annu. Rev. Microbiol* 71, 519–538. doi:10.1146/annurev-micro-102215-095630

Svetlovics, J., Wheaten, S., and Almeida, P. (2012). Phase separation and fluctuations in mixtures of a saturated and an unsaturated phospholipid. *Biophys. J* 102, 2526–2535. doi:10.1016/j.bpj.2012.04.017

Tayebi, L., Ma, Y., Vashaee, D., Chen, G., Sinha, S., and Parikh, A. (2012). Long-range interlayer alignment of intralayer domains in stacked lipid bilayers. *Nat. Mater* 11, 1074–1080. doi:10.1038/nmat3451

Tristram-Nagle, S. (2007). Preparation of oriented, fully hydrated lipid samples for structure determination using x-ray scattering. *Methods Mol. Biol* 400, 63–75. doi:10.1007/978-1-59745-519-0_5

van Meer, G., and Voelker, D. R. (2008). Membrane lipids: where they are and how they behave. *Nat. Rev. Mol. Cell Biol* 9, 112–124. doi:10.1038/nrm2330

Vitiello, G., Falanga, A., Petruk, A. A., Merlino, A., Fragneto, G., Paduano, L., et al. (2015). Fusion of raft-like lipid bilayers operated by a membranotropic domain of the hsv-type i glycoprotein gh occurs through a cholesterol-dependent mechanism. *Soft Matter* 11, 3003–3016. doi:10.1039/C4SM02769H

Conflict of Interest: The authors declare that the research was conducted in the absence of any commercial or financial relationships that could be construed as a potential conflict of interest.

frontiers in Chemistry

REVIEW
published: 19 April 2021
doi: 10.3389/fchem.2021.631370

Small-Angle X-Ray and Neutron Scattering on Photosynthetic Membranes

Dainius Jakubauskas[1], *Kell Mortensen*[1], *Poul Erik Jensen*[2] *and Jacob J. K. Kirkensgaard*[1,2]*

[1]X-ray and Neutron Science, Niels Bohr Institute, University of Copenhagen, Copenhagen, Denmark, [2]Department of Food Science, University of Copenhagen, Copenhagen, Denmark

Ultrastructural membrane arrangements in living cells and their dynamic remodeling in response to environmental changes remain an area of active research but are also subject to large uncertainty. The use of noninvasive methods such as X-ray and neutron scattering provides an attractive complimentary source of information to direct imaging because *in vivo* systems can be probed in near-natural conditions. However, without solid underlying structural modeling to properly interpret the indirect information extracted, scattering provides at best qualitative information and at worst direct misinterpretations. Here we review the current state of small-angle scattering applied to photosynthetic membrane systems with particular focus on data interpretation and modeling.

Keywords: SAXS, SANS, thylakoids, photosynthesis, structural modeling, small-angle scattering

OPEN ACCESS

Edited by:
Olaf Holderer,
Helmholtz-Verband Deutscher Forschungszentren (HZ), Germany

Reviewed by:
Frank Heinrich,
Carnegie Mellon University, United States
Georg Pabst,
University of Graz, Austria

***Correspondence:**
Jacob J. K. Kirkensgaard
jjkk@nbi.ku.dk
jjkk@food.ku.dk

Specialty section:
This article was submitted to Physical Chemistry and Chemical Physics, a section of the journal Frontiers in Chemistry

Received: *19 November 2020*
Accepted: *01 February 2021*
Published: *19 April 2021*

Citation:
Jakubauskas D, Mortensen K, Jensen PE and Kirkensgaard JJ K (2021) Small-Angle X-Ray and Neutron Scattering on Photosynthetic Membranes. Front. Chem. 9:631370. doi: 10.3389/fchem.2021.631370

1 INTRODUCTION

The lamellar nature of thylakoids was shown in the pioneering works of Menke in 1940 (Menke, 1940a; Menke, 1940b) who studied the inner structure of chloroplasts by light and electron microscopies. From these studies, it became evident that photosynthetic membranes are not randomly dispersed within the cell but organize into highly complex ultrastructures. **Figure 1** depicts representative transmission electron microscopy (TEM) images of photosynthetic membrane systems: from the remarkably intricate network structure of the prolamellar body found inside developing etioplasts to individual cyanobacterial thylakoids and finally stacked grana thylakoid arrays in higher plants. The structural regularity in these TEM images suggests that structural information can be extracted from X-ray or neutron scattering methods. In this review, we focus on small-angle scattering techniques: small-angle X-ray (SAXS) and neutron (SANS) scattering.

Small-angle scattering enables investigating structures of ca. 1–200 nm in near *in vivo* conditions and is widely applied in structural biology and soft matter sciences. Small-angle scattering complements various microscopic techniques, such as TEM (Menke, 1960; Paolillo and Paolillo, 1970; Staehelin, 1986; Austin and Staehelin, 2011; Armbruster et al., 2013; Heinz et al., 2016; Kowalewska et al., 2016; Wood et al., 2018; Kowalewska et al., 2019; Wood et al., 2019; Li et al., 2020), scanning electron microscopy (Mustárdy and Jánossy, 1979; Armbruster et al., 2013), cryo-EM (Ford et al., 2002; Kirchhoff et al., 2011; Engel et al., 2015), cryoelectron tomography (Shimoni et al., 2005; Austin and Staehelin, 2011; Daum and Kühlbrandt, 2011; Kouřil et al., 2011; Ford and Holzenburg, 2014; Bussi et al., 2019; Rast et al., 2019), atomic force microscopy (Kaftan et al., 2002; Sturgis et al., 2009; Sznee et al., 2011; Grzyb et al., 2013; Onoa et al., 2014), confocal laser scanning microscopy (Kowalewska et al., 2016; Mazur et al., 2019), and live cell imaging (Iwai et al., 2014; Iwai et al., 2016). The first scattering studies on photosynthetic membranes were performed in 1953 by Finean et al. (1953) and has continued ever since. There are currently about 40–50 works published on scattering from photosynthetic systems—photosynthetic bacteria, diatoms and other algae and of

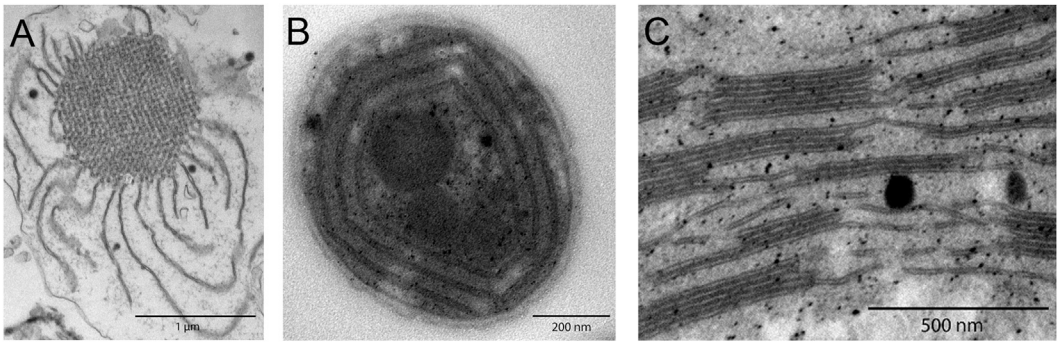

FIGURE 1 | TEM images of photosynthetic membrane systems, revealing complex structural characteristics. **(A)** Etiolated maize prolamellar body. **(B)** Concentric *Synechocystis* sp. PCC 6803 cyanobacterial thylakoids. **(C)** Higher plant grana stacks of *Arabidopsis* Col0, interconnected by stromal thylakoids.

course from higher plants. Small-angle scattering has been used to investigate structure and dynamic changes of thylakoid membrane systems of plants (Finean et al., 1953; Kratky et al., 1959; Kreutz and Menke, 1960a; Kreutz and Menke, 1960b; Kreutz and Menke, 1962; Kreutz, 1963a; Kreutz, 1963b; Kreutz, 1964; Sadler, 1976; Li, 1979; Sadler and Worcester, 1982a; Sadler and Worcester, 1982b; Diederichs et al., 1985; Garab et al., 1997; Kirkensgaard et al., 2009; Nagy, 2011; Nagy et al., 2011;Nagy et al., 2013; Ünnep et al., 2014b; Herdean et al., 2016; Ünnep et al., 2017; Zsiros et al., 2020; Ünnep et al., 2020), protists (Sadler et al., 1973; Worcester, 1976; Sadler and Worcester, 1982a), diatoms (Nagy et al., 2011; Nagy et al., 2012), photosynthetic bacteria (Pape et al., 1974; Hodapp and Kreutz, 1980; Liberton et al., 2013b; Ünnep et al., 2014a; Li et al., 2016; Stingaciu et al., 2016; Eyal et al., 2017; Jakubauskas et al., 2019), algae (Nagy et al., 2011; Nagy et al., 2012; Nagy et al., 2014), light harvesting complexes (Smidijiev et al., 2000; Tang and Blankenship, 2012), phycobiliproteins (Golub et al., 2017), and higher-plant prolamellar bodies (Williams et al., 1998; Selstam et al., 2007). The aim of applying small-angle scattering in biological sciences is to investigate structural changes of the biological system and correlate them with underlying physiological processes *in vivo*. This article critically reviews the current state of small angle scattering applied to photosynthetic membrane systems with a three-fold agenda: (1) to describe the basics of the method and present an overview of existing small-angle scattering results on photosynthetic membrane systems, (2) to discuss scattering results and their correlation with microscopy, critical points of result interpretation, and method limitations, and (3) to envision the development of the small angle scattering method with focus on data analysis and modeling in the field of photosynthetic membrane systems. The review is organized as follows: small-angle scattering terminology and relevant background is introduced in **Section 2**. Scattering results from plant, cyanobacterial, algae, and diatom thylakoid membranes including dynamic changes during illumination are critically evaluated in **Sections 3–6**. Finally, an outlook is presented in **Section 7**.

2 SMALL-ANGLE X-RAY AND NEUTRON SCATTERING

2.1 The Small-Angle Scattering Experiment

The concepts described below are valid for both X-rays and neutrons; however, certain differences arise due to the different physical nature and interactions of photons and neutrons with materials (see **Table 1**). In a material, either the electrons (for X-ray scattering) or nuclei (for neutron scattering) interact with the incoming radiation and deflect X-ray photons or neutrons from their original path. The electrons or nuclei become sources of elastically scattered secondary waves, whose intensities are registered by a detector as a function of the angle relative to the incoming beam (see **Figure 2A**) (Glatter and Kratky, 1982; Willis and Carlile, 2009). Contemporary detection systems typically produce a 2-dimensional output as shown in **Figure 2**. If a sample scatters azimuthally isotropic (**Figure 2A**), the 2-dimensional pattern is centrosymmetric (**Figure 2B**). For analysis, these 2-D patterns are typically azimuthally averaged and collapsed into a 1-dimensional curve (**Figure 3B**) showing scattering intensity as a function of the scattering vector magnitude:

$$q = |\boldsymbol{q}| = \frac{4\pi}{\lambda}\sin\theta, \tag{1}$$

where λ is the wavelength of the incident radiation (for neutrons the de Broglie wavelength) and θ is half the scattering angle (see **Figure 2**). Thus, the scattering vector magnitude is a direct measure of the scattering angle, but normalized by the wavelength of the radiation. These 1D scattering data are analyzed analytically or numerically to reveal the underlying structure, as described below. For nonisotropic systems (**Figure 2C**), sector averaging can be employed to yield 1-dimensional curves for each of the sectors, but in some cases analysis is performed directly on the 2-dimensional dataset. By combining **Eq. 1** with Bragg's law for periodic structures:

TABLE 1 | Differences and practicalities of SAXS and SANS experimental techniques [adapted from Tang and Blankenship (2012)].

	SAXS	SANS
Interacting field	Electrons	Nuclei
Incident beam wavelength, Å	0.8–1.6	2.0–25.0
Flux of the source (particles/s/mm^2)	Medium to high (10^{8-9}–10^{11})	Very low to low (10^{5}–10^{8-9})
Coherent scattering length density, 10^{-12} cm	H: 0.28, D: 0.28	H: −0.374, D: 0.667
Sample volumes required in 1–2 mm path length cell	20–30 μL	150–500 μL
Radiation damage to the sample	Low for laboratory sources, high for synchrotron sources	Low
Structural information extracted for individual Moieties in multicomponent systems	No (electron density average of the entire sample)	Yes (lipid, nucleic acid, protein can be investigated separately)
Contrast variation use	Rare	Common
Resolution	Low-medium	Low-medium
Experimental facilities	Laboratory and synchrotron radiation sources	Large facilities only

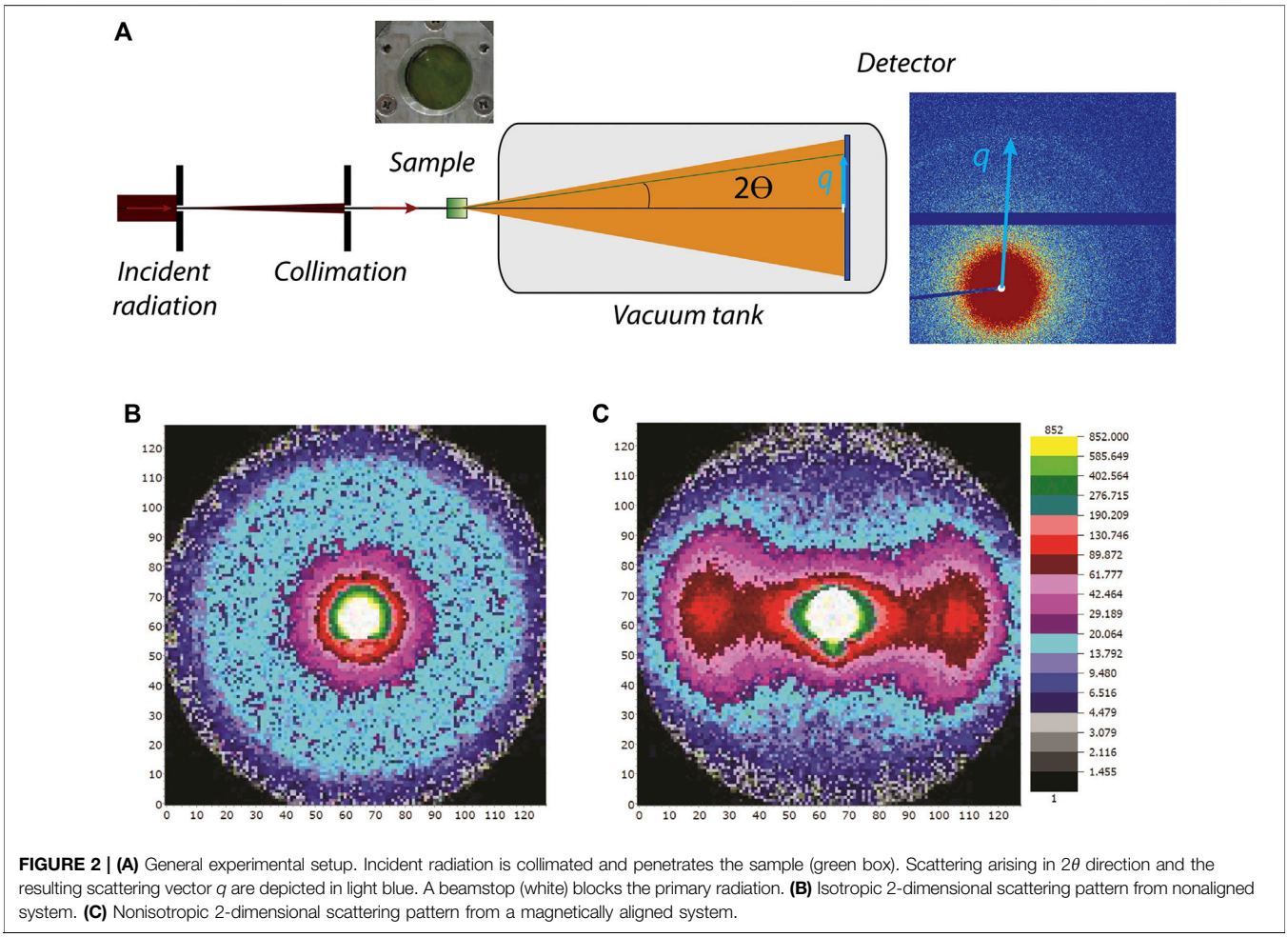

FIGURE 2 | (A) General experimental setup. Incident radiation is collimated and penetrates the sample (green box). Scattering arising in 2θ direction and the resulting scattering vector q are depicted in light blue. A beamstop (white) blocks the primary radiation. **(B)** Isotropic 2-dimensional scattering pattern from nonaligned system. **(C)** Nonisotropic 2-dimensional scattering pattern from a magnetically aligned system.

$$n\lambda = 2D_R \sin\theta \quad (n = 1, 2, 3, \ldots), \tag{2}$$

a direct relation between q and a real-space structural periodicity D_R is obtained:

$$D_R = \frac{2\pi n}{q}. \tag{3}$$

The fundamental inverse relation between angles and distances is defined in **Eqs 1** and **3**: larger angles (larger q) probe smaller distances and vice versa. The integer n from Bragg's law appearing in **Eq. 3** is called the "peak order" and indicates that a certain distance D_R, repeating in the material, gives rise to a series of peaks in the reciprocal space, ideally one for each value of $n = 1, 2, 3, \ldots$. For an ordered lamellar stack, all peaks are placed equidistantly. For more complex structures, different peak positions reflect other crystallographic symmetries and require more detailed analysis. Once a scattering intensity pattern is recorded and corrected for background contributions,

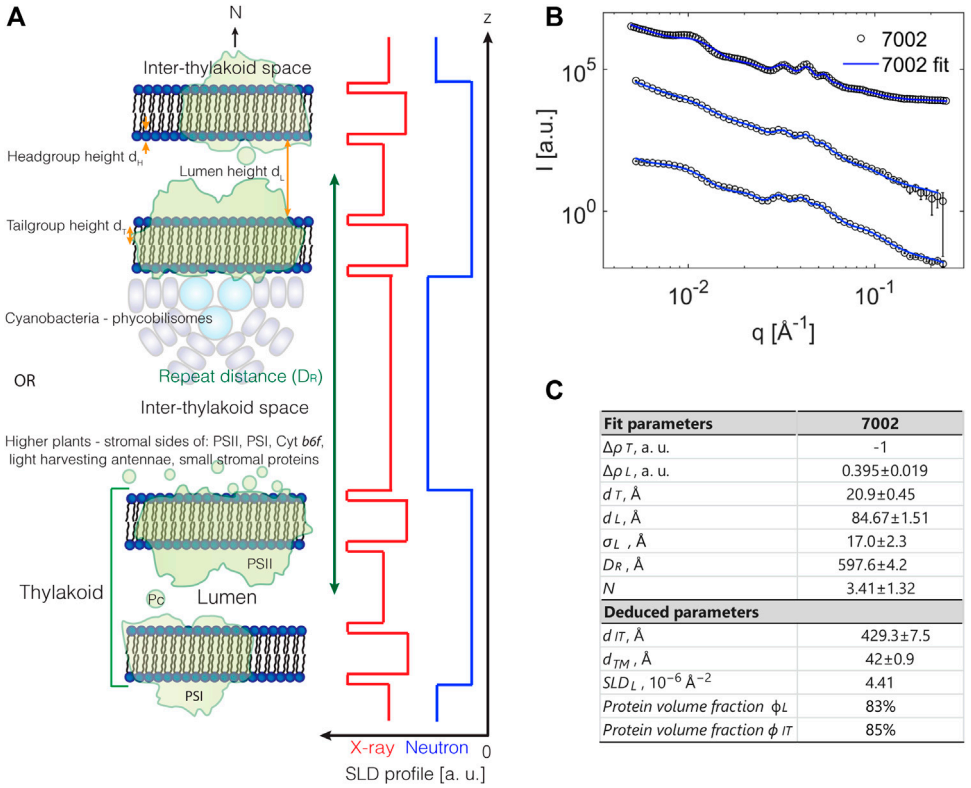

Fit parameters	7002
$\Delta\rho_T$, a. u.	-1
$\Delta\rho_L$, a. u.	0.395±0.019
d_T, Å	20.9±0.45
d_L, Å	84.67±1.51
σ_L , Å	17.0±2.3
D_R , Å	597.6±4.2
N	3.41±1.32
Deduced parameters	
d_{IT}, Å	429.3±7.5
d_{TM} , Å	42±0.9
SLD_L , 10^{-6} Å^{-2}	4.41
Protein volume fraction ϕ_L	83%
Protein volume fraction ϕ_{IT}	85%

FIGURE 3 | (A) Illustration of structural model for a photosynthetic membrane system with a stack of double layered thylakoids. Neutron (light blue) and X-ray (red) SLD profiles are schematically depicted. **(B)** Full *q*-range model fits to SANS data from three independent replicas of *Synechococcus* sp. PCC 7002 [from Jakubauskas et al. (2019)]. **(C)** Extracted structural numbers from fits in B.

structural sample parameters can be extracted from the scattering pattern by means of modeling as described below.

2.2 Scattering Length Density and Contrast

In analogy to scattering of visible light where differences in refractive index give rise to scattering, for example air-material contrast, differences in *scattering length density* enable one to "see" material constituents with X-rays and neutrons. The scattering length density describes the degree of interaction between the sample molecules and the incoming radiation and thereby quantifies the scattering power of different molecular components (see **Figures 4A,B**). In terms of scattering intensity, the relevant concept becomes the *contrast*—the difference in scattering length density between different components. For X-rays, contrast arises from variations in the electron density of the material, and for neutrons the contrast arises from the different atomic nuclear structures.

The different physical nature of the two methods is advantageous and complementary in ultrastructural analysis—SAXS and SANS enable extracting different structural information from the same sample. The X-ray scattering power of atoms increases roughly linearly with atomic number while for neutrons the variation is less systematic and differs significantly between different isotopes (Sears, 1992). This isotope difference is particularly important for biological and soft matter samples, since the exchange of hydrogen (H) atoms with the heavy-hydrogen isotope deuterium (D) allows fine-tuning the neutron scattering contrast, hence called contrast variation. For example, if the scattering length density of a surrounding medium is equal to the scattering length density of a specific molecular component, no scattering is observed from that component—we say that the scattering has been "matched out." In its simplest form, mixing H_2O- and D_2O-based buffers in specific ratios enables enhancing or diminishing the contrast of different cellular components (Serdyuk et al., 2007; Heller, 2010) (**Figure 4B**). To exemplify, the contrast variation technique allows an individual investigation of either lipid or protein components in a complex biological membrane system. In order to match out membrane lipids, 5–25% D_2O containing solutions are used, and 40–45% D_2O containing solutions are used to match out protein components of the membrane (**Figure 4C**). So by designing a series of measurements with varying contrasts, one can effectively build up a series of structural snapshots which allows to extract detailed information very hard to obtain in other ways. Part of such an experimental design is to estimate the scattering length densities of the sample material; however, calculating precise scattering length densities for biological systems is not straightforward, since the exact protein and lipid composition

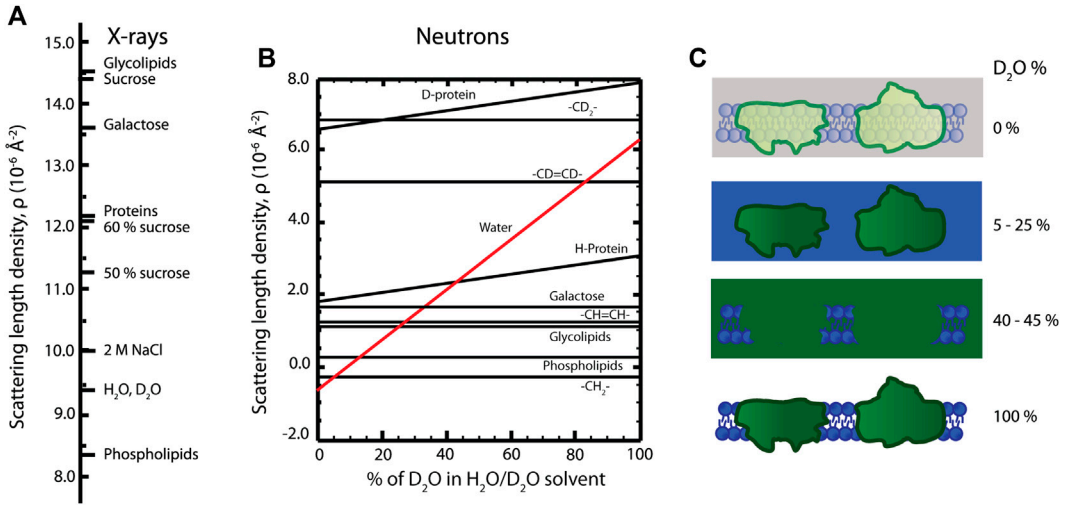

FIGURE 4 | (A) X-ray scattering length densities for various molecules. **(B)** Dependence of neutron scattering length densities of lipid and protein moieties on D_2O amount in the sample. **(C)** Contrast variation technique, where a photosynthetic membrane is visualized in different D_2O buffers. The signal from lipid (5–25% D_2O) or protein components (40–45% D_2O) is "masked out." The total scattering signal is enhanced in 100% D_2O, as indicated by more intense colors than in 0% D_2O.

TABLE 2 | Scattering length densities of thylakoid components [taken from Jakubauskas (2016) and Jakubauskas et al. (2019)].

	Neutron SLD, Å^{-2}	X-Ray SLD, Å^{-2}
Lipid headgroups: plants	1.77×10^{-6}	1.30×10^{-5}
Lipid tailgroups: plants	1.36×10^{-6}	1.12×10^{-5}
Lipid headgroups: cyanobacteria	1.83×10^{-6}	$1.19–1.34 \times 10^{-5}$
Lipid tailgroups: cyanobacteria	1.33×10^{-6}	1.12×10^{-5}
Thylakoid proteins (10% H-D exchange): plants	2.43×10^{-6}	1.22×10^{-5}
Thylakoid membrane: cyanobacteria	1.58×10^{-6}	1.23×10^{-5}
Lumen: cyanobacteria	$4.29–4.41 \times 10^{-6}$	$1.15–1.18 \times 10^{-5}$
Interthylakoid space: cyanobacteria	$3.61–4.43 \times 10^{-6}$	$1.16–1.19 \times 10^{-5}$
Chloroplast average	5.35×10^{-6}	9.98×10^{-5}
Stroma average	6.34×10^{-6}	9.44×10^{-5}
D_2O	6.393×10^{-6}	9.455×10^{-5}
H_2O	-5.61×10^{-6}	9.469×10^{-5}

of the membrane, their volume fractions, protein H-D exchange degree, membrane-associated water content, and solvent composition need to be known. Some recently calculated scattering length density values of thylakoid membranes are given in **Table 2** (Jakubauskas, 2016; Jakubauskas et al., 2019).

2.3 Small Angle Scattering Analysis

Typical interpretations of small angle scattering data on photosynthetic membranes have so far been limited to the estimation of the average thylakoid membrane repeat distance from the observed peak position by directly applying **Eq. 3**. This method provides an approximation of the average spacing between thylakoid membranes and is typically used to follow system behavior in changing conditions: for example, illumination intensity, temperature, pH, or different ionic strength (see below). However, a number of factors are not accounted for in such an approach: interthylakoid space/lumen or membrane bilayer thicknesses, the number of thylakoid layers, the degree of system orientation, and, for neutron scattering in particular, instrument resolution effects. Therefore, more sophisticated analyses of scattering data on photosynthetic systems are required. Theoretical calculations of Kirkensgaard et al. (2009), based on simulated scattering patterns, suggested a possible route for further modeling which was recently demonstrated to provide a framework for the analysis of the full scattering curve from cyanobacterial membranes (Jakubauskas et al., 2019). The general equation for the scattering intensity of particles in solution is

$$I(q) = \Delta\rho^2 \Phi_p V_p P(q) S(q). \quad (4)$$

Here $\Delta\rho^2$ is the contrast of the particles relative to the solution, Φ_p the volume fraction of the particles in the solvent, and V_p the particle volume. The terms $P(q)$ and $S(q)$ are named the *form factor* and *structure factor*, respectively. The form factor describes the scattering from an individual particle or unit cell, and the structure factor describes the interactions between these particles/

units. The modeling of small-angle scattering data requires either an educated choice of the precise expression to use for the form and structure factors or, in cases where such expressions does not exist, the derivation of them which can be a complicated matter (Oliveira et al., 2012). The advantage of a full-scale modeling is a much more detailed idea about the structural organization of the system. Compared to simply applying **Eq. 3**, which provides the overall stacking repeat distance, the data analysis can now also give information on the internal distribution of distances as described below and take into account instrument effects and polydispersity for example. The overall goal of modeling thylakoid scattering is to construct a mathematical model that incorporates these parameters and properly reproduces the experimentally measured scattering curve without undue overparametrization. As described in detail in Jakubauskas et al. (2019), such a model is possible to construct and captures the main features of scattering from stacked thylakoids over basically the full q-range obtained in a SAXS/SANS experiment.

2.4 A Full Scattering Model

In **Figure 3A** a structural model for a stacked thylakoid system is illustrated. A complication in photosynthetic membrane systems is that the repeating unit is usually not a single bilayer sheet, but a double bilayer separated by inner and outer liquid compartments, the lumen and the interthylakoid space, respectively. Thus, the form factor needs to reflect this organization while the structure factor should account for the stacking order of these units. In principle, the form and structure factor are coupled, but for highly anisotropic systems like the membrane stacks described here they can be treated separately (Oliveira et al., 2012) as also demonstrated by simulations in Jakubauskas et al. (2019). The stacking order of lamellar systems is known to be well described by the structure factor from Nallet et al. (1993) while the double bilayer form factor is derived explicitly in Jakubauskas et al. (2019). As shown in **Figure 3A**, the form factor is built from a step model, or "box" model, which is probably the simplest possible description of the scattering density variation. Other options include smoother Gaussian variations and multilayer models (Oliveira et al., 2012). Regardless, the model presented in **Figure 3A** can be considered a reasonable first approach of modeling this complex biological system, and as shown in **Figure 3B**, the model fits the data very well. The parameters entering the form factor equations are all the "local" distances of the double bilayer structural unit cell, that is, the headgroup, tailgroup, and lumen heights along with the scattering length densities of those domains. The structure factor on the other hand relies on the "global" parameters: the number of layers in the stack, the overall stacking repeat distance, and finally a measure of the membrane rigidity. The final intensity is also influenced by the instrument resolution, inherent sample disorder, and dispersity in the number of layers of each stacked system, dispersity in the water layers, etc., all of which affect the "clarity" of scattering peaks and have to be accounted for. The output of the fitting routine based on the structural model shown in **Figure 3B** is summarized in **Figure 3C**, showing that the overall stacking repeat distance is around 60 nm, the average number of layers in a stack ca. 4, the lumen width ca. 8–9 nm, the membrane thickness 4–5 nm, and the interthylakoid space size ca. 45 nm. Finally, from the relative scattering length density levels of the inner and outer liquid compartments, it is concluded that the lumenal protein content is higher than that in the thylakoid membrane, but lower than that of the interthylakoid space.

Despite the reasonable fits to the data provided by the model presented in Jakubauskas et al. (2019), this is not a universal answer to scattering analysis from photosynthetic membrane systems, but it provides one solution. As already hinted above, one could make other choices for the precise implementation of the structure and form factors or the implementation of polydispersity could be done differently. Finally, there are also inherent assumptions which may turn out to be nonoptimal; one example is the form factor where the individual bilayers in the above modeling are assumed to be symmetric which is probably biologically unrealistic. The combination of next-generation neutron facilities and optimized sample preparations could mean that such increased details will become possible to model and extract in the future.

2.5 Scattering versus Microscopy

Structural studies of photosynthetic membranes are dominated by microscopy, so we briefly comment on the differences between such direct imaging methods and the indirect methods provided by scattering. Electron microscopy allows investigating an ensemble of individual sample features in Å resolution, but the statistical analysis of ultrastructures from TEM micrographs requires choosing a number of well-preserved and representative structures from the sample volume of the order of approximately 5×10^{-7} mm^3. To compare, a relatively large sample volume of 0.1–1 mm^3 is probed by X-rays or neutrons simultaneously and a statistical low-resolution structure of the total-volume averaged system is obtained. Microscopy methods are therefore complementary to scattering in accounting for sample heterogeneity, as minute differences of individual structure are clearly observed. In electron microscopy studies, artifacts from sample preparation are common due to fixation, dehydration, and image contrast (**Table 3**). This is contrary to scattering methods where the sample is either in a natural state, measuring directly on a leave for example, or in controlled conditions closely mimicking or perturbing the natural conditions. Besides requiring a minimal sample preparation, scattering methods enable a relatively quick system analysis under near-native conditions and importantly allows following sample dynamics. The investigation of sample dynamics on the nanometer length scale *in situ* is only possible using scattering methods, as electron microscopy requires sample immobilization, and light super-resolution microscopy techniques do not yet provide sufficient resolution (Iwai et al., 2014; Iwai et al., 2016). Cryomicroscopy techniques allow preserving an *in vivo*-like environment, but the investigation of thick samples (e.g., the entire grana stack (Kouřil et al., 2011) is yet impossible due to method restrictions and the generally insufficient contrast of membranes. Although being straight forward to execute in principle, scattering methods also have challenges. Primarily, obtaining sharp Bragg peaks on photosynthetic membranes in physiological conditions (large protein content, required H-D contrast adjustments, measurements in room temperature, and high osmolarity) can be

TABLE 3 | Comparison of scattering and microscopy techniques (Schnablegger and Singh, 2013).

Feature	Scattering	Electron microscopy
Space	Reciprocal (inverse)	Real (direct)
Resolution	Averaged sample details on the nm-scale	Local details on the nm-scale
Local structure details	Cannot be extracted	Can be extracted
Results	Representative of the entire sample average	Unique, but may not represent the entire sample
	Result interpretation is ambiguous	Average structures are hard to obtain
Preparation/experimental artifacts	Scarce in *in vitro* experiments	Artifacts inherent with chemical fixation
	Sample shall not degrade/change during measurement	Artifacts scarce for cryofixation methods
		Overall cryo-EM contrast is lower than that of TEM

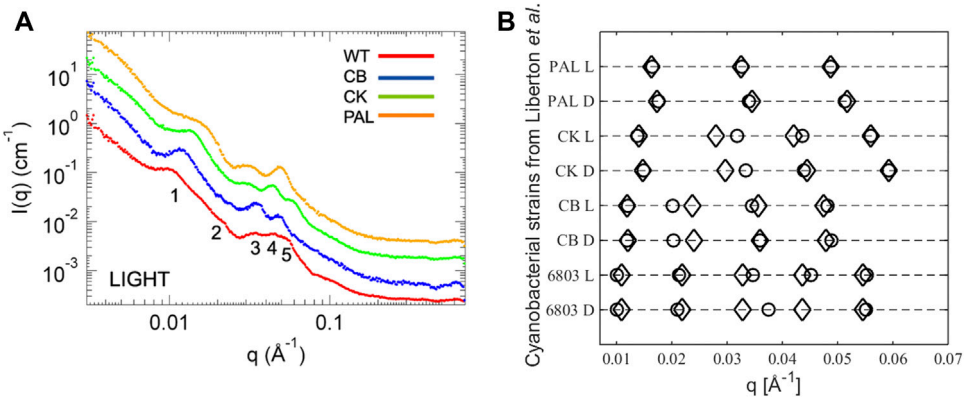

FIGURE 5 | (A) X-ray scattering curves of cyanobacterial systems: *Synechocystis* sp. PCC 6803 (WT), CB, CK, PAL mutants. **(B)** Plot of the peak positions from Liberton et al., 2013b. Circles are data values as reported and diamonds are the *q* values calculated using the Bragg equation (**Eq. 2**) with the lowest *q* value as the first-order peak.

demanding. Large system inhomogeneity smears peaks and burdens precise structural parameter calculations. Centrifugation, controlled drying (Kratky et al., 1959; Kreutz and Menke, 1960b; Diederichs et al., 1985), or application of an external magnetic field (Geacintov et al., 1972; Sadler, 1976; Nagy et al., 2011; Posselt et al., 2012; Nagy et al., 2013) can be used to increase internal order of the sample during the scattering experiment but might complicate modeling where there typically is an assumption of isotropy and of course also might alter the natural state of the system. Overall, small-angle scattering and microscopy methods complement each other, and their parallel usage is advocated. Complementary investigation of the same sample with both techniques provides detailed structural information accounting for sample inhomogeneities (electron microscopy) and following sample behavior *in vivo* (scattering).

3 CYANOBACTERIAL THYLAKOIDS

The ultrastructure of thylakoids from cyanobacteria is characterized by various arrangements of sheet-like membrane layers subject to the confinement of the surrounding cell wall. These strain-dependent arrangements are either concentric layers neighboring the cell periphery or near-radial distributions emanating from focal points on the cell membrane (Olive et al., 1997; Rast et al., 2015) (see **Figure 1**). From TEM data, the thylakoid repeat distance for *Synechocystis* sp. PCC 6803 (WT) and photosynthetic mutants is 340–550 Å and 430 Å for *Halomicronema hongdechloris* (Liberton et al., 2013b; Li et al., 2016). In terms of scattering studies, the wild-type strain *Synechocystis* sp. PCC 6803 is by far the most studied cyanobacteria (Liberton et al., 2013a; Liberton et al., 2013b; Ünnep et al., 2014a; Stingaciu et al., 2016). Liberton et al. (2013b) recently described neutron scattering on *Synechocystis* sp. PCC 6803 and three mutant strains with various degrees of phycobilisome deficiency (see **Figure 5A**). In Stingaciu et al. (2016), Stingaciu et al. (2019), the work was expanded with inelastic neutron scattering probing the dynamics of the membranes under different illumination conditions correlating the membrane mobility with photosynthetic activity. This analysis indicates a significantly softer membrane under dark conditions, supporting the result obtained for *Chlamydomonas* (Nagy et al., 2014). Finally, Li et al. (2016) recently published a study on *H. hongdechloris* where SANS work on the intact cells complements microscopy work in establishing a structural understanding of a new cyanobacterial complex showing far-red light induced decrease of thylakoid repeat distance.

Common in all these SANS studies is that the data analysis and interpretation are based on peak position readings with no underlying structural model. The interpretation leans on TEM images and treats all peaks as the first-order Bragg peaks, which we will argue in the following to be erroneous. To prove our point, in **Figure 5B** we plot the reported peak positions from Liberton

et al. (2013b) together with peak predictions calculated from **Eq. 2** with the lowest q value taken as the first-order peak, that is, simply treating the cyanobacterial membrane system as a stack of thylakoid lamellae. Judging from higher order peak positions, almost all data points fit with this obvious explanation. The main outliers are the second-order peaks from the CK and CB mutants, but on inspection of the original scattering curves there are no immediately apparent peaks visible, so these particular peak positions are to be regarded with a high level of uncertainty. Given the broadness of the peaks, the general noise level in the biological systems, and the neglect of form factor effects in this approach, it is hardly surprising that there are some deviations from a perfect Bragg lattice. Thus, we challenge the correlations done in Liberton et al. (2013b), where the individual peaks are interpreted to originate from specific distances in the membrane to be speculative, as all peaks clearly originate from the fundamental repeat distance of the lamellar stack which without invoking a structural model is the only information available. Nevertheless, two conclusions can be drawn from the existing cyanobacterial scattering experiments: light induces a slight shrinkage in the overall lamellar repetition which is correlated with the size of the antenna system. Knowing that plant chloroplasts are evolutionarily derived from cyanobacteria, one might expect a similar behavior of plant thylakoid membranes.

4 PLANT THYLAKOIDS

The first SAXS experiment on isolated osmium-fixed *Aspidistra* chloroplasts (Finean et al., 1953) indicated the existence of a structure with a repeat distance of 250 Å, and a similar D_R was measured by Kratky et al. (1959) for *Allium porrum* chloroplast pellets. Kreutz et al. measured X-ray scattering of the thin layer of dried chloroplast pellets from *Antirrhinum majus* (Kreutz and Menke, 1960a; Kreutz and Menke, 1960b; Kreutz, 1963b). Isotropic scattering curves with peaks corresponding to the repeat distances of 177–248 Å, which putatively occurred from the ordered-layered thylakoid structure, had been obtained (Kreutz and Menke, 1962; Kreutz, 1964). A wide variation of repeat distance values from early experiments has been explained by different sample preparations and different degrees of thylakoid membrane swelling (Kreutz, 1970). Common in all early works is that scattering was used to investigate the composition and internal structure of an individual thylakoid membrane and not thylakoid membrane stacking. A systematic work trying to explain thylakoid membrane scattering was conducted by Sadler et al. (1973), Sadler (1976), on isolated chloroplasts from *Euglena gracilis* and spinach using aligned thylakoid pellets by centrifugation, partial dehydration or external magnetic field and measured X-ray or neutron diffraction: four orders of diffraction peaks having a lamellar periodicity of 165–170 Å were observed (Sadler et al., 1973). Complementing X-rays with neutron scattering experiments in a magnetic field, Sadler et al. suggested a realistic thylakoid ultrastructure model with a thylakoid repeat distance of 240–250 Å (*Euglena*) or 170–190 Å (spinach) and thylakoid membrane thickness of 50 Å (Sadler and Worcester, 1982a; Sadler and Worcester, 1982b). These values are comparable with the current (cryo-)electron microscopy measurements (Shimoni et al., 2005; Kirchhoff et al., 2011). Overall, the main outcomes of early scattering investigations were establishing the protein, lipid, and pigment arrangement in the thylakoid membrane (Kreutz, 1970; Sadler and Worcester, 1982b); estimating the thylakoid membrane thickness (Li, 1978); and providing the understanding that both the interthylakoid space and thylakoid lumen are hydrophilic compartments (Sadler and Worcester, 1982a).

4.1 Isolated Thylakoids

Isolation upconcentrates thylakoid membranes in the sample and reduces scattering from other plant cell components (i.e., cell wall, endoplasmic reticulum membranes, etc.), which makes the sample more pure and the interpretation of the scattering curve easier. However, an osmotic environment of an isolated sample differs from the thylakoid environment *in vivo*. Therefore, measurements on isolated and *in vivo* thylakoids are not equivalent—thylakoids swell in hypotonic (Deamer and Packer, 1967; Opanasenko et al., 1999) and shrink in hypertonic solutions (Robinson, 1985; Posselt et al., 2012; Ünnep et al., 2014b). As shown by scattering experiments (Finean et al., 1953; Kratky et al., 1959; Kreutz and Menke, 1960a; Kreutz and Menke, 1960b; Posselt et al., 2012; Ünnep et al., 2014b; Herdean et al., 2016), different sample treatments yield different thylakoid repeat distances and increased thylakoid disorder (Sadler and Worcester, 1982b) due to osmolarity and ionic force-related changes. However, due to relatively easy and fast measurements, scattering can be used to improve thylakoid or chloroplast isolation procedures with the aim of finding buffers where thylakoid membranes closely resemble the situation *in vivo* (Ünnep et al., 2014a). For example, from scattering experiments NaCl is suggested to be a better osmoticum than sorbitol for thylakoid isolation (Ünnep et al., 2014a; Ünnep et al., 2014b).

4.2 Plant Leaves

To avoid thylakoid ultrastructure changes due to isolation, scattering experiments on intact plant leaves have been performed. In the first SAXS experiment, *Allium porrum* (leek) leaves were stacked perpendicularly to the X-ray beam to suppress cell wall scattering (Kratky et al., 1959; Kreutz and Menke, 1962). Measuring scattering of both green and variegated snapdragon leaf parts (Wild, 1957) allowed subtracting background scattering and obtaining scattering solely from thylakoid membrane stacks (Kreutz, 1964). SANS measurements of the yellow part of *Schefflera arboricola* leaf or red bracts of *Euphorbia pulcherrima*, where thylakoid stacking is either absent or disordered, also did not exhibit scattering peaks (Ünnep et al., 2014a).

As shown in **Figure 6**, repeat distance values obtained from SANS experiments are generally higher than those obtained from TEM measurements of the same sample (Ünnep et al., 2014b; Eyal et al., 2017). As discussed in Ünnep et al. (2014b), to improve

the neutron scattering signal leaves need to be D_2O infiltrated, which might change the thylakoid organization in the leaf. Slightly expanded thylakoid membranes with D_2O-infiltrated lumen produce a higher contrast and thus can dominate the scattering, yielding a larger average D_R of the scattering peak (Ünnep et al., 2014a). On the other hand, TEM sample preparation involves fixation and dehydration, invoking sample shrinkage. Therefore, D_R values *in vivo* can be larger than in TEM micrographs.

5 THYLAKOID DYNAMICS

Illumination-induced thylakoid ultrastructure changes are versatile: both shrinkage and expansion of thylakoid repeat distance have been observed in different ionic environments (Deamer and Packer, 1967). Numerous TEM experiments suggest that thylakoid membranes both *in vivo* and *in vitro* contract in response to illumination; this shrinkage is dark-reversible, and its degree depends on light intensity (Murakami and Packer, 1969; Murakami and Packer, 1970a; Murakami and Packer, 1970b; Sundquist and Burris, 1970; Miller and Nobel, 1972; Yamamoto et al., 2013; Yoshioka-Nishimura et al., 2014; Wood et al., 2018). Scattering can also follow thylakoid stacking repeat distance changes—experiments on isolated thylakoids show that thylakoid repeat distance decreases in a matter of minutes when illuminated with white light intensities up to 1,000 μmol photons m^{-2} s^{-1} and is restored when the light is turned off (Nagy et al., 2011; Posselt et al., 2012; Nagy et al., 2013); the higher the applied light intensity, the larger and quicker the D_R decrease (Nagy et al., 2013). If illumination intensity on isolated thylakoids is increased to 2,500 μmol photons m^{-2} s^{-1}, thylakoid damage occurs and dark readaptation after shrinkage is no longer observed (Posselt et al., 2012). Ultrastructural changes of isolated thylakoids with uncouplers limiting electron transport and pH gradient buildup are not observed upon illumination (Nagy et al., 2013); however, for higher plant thylakoids the role of uncouplers is less clear, and nonphotochemical quenching is proposed to take part in light-induced thylakoid dynamics as well (Ünnep et al., 2020).

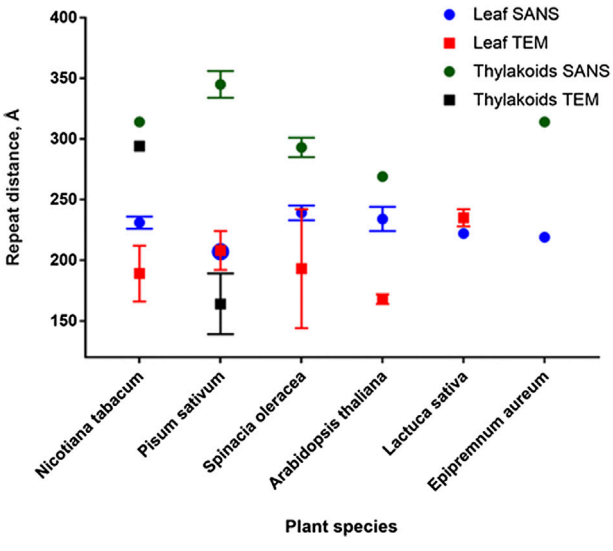

FIGURE 6 | Comparison of repeat distances obtained by SANS and TEM for isolated thylakoids and plant leaves.

Compared to isolated systems, light-induced thylakoid dynamics *in vivo* is more versatile and organism dependent. Several structural outcomes have been observed in plant leaves: thylakoid expansion (Kirchhoff et al., 2011; Yoshioka-Nishimura et al., 2014; Tsabari et al., 2015), thylakoid shrinkage (Miller and Nobel, 1972; Yamamoto et al., 2013; Ünnep et al., 2014b; Tsabari et al., 2015; Wood et al., 2018; Ünnep et al., 2020), and simultaneous thylakoid shrinkage and expansion (Puthiyaveetil et al., 2014; Yoshioka-Nishimura et al., 2014). Apart from that in plants, thylakoid shrinkage was also observed in algal *Porphyra* and *Ulva* cells *in vivo* (Murakami and Packer, 1970a). Light-induced increase of thylakoid repeat distance was observed in *Chlamydomonas* (Nagy et al., 2014), diatoms (Nagy et al., 2012), and cyanobacterial phycobilisome mutant cells (Liberton et al., 2013a), but no D_R change was observed in *Synechocystis* sp. PCC 6803 (WT) cells (Nagy, 2011; Liberton et al., 2013a).

As discussed above, SANS data analysis based on peak position readings cannot infer lumen height or thylakoid membrane thickness or their illuminated-induced changes. Therefore, elucidations of dark–light–dark thylakoid dynamics based on scattering data (Liberton et al., 2013a; Ünnep et al., 2020) are so far incomplete. Suitable modeling which investigates the entire scattering curve behavior is of high importance to investigate lumen changes and thylakoid dynamics in general. Furthermore, inelastic neutron scattering can be used to study dynamics of individual membranes. An investigation of dark-adapted and illuminated cyanobacterial thylakoid membrane dynamics shows that the dark-adapted thylakoid membrane is softer before its illumination with 100 μmol photons m^{-2} s^{-1} white light (Stingaciu et al., 2016; Stingaciu et al., 2019). From SANS, thylakoids in *Chlamydomonas* cells are suggested to exhibit the same behavior (Nagy et al., 2014). However, an experiment with a fluorescence probe suggests that spinach thylakoid membrane fluidity is lower in dark-adapted than in low-light-illuminated state (Yamamoto et al., 2013), which calls for a more detailed investigation.

To conclude, the observation of thylakoid (lumen) shrinkage or expansion is only a single facet of thylakoid dynamics *in vivo* and shall not be the sole experimental purpose, as it depends and is probably governed by numerous environmental factors. It has been extensively demonstrated that thylakoid ultrastructure and degree of thylakoid dynamics *in vivo* depend on the organism (Nagy, 2011; Liberton et al., 2013a; Ünnep et al., 2014a; Demmig-Adams et al., 2015; Ünnep et al., 2020), arrangement and composition of photosynthetic proteins and lipids in the thylakoid membrane (Demmig-Adams et al., 2015; Mazur

et al., 2019), "previous-growth-history" of a plant (Demmig-Adams et al., 2015; Schumann et al., 2017), illumination spectral quality (Mustárdy et al., 1976; Clausen et al., 2014; Nagy et al., 2014; Bína et al., 2016; Li et al., 2016; Schumann et al., 2017; Ünnep et al., 2020), and illumination intensity (Posselt et al., 2012; Nagy et al., 2013; Yamamoto et al., 2013; Puthiyaveetil et al., 2014; Wood et al., 2019). Understanding the interplay of these factors will yield a much more comprehensive picture of thylakoid dynamics.

6 OTHER ORGANISMS AND PROLAMELLAR BODIES

6.1 *Phaeodactylum tricornutum*

Intact marine diatom *Phaeodactylum tricornutum* cells have stacked thylakoid membranes, organized in groups of three (Pyszniak and Gibbs, 1992), although cells cultivated under low intensity red-enhanced illumination were shown to increase the number of homogeneously stacked thylakoids (Bína et al., 2016). In these conditions, large thylakoid membrane areas are occupied exclusively by densely packed elliptical PSI-Lhcr supercomplexes. An inhomogeneous photosystem distribution is proposed for *P. tricornutum* thylakoids, where the outer thylakoid lamellae contain more PSI and ATP synthase complexes, compared to the inner membranes of the stacks (Bína et al., 2016).

Day-light-grown *P. tricornutum* cells exhibit a characteristic scattering profile with two characteristic diffraction peaks positioned at q = 0.037 $Å^{-1}$ (170 Å) and 0.065 $Å^{-1}$ (97 Å) and with a weak peak in between at q 0.052 $Å^{-1}$ (121 Å) [see Figure 1 in Nagy et al. (2012)]. In Nagy et al. (2012), the latter is tentatively assigned to adjacent membrane pairs while no account of the weak central peak is given. In line with the above statements, we conjecture that a full modeling approach accounting for the distinct triplet organization and the possible asymmetric composition of the membranes will account for the full scattering curve.

Nevertheless, qualitative information can still be extracted. Upon white light illumination (150 or 1,200 µmol photons $m^{-2}\,s^{-1}$), q of the peak decreases, indicating an expansion of the stacking—the higher the light intensity, the higher the expansion. This illumination effect was reversible and could not be inhibited by uncouplers, suggesting that thylakoid dynamics are caused by changes in the electrostatic interactions of local electric fields and/or constitutive redistribution of the ions—and not due to pH changes, as in the case of isolated thylakoids (Zimanyi and Garab, 1989). As discussed, light-induced thylakoid expansion in live cells is similar to the thylakoid membrane behavior in intact *Arabidopsis* leaves, which strongly supports the need to analyze thylakoid membrane behavior in a variety of organisms.

In line with experiments on isolated thylakoid membranes, q-values of the peaks increase after addition of 100–600 mM sorbitol whereas peak intensity decreases—indicating thylakoid membrane shrinkage in higher osmolarities. Osmoticum-induced shrinkage is reversible—if sorbitol is removed, scattering signal intensity of the first peak is restored, although the intensity of the second peak remains lower. After dark readaptation q of the two peaks even decrease to slightly lower values than of nontreated cells, indicating a slight thylakoid membrane swelling during readaptation (Nagy et al., 2012). Similar thylakoid membrane shrinkage is also observed after heat treatment of *P. tricornutum* cells: the entire SANS profile shifts to higher q values and peak intensities are decreased.

6.2 *Chlamydomonas reinhardtii*

Single-cell green algae *Chlamydomonas* contain well-defined separate regions of stacked and unstacked thylakoid membranes with distinct protein contents and supramolecular structures. *Chlamydomonas* is an attractive organism to study thylakoid ultrastructure and dynamics *in vivo*, especially because of state transitions. Although *Chlamydomonas* thylakoids are organized less regularly (Engel et al., 2015), distinct regions with predominantly grana-like stacks or stroma lamellae are present—an overall organization similar to higher plants, although with a lower number of lamellae in the stacks. From tomography experiments, *Chlamydomonas* thylakoid stacks are composed of 3–10 thylakoids, which have a lateral repeat distance of 224 ± 13 Å. A single thylakoid membrane thickness is 49 ± 5 Å, thylakoid lumen thickness 90 ± 14 Å, and interthylakoid stromal space 36 ± 5 Å (Engel et al., 2015). From SANS experiments, living *Chlamydomonas* cells exhibit a scattering profile with two characteristic diffraction peaks corresponding to q 0.033–0.0035 $Å^{-1}$ (180–190 Å) and 0.055 $Å^{-1}$ (114 Å). The first peak/feature is proposed to originate from the repeat distance of stacked thylakoid membranes and the second from the membrane pairs (Nagy et al., 2014). If so, the repeat distance obtained from SANS correlates well with electron tomography data, although the overall appearance of the scattering curve is currently not accounted for and needs to be investigated in more detail to clarify if the offset of the peaks from a lamellar pattern is not simply an effect of the form factor and the low number of layers.

6.3 Prolamellar Bodies

We will finish this excursion of scattering work on photosynthetic membranes by returning to the plant prolamellar bodies (PLBs) illustrated in **Figure 1A**. In contrast to all the other membrane systems described so far, prolamellar bodies are not flat sheet stacks so the modeling approach from Jakubauskas et al. (2019)) is not relevant directly. Instead, the analysis of the scattering requires one to index peaks based on symmetry considerations akin to the analysis routinely performed in, for example, lyotropic liquid crystalline systems. Lachmann and Kesselmeier (1989) classified the isolated PLB ultrastructures according to their internal structure as paracrystalline, spongy, or tubular. Paracrystalline PLBs are well organized and ordered; spongy PLBs maintain elements of the original lattice, but their long-range order

is lost; tubular PLBs have tubules from the original structure, but PLBs look torn apart, with no apparent order.

X-ray scattering on isolated PLBs was successfully employed by P. Williams and E. Selstam, when they isolated PLBs and used them for parallel SAXS and TEM studies (Williams et al., 1998; Selstam et al., 2007). Judged from TEM pictures, 70–80% of isolated PLBs in the samples were paracrystalline, the remaining PLBs were spongy, with a very low numbers of tubular PLBs or membrane debris from damaged PLBs, although the latter did not interfere with X-ray scattering from highly ordered PLB structures. Concentrated PLB pellets gave rise to X-ray diffraction patterns resembling a F*d*3*m* lattice with unit cell length a = 78 nm (see **Figure 7**). Scattering was then used to study PLB ultrastructure changes with focus on the impact of salts, cryoprotectant, pH, and freeze–thaw cycles (Williams et al., 1998; Selstam et al., 2007). Although promising in essence, PLB studies proved to be technically difficult—mainly, a robust etiolated plant growth setup and sample preparation are necessary to obtain homogeneous PLB preparations for the scattering measurements. Furthermore, to investigate PLB ultrastructure, the sample enclosure itself needs to be light impermeable and the sample needs to be loaded into it under a very low intensity green light, as 1 ms flash of white light can be sufficient to destroy the paracrystalline order of the PLB. One of the possible ways to tackle the issue of PLB sample resolution is the usage of neutron scattering. Here, scattering from lipids is enhanced if isolated PLBs are resuspended in D_2O-based medium. Furthermore, as is the case for thylakoids, scattering of fresh etiolated and D_2O-infiltrated leaf stack can be investigated. Since the neutron beam is in most cases larger than that with X-rays, lower concentration of PLBs in the leaf can be compensated by the higher screened sample area and leaf stacking, putatively leading to a comparable signal intensity as for concentrated PLBs investigated by a small X-ray beam. Such an experiment does not require any special sample preparation—PLBs can in principle be investigated in *in vivo* conditions, directly in ethiolated leaves, thus yielding more precise average unit cell values and space group assignment. Ultimately, PLB ultrastructures from various plants and photosynthetic mutants can be investigated and compared, as in Bykowski et al. (2020), and a continuous light-induced PLB disassembly can be ideally followed as well.

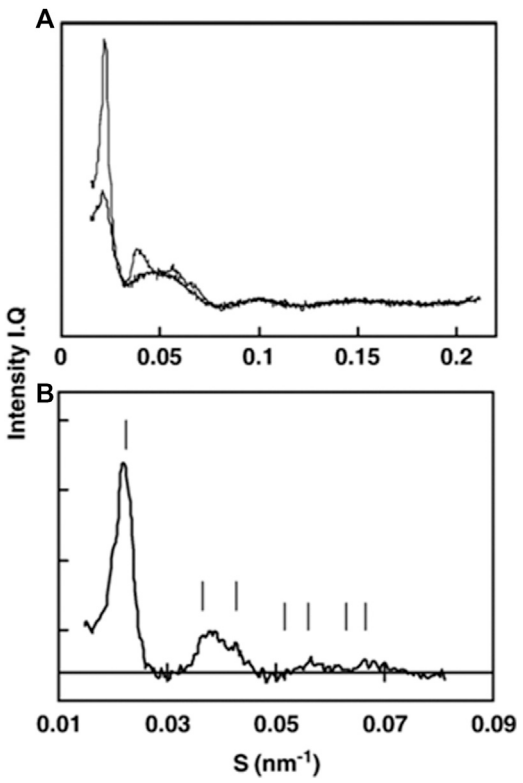

FIGURE 7 | SAXS pattern changes after single freeze–thaw cycle of prolamellar bodies. **(A)** Prior to freezing (thin line) and immediately after melting (thick line). **(B)** Difference between curves from **(A)** indexed to a F*d*3*m* lattice [figure from Selstam et al. (2007)].

7 OUTLOOK

Here we have presented an overview of scattering results obtained so far on photosynthetic membranes and advocate for a holistic modeling approach to scattering data as well as the joint utilization of the complementary methods of scattering and microscopy/tomography to study biological samples as close to their native state as possible. Ideally, a study of high biological relevance could investigate thylakoid dynamics in plants with different degrees of thylakoid stacking and diverse photosynthetic and environmental phenotypes: photosynthetic, pigment, or antennae-deficient mutants, draught, and cold-resistant species. Systematically varying white light intensities and using certain wavelengths, causing state transitions in illumination studies, would enable studying the photosynthetic response and changes in thylakoid ultrastructure and evaluating small-scale dynamics of thylakoid membranes, which would greatly benefit biological investigations in plants and cyanobacteria. Furthermore, the entire PLB-to-thylakoid membrane transition could in principle be followed with scattering experiments, which is one of the most spectacular membrane remodelings known in biology.

To conclude, we believe scattering techniques will ultimately enable one to investigate, follow, and model ultrastructural changes of complex biological membrane systems in their native environment in near-second range. In complement to "static" microscopy techniques and together with the fact that comprehensive mathematical models explaining scattering data from complex systems are underway, an advent of new discoveries using scattering methods on complex biological system dynamics is anticipated.

AUTHOR CONTRIBUTIONS

DJ, KM, PJ, and JK all conceived and wrote the manuscript.

FUNDING

The authors acknowledge financial support from (1) DanScatt, support for travel to large scale facilities (2) Center for Synthetic Biology bioSYNergy™, hosting and running costs (3) Copenhagen Plant Science Centre, hosting and running costs.

ACKNOWLEDGMENTS

The authors acknowledge financial support from (1) DanScatt, (2) the Center for Synthetic Biology 'bioSYNergy', (3) Copenhagen Plant Science Centre, and (4) the VILLUM Foundation (Project no. 13363). Łucja Kowalewska and Beata Bieniak (Faculty of Biology, University of Warsaw) and Catherine Nielsen (Center for Advanced Bioimaging, University of Copenhagen) are acknowledged for the help with TEM imaging. Finally, the authors gratefully acknowledge fruitful discussions with Eva Selstam (Umea University).

REFERENCES

Armbruster, U., Labs, M., Pribil, M., Viola, S., Xu, W., Scharfenberg, M., et al. (2013). Arabidopsis CURVATURE THYLAKOID1 proteins modify thylakoid architecture by inducing membrane curvature. *Plant Cell* 25, 2661–2678. doi:10.1105/tpc.113.113118

Austin, J. R., and Staehelin, L. A. (2011). Three-dimensional architecture of grana and stroma thylakoids of higher plants as determined by electron tomography. *Plant Physiol.* 155, 1601–1611. doi:10.1104/pp.110.170647

Bína, D., Herbstová, M., Gardian, Z., Vácha, F., and Litvín, R. (2016). Novel structural aspect of the diatom thylakoid membrane: lateral segregation of photosystem I under red-enhanced illumination. *Nat. Sci. Rep.* 6, 255. doi:10.1038/srep25583

Bussi, Y., Shimoni, E., Weiner, A., Kapon, R., Charuvi, D., Nevo, R., et al. (2019). Fundamental helical geometry consolidates the plant photosynthetic membrane. *Proc. Natl. Acad. Sci. USA* 116, 22366–22375. doi:10.1073/pnas.1905994116

Bykowski, M., Mazur, R., Buszewicz, D., Szach, J., Mostowska, A., and Kowalewska, L. (2020). Spatial nano-morphology of the prolamellar body in etiolated arabidopsis thaliana plants with disturbed pigment and polyprenol composition. *Front. Cell Dev. Biol.* 8, 586628. doi:10.3389/fcell.2020.586628

Clausen, C. H., Brooks, M. D., Li, T.-D., Grob, P., Kemalyan, G., Nogales, E., et al. (2014). Dynamic mechanical responses of Arabidopsis thylakoid membranes during PSII-specific illumination. *Biophys. J.* 106, 1864–1870. doi:10.1016/j.bpj.2014.03.016

Daum, B., and Kühlbrandt, W. (2011). Electron tomography of plant thylakoid membranes. *J. Exp. Bot.* 62, 2393–2402. doi:10.1093/jxb/err034

Deamer, D. W., and Packer, L. (1967). Correlation of ultrastructure with light-induced ion transport in chloroplasts. *Arch. Biochem. Biophys.* 119, 83–97. doi:10.1016/0003-9861(67)90432-8

Demmig-Adams, B., Muller, O., Stewart, J. J., Cohu, C. M., and Adams, W. W., III (2015). Chloroplast thylakoid structure in evergreen leaves employing strong thermal dissipation. *J. Photochem. Photobiol. B: Biol.* 152, 1011–1344. doi:10.1016/j.jphotobiol.2015.03.014

Diederichs, K., Welte, W., and Kreutz, W. (1985). Determination of interaction forces between higher plant thylakoids and electron-density-profile evaluation using small-angle X-ray scattering. *Biochim. et Biophys. Acta (BBA) Bioenergetics* 809, 107–116. doi:10.1016/0005-2728(85)90173-2

Engel, B. D., Schaffer, M., Kuhn Cuellar, L., Villa, E., Plitzko, J. M., and Baumeister, W. (2015). Native architecture of the *Chlamydomonas* chloroplast revealed by *in situ* cryo-electron tomography. *eLife* 4, e04889. doi:10.7554/elife.04889

Eyal, L. B., Choubrh, R. R., Cohen, E., Eisenberg, I., Tamburu, C., Dorogi, M., et al. (2017). Changes in aggregation states of light-harvesting complexes as mechanism for modulating energy transfer in desert crust cyanobacteria. *Proc. Natl. Acad. Sci. USA* 114, 9481–9486. doi:10.1073/pnas.1708206114

Finean, J. B., Sjöstrand, F. S., and Steinmann, E. (1953). Submicroscopic organisation of some layered lipoprotein structures (Nerve myelin, retinal rods, and chloroplasts). *Exp. Cell Res.* 5, 557–559. doi:10.1016/0014-4827(53)90247-x

Ford, R. C., and Holzenburg, A. (2014). Organization of protein complexes and a mechanism for grana formation in photosynthetic membranes as revealed by cryo-electron microscopy. *Cryst. Res. Technol.* 49, 637–644. doi:10.1002/crat.201300116

Ford, R. C., Stoylova, S. S., and Holzenburg, A. (2002). An alternative model for photosystem II/light harvesting complex II in grana membranes based on cryo-electron microscopy studies. *Eur. J. Biochem.* 269, 326–336. doi:10.1046/j.0014-2956.2001.02652.x

Garab, G., Javorfi, T., Amenitsch, H., Cseh, Z., Mustárdy, L., Borbély, S., et al. (1997). Small angle X-ray and neutron scattering profiles of chloroplast thylakoid membranes determined by the aids of magnetic alignment. *Nat. Irrevers. Struct.* 65, 63.

Geacintov, N. E., Van Nostrand, F., Becker, J. F., Tinkel, J. B., and Nostrand, F. (1972). Magnetic field induced orientation of photosynthetic systems. *Biochim. et Biophys. Acta (BBA) Bioenergetics* 267, 65–79. doi:10.1016/0005-2728(72)90138-7

Glatter, O., and Kratky, O. (1982). *Small angle x-ray scattering*. London: Academic Press.

Golub, M., Combet, S., Wieland, D. C. F., Soloviov, D., Kuklin, A., et al. (2017). Solution structure and excitation energy transfer in phycobiliproteins of *Acaryochloris marina* investigated by small angle scattering. *Biochim. et Biophys. Acta (BBA) Bioenergetics* 1858, 318–324. doi:10.1016/j.bbabio.2017.01.010

Heinz, S., Rast, A., Shao, L., Gutu, A., Gügel, I. L., Heyno, E., et al. (2016). Thylakoid membrane architecture in Synechocystis depends on CurT, a homolog of the granal CURVATURE THYLAKOID1 proteins. *Plant Cell* 28, 2238–2260. doi:10.1105/tpc.16.00491

Heller, W. T. (2010). Small-angle neutron scattering and contrast variation: a powerful combination for studying biological structures. *Acta Crystallogr. D Biol. Cryst.* 66, 1213–1217. doi:10.1107/s0907444910017658

Herdean, A., Teardo, E., Nilsson, A. K., Pfeil, B. E., Johansson, O. N., Ünnep, R., et al. (2016). A voltage-dependent chloride channel fine-tunes photosynthesis in plants. *Nat. Commun.* 7, 11654. doi:10.1038/ncomms11654

Hodapp, N., and Kreutz, W. (1980). Electrondensity profile determination of bacterial photosynthetic membranes. *Biophys. Struct. Mechan.* 7, 65–95. doi:10.1007/bf00538399

Iwai, M., Yokono, M., Kurokawa, K., Ichihara, A., and Nakano, A. (2016). Live-cell visualization of excitation energy dynamics in chloroplast thylakoid structures. *Sci. Rep.* 6, 29940. doi:10.1038/srep29940

Iwai, M., Yokono, M., and Nakano, A. (2014). Visualizing structural dynamics of thylakoid membranes. *Sci. Rep.* 4, 3768. doi:10.1038/srep03768

Jakubauskas, D., Kowalewska, L., Sokolova, A., Garvey, C., Mortensen, K., Jensen, P., et al. (2019). Ultrastructural modeling of small angle scattering from photosynthetic membranes. *Sci. Rep.* 9, 19405. doi:10.1038/s41598-019-55423-0

Jakubauskas, D. (2016). *Structural investigation of photosynthetic membranes using small-angle scattering, PhD thesis*. Copenhagen: Niels Bohr Institute, University of Copenhagen.

Kaftan, D., Brumfeld, V., Nevo, R., Scherz, A., and Reich, Z. (2002). From chloroplasts to photosystems: in situ scanning force microscopy on intact thylakoid membranes. *Embo J.* 21, 6146–6153. doi:10.1093/emboj/cdf624

Kirchhoff, H., Hall, C., Wood, M., Herbstová, M., Tsabari, O., Nevo, R., et al. (2011). Dynamic control of protein diffusion within the granal thylakoid lumen. *Proc. Natl. Acad. Sci.* 108, 20248–20253. doi:10.1073/pnas.1104141109

Kirkensgaard, J. J. K., Holm, J. K., Larsen, J. K., and Posselt, D. (2009). Simulation of small-angle X-ray scattering from thylakoid membranes. *J. Appl. Cryst.* 42, 649–659. doi:10.1107/s0021889809017701

Kouřil, R., Oostergetel, G. T., and Boekema, E. J. (2011). Fine structure of granal thylakoid membrane organization using cryo electron tomography. *Biochim. et Biophys. Acta (BBA) Bioenerget.* 1807, 368–374.

Kowalewska, Ł., Bykowski, M., and Mostowska, A. (2019). Spatial organization of thylakoid network in higher plants. *Bot. Lett.* 166, 326–343. doi:10.1080/23818107.2019.1619195

Kowalewska, Ł. M., Mazur, R., Suski, S., Garstka, M., and Mostowska, A. (2016). Three-dimensional visualization of the internal plastid membrane network during runner bean chloroplast biogenesis. Dynamic model of the tubular-lamellar transformation. *Plant Cell.* 28 (4), 153.

Kratky, O., Menke, W., Sekora, A., Paletta, B., and Bischof, M. (1959). Orientierende Röntgen-Kleinwinkelmessungen an Chloroplasten von Allium porrum. *Z. Naturforsch.* 14, 307–311. doi:10.1515/znb-1959-0505

Kreutz, W., and Menke, W. (1960a). Strukturuntersuchungen an plastiden. *Z. Naturforsch.* 15, 402–410. doi:10.1515/znb-1960-0613

Kreutz, W., and Menke, W. (1960b). Strukturuntersuchungen an plastiden. *Z. Naturforsch.* 15, 483–487. doi:10.1515/znb-1960-0802

Kreutz, W., and Menke, W. (1962). Strukturuntersuchungen an plastiden. *Z. Naturforsch.* 17, 675–683. doi:10.1515/znb-1962-1008

Kreutz, W. (1964). Strukturunterschungen an plastiden VI. Uber die struktur der lipoproteinlamellen in chloroplasten lebender zellen. *Z. Naturforsch.* 19b, 441–446.

Kreutz, W. (1963a). Strukturuntersuchungen an plastiden. *Z. Naturforsch.* 18, 567–571. doi:10.1515/znb-1963-0713

Kreutz, W. (1963b). Strukturuntersuchungen an plastiden. *Zeitschrift fur Naturforschung* 18, 1098–1104. doi:10.1515/znb-1963-1220

Kreutz, W. (1970). *X-ray structure research on the photosynthetic membrane. Advances in Botanical Research*. New York: Academic Press, 53–169.

Lachmann, K. U., and Kesselmeier, J. (1989). Influence of divalent cations and chelators on the structure of prolamellar bodies of *Avena sativa*. *Plant Cell Physiol.* 30, 1081–1088. doi:10.1093/oxfordjournals.pcp.a077848

Li, J. (1978). *An x-ray diffraction study of chloroplast thylakoid membrane structure*. Ph.D. thesis, Harward University.

Li, J. (1979). X-ray analysis of chloroplast thylakoid membrane structure. *Biophys. J.* 25, 190.

Li, M., Mukhopadhyay, R., Svoboda, V., Oung, H. M. O., Mullendore, D. L., and Kirchhoff, H. (2020). Measuring the dynamic response of the thylakoid architecture in plant leaves by electron microscopy. *Plant Direct.* 4, 1–14. doi:10.1002/pld3.280

Li, Y., Lin, Y., Garvey, C. J., Birch, D., Corkery, R. W., Loughlin, P. C., et al. (2016). Characterization of red-shifted phycobilisomes isolated from the chlorophyll f -containing cyanobacterium Halomicronema hongdechloris. *Biochim. et Biophys. Acta (BBA) Bioenergetics* 1857, 107–114. doi:10.1016/j.bbabio.2015.10.009

Liberton, M., Collins, A. M., Page, L. E., O'Dell, W. B., O'Neill, H., Urban, V. S., et al. (2013a). Probing the consequences of antenna modification in cyanobacteria. *Photosynth Res.* 118, 17–24. doi:10.1007/s11120-013-9940-0

Liberton, M., Page, L. E., O'Dell, W. B., O'Neill, H., Mamontov, E., Urban, V. S., et al. (2013b). Organization and flexibility of cyanobacterial thylakoid membranes examined by neutron scattering. *J. Biol. Chem.* 288, 3632–3640. doi:10.1074/jbc.m112.416933

Lokstein, J. M., Solymosi, K., Strzałka, K., and Mysliwa-Kurdziel, B. (2013). Visualization and characterization of prolamellar bodies with atomic force microscopy. *J. Plant Physiol.* 170, 1217–1227. doi:10.1016/j.jplph.2013.04.017

Mazur, R., Mostowska, A., Szach, J., Gieczewska, K., Wójtowicz, J., Bednarska, K., et al. (2019). Galactolipid deficiency disturbs spatial arrangement of the thylakoid network in *Arabidopsis thaliana* plants. *J. Exp. Bot.* 70, 4689–4704. doi:10.1093/jxb/erz219

Menke, W. (1960). Das allgemeine Bauprinzip des Lamellarsystems der Chloroplasten. *Experientia* 16, 537–538. doi:10.1007/bf02158442

Menke, W. (1940a). Die lamellarstruktur der chloroplasten im ultravioletten licht. *Naturwissenschaften* 28, 158–159.

Menke, W. (1940b). Untersuchungen über den Feinbau des Protoplasmas mit dem Universal-Elektronenmikroskop. *Protoplasma* 35, 115–130. doi:10.1007/bf02807310

Miller, M. M., and Nobel, P. S. (1972). Light-induced changes in the ultrastructure of pea chloroplasts *in vivo*. *Plant Physiol.* 49, 535–541. doi:10.1104/pp.49.4.535

Murakami, S., and Packer, L. (1970a). Light-induced changes in the conformation and configuration of the thylakoid membrane of *Ulva* and *Porphyra* chloroplasts *in vivo*. *Plant Physiol.* 45, 289–299. doi:10.1104/pp.45.3.289

Murakami, S., and Packer, L. (1970b). Protonation and chloroplast membrane structure. *J. Cel. Biol.* 47, 332–351. doi:10.1083/jcb.47.2.332

Murakami, S., and Packer, L. (1969). Reversible changes in the conformation of thylakoid membranes accompanying chloroplast contraction or expansion. *Biochim. et Biophys. Acta (BBA) Bioenergetics* 180, 420–423. doi:10.1016/0005-2728(69)90128-5

Mustárdy, L., and Jánossy, A. G. S. (1979). Evidence of helical thylakoid arrangement by scanning electron microscopy. *Plant Sci. Lett.* 16, 281–284. doi:10.1016/0304-4211(79)90039-7

Mustárdy, L., Machowicz, E., and Faludi-Dániel, A. (1976). Light-induced structural changes if thylakoids in normal and carotenoid deficient chloroplasts of maize. *Protoplasma* 88, 65–73.

Nagy, G., Zsiros, O. R., Takizawa, K., and Porcar, L. (2014). Chloroplast remodeling during state transitions inChlamydomonas reinhardtiias revealed by noninvasive techniques *in vivo*. *Proc. Natl. Acad. Sci. USA* 111, 5042–5047. doi:10.1073/pnas.1322494111

Nagy, G., Kovács, L., Ünnep, R., Zsiros, L., Almásy, L., et al. (2013). Kinetics of structural reorganizations in multilamellar photosynthetic membranes monitored by small-angle neutron scattering. *Eur. Phys. J. E* 36, 69. doi:10.1140/epje/i2013-13069-0

Nagy, G., Posselt, D., Kovács, L., Holm, J. K., Szabó, M., Ughy, B., et al. (2011). Reversible membrane reorganizations during photosynthesis *in vivo*: revealed by small-angle neutron scattering. *Biochem. J.* 436, 225–230. doi:10.1042/bj20110180

Nagy, G. (2011). *Structure and dynamics of photosynthetic membranes as revealed by neutron Scattering, PhD thesis*. University of Grenoble and Eötvös Loránd University.

Nagy, G., Szabó, M., Ünnep, R., Káli, G., Miloslavina, Y., Lambrev, P. H., et al. (2012). Modulation of the multilamellar membrane organization and of the chiral macrodomains in the diatom *Phaeodactylum tricornutum* revealed by small-angle neutron scattering and circular dichroism spectroscopy. *Photosynth Res.* 111, 71–79. doi:10.1007/s11120-011-9693-6

Nallet, F., Laversanne, R., and Roux, D. (1993). Modeling X-ray or neutron scattering spectra of lyotropic lamellar phases : interplay between form and structure factors. *J. Phys. II France* 3, 487–502. doi:10.1051/jp2:1993146

Olive, J., Ajlani, G., Astier, C., Recouvreur, M., and Vernotte, C. (1997). Ultrastructure and light adaptation of phycobilisome mutants of Synechocystis PCC 6803. *Biochim. et Biophys. Acta (BBA) Bioenergetics* 1319, 275–282. doi:10.1016/s0005-2728(96)00168-5

Oliveira, C. L. P., Gerbelli, B. B., Silva, E. R. T., Nallet, F., Navailles, L., Oliveira, E. A., et al. (2012). Gaussian deconvolution: a useful method for a form-free modeling of scattering data from mono- and multilayered planar systems. *J. Appl. Cryst.* 45, 1278–1286. doi:10.1107/s002188981204191x

Onoa, B., Schneider, A. R., Brooks, M. D., Grob, P., Nogales, E., Geissler, P. L., et al. (2014). Atomic force microscopy of photosystem II and its unit cell clustering quantitatively delineate the mesoscale variability in *Arabidopsis* thylakoids. *PLoS ONE* 9. doi:10.1371/journal.pone.0101470

Opanasenko, V., Semenova, G., and Agafonov, A. (1999). Changes in the structure and the functional state of thylakoids under the conditions of osmotic shock. *Photosynthesis Res.* 62, 281–290. doi:10.1023/a:1006327920100

Paolillo, D., Jr., and Paolillo, D. J. (1970). The three-dimensional arrangement of intergranal lamellae in chloroplasts. *J. Cell Sci.* 6, 243–255.

Pape, E. H., Menke, W., Weick, D., and Hosemann, R. (1974). Small angle X-ray scattering of the thylakoid membranes of *Rhodopseudomonas spheroides* in aqueous suspensions. *Biophys. J.* 14, 221–232. doi:10.1016/s0006-3495(74)85909-6

Posselt, D., Nagy, G., Kirkensgaard, J. J. K., Holm, J. K., Aagaard, T. H., Timmins, P., et al. (2012). Small-angle neutron scattering study of the ultrastructure of chloroplast thylakoid membranes - periodicity and structural flexibility of the stroma lamellae. *Biochim. et Biophys. Acta (BBA) Bioenergetics* 1817, 1220–1228. doi:10.1016/j.bbabio.2012.01.012

Puthiyaveetil, S., Tsabari, O., Lowry, T., Lenhert, S., Lewis, R. R., Reich, Z., et al. (2014). Compartmentalization of the protein repair machinery in

photosynthetic membranes. *Proc. Natl. Acad. Sci.* 111, 15839–15844. doi:10.1073/pnas.1413739111

Pyszniak, A. M., and Gibbs, S. P. (1992). Immunocytochemical localization of photosystem I and the fucoxanthin-chlorophylla/c light-harvesting complex in the diatom *Phaeodactylum tricornutum*. *Protoplasma* 166, 208–217. doi:10.1007/bf01322783

Rast, A., Heinz, S., and Nickelsen, J. (2015). Biogenesis of thylakoid membranes. *Biochim. Biophys. Acta*, 1847, 821. doi:10.1016/j.bbabio.2015.01.007

Rast, A., Schaffer, M., Albert, S., Wan, W., Pfeffer, S., Beck, F., et al. (2019). Biogenic regions of cyanobacterial thylakoids form contact sites with the plasma membrane. *Nat. Plants* 5, 436–446. doi:10.1038/s41477-019-0399-7

Robinson, S. P. (1985). Osmotic adjustment by intact isolated chloroplasts in response to osmotic stress and its effect on photosynthesis and chloroplast volume. *Plant Physiol.* 79, 996–1002. doi:10.1104/pp.79.4.996

Sadler, D. M., Lefort-Tran, M., and Pouphile, M. (1973). Structure of photosynthetic membranes of *Euglena* using X-ray diffraction. *Biochim. et Biophys. Acta (BBA) Biomembranes* 298, 620–629. doi:10.1016/0005-2736(73)90078-3

Sadler, D. M., and Worcester, D. L. (1982a). Neutron diffraction studies of oriented photosynthetic membranes. *J. Mol. Biol.* 159, 467–482. doi:10.1016/0022-2836(82)90295-9

Sadler, D. M., and Worcester, D. L. (1982b). Neutron scattering studies of photosynthetic membranes in aqueous dispersion. *J. Mol. Biol.* 159, 485–499. doi:10.1016/0022-2836(82)90297-2

Sadler, D. M. (1976). X-ray diffraction from chloroplast membranes oriented in a magentic field. *FEBS Lett.* 67, 289–293. doi:10.1016/0014-5793(76)80549-2

Schnablegger, H., and Singh, Y. (2013). The SAXS guide. Getting acquainted with the principles (Anton Paar GmbH).

Schumann, T., Paul, S., Melzer, M., Dormann, P., and Jahns, P. (2017). Plant growth under natural light conditions provides highly flexible short-term acclimation properties toward high light stress. *Front. Plant Sci.* 8, 681. doi:10.3389/fpls.2017.00681

Sears, V. F. (1992). Neutron scattering lengths and cross sections. *Neutron News* 3, 26–37. doi:10.1080/10448639208218770

Selstam, E., Schelin, J., Williams, W. P., and Brain, A. P. R. (2007). Structural organisation of prolamellar bodies (PLB) isolated from Zea mays. parallel TEM, SAXS and absorption spectra measurements on samples subjected to freeze-thaw, reduced pH and high-salt perturbation. *Biochim. et Biophys. Acta (BBA) Biomembranes* 1768, 2235–2245. doi:10.1016/j.bbamem.2007.05.005

Serdyuk, I. N., Zaccai, N. R., Zaccai, J., Zaccal, N., and Zaccal, P. (2007). *Methods in molecular Biophysics*. Cambridge: Cambridge University Press.

Shimoni, E., Rav-Hon, O., Ohad, I., Brumfeld, V., and Reich, Z. (2005). Three-dimensional organization of higher-plant chloroplast thylakoid membranes revealed by electron tomography. *Plant Cell* 17, 2580–2586. doi:10.1105/tpc.105.035030

Smidijiev, I., Stoylova, S., Amenitsch, H., Jávorfi, T., Mustárdy, L., Laggner, P., et al. (2000). Self-assembly of large, ordered lamellae from non-bilayer lipids and integral membrane proteins *in vivo*. *Proc. Natl. Acad. Sci. USA* 97, 1473–1476.

Staehelin, L. A. (1986). "Chloroplast structure and supramolecular organization of photosynthetic membranes,". *Photosynthesis III. Photosynthetic membranes and light harvesting systems*. Editors L. A. Staehelin and C. J. Arntzen (New York: Springer), 19, 1–84.

Stingaciu, L.-R., O'Neill, H., Liberton, M., Urban, V. S., Pakrasi, H. B., and Ohl, M. (2016). Revealing the dynamics of thylakoid membranes in living cyanobacterial cells. *Sci. Rep.* 6, 19627. doi:10.1038/srep19627

Stingaciu, L.-R., O'Neill, H. M., Liberton, M., Pakrasi, H. B., and Urban, V. S. (2019). Influence of chemically disrupted photosynthesis on cyanobacterial thylakoid dynamics in *Synechocystis* sp. pcc 6803. *Sci. Rep.* 9. doi:10.1038/s41598-019-42024-0

Sturgis, J. N., Tucker, J. D., Olsen, J. D., Hunter, C. N., and Niederman, R. A. (2009). Atomic force microscopy studies of native photosynthetic membranes†. *Biochemistry* 48, 3679–3698. doi:10.1021/bi900045x

Sundquist, J. E., and Burris, R. H. (1970). Light-dependent structural changes in the lamellar membranes of isolated spinach chloroplasts: measurement by electron microscopy. *Biochim. et Biophys. Acta (BBA) Bioenergetics* 223, 115–121. doi:10.1016/0005-2728(70)90136-2

Sznee, K., Dekker, J. P., Dame, R. T., van Roon, H., Wuite, G. J. L., and Frese, R. N. (2011). Jumping mode atomic force microscopy on grana membranes from spinach. *J. Biol. Chem.* 286, 39164–39171. doi:10.1074/jbc.m111.284844

Tang, K.-H., and Blankenship, R. E. (2012). Neutron and light scattering studies of light-harvesting photosynthetic antenna complexes. *Photosynth Res.* 111, 205–217. doi:10.1007/s11120-011-9665-x

Tsabari, O., Nevo, R., Meir, S., Carrillo, L. R., Kramer, D. M., and Reich, Z. (2015). Differential effects of ambient or diminished CO2 and O2 levels on thylakoid membrane structure in light-stressed plants. *Plant J.* 81, 884–894. doi:10.1111/tpj.12774

Ünnep, R., Nagy, G., Markó, M., and Garab, G. (2014a). Monitoring thylakoid ultrastructural changes *in vivo* using small-angle neutron scattering. *Plant Physiol. Biochem. PPB/Societe francaise de physiologie vegetale* 81, 1–11. doi:10.1016/j.plaphy.2014.02.005

Ünnep, R., Paul, S., Zsiros, O., Kovács, L., Székely, N. K., Steinbach, G., et al. (2020). Thylakoid membrane reorganizations revealed by small-angle neutron scattering of *Monstera deliciosa* leaves associated with non-photochemical quenching. *Open Biol.* 10, 200144. doi:10.1098/rsob.200144

Ünnep, R., Zsiros, O., Hörcsik, Z., Markó, M., Jajoo, A., Kohlbrecher, J., et al. (2017). Low-pH induced reversible reorganizations of chloroplast thylakoid membranes - as revealed by small-angle neutron scattering. *Biochim. et Biophys. Acta (BBA) Bioenergetics* 1858, 360–365. doi:10.1016/j.bbabio.2017.02.010

Ünnep, R., Zsiros, O., Solymosi, K., Kovács, L., Lambrev, P. H., Tóth, T., et al. (2014b). The ultrastructure and flexibility of thylakoid membranes in leaves and isolated chloroplasts as revealed by small-angle neutron scattering. *Biochim. et Biophys. Acta (BBA) Bioenergetics* 1837, 1572–1580. doi:10.1016/j.bbabio.2014.01.017

Wild, A. (1957). *Beitraege zur biologie der pflanzen* 37, 137.

Williams, W. P., Selstam, E., and Brain, T. (1998). X-ray diffraction studies of the structural organisation of prolamellar bodies isolated from *Zea mays*. *FEBS Lett.* 422, 252–254. doi:10.1016/s0014-5793(98)00019-2

Willis, B. T. M., and Carlile, C. J. (2009). *Experimental neutron scattering*. Oxford University Press.

Wood, W. H. J., Barnett, S. F. H., Flannery, S., Hunter, C. N., and Johnson, M. P. (2019). Dynamic thylakoid stacking is regulated by lhcii phosphorylation but not its interaction with psi. *Plant Physiol.* 180, 2152–2166. doi:10.1104/pp.19.00503

Wood, W. H. J., MacGregor-Chatwin, C., Barnett, S. F. H., Mayneord, G. E., Huang, X., Hobbs, J. K., et al. (2018). Dynamic thylakoid stacking regulates the balance between linear and cyclic photosynthetic electron transfer. *Nat. Plants* 4, 116–127. doi:10.1038/s41477-017-0092-7

Worcester, D. L. (1976). *Neutron beam studies of biological membranes and membrane components Biological membranes*, vol. 3. New York: Academic Press, 1–46.

Yamamoto, Y., Hori, H., Kai, S., Ishikawa, T., Ohnishi, A., Tsumura, N., et al. (2013). Quality control of photosystem II: reversible and irreversible protein aggregation decides the fate of photosystem II under excessive illumination. *Front. Plant Sci.* 4 (433), 1–9. doi:10.3389/fpls.2013.00433

Yoshioka-Nishimura, M., Nanba, D., Takaki, T., Ohba, C., Tsumura, N., Morita, N., et al. (2014). Quality control of photosystem II: direct imaging of the changes in the thylakoid structure and distribution of ftsh proteases in spinach chloroplasts under light stress. *Plant Cell Physiol.* 55, 1255–1265. doi:10.1093/pcp/pcu079

Zimányi, L., and Garab, G. (1989). Configuration of the electric field and distribution of ions in energy transducing biological membranes: model calculations in a vesicle containing discrete charges. *J. Theor. Biol.* 138, 59–76. doi:10.1016/s0022-5193(89)80178-x

Zsiros, O., Ünnep, R., Nagy, G., Almásy, L., Patai, R., Székely, J., et al. (2020). Role of protein-water interface in the stacking interactions of granum thylakoid membranes as revealed by the effects of Hofmeister salts. *Front. Plant Sci.* 11, 1257. doi:10.3389/fpls.2020.01257

Conflict of Interest: The authors declare that the research was conducted in the absence of any commercial or financial relationships that could be construed as a potential conflict of interest.

frontiers in Chemistry

REVIEW
published: 27 April 2021
doi: 10.3389/fchem.2021.642851

Biomembrane Structure and Material Properties Studied With Neutron Scattering

Jacob J. Kinnun[1,2]*, *Haden L. Scott*[1,2]*, *Rana Ashkar*[3,4]* and *John Katsaras*[2,5,6]*

[1] Large Scale Structures Group, Neutron Scattering Division, Oak Ridge National Laboratory, Oak Ridge, TN, United States, [2] Oak Ridge National Laboratory, Shull-Wollan Center, Oak Ridge, TN, United States, [3] Department of Physics, Virginia Tech, Blacksburg, VA, United States, [4] Center for Soft Matter and Biological Physics, Virginia Tech, Blacksburg, VA, United States, [5] Sample Environment Group, Neutron Scattering Division, Oak Ridge National Laboratory, Oak Ridge, TN, United States, [6] Department of Physics and Astronomy, University of Tennessee, Knoxville, TN, United States

OPEN ACCESS

Edited by:
Olaf Holderer,
Julich-Forschungszentrum,
Helmholtz-Verband Deutscher
Forschungszentren (HZ), Germany

Reviewed by:
Norbert Kučerka,
Joint Institute for Nuclear Research
(JINR), Russia
Jaydeep Kumar Basu,
Indian Institute of Science (IISc), India

***Correspondence:**
Jacob J. Kinnun
kinnunjj@ornl.gov
Haden L. Scott
scotthl@ornl.gov
Rana Ashkar
ashkar@vt.edu
John Katsaras
katsarasj@ornl.gov

Specialty section:
This article was submitted to
Physical Chemistry and Chemical
Physics,
a section of the journal
Frontiers in Chemistry

Received: 16 December 2020
Accepted: 16 March 2021
Published: 27 April 2021

Citation:
Kinnun JJ, Scott HL, Ashkar R and
Katsaras J (2021) Biomembrane
Structure and Material Properties
Studied With Neutron Scattering.
Front. Chem. 9:642851.
doi: 10.3389/fchem.2021.642851

Cell membranes and their associated structures are dynamical supramolecular structures where different physiological processes take place. Detailed knowledge of their static and dynamic structures is therefore needed, to better understand membrane biology. The structure–function relationship is a basic tenet in biology and has been pursued using a range of different experimental approaches. In this review, we will discuss one approach, namely the use of neutron scattering techniques as applied, primarily, to model membrane systems composed of lipid bilayers. An advantage of neutron scattering, compared to other scattering techniques, is the differential sensitivity of neutrons to isotopes of hydrogen and, as a result, the relative ease of altering sample contrast by substituting protium for deuterium. This property makes neutrons an ideal probe for the study of hydrogen-rich materials, such as biomembranes. In this review article, we describe isotopic labeling studies of model and viable membranes, and discuss novel applications of neutron contrast variation in order to gain unique insights into the structure, dynamics, and molecular interactions of biological membranes. We specifically focus on how small-angle neutron scattering data is modeled using different contrast data and molecular dynamics simulations. We also briefly discuss neutron reflectometry and present a few recent advances that have taken place in neutron spin echo spectroscopy studies and the unique membrane mechanical data that can be derived from them, primarily due to new models used to fit the data.

Keywords: neutron scattering, membrane biophysical properties, lipid domains/rafts, membrane dynamics, MD simulation

1. INTRODUCTION

Membranes are critical structural and dynamic assemblies in biological cells, whose underlying structure is a lipid bilayer. In addition to acting as barriers separating cells and cell organelles from their external environments, cellular membranes perform a range of critical roles, such as the compartmentalization of cellular processes, hosting resident proteins, mediating cell signaling, and responding to environmental cues (Singer and Nicolson, 1972; Simons and Toomre, 2000; Phillips et al., 2009). In particular, the plasma membrane (PM), which performs the aforementioned role of enveloping cells and whose general structure was proposed in 1972 by Singer and Nicolson

(Singer and Nicolson, 1972), has received a great deal of attention. Specifically, the PM differentiates itself from other cell membranes by being chemically asymmetric, where the chemical composition between its two bilayer leaflets is different (Verkleij et al., 1973). For example, saturated acyl chain phosphatidylcholines are predominantly located in the outer or exoplasmic leaflet, whereas phosphatidylserine (PS), phosphatidylethanolamine (PE), and phosphatidylinositol headgroup lipids, with varying degrees of unsaturation in their acyl chains, are located in the inner, cytoplasmic bilayer leaflet (Verkleij et al., 1973; Op den Kamp, 1979; Van Meer et al., 2008; Lorent et al., 2020). PM asymmetry is actively maintained by ATP driven processes that locate and maintain the individual lipid species in their respective bilayer leaflet, as lipids, if left to their own devices are able to spontaneously migrate between the two bilayer leaflets, a process known as lipid flip-flop (Seigneuret and Devaux, 1984; van Helvoort et al., 1996; Manno et al., 2002; Smith and Lambert, 2003). The breakdown of PM asymmetry can eventually lead to cell death or apoptosis (Williamson et al., 2001; Doktorova et al., 2020a).

Membranes are also dynamic structures, displaying a diversity of motions ranging from axial rotation of individual lipid molecules, to collective membrane fluctuations involving hundreds of lipids (Woodka et al., 2012). Since membrane dynamics are an integral component of the structure–function relationship, much effort has been expended in studying this relationship and different techniques have been brought to bear in trying to determine the structural and material properties of model membrane systems, including different neutron and x-ray scattering techniques (Wiener and White, 1992; Henriksen and Ipsen, 2004; Kučerka et al., 2008; Yi et al., 2009; Heberle et al., 2016).

Neutron scattering techniques have over the years evolved into unique and powerful nanoscopic probes of membrane structure and dynamics (Pfeiffer et al., 1993; Pan et al., 2013). Results from neutron scattering experiments have produced new insights, not only with regard to the material properties of membranes (e.g., bending rigidity), but also pertaining to their physical properties and how they relate to biological function. These insights have led to a better understanding of protein–lipid interactions, lipid domain formation and size, and PM asymmetry (Clifton et al., 2013; Marquardt et al., 2015; Heberle et al., 2016; Nickels et al., 2017; Rickeard et al., 2020).

Although less abundant than x-rays, neutrons have unique properties that make them ideal probes for the study of hydrogen-rich materials, such as biological membranes. One of those properties is that neutrons interact differently with protium, the most common isotope of hydrogen, and deuterium, the other stable hydrogen isotope (Svergun et al., 2013). This ability to differentiate between the isotopes of hydrogen enables a technique, commonly known as contrast variation, that permits one to highlight the membrane feature of interest. For example, by substituting normal water (H_2O) for heavy water (D_2O), the penetration depth of water into the membrane can be measured with a high degree of accuracy (Fitter et al., 1999). Although atomistic detail can be challenging, neutron scattering can reveal structures down to nanometer length scales, particularly when deuteration strategies are combined with robust membrane models and computer simulations, as was done in the case of the scattering density profile (SDP) model (Eicher et al., 2017). This combination allows neutron scattering to accurately determine bilayer thicknesses and the location of molecular species within the membrane (Kučerka et al., 2008; Marquardt et al., 2013, 2016). Further, deuterated lipids and proteins can be used to study lipid domain formation and protein–lipid interactions (Clifton et al., 2013).

The utility of neutron scattering not only lies in the structural determination of nanoscale membrane features, but also in the measurement of membrane dynamics that can be used to determine membrane mechanical properties using the collective motions of the membrane. Techniques, such as inelastic and quasielastic neutron scattering are sensitive to energy transfers commensurate with the energy of select dynamical modes, much of which remain poorly understood. Among these techniques, neutron spin echo (NSE) spectroscopy is sensitive to dynamical modes that take place over a range of length (∼1–100 nm) and time scales (∼1–1,000 ns), thus enabling studies of collective lipid dynamics and membrane fluctuations (Nagao, 2009). Similar to structural studies involving contrast variation, studies of membrane dynamics using NSE can similarly make use of contrast variation to tease out additional dynamic modes. Thus, the ability to adjust the contrast of specific chemical moieties within the membrane *via* deuteration enables different neutron scattering techniques to access structural and dynamical information that are not easily accessible by other commonly available methods.

In the first part of the review, studies that have made use of isotopic labeling to locate biomolecules, understand membrane asymmetry, and measure the bilayer thickness of the PM of a bacterium will be discussed. This will be followed by an overview of neutron contrast variation and how it has been applied to detect and understand nanoscopic lipid domains, including those in fully functioning bacteria. Later, a detailed description of the SDP model, whose derived structural parameters are widely used in different contexts, including to validate computer simulations of single component lipid bilayers will be presented. The review concludes with a summary of the NSE technique that was developed in the 1970s and is currently experiencing renewed interest in membrane research as a result of robust new models to analyze the experimental data.

2. NEUTRON CONTRAST VARIATION

One of the parameters used to quantify how neutrons interact with nuclei is the coherent scattering length, a_0, which is related to the scattering cross section *via* $\sigma \simeq 4\pi a_0^2$; this parameter also depends on the interactions between the neutron spin and nuclear spin of the scatterers. Thus, the scattering length is negative when the pseudopotential for the nuclear interaction is attractive and positive when repulsive. Of significance to biology, the neutron scattering lengths of protium and deuterium have opposite signs; specifically, protium has a scattering length of −3.74 fm, while that of deuterium is + 6.67 fm (Svergun et al.,

2013). Importantly, this difference in scattering length between the two stable isotopes of hydrogen can be used to great effect by altering the scattering contrast between the membrane and its surrounding, or locating biomolecules within the membrane through the use of deuterated analogs. However, some caution should be observed when making use of deuteration, as it can reduce lipid phase transition temperatures (Guard-Friar et al., 1985; Bryant et al., 2019) and adversely affect the viability of living organisms (Bild et al., 2004; Mosin and Ignatov, 2012). Nevertheless, when used methodically, deuteration is a powerful tool that can uncover unique structural and dynamical membrane features that can lead to new biological insights.

Because of the cost and limited availability of deuterated lipids, protiated lipids are commonly studied in the presence of D_2O, where the scattering length density for H_2O is -0.56×10^{-6} Å^2, while that of D_2O is $+6.35 \times 10^{-6}$ Å^2 (Clifton et al., 2013). Replacing H_2O by D_2O alters the contrast between the water and the membrane, with maximum contrast for a protiated membrane nominally achieved at 100% D_2O. In addition to deuterated water, other components, such as polymers, detergents, and osmolytes can be deuterated to impart maximum contrast between the various components (Naumann et al., 1994; Toppozini et al., 2012; Oliver et al., 2017). The ability to contrast match the coherent neutron scattering of specific molecules or moieties, by matching their scattering length densities to the scattering length density of the buffer in which they reside in distinguishes neutron scattering from other scattering methods, such as x-ray and light scattering. This "probe-free" feature of neutrons thus enables a wide range of physicochemical studies that are nominally not accessible to other techniques (Knoll et al., 1981; Kučerka et al., 2009a; Clifton et al., 2013; Oliver et al., 2017).

2.1. Cholesterol's Location in Membranes

Cholesterol is an essential biomolecule of animal cell membranes and is closely associated with functional lipid domains, commonly referred to as lipid rafts. Cholesterol is also known to modulate membrane structure by altering its fluidity, thickness, and water penetration (Yang et al., 2016), properties that are most likely associated with the location of the sterol in the membrane. Despite cholesterol's importance in biology, its location in membranes is not as simple as was once thought and, as a result, has been the subject of much recent research.

In 2001, Léonard et al., using 14:0 phosphatidylcholine (PC) multibilayer stacks and deuterated or protiated cholesterol, carried out neutron diffraction studies on aligned multibilayers that showed the sterol oriented in its nominal upright position with its hydroxyl group near the lipid-water interface (**Figure 1A**) (Léonard et al., 2001). The neutron diffraction results by Léonard et al. were supported by MD simulations that were used to reconstruct the one-dimensional neutron SDP that was then compared to the one obtained from experiment.

The neutron scattering studies by Léonard et al. (2001) were subsequently followed by several studies detailing the location of cholesterol in lipid bilayers with saturated and polyunsaturated fatty acid (PUFA) chains (Harroun et al., 2006, 2008; Marrink et al., 2008; Marquardt et al., 2016). In contrast to bilayers with saturated acyl chains, neutron scattering, nuclear magnetic resonance (NMR), and MD simulations found that the location of cholesterol can deviate from its upright orientation (**Figure 1A**), to one where the sterol snorkels toward the middle of the bilayer (**Figure 1B**). Specifically, the study by Marquardt et al. (2016) that made use of tail and head group deuterated cholesterol and a series of PC lipids with different acyl chain lengths and degrees of unsaturation determined that cholesterol reorients rapidly about the bilayer normal in all PC membranes studied. However, in bilayers with a very thin hydrophobic core (i.e., bilayers with short, saturated fatty acid chains and those with PUFA chains), the sterol is tilted and forced to span the bilayer midplane (**Figure 1B**). Marquardt et al. also noted that the highly disordered nature of PUFA chains allows them to interact differently with cholesterol than with other types of fatty acids. In general, neutron scattering techniques have provided vital insight on how lipid species can alter the location of cholesterol.

To add nuance to the location of cholesterol in membranes, neutron scattering experiments have also provided insight into cholesterol transport in membranes. For example, Garg et al. (2011) used time-resolved small-angle neutron scattering to observe intermembrane exchange and intramembrane flipping rates of cholesterol. They discovered that other techniques, which may use tags or other compounds to facilitate such measurements, can greatly accelerate cholesterol exchange and flipping rates. As a result of the different neutron scattering studies, we currently have a better understanding of the location of cholesterol in biological membranes, as well as its transport in them.

2.2. Biomolecular-Membrane Interactions

Neutron reflectometry (NR) is a powerful technique for determining the nanoscale structure of model membranes. For NR, membranes of interest are deposited either as bilayers or monolayers on solid substrates (e.g., single crystal Si) or as monolayers at the liquid–air interface. In contrast to scattering methods used to study powder or isotropic samples, NR makes use of a shallow incident beam to interact with the sample. The scattered intensity using NR geometry is then used to determine the one-dimensional SLD along the bilayer normal with nanoscale resolution. In the case of membranes, this includes membrane thickness, membrane asymmetry, and the location of molecules interacting with the membrane (Wong et al., 1999; Richter et al., 2006; Heinrich and Lösche, 2014; Heinrich, 2016; Campbell, 2018; Kurniawan et al., 2018). **Figure 2** is a schematic of such an experiment, where Soranzo et al. used NR to study the conformation of the hepatitis C virus p7 protein in a lipid membrane and its effect on membrane structure (Soranzo et al., 2017).

A recent highlight of NR's capability to shed light on biomolecular-membrane interaction involved α-synuclein, a protein whose function is currently unknown, but abnormal deposits of the protein are found in the brain. These protein deposits are associated with Lewy body dementia (LBD), a disease that can lead to changes in mood, behavior, and motor skills. Recently, Pfefferkorn et al. (2012) used NR and computer simulations to determine the depth at which α-synuclein resides

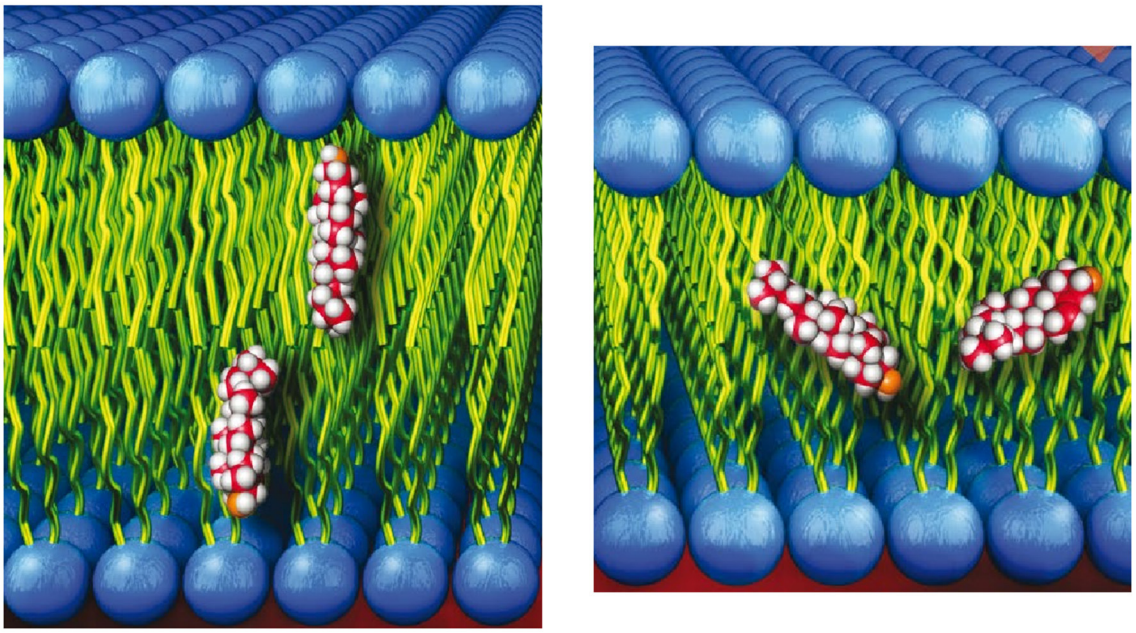

FIGURE 1 | (A) Cholesterol shown in its commonly accepted upright orientation with its hydroxyl group near the lipid-water interface. **(B)** Cholesterol shown spanning the bilayer leaflets of membranes with "thin" hydrophobic cores.

in lipid membranes and its associated membrane thinning effect. Further, Yap et al. (2015) studied glucocerebrosidase and α-synuclein interactions at the membrane surface using NR and fluorescence – it is believed that mutations of glucocerebrosidase increase the risk factors of Parkinson's disease. Using deuterated α-synuclein and protiated glucocerebrosidase, Yap et al. showed a large change in the membrane-bound structure of α-synuclein. Importantly, they proposed a model of α-synuclein and glucocerebrosidase for interacting at the membrane, where glucocerebrosidase is inhibited by α-synuclein, displacing glucocerebrosidase away from the membrane and perturbing the active site. In doing so, glucocerebrosidase alters the structure of α-synuclein, impacting its degradation. According to Yap et al. (2015), these events can lead to the development of Parkinson's disease. In another NR study, Jiang et al. (2017) used native chemical ligation and segmental deuteration to determine the regions of α-synuclein that bind to cellular membranes, and in 2019, Perissinotto combined NR, NSE, and atomic force microscopy to show that GM1 ganglioside can act as a membrane-binding mediator for α-synuclein (Perissinotto et al., 2019). The series of NR α-synuclein studies recounted in this review, is only one example among many demonstrating the impact that NR can have on membrane-related research of α-synuclein (Hellstrand et al., 2013; Jiang et al., 2015; Kaur and Lee, 2021).

Although α-synuclein was used as a primary example to highlight how NR can be used to elucidate biomolecular-membrane interactions, the utility of NR extends far beyond this protein. For example, NR has been used in the study of prions (Le Brun et al., 2014), synthetic peptides (Smith et al., 2010), Alzheimer's disease (Rondelli et al., 2016), toxins (Chenal et al., 2009; Wacklin et al., 2016; Sani et al., 2020), and ion channels (Holt et al., 2005, 2009; Rondelli et al., 2018). Of note, in the past decade, the field of biomolecular-membrane interactions has grown significantly, highlighting the utility of NR as an essential tool in the study of surface interactions in biology.

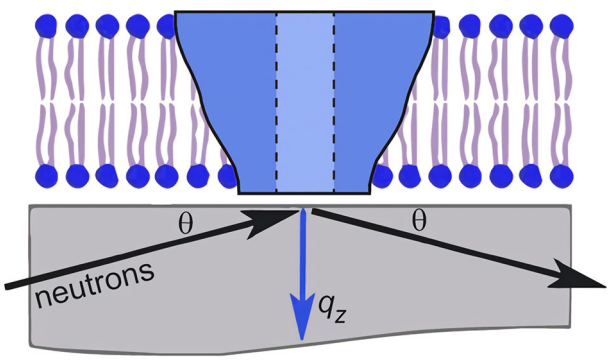

FIGURE 2 | Schematic of an neutron reflectometry (NR) experiment involving a single lipid bilayer with an integral protein adsorbed to a solid support (usually single crystal Si). An incident beam of neutrons is transmitted through the substrate and is reflected from the different interfaces of the sample. The scattering vector, q_z, is denoted by the blue arrow. The detection and analysis of the reflected beam allows for the determination of the one-dimensional SLD along the bilayer normal. Figure was adapted from Soranzo et al. (2017).

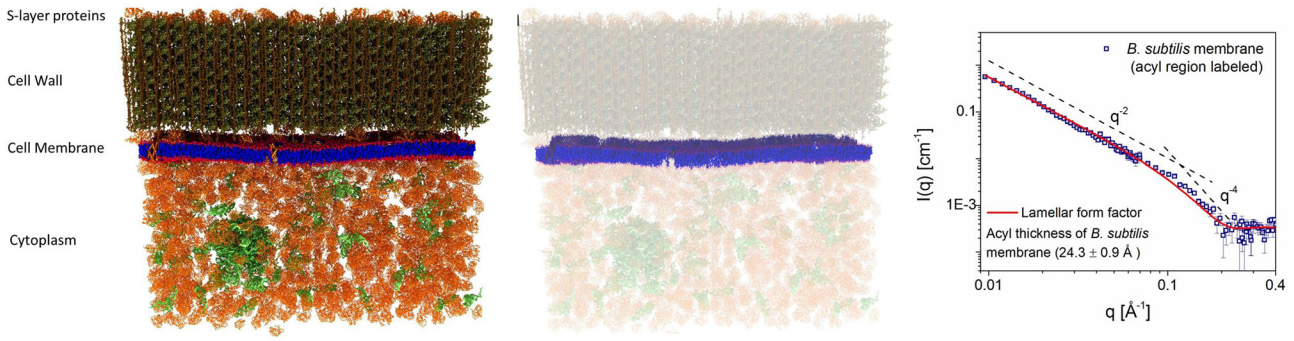

FIGURE 3 | (A) Schematics of the wild type *Bacillus subtilis* cell wall, membrane, and cytoplasm. **(B)** Bacteria grown in deuterated media, replacing its protium for deuterium, were fed protiated fatty acids to introduce neutron contrast. Under these conditions, the protium-labeled membrane is the only structure visible to neutrons when the bacteria were immersed in 85% heavy water (D_2O). **(C)** Small angle neutron scattering (SANS) data from the system in B were fitted using a lamellar form factor, resulting in an average hydrophobic membrane thickness of 24.3 ± 0.9 Å. Figure adapted from Nickels et al. (2017).

2.3. Membrane Hydrophobic Thickness of Viable Bacteria

Because of their inherent complexity, viable cells are rarely used to study their nanoscale structures and, for the most part, researchers rely on model systems to provide nanoscopic information to infer biological function. Nickels et al. (2017) used a novel approach to allow for the determination of detailed membrane structure in the Gram-positive bacterium, *Bacillus subtilis*. Through genetic and chemical manipulations, Nickels et al. were able to label the bacterium and its membrane independently with deuterium and protium, respectively, enabling them to determine the average hydrophobic thickness (24.3 ± 0.9 Å) of the bacterium's PM (**Figure 3**). Specifically, most of the protium of *B. subtilis* was replaced with deuterium, making the entire organism invisible to neutrons when immersed in ≈85% D_2O. With its fatty acid synthesis and degradation pathways shutdown, the bacteria were fed protiated fatty acids to introduce neutron contrast (**Figure 3B**) and were then subjected to experimentation. **Figure 3C** is the first direct SANS measurement of the hydrophobic thickness of a PM in a viable organism.

2.4. Plasma Membrane Asymmetry

It should not come as a surprise that biology has evolved to create membranes with great lipid diversity that impart to it remarkable functionality. In addition to being laterally heterogeneous (see page 6), the PM is also asymmetric. In other words, the lipids found in the inner and outer leaflets of the bilayer are chemically different (**Figure 4A**). However, many biophysical studies investigating the PM have not included this feature. Therefore, even though we have known that lipid diversity and lipid asymmetry are natural features of biological membranes (Verkleij et al., 1973), symmetric lipid bilayer systems have been used to study the physical properties of membranes. This is due, to a great extent, to the fact that the techniques needed to produce stable PM mimetics have proven to be difficult to implement and have produced mixed results.

Recently, a method was developed to reproducibly generate stable asymmetric unilamellar vesicles (aULVs) through the use of cyclodextrin carrier molecules (Cheng and London, 2009). Since the production of aULVs using this technique uses aggressive cyclodextrin and centrifugal filtration, possibly adversely affecting the membranes, Heberle et al. (2016) prepared isotopically asymmetric 16:0/18:1 PC (POPC) aULVs, where the 16:0 chain and headgroup of the lipid were deuterated, in order to determine any adverse effects to the membrane as a result of the method used to prepare them. From the fits to their SANS data, Heberle et al. determined that isotopically asymmetric POPC vesicles had the same bilayer thickness and area per lipid (AL) as symmetric POPC ULVs. In addition, again using deuterated lipids, they partially exchanged 16:0/16:0 PC (DPPC) into the outer bilayer leaflet of POPC ULVs, producing aULVs with chemical asymmetry. At 20°C, the outer bilayer leaflet was phase separated (i.e., gel DPPC and fluid POPC), while the POPC-rich inner leaflet was fluid (**Figure 4B**). Using this experimental approach, Heberle et al. (2016) were able to resolve structural details of the individual bilayer leaflets and discovered that the fluid POPC-rich was able to partially "fluidize" the gel-like outer leaflet, implying the presence of interleaflet coupling and the possibility that bilayer asymmetry may be an integral part of lateral membrane organization.

Following the studies by Heberle et al. (2016), additional neutron scattering studies have appeared reporting on membrane asymmetry. The asymmetric DPPC/POPC membrane system studied by Heberle et al. at 20°C was revisited by Eicher et al. (2017) They reported that, at 50°C, where both bilayer leaflets are in the fluid phase – above the melting transition of both lipids – there was no evidence of transbilayer coupling between the inner and outer bilayer leaflets. In other studies, membrane asymmetry was used to report on lipid flip-flop rates in pure lipid aULVs (Nguyen et al., 2019) and in aULVs with membrane associated peptides (Doktorova et al., 2019a; Nguyen et al., 2019). For example, in pure lipid systems the lipid flip-flop rates in a closed vesicle system were much slower than previously reported values

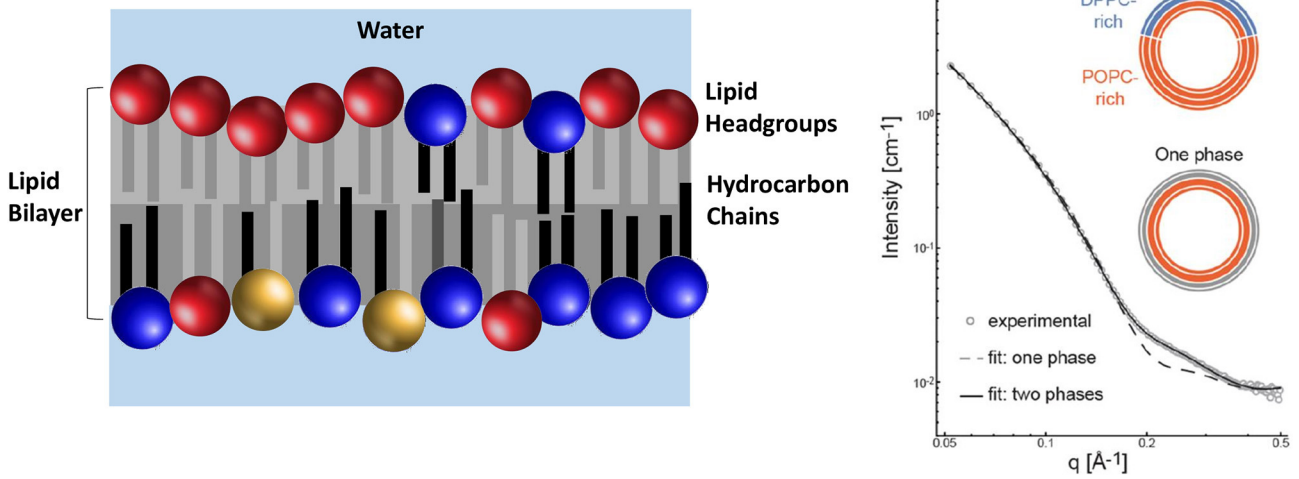

FIGURE 4 | The lipid composition of the PM is asymmetric with regard to the location of its chemically different lipid molecules. **(A)** The outer (upper) leaflet contains different lipid headgroups (primarily PC headgroups lipids shown in red) in relation to the inner (lower) leaflet (primarily blue and yellow depicting PE and PS headgroups, respectively). Additionally, the composition of the acyl chains between the two leaflets is also different. The outer leaflet has lipids with mostly saturated acyl chains (gray), whereas the inner leaflet lipids have acyl chains with different levels of unsaturation (black and light gray). **(B)** SANS data of aULVs where the outer leaflet contains 34 mol% of a rigid saturated lipid (DPPC) and the inner leaflet contains 98 mol% of a fluid state unsaturated lipid (POPC). The best fit to the data was obtained using a model that took in to account the presence of two lipid phases in the outer leaflet. Importantly, DPPC was found to be more fluid, compared to a pure DPPC bilayer, suggesting an interaction between the two bilayer leaflets. Adapted from Heberle et al. (2016).

from supported asymmetric bilayer systems (Liu and Conboy, 2005; Marquardt et al., 2017; Nguyen et al., 2019). Additionally, lipid flip-flop rates were shown to be influenced by the presence of methanol as well as, membrane peptides, suggesting that membrane defects are a contributing factor to lipid flip-flop (Doktorova et al., 2019a; Nguyen et al., 2019).

2.5. Detecting Lipid Domains in Model Membranes

The lateral organization of biological membranes seems to play a substantial role in biology and its existence has been debated since the unveiling of the fluid mosaic model in 1972 (Singer and Nicolson, 1972) – certainly since the development of the raft hypothesis (Simons and Ikonen, 1997; Kinnun et al., 2020). In fact, lipid domains have been implicated in membrane processes such as, vesicular transport, protein sorting, and cell signaling, to name just a few. Early on, it was determined that model membranes whose lipids were homogeneously distributed could be contrast matched, but those with inclusions or heterogeneities (e.g., domains) could not (Knoll et al., 1981). This is due to the fact that the domains have a different SLD than the bulk membrane in which they reside. However, by varying the percent D_2O to contrast match the bulk membrane, the domains become "visible" to neutrons and one can isolate their scattering signal. Taking this one step further by using a mixture of deuterated and protiated lipids that colocate within the membrane domain, a scattering signal with an improved signal-to-noise ratio can be obtained (Pencer et al., 2005; Masui et al., 2008).

This approach was demonstrated by Heberle et al. using a 60-nm diameter unilamellar ULVs composed of a four-component phase separating lipid mixture with fixed amounts of cholesterol and a chain deuterated phospholipid (DSPC), and varying amounts of monosaturated (POPC) and/or diunsaturated (DOPC) lipids (Heberle et al., 2013). Since the detection of domains requires that they have an SLD different from the coexisting bulk phase, chain deuterated DSPC was used. Using this approach, Heberle et al. were able to observe the presence of nanoscopic lipid domains whose size increased with increasing amounts of DOPC, as shown in **Figure 5**. Further, bilayer thickness mismatch between the domains and the bulk membrane also increased with the increasing domain size, in agreement with line tension, theories and the first experimental verification of said theories in free-floating bilayers. Moreover, the results by Heberle et al. suggested a mechanism by which the size of functional domains in homeothermic organisms may be regulated through changes in lipid composition. The experimental approach by Heberle et al. (2013) was subsequently extended by Nickels et al. to study the mechanical properties of membranes and their lipid domains by NSE (Nickels et al., 2015). Using a combination of deuterated lipids and different solvent deuteration schemes, Nickels et al. were able to highlight or mute the nanoscopic lipid domains populating 60 nm diameter ULVs.

2.6. Lipid Domains in Viable Bacteria

As mentioned in the previous section, because of their inherent complexity viable cells are rarely used in scattering studies of nanoscale membrane structures. As such, we have relied

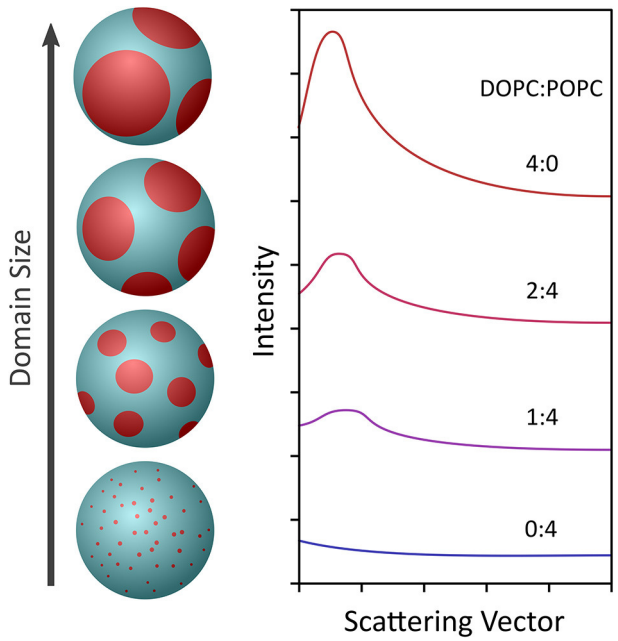

FIGURE 5 | Schematic showing the use of contrast variation to observe the formation of nanoscopic lipid domains in 60 nm diameter ULVs (left) made from a lipid composition (i.e., DSPC/DOPC/POPC/cholesterol) mimicking the outer leaflet of a mammalian PM. At a DOPC:POPC ratio of 0:4, the domains were extremely small, producing minimal scattering (right). However, as the amount of DOPC with respect to POPC increased, the domains grew larger and the scattering signal increased. The scattering data were fitted using Monte Carlo simulations, which gave an indication of the diameter and number of nanoscopic domains in a ULV of given lipid composition. Figure adapted from Heberle et al. (2013).

extensively on the use of model membrane systems to gain biological insights. However, model membranes are often simplified in composition and structure, and always lack the active processes found in cells. One of the pressing questions in cell biology is whether living cell membranes also exhibit nanoscopic lipid organization, i.e., lipid domains that are routinely observed in model membrane systems. It is now widely accepted that lipid domains are nanoscopic, as well as transient, making them difficult to detect experimentally (Mukherjee and Maxfield, 2004; Lingwood and Simons, 2010). *In vivo* membrane studies at lower resolution have provided details of lateral membrane structure, as well as important information pertaining to dynamic processes (Eggeling et al., 2009).

Recently, Nickels et al. (2017) were able to use genetic and chemical manipulations to label a live bacterium and its membrane with deuterium and protium, respectively, enabling them to determine the average hydrophobic thickness of the bacterium's PM (see **Figure 6**). Their next step was to determine whether or not lipid domains existed in *B. subtilis*' PM. Since they could not use the approach of Heberle et al. (2013), where the homogeneously mixed membranes at an elevated temperature were contrast matched to the solvent and their presence detected once the lipids phase separated at low temperature, Nickels et al. developed a novel approach of detecting lipid domains in a living organism.

The approach by Nickels et al. (2017) consisted of growing cells with two different ratios of anteiso 15:0 (a15:0) and normal 16:0 (n16:0) fatty acids, the only fatty acids present in the membrane of the genetically manipulated bacteria in protiated/deuterated ratios such that the two mixtures had, on average, the same scattering lengths and could be contrast matched to 85% D_2O. The "control" fatty acid mixture consisted of 15:0 (low melting) and n16:0 (high melting) fatty acids, each 30% protiated and 70% deuterated (**Figure 6A**). The SANS curve for this fatty acid mixture is shown in **Figure 6B**. The so-called "experimental" mixture contained the same fatty acids, but with an isotopic distribution for a15:0 of 40:60 protiated:deuterated, and 100% deuterated n16:0. Since the neutron scattering lengths of these two fatty acid mixtures are the same, and if the membranes lacked lateral heterogenity, the SANS patterns from both the control and experimental mixtures would be the same. However, as can be observed from **Figure 6B**, this was not the case, implying that the PM of *B. subtilis* is populated with lipid domains specifically, domains ranging in size between 3 and 40 nm (Nickels et al., 2017).

The observation of nanoscopic lipid domains in the PM of *B. subtilis* is consistent with the notion of lipid rafts. This experimental approach developed by Nickels et al. (2017) allows for a wide range of structural studies of the cell membrane (and possibly other classes of biomolecules) without the need for bulky extrinsic probes or labels. In this way, it fundamentally changes the scope of nanoscale structural questions that can be addressed in living organisms.

2.7. The SDP Model

A tenet in biology is that structure enables function. Structure–function relationships have arisen over the millennia through processes of natural selection and in order to understand how individual or ensembles of biomolecules function in biology, it is necessary to obtain accurate structural and dynamical data. In general, protein crystallography has resulted in excellent structures of predominantly water soluble proteins (Wiener and White, 1991a), but this holds less true for membranes and membrane associated proteins, partly because they are highly heterogeneous, disordered assemblies, whose structure–function relationships begin to emerge only with ensembles of hundreds of cooperating molecules and at length scales greater than about 10 nm (Wiener and White, 1991a; Nagle and Tristram-Nagle, 2000; Heberle et al., 2012). This generally makes membranes unsuitable for study by traditional structural biology methods (e.g., crystallography) that have revolutionized the study of water soluble proteins and nucleic acids.

Neutron scattering data has been analyzed using different models of the bilayer. The most basic of these models are the so-called strip models. In a strip model, the membrane is subdivided, not surprisingly, into strips of given SLD, with the simplest strip models treating the bilayer as one single strip of constant SLD (Knoll et al., 1981; Komura et al., 1982; Nawroth et al., 1989; Mason et al., 1999; Pencer and Hallett,

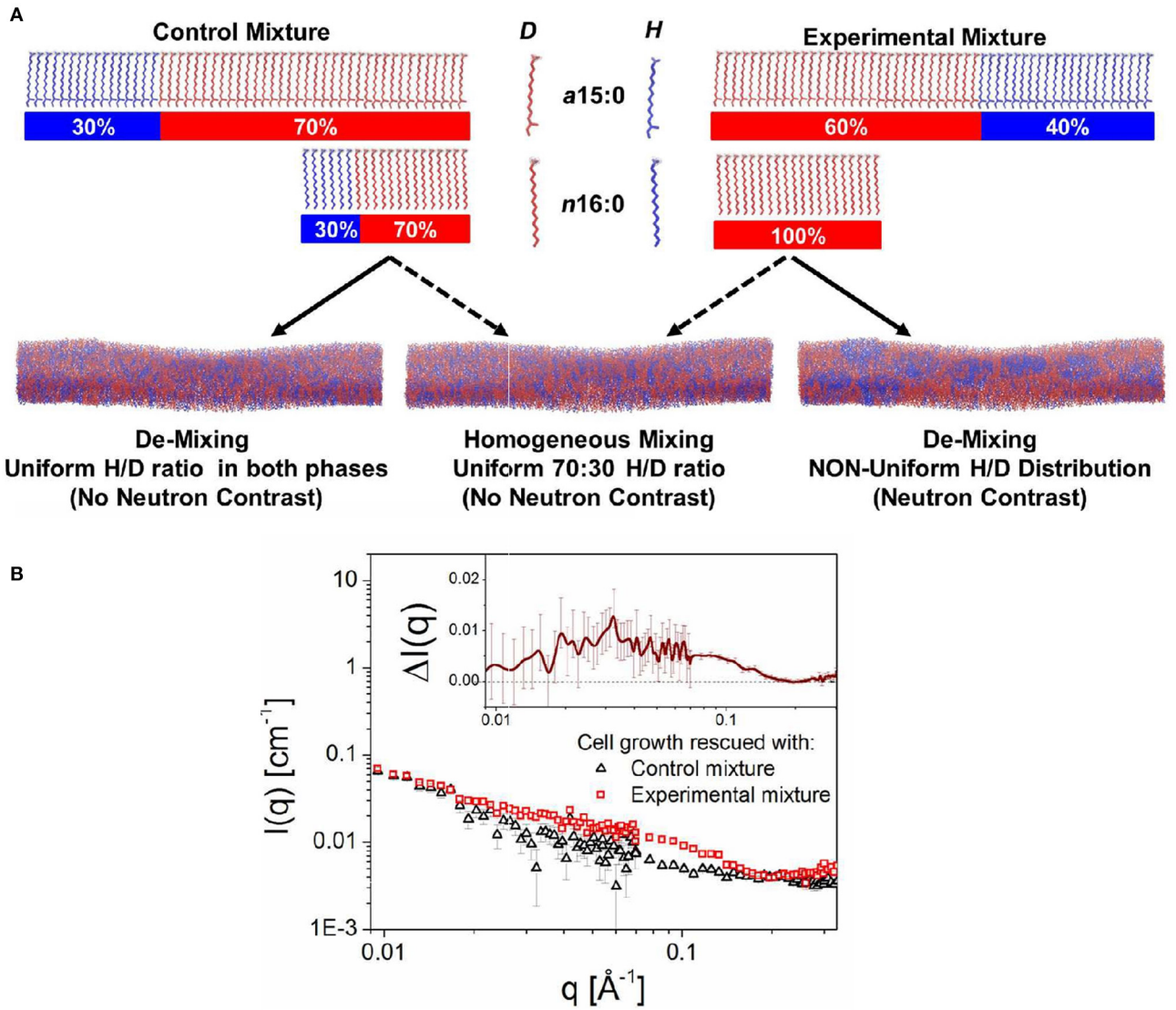

FIGURE 6 | Schematic showing the approach that was used to detect lipid domains in the PM of *B. subtilis*. The bacteria were genetically and chemically manipulated to contain only two fatty acids, namely the low temperature melting a15:0 and the high temperature melting n16:0. Note, that *B. subtilis* incorporates a15:0 at more than twice the amount of n16:0. **(A)** The control fatty acid mixture consisted of a15:0 and n16:0, each of ratio 30% protiated:70% deuterated. On the other hand, the experimental fatty acid mixture consisted of an isotopic distribution of 40:60 protiated:deuterated for a15:0 and 100% deuteration for n16:0. **(B)** Scattering curves from bacteria with control and experimental fatty acid mixtures. The excess scattering is shown in the inset to the figure. Figure adapted from Nickels et al. (2017).

2000). Refinements include additional strips with different SLDs (Balgavỳ et al., 2001; Schmiedel et al., 2001). Strips can represent, for example, lipid headgroups, hydrocarbon chains, and acyl chain terminal methyl groups. Additional geometric considerations, such as bilayer asymmetry not only improve the fits to the data but can also introduce a problem namely, that the system cannot have more parameters than observations or the system becomes over parameterized (Kučerka et al., 2004). However, this problem can be mitigated when different neutron contrast scattering data are combined with x-ray scattering – providing yet another contrast – and MD simulations.

Besides strip or slab models (King and White, 1986; Kučerka et al., 2004; Kiselev et al., 2006; Pencer et al., 2006), other models used over the years to analyze the structure of membranes and their individual lipid molecules were so-called Gaussian models (Kučerka et al., 2004, 2007; Kiselev et al., 2006; Pencer et al., 2006) and hybrid models (combination of Gaussian and strip/slab models) (Wiener et al., 1989). However, all these methods had one thing in common, an inability to jointly analyze different contrast data sets. Since neutrons are inherently sensitive to regions of the lipid membrane lacking in naturally abundant hydrogen (i.e., acyl chain carbonyl groups) and x-rays are uniquely sensitive to regions of high electron density (e.g.,

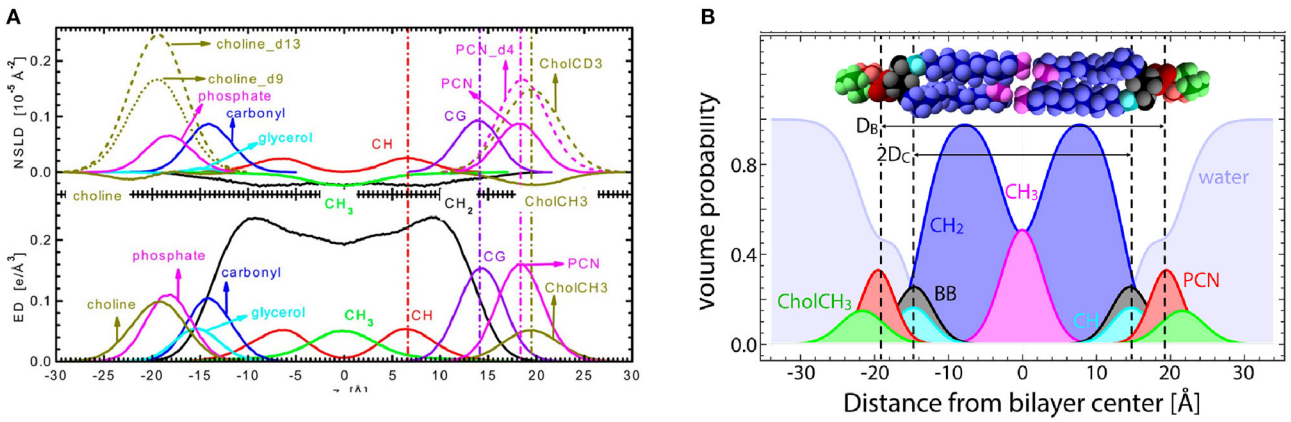

FIGURE 7 | The SDP model. **(A)** Neutron SLD (NSLD) and electron density (ED) profiles obtained from MD simulations as a function of distance (z) along the bilayer normal of a PC bilayer. The left-hand side of the panel shows the individual components of a PC lipid molecule, whereas the right-hand side shows the appropriately parsed component groups. Dashed vertical lines indicate the peak location in the NSLD (upper) and ED (lower) profiles. For the parsing scheme used in the SDP model, component grouping peak profiles align for both NSLD and ED profiles, even when certain component groups are deuterated, as is often done in neutron scattering. **(B)** Volume probability distributions for the parsed component groups as a function of z along the bilayer normal used in the structural determination of sphingomyelin bilayers. Volume probability distributions are used to model raw scattering form factors by calculating ED or NSLD profiles and then Fourier transforming them to fit the raw scattering data. Figure was adapted from Kučerka et al. (2008) and Doktorova et al. (2020a).

the phosphate groups in lipid head groups), having the ability to jointly analyze both types of different contrast data with a single model greatly increases the robustness of the proposed structural solution (Wiener and White, 1992). To address this problem, Wiener and White developed the composition space model (CSM) that enabled, for the first time, the joint analysis of neutron and x-ray lipid bilayer datasets (Wiener and White, 1991b).

CSM was based on the approach, initially developed by King and White, invoking a quasimolecular model, where the different moieties of a lipid molecule are described by Gaussians, thereby reducing the amount of parameters needed to accurately model the membrane (King and White, 1986). CSM was expanded on the model of King and White by including x-ray data to the neutron data, thus increasing the number of observations relative to the number of parameters used in the model – as mentioned, membranes are inherently under determined systems. In the CSM method of analysis, this inclusion was achieved by devising a parsing scheme for the lipid molecule that aligned the neutron and x-ray centers-of-scattering using atomic coordinates from lipid crystal structures projected onto the bilayer normal (Wiener and White, 1991b). Once the parsing scheme is defined, the modeling is carried out by scaling the time-averaged distributions of the different Gaussians describing the bilayer, using either neutron or x-ray scattering lengths, eventually giving rise to membrane structural parameters (Wiener and White, 1991b). Although this approach was highly successful, there were also drawbacks. First, the parsing scheme was, for the most part, based on trial and error (Wiener and White, 1991b, 1992). Second, CSM made use of structure factors from aligned membrane stacks hydrated to only 66% relative humidity (RH), a level of hydration that led to better quality data, as membranes are more ordered when not fully hydrated, thus resulting in more orders of Bragg diffraction, i.e., higher resolution data (Wiener and White, 1992). Third, and as pointed out by Armen et al. (1998), CSM allowed for RMS variability in the local volume of 7%.

Kučerka et al. (2008) introduced the SDP model that made use of continuous form factors obtained from small angle scattering experiments. In a similar spirit, Shekhar et al. (2011) developed the continuous distribution model that utilized error functions as opposed to Gaussian distributions in 2011. The SDP model relies on the use of different contrast neutron and x-ray data from ULVs under physiologically relevant conditions (i.e., vesicles in bulk water, a condition that is equivalent to hydration under 100% RH conditions) (Katsaras, 1997, 1998). Importantly, and in contrast to CSM, MD simulations were used to optimize the parsing of lipid molecules, an integral and novel part of the SDP model. In addition, SLDs were obtained by scaling the volume distributions of the individual lipid moieties with the appropriate neutron or x-ray scattering lengths (**Figure 7**) (Kučerka et al., 2008). The SDP also allowed for water to penetrate any voids in the bilayer, such that the volume probability distributions along the bilayer normal always added up to unity.

Although the data from ULVs does not extend as far out in reciprocal space as data from aligned multibilayer lipid stacks, the combined use of lipid parsing schemes determined by MD simulations, the inclusion of independent volumetric data, the notion of volume probability distributions, and the use of fully hydrated samples with different contrast data have enabled SDP to consistently produce robust structural results. For example, one of the most important lipid bilayer structural parameters is area per lipid (AL). AL is used to understand bilayer structure and gain insights into lipid–lipid and lipid–protein interactions (Wiener and White, 1992; Kučerka et al., 2008). Moreover, AL allows for comparisons between different lipid types and is central to MD simulations. In fact, MD force fields are considered

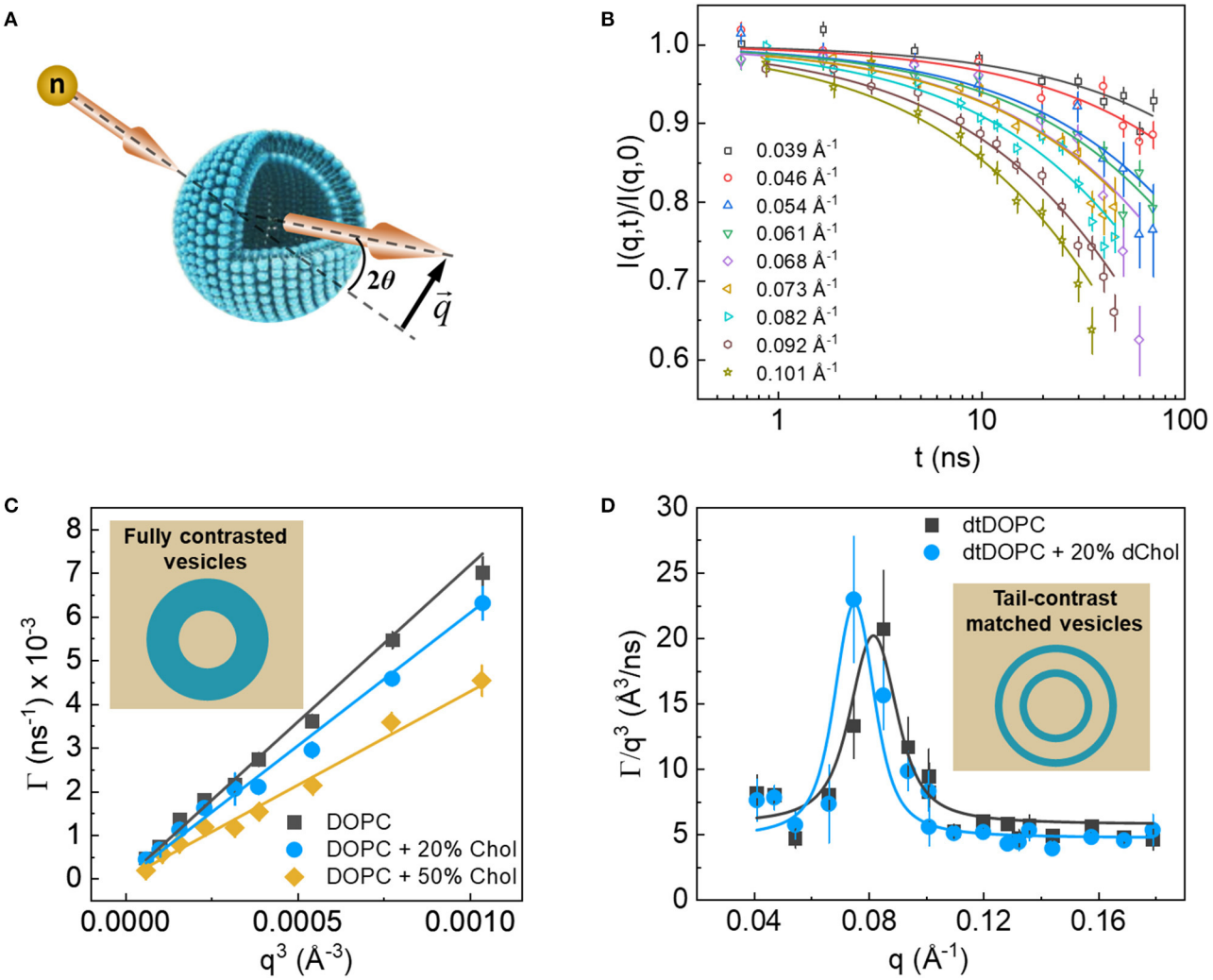

FIGURE 8 | (A) Schematic of the scattering geometry used in NSE experiments. **(B)** Example of the NSE intermediate dynamic structure factors resulting from ULVs. **(C)** Plot of the q^3 dependence of fluctuation decay rates of protiated membranes in D_2O (inset), where shallower slopes indicate stiffer membranes according to the Zilman-Granek theory. **(D)** Excess dynamics, typical of thickness fluctuation signals from tail contrast matched membranes (inset). Data are adapted from Chakraborty et al. (Figures 2, 5).

to be accurate if they are able to reproduce experimentally determined lipid areas. ALs derived from SDP model analysis are now widely used to validate experimental approaches, including MD force fields (Lee et al., 2014; Doktorova et al., 2017; Grote and Lyubartsev, 2020).

To date, the SDP model has been successfully used to determine the structure of different membranes, including PC (Kučerka et al., 2008, 2009b, 2011; Marquardt et al., 2020), phosphatidylglycerol (PG) (Kučerka et al., 2012; Pan et al., 2014a), PS (Pan et al., 2014b), PE (Kučerka et al., 2015), and sphingomyelin (Doktorova et al., 2020b) lipids. Many of these studies focused on a single head group species, while sweeping through different acyl chains (both in length and degree of unsaturation). From these studies, the idea that lipid head groups control lipid packing, while the acyl chains dictate the response to changes in temperature, has been, for the most part, validated (Kučerka et al., 2015). Additionally, it has been shown that exchangeable hydrogens should be taken into consideration as they can alter the overall scattering signal (Pan et al., 2014a). One clear conclusion from the development of the SDP model is that the understanding of the structure of individual lipid molecules has been both changed and enhanced since its development. As more structures are determined, they will enable us to better understand the structure–function relationship in cellular membranes.

3. NEUTRON SPIN ECHO

Neutron spin echo spectroscopy (**Figure 8A**) offers a unique approach for direct quantitative measurements of collective membrane dynamics over length (∼100 nm) and time (∼1–1,000 ns) scales corresponding to key membrane processes,

including membrane trafficking, viral budding, tubulation, and vesiculation (Reynwar et al., 2007; Tian et al., 2009; Bradley and Radhakrishnan, 2016). These length and time scales also correspond with the conformational dynamics of membrane proteins (Perozo et al., 2002; Henzler-Wildman and Kern, 2007), making NSE well-suited for studies of protein/membrane interactions and understanding the role of membrane dynamics in regulating protein function and spatiotemporal signaling. Indeed, NSE studies on lipid membranes over the last few years have provided remarkable insights into the fundamental biophysical laws that govern nanoscopic membrane dynamics as well as, the interaction of membranes with inclusions and with their surrounding environment.

To date, the majority of NSE studies target membrane bending properties using protiated ULVs in D_2O, thus taking advantage of the amplified contrast between the membrane and its deuterated surrounding. NSE detects these fluctuations in the form of decays in the intermediate dynamic structure factor, $I(q,t)/I(q,0)$, as a function of the Fourier time, t (**Figure 8B**). The obtained signals are generally interpreted using the elastic sheet model with a stretched exponential function (Helfrich, 1973): $I(q,t)/I(q,0) = \exp -(\Gamma(q)t)^{\frac{2}{3}}$, yielding the q-dependent decay rates, $\Gamma(q)$, of the measured fluctuations. In NSE measurements of bending fluctuations, $\Gamma(q)$ typically exhibits a q^3 dependence (**Figure 8C**), as predicted by Zilman and Granek for thermally undulating elastic thin sheets, such that (Zilman and Granek, 1996):

$$\Gamma(q)_{bend}(q) = 0.025\alpha \frac{k_B T}{\eta_{sol}} \sqrt{\frac{k_B T}{\tilde{\kappa}}} q^3, \tag{1}$$

where $k_B T$ is the thermal energy, η_{sol} is the solvent viscosity, and α is a parameter that results from angular averaging of $\vec{q}$ relative to the membrane normal. Such theoretical analysis of NSE data enables direct calculations of an important membrane property, i.e., the effective bending rigidity modulus, $\tilde{\kappa}$. With these powerful capabilities in mind, NSE has become an important neutron scattering tool to answer questions related to membrane dynamics.

In recent years, NSE has been used to a great effect to measure the bending moduli of lipid membranes with various degrees of complexity, ranging from single component to multi-component lipid membranes that more closely resemble biological cell membranes. For instance, bending rigidity measurements of membranes comprised of lipids with different acyl chain lengths and unsaturations (Yi et al., 2009; Brüning et al., 2014; Nagao et al., 2017) have provided important insights into how the physicochemical properties of the membrane affect its mechanical properties when paired with structural information, such as membrane thickness or molecular packing, as discussed earlier (Kučerka et al., 2009b). Collectively, these measurements can shed new light on membrane structure-property relations and how they influence membrane function. This topic was recently explored in two NSE studies on cholesterol-rich lipid membranes by Chakraborty et al. (2020) and on binary lipid membranes with hydrophobic lipid mismatch by Kelley et al. (2020) Both studies found strong evidence that membrane mechanics scale with the AL, emphasizing the strong interdependence of the structural and dynamical properties in lipid membranes.

Notably, using NSE Chakraborty et al. (2020) resolved a long debated question about the role of cholesterol in membrane mechanics, one that has far-reaching implications with regard to membrane function. They discovered that cholesterol has a non-trivial local stiffening effect on membranes with unsaturated lipids commonly found in cell membranes (Chakraborty et al., 2020). Their results showed that on the collective molecular level (i.e., small molecular assemblies), membrane mechanics scale with cholesterol-induced "densification" of the membrane, as can be deduced from membrane structure-property relations. However, these conclusions contradicted previous studies reporting null mechanical effects of cholesterol in unsaturated lipid membranes when measured over extended spatial and temporal scales (Pan et al., 2009; Gracia et al., 2010), suggesting the presence of scale-dependent membrane dynamics. This notion of dynamical hierarchy in membranes is not surprising or new, but is experimentally challenging due to the difficulty in reconciling dynamics over very different length scales (ranging from molecular to macroscopic length scales). NSE thus offers great potential in bridging these two length scales through direct experimental observations of membrane dynamics that are intermediate between molecular motions and continuum deformations.

Other applications of NSE spectroscopy include studies involving changes in membrane bending rigidity in response to additive molecules, such as trehalose (Brüning et al., 2014), melittin (Sharma et al., 2015; Sharma and Qian, 2019), and inorganic nanoparticles used in drug delivery (Chakraborty et al., 2018). These studies provide a nanoscale perspective of how small molecules could affect the softening or stiffening of lipid membranes under biologically relevant conditions and in targeted applications. NSE has also been used to interrogate the mechanical response of membranes to environmental conditions, including temperature (Brüning et al., 2014), pH (Boggara et al., 2010), and the presence of surrounding macromolecules (Yu et al., 2020). As a result, this body of experiments is now starting to shape our understanding of how membranes respond to external cues that mimic the different conditions experienced by cell membranes, a current area of research.

Other applications of NSE involve the utilization of neutron isotope sensitivity to investigate the dynamics of selective features within lipid membranes. For example, Rickeard et al. (2020) used asymmetric lipid membranes with one of their bilayer leaflets selectively deuterated to investigate the effect of asymmetry and leaflet coupling on membrane bending fluctuations. Surprisingly, they found that asymmetric membranes possessed a larger bending modulus than symmetric bilayers with the same average lipid composition, a result that was uniquely enabled by NSE. In an earlier study, Nickels et al. (2015) used a combination of protiated and deuterated lipids to generate lateral contrast within domain-forming lipid membranes in order to study the mechanical properties of the nanoscopic lipid domains populating 60-nm diameter ULVs (**Figure 9**). By adjusting the percent D_2O, they were able to perform NSE measurements

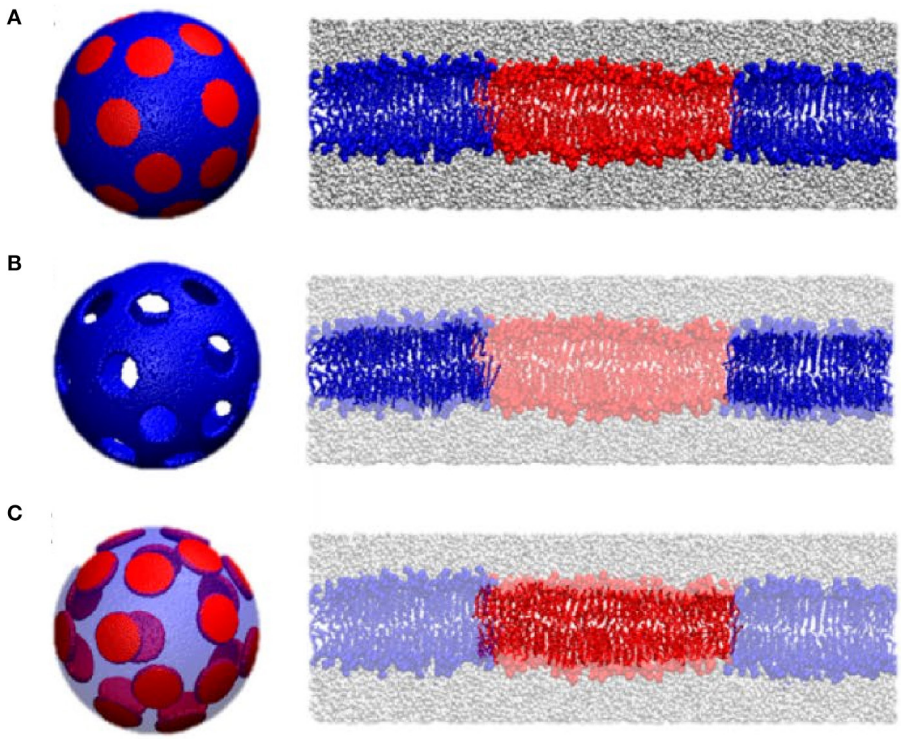

FIGURE 9 | Contrast matching used to study the mechanical properties of lipid domains in 60 nm diameter ULV model membranes. Three contrast matching schemes were used to change the neutrons sensitivity of lipid domains in model membranes. They were: **(A)** no contrast matching, where the entire ULV is visible to neutrons; **(B)** domains contrast matched to the solvent in order to highlight the surrounding membrane; and **(C)** the membrane is contrast matched to the solvent highlighting the nanodomains; Transparent colors indicate contrast matching to the solvent using these three different contrast matching schemes. Figure adapted from Nickels et al. (2015).

targeting the nanoscopic lipid heterogeneities in ULVs in order to study their bending rigidity.

Isotope labeling has also been used in NSE experiments to access thickness fluctuations in lipid membranes by using tail-deuterated membranes, such that the acyl chain region of the membrane matches the SLD of the solvent or buffer. This fluctuation mode has long been predicted but was only recently observed experimentally with NSE (Nagao, 2009; Woodka et al., 2012), where thickness fluctuations manifest themselves as enhanced dynamics in addition to the bending fluctuations (**Figure 8D**). The dynamics are most pronounced at q-values that correspond to the membrane thickness, as was recently verified by coarse-grained MD simulations (Carrillo et al., 2017). Analysis of this dynamic mode using an approach developed by Nagao et al. (2017) and based on the theoretical framework of membrane fluctuations by Bingham et al. (2015) has enabled the extraction of other biophysical membrane parameters namely, membrane viscosity. With these recent advances, NSE is rapidly becoming the tool of choice when it comes to understanding membrane dynamics and gaining new biophysical insights.

4. CONCLUDING REMARKS

Although much research has been focused at addressing the structure–function relationship of biological membranes, there are many open questions that remain. Nevertheless, what has become clear over the last 10 years, or so, is that neutron scattering techniques are invaluable tools in studies of biological or biologically relevant membranes. Neutron scattering techniques offer a range of capabilities, some of which are unique to them. For instance, the ability to easily alter the neutron contrast of the sample enabled Heberle et. al. to study nanoscopic lipid domains and relate thickness mismatch between the domains and their surrounding to line tension theories (Heberle et al., 2013). This approach by Heberle et al. was then extended by Nickels et al. to separately study the bending rigidities of the lipid domains populating the membrane and their surrounding lipids using NSE (Nickels et al., 2015).

The ability to reconcile different contrast x-ray and neutron scattering data using a single model was addressed by the CSM approach of Wiener and White (1991b). However, it took almost 20 years to develop an approach whereby, multiple sets of different contrast data were fitted using a robust model guided by MD simulations (Kučerka et al., 2008). Importantly, the approach by Kučerka et al. made use of fully hydrated ULVs, model systems that are considered excellent mimics of the PM.

Neutron spin echo, a technique capable of interrogating membrane dynamics over spatial and temporal scales relevant to critical biological functions is rapidly becoming the technique of choice when it comes to measuring the mechanical properties of membranes. Combined with different deuteration strategies,

NSE enables non-invasive measurements of collective membrane dynamics that would otherwise be challenging to explore using traditional spectroscopic methods. When combined with MD simulations, which are sensitive to similar length and time scales as NSE, a molecular level understanding of the different components making up membranes can be achieved (Nickels et al., 2015; Chakraborty et al., 2020). Moreover, NSE studies combined with SDP analysis can be used to further refine the currently used MD force fields and aid in the development of new experimental and computational approaches (Doktorova et al., 2019b).

In summary, we envision the different neutron scattering techniques playing leading roles in understanding the static and dynamic structures of membranes. When combined with MD simulations, neutron scattering techniques offer the possibility of providing unique insights into individual molecules making up membranes and micrometer patches of membrane comprised of thousands of individual molecules. Complementary dynamic studies will range from picoseconds to tens of microseconds. In particular, NSE data analysis is still in its infancy, and developing new physical models to interpret the data will enable NSE to become a mainstream technique. Finally, in order to make neutron scattering more relevant to biologists, it needs to expand, with greater frequency, into the study of fully functioning biological systems, similar to the one reported by Nickels et al. (2017).

AUTHOR CONTRIBUTIONS

JJK, HLS, RA, and JK wrote the manuscript. All authors contributed to the article and approved the submitted version.

FUNDING

JJK was supported through the Scientific User Facilities Division of the Department of Energy (DOE) Office of Science, sponsored by the Basic Energy Science (BES) Program, DOE Office of Science, under Contract No. DEAC05-00OR22725. Oak Ridge National Lab's Center for Structural Molecular Biology was funded by the DOE Office of Biological and Environmental Research, using facilities supported by the Scientific User Facilities Division, Office of Basic Energy Sciences, U.S. Department of Energy.

ACKNOWLEDGMENTS

RA acknowledges support from the Ralph E. Powe Junior Faculty Enhancement Program.

REFERENCES

Armen, R. S., Uitto, O. D., and Feller, S. E. (1998). Phospholipid component volumes: determination and application to bilayer structure calculations. *Biophys. J.* 75, 734–744. doi: 10.1016/S0006-3495(98)77563-0

Balgavỳ, P., Dubničková, M., Kučerka, N., Kiselev, M. A., Yaradaikin, S. P., and Uhrıková, D. (2001). Bilayer thickness and lipid interface area in unilamellar extruded 1, 2-diacylphosphatidylcholine liposomes: a small-angle neutron scattering study. *Biochim. Biophys. Acta Biomembr.* 1512, 40–52. doi: 10.1016/S0005-2736(01)00298-X

Bild, W., Năstasă, V., and Haulică, I. (2004). *In vivo* and *in vitro* research on the biological effects of deuterium-depleted water: 1. Influence of deuterium-depleted water on cultured cell growth. *Rom. J. Physiol.* 41, 53–67.

Bingham, R., Smye, S., and Olmsted, P. (2015). Dynamics of an asymmetric bilayer lipid membrane in a viscous solvent. *Europhys. Lett.* 111:18004. doi: 10.1209/0295-5075/111/18004

Boggara, M. B., Faraone, A., and Krishnamoorti, R. (2010). Effect of pH and ibuprofen on the phospholipid bilayer bending modulus. *J. Phys. Chem. B* 114, 8061–8066. doi: 10.1021/jp100494n

Bradley, R. P., and Radhakrishnan, R. (2016). Curvature–undulation coupling as a basis for curvature sensing and generation in bilayer membranes. *Proc. Natl. Acad. Sci. U.S.A.* 113, E5117–E5124. doi: 10.1073/pnas.1605259113

Brüning, B. A., Prevost, S., Stehle, R., Steitz, R., Falus, P., Farago, B., et al. (2014). Bilayer undulation dynamics in unilamellar phospholipid vesicles: effect of temperature, cholesterol and trehalose. *Biochim. Biophys. Acta Biomembr.* 1838, 2412–2419. doi: 10.1016/j.bbamem.2014.06.006

Bryant, G., Taylor, M. B., Darwish, T. A., Krause-Heuer, A. M., Kent, B., and Garvey, C. J. (2019). Effect of deuteration on the phase behaviour and structure of lamellar phases of phosphatidylcholines–deuterated lipids as proxies for the physical properties of native bilayers. *Colloids Surf. B Biointerfaces* 177, 196–203. doi: 10.1016/j.colsurfb.2019.01.040

Campbell, R. A. (2018). Recent advances in resolving kinetic and dynamic processes at the air/water interface using specular neutron reflectometry. *Curr. Opin. Colloid Interface Sci.* 37, 49–60. doi: 10.1016/j.cocis.2018.06.002

Carrillo, J. M. Y., Katsaras, J., Sumpter, B. G., and Ashkar, R. (2017). A computational approach for modeling neutron scattering data from lipid bilayers. *J. Chem. Theory Comput.* 13, 916–925. doi: 10.1021/acs.jctc.6b00968

Chakraborty, S., Abbasi, A., Bothun, G. D., Nagao, M., and Kitchens, C. L. (2018). Phospholipid bilayer softening due to hydrophobic gold nanoparticle inclusions. *Langmuir* 34, 13416–13425. doi: 10.1021/acs.langmuir.8b02553

Chakraborty, S., Doktorova, M., Molugu, T. R., Heberle, F. A., Scott, H. L., Dzikovski, B., et al. (2020). How cholesterol stiffens unsaturated lipid membranes. *Proc. Natl. Acad. Sci. U.S.A.* 117, 21896–21905. doi: 10.1073/pnas.2004807117

Chenal, A., Prongidi-Fix, L., Perier, A., Aisenbrey, C., Vernier, G., Lambotte, S., et al. (2009). Deciphering membrane insertion of the diphtheria toxin T domain by specular neutron reflectometry and solid-state NMR spectroscopy. *J. Mol. Biol.* 391, 872–883. doi: 10.1016/j.jmb.2009.06.061

Cheng, H. T., and London, E. (2009). Preparation and properties of asymmetric vesicles that mimic cell membranes effect upon lipid raft formation and transmembrane helix orientation. *J. Biol. Chem.* 284, 6079–6092. doi: 10.1074/jbc.M806077200

Clifton, L. A., Neylon, C., and Lakey, J. H. (2013). Examining protein-lipid complexes using neutron scattering. *Methods Mol. Biol.* 974, 119–150. doi: 10.1007/978-1-62703-275-9_7

Doktorova, M., Harries, D., and Khelashvili, G. (2017). Determination of bending rigidity and tilt modulus of lipid membranes from real-space fluctuation analysis of molecular dynamics simulations. *Phys. Chem. Chem. Phys.* 19, 16806–16818. doi: 10.1039/C7CP01921A

Doktorova, M., Heberle, F. A., Marquardt, D., Rusinova, R., Sanford, R. L., Peyear, T. A., et al. (2019a). Gramicidin increases lipid flip-flop in symmetric and asymmetric lipid vesicles. *Biophys. J.* 116, 860–873. doi: 10.1016/j.bpj.2019.01.016

Doktorova, M., Kučerka, N., Kinnun, J. J., Pan, J., Marquardt, D., Scott, H. L., et al. (2020b). Molecular structure of sphingomyelin in fluid phase bilayers determined by the joint analysis of small-angle neutron and X-ray scattering data. *J. Phys. Chem. B* 124, 5186–5200. doi: 10.1021/acs.jpcb.0c03389

Doktorova, M., LeVine, M. V., Khelashvili, G., and Weinstein, H. (2019b). A new computational method for membrane compressibility: bilayer mechanical thickness revisited. *Biophys. J.* 116, 487–502. doi: 10.1016/j.bpj.2018.12.016

Doktorova, M., Symons, J. L., and Levental, I. (2020a). Structural and functional consequences of reversible lipid asymmetry in living membranes. *Nat. Chem. Biol.* 16, 1321–1330. doi: 10.1038/s41589-020-00688-0

Eggeling, C., Ringemann, C., Medda, R., Schwarzmann, G., Sandhoff, K., Polyakova, S., et al. (2009). Direct observation of the nanoscale dynamics of membrane lipids in a living cell. *Nature* 457, 1159–1162. doi: 10.1038/nature07596

Eicher, B., Heberle, F. A., Marquardt, D., Rechberger, G. N., Katsaras, J., and Pabst, G. (2017). Joint small-angle X-ray and neutron scattering data analysis of asymmetric lipid vesicles. *J. Appl. Crystallogr.* 50, 419–429. doi: 10.1107/S1600576717000656

Fitter, J., Lechner, R., and Dencher, N. (1999). Interactions of hydration water and biological membranes studied by neutron scattering. *J. Phys. Chem. B* 103, 8036–8050. doi: 10.1021/jp9912410

Garg, S., Porcar, L., Woodka, A., Butler, P., and Perez-Salas, U. (2011). Noninvasive neutron scattering measurements reveal slower cholesterol transport in model lipid membranes. *Biophys. J.* 101, 370–377. doi: 10.1016/j.bpj.2011.06.014

Gracia, R. S., Bezlyepkina, N., Knorr, R. L., Lipowsky, R., and Dimova, R. (2010). Effect of cholesterol on the rigidity of saturated and unsaturated membranes: fluctuation and electrodeformation analysis of giant vesicles. *Soft Matter* 6, 1472–1482. doi: 10.1039/b920629a

Grote, F., and Lyubartsev, A. P. (2020). Optimization of slipids force field parameters describing headgroups of phospholipids. *J. Phys. Chem. B* 124, 8784–8793. doi: 10.1021/acs.jpcb.0c06386

Guard-Friar, D., Chen, C. H., and Engle, A. S. (1985). Deuterium isotope effect on the stability of molecules: phospholipids. *J. Phys. Chem.* 89, 1810–1813. doi: 10.1021/j100255a054

Harroun, T. A., Katsaras, J., and Wassall, S. R. (2006). Cholesterol hydroxyl group is found to reside in the center of a polyunsaturated lipid membrane. *Biochemistry* 45, 1227–1233. doi: 10.1021/bi0520840

Harroun, T. A., Katsaras, J., and Wassall, S. R. (2008). Cholesterol is found to reside in the center of a polyunsaturated lipid membrane. *Biochemistry* 47, 7090–7096. doi: 10.1021/bi800123b

Heberle, F. A., Marquardt, D., Doktorova, M., Geier, B., Standaert, R. F., Heftberger, P., et al. (2016). Subnanometer structure of an asymmetric model membrane: interleaflet coupling influences domain properties. *Langmuir* 32, 5195–5200. doi: 10.1021/acs.langmuir.5b04562

Heberle, F. A., Pan, J., Standaert, R. F., Drazba, P., Kučerka, N., and Katsaras, J. (2012). Model-based approaches for the determination of lipid bilayer structure from small-angle neutron and X-ray scattering data. *Eur. Biophys. J.* 41, 875–890. doi: 10.1007/s00249-012-0817-5

Heberle, F. A., Petruzielo, R. S., Pan, J., Drazba, P., Kučerka, N., Standaert, R. F., et al. (2013). Bilayer thickness mismatch controls domain size in model membranes. *J. Am. Chem. Soc.* 135, 6853–6859. doi: 10.1021/ja3113615

Heinrich, F. (2016). Deuteration in biological neutron reflectometry. *Methods Enzymol.* 566, 211–230. doi: 10.1016/bs.mie.2015.05.019

Heinrich, F., and Lösche, M. (2014). Zooming in on disordered systems: neutron reflection studies of proteins associated with fluid membranes. *Biochim. Biophys. Acta Biomembr.* 1838, 2341–2349. doi: 10.1016/j.bbamem.2014.03.007

Helfrich, W. (1973). Elastic properties of lipid bilayers: theory and possible experiments. *Z. Naturforsch. C* 28, 693–703. doi: 10.1515/znc-1973-11-1209

Hellstrand, E., Grey, M., Ainalem, M. L., Ankner, J., Forsyth, V. T., Fragneto, G., et al. (2013). Adsorption of α-synuclein to supported lipid bilayers: positioning and role of electrostatics. *ACS Chem. Neurosci.* 4, 1339–1351. doi: 10.1021/cn400066t

Henriksen, J. R., and Ipsen, J. H. (2004). Measurement of membrane elasticity by micro-pipette aspiration. *Eur. Phys. J. E* 14, 149–167. doi: 10.1140/epje/i2003-10146-y

Henzler-Wildman, K., and Kern, D. (2007). Dynamic personalities of proteins. *Nature* 450, 964–972. doi: 10.1038/nature06522

Holt, S. A., Lakey, J. H., Daud, S. M., and Keegan, N. (2005). Neutron reflectometry of membrane protein assemblies at the solid/liquid interface. *Aust. J. Chem.* 58, 674–677. doi: 10.1071/CH05112

Holt, S. A., Le Brun, A. P., Majkrzak, C. F., McGillivray, D. J., Heinrich, F., Lösche, M., et al. (2009). An ion-channel-containing model membrane: structural determination by magnetic contrast neutron reflectometry. *Soft Matter* 5, 2576–2586. doi: 10.1039/b822411k

Jiang, Z., Heinrich, F., McGlinchey, R. P., Gruschus, J. M., and Lee, J. C. (2017). Segmental deuteration of α-synuclein for neutron reflectometry on tethered bilayers. *J. Phys. Chem. Lett.* 8, 29–34. doi: 10.1021/acs.jpclett.6b02304

Jiang, Z., Hess, S. K., Heinrich, F., and Lee, J. C. (2015). Molecular details of α-synuclein membrane association revealed by neutrons and photons. *J. Phys. Chem. B* 119, 4812–4823. doi: 10.1021/jp512499r

Katsaras, J. (1997). Highly aligned lipid membrane systems in the physiologically relevant "excess water" condition. *Biophys. J.* 73, 2924–2929. doi: 10.1016/S0006-3495(97)78320-6

Katsaras, J. (1998). Adsorbed to a rigid substrate, dimyristoylphosphatidylcholine multibilayers attain full hydration in all mesophases. *Biophys. J.* 75, 2157–2162. doi: 10.1016/S0006-3495(98)77658-1

Kaur, U., and Lee, J. C. (2021). Membrane interactions of α-synuclein probed by neutrons and photons. *Acc. Chem. Res.* 54, 302–310. doi: 10.1021/acs.accounts.0c00453

Kelley, E. G., Butler, P. D., Ashkar, R., Bradbury, R., and Nagao, M. (2020). Scaling relationships for the elastic moduli and viscosity of mixed lipid membranes. *Proc. Natl. Acad. Sci. U.S.A.* 117, 23365–23373. doi: 10.1073/pnas.2008789117

King, G. I., and White, S. H. (1986). Determining bilayer hydrocarbon thickness from neutron diffraction measurements using strip-function models. *Biophys. J.* 49, 1047–1054. doi: 10.1016/S0006-3495(86)83733-X

Kinnun, J. J., Bolmatov, D., Lavrentovich, M. O., and Katsaras, J. (2020). Lateral heterogeneity and domain formation in cellular membranes. *Chem. Phys. Lipids* 232, 104976. doi: 10.1016/j.chemphyslip.2020.104976

Kiselev, M., Zemlyanaya, E., Aswal, V., and Neubert, R. (2006). What can we learn about the lipid vesicle structure from the small-angle neutron scattering experiment? *Eur. Biophys. J.* 35, 477–493. doi: 10.1007/s00249-006-0055-9

Knoll, W., Haas, J., Stuhrmann, H. B., Füldner, H. H., Vogel, H., and Sackmann, E. (1981). Small-angle neutron scattering of aqueous dispersions of lipids and lipid mixtures. A contrast variation study. *J. Appl. Crystallogr.* 14, 191–202. doi: 10.1107/S0021889881009102

Komura, S., Toyoshima, Y., and Takeda, T. (1982). Neutron small-angle scattering from single-walled liposomes of egg phosphatidylcholine. *Jpn. J. Appl. Phys.* 21, 1370. doi: 10.1143/JJAP.21.1370

Kučerka, N., Gallová, J., Uhríková, D., Balgavỳ, P., Bulacu, M., Marrink, S. J., et al. (2009b). Areas of monounsaturated diacylphosphatidylcholines. *Biophys. J.* 97, 1926–1932. doi: 10.1016/j.bpj.2009.06.050

Kučerka, N., Heberle, F. A., Pan, J., and Katsaras, J. (2015). Structural significance of lipid diversity as studied by small angle neutron and X-ray scattering. *Membranes* 5, 454–472. doi: 10.3390/membranes5030454

Kučerka, N., Holland, B. W., Gray, C. G., Tomberli, B., and Katsaras, J. (2012). Scattering density profile model of POPG bilayers as determined by molecular dynamics simulations and small-angle neutron and X-ray scattering experiments. *J. Phys. Chem. B* 116, 232–239. doi: 10.1021/jp208920h

Kučerka, N., Marquardt, D., Harroun, T. A., Nieh, M. P., Wassall, S. R., and Katsaras, J. (2009a). The functional significance of lipid diversity: orientation of cholesterol in bilayers is determined by lipid species. *J. Am. Chem. Soc.* 131, 16358–16359. doi: 10.1021/ja907659u

Kučerka, N., Nagle, J. F., Feller, S. E., and Balgavỳ, P. (2004). Models to analyze small-angle neutron scattering from unilamellar lipid vesicles. *Phys. Rev. E* 69:051903. doi: 10.1103/PhysRevE.69.051903

Kučerka, N., Nagle, J. F., Sachs, J. N., Feller, S. E., Pencer, J., Jackson, A., et al. (2008). Lipid bilayer structure determined by the simultaneous analysis of neutron and X-ray scattering data. *Biophys. J.* 95, 2356–2367. doi: 10.1529/biophysj.108.132662

Kučerka, N., Nieh, M. P., and Katsaras, J. (2011). Fluid phase lipid areas and bilayer thicknesses of commonly used phosphatidylcholines as a function of temperature. *Biochim. Biophys. Acta. Biomembr.* 1808, 2761–2771. doi: 10.1016/j.bbamem.2011.07.022

Kučerka, N., Pencer, J., Nieh, M. P., and Katsaras, J. (2007). Influence of cholesterol on the bilayer properties of monounsaturated phosphatidylcholine unilamellar vesicles. *Eur. Phys. J. E* 23, 247–54. doi: 10.1140/epje/i2007-10202-8

Kučerka, N., van Oosten, B., Pan, J., Heberle, F. A., Harroun, T. A., and Katsaras, J. (2015). Molecular structures of fluid phosphatidylethanolamine bilayers obtained from simulation-to-experiment comparisons and experimental scattering density profiles. *J. Phys. Chem. B* 119, 1947–1956. doi: 10.1021/jp511159q

Kurniawan, J., Ventrici de Souza, J. F., Dang, A. T., Liu, G., and Kuhl, T. L. (2018). Preparation and characterization of solid-supported lipid bilayers formed by Langmuir–Blodgett deposition: a tutorial. *Langmuir* 34, 15622–15639. doi: 10.1021/acs.langmuir.8b03504

Le Brun, A. P., Haigh, C. L., Drew, S. C., James, M., Boland, M. P., and Collins, S. J. (2014). Neutron reflectometry studies define prion protein N-terminal peptide membrane binding. *Biophys. J.* 107, 2313–2324. doi: 10.1016/j.bpj.2014.09.027

Lee, S., Tran, A., Allsopp, M., Lim, J. B., Hnin, J., and Klauda, J. B. (2014). CHARMM36 united atom chain model for lipids and surfactants. *J. Phys. Chem. B* 118, 547–556. doi: 10.1021/jp410344g

Léonard, A., Escrive, C., Laguerre, M., Pebay-Peyroula, E., Néri, W., Pott, T., et al. (2001). Location of cholesterol in DMPC membranes. A comparative study by neutron diffraction and molecular mechanics simulation. *Langmuir* 17, 2019–2030. doi: 10.1021/la001382p

Lingwood, D., and Simons, K. (2010). Lipid rafts as a membrane-organizing principle. *Science* 327, 46–50. doi: 10.1126/science.1174621

Liu, J., and Conboy, J. C. (2005). 1,2-diacyl-phosphatidylcholine flip-flop measured directly by sum-frequency vibrational spectroscopy. *Biophys. J.* 89, 2522–2532. doi: 10.1529/biophysj.105.065672

Lorent, J., Levental, K., Ganesan, L., Rivera-Longsworth, G., Sezgin, E., Doktorova, M., et al. (2020). Plasma membranes are asymmetric in lipid unsaturation, packing and protein shape. *Nat. Chem. Biol.* 16, 644–652. doi: 10.1038/s41589-020-0529-6

Manno, S., Takakuwa, Y., and Mohandas, N. (2002). Identification of a functional role for lipid asymmetry in biological membranes: phosphatidylserine-skeletal protein interactions modulate membrane stability. *Proc. Natl. Acad. Sci. U.S.A.* 99, 1943–1948. doi: 10.1073/pnas.042688399

Marquardt, D., Heberle, F. A., Miti, T., Eicher, B., London, E., Katsaras, J., et al. (2017). ^{1}H NMR shows slow phospholipid flip-flop in gel and fluid bilayers. *Langmuir* 33, 3731–3741. doi: 10.1021/acs.langmuir.6b04485

Marquardt, D., Heberle, F. A., Nickels, J. D., Pabst, G., and Katsaras, J. (2015). On scattered waves and lipid domains: detecting membrane rafts with X-rays and neutrons. *Soft Matter* 11, 9055–9072. doi: 10.1039/C5SM01807B

Marquardt, D., Heberle, F. A., Pan, J., Cheng, X., Pabst, G., Harroun, T. A., et al. (2020). The structures of polyunsaturated lipid bilayers by joint refinement of neutron and X-ray scattering data. *Chem. Phys. Lipids* 229:104892. doi: 10.1016/j.chemphyslip.2020.104892

Marquardt, D., Kučerka, N., Wassall, S. R., Harroun, T. A., and Katsaras, J. (2016). Cholesterol's location in lipid bilayers. *Chem. Phys. Lipids* 199, 17–25. doi: 10.1016/j.chemphyslip.2016.04.001

Marquardt, D., Williams, J. A., Kučerka, N., Atkinson, J., Wassall, S. R., Katsaras, J., et al. (2013). Tocopherol activity correlates with its location in a membrane: a new perspective on the antioxidant vitamin E. *J. Am. Chem. Soc.* 135, 7523–7533. doi: 10.1021/ja312665r

Marrink, S. J., de Vries, A. H., Harroun, T. A., Katsaras, J., and Wassall, S. R. (2008). Cholesterol shows preference for the interior of polyunsaturated lipid membranes. *J. Am. Chem. Soc.* 130, 10–11. doi: 10.1021/ja076641c

Mason, P., Gaulin, B., Epand, R., Wignall, G., and Lin, J. (1999). Small angle neutron scattering and calorimetric studies of large unilamellar vesicles of the phospholipid dipalmitoylphosphatidylcholine. *Phys. Rev. E* 59:3361. doi: 10.1103/PhysRevE.59.3361

Masui, T., Urakami, N., and Imai, M. (2008). Nano-meter-sized domain formation in lipid membranes observed by small angle neutron scattering. *Eur. Phys. J. E* 27, 379–389. doi: 10.1140/epje/i2008-10400-x

Mosin, O., and Ignatov, I. (2012). Studying of isotopic effects of heavy water in biological systems on example of prokaryotic and eukaryotic cells. *Biomedicine* 1, 31–50.

Mukherjee, S., and Maxfield, F. R. (2004). Membrane domains. *Annu. Rev. Cell Dev. Biol.* 20, 839–866. doi: 10.1146/annurev.cellbio.20.010403.095451

Nagao, M. (2009). Observation of local thickness fluctuations in surfactant membranes using neutron spin echo. *Phys. Rev. E* 80:031606. doi: 10.1103/PhysRevE.80.031606

Nagao, M., Kelley, E. G., Ashkar, R., Bradbury, R., and Butler, P. D. (2017). Probing elastic and viscous properties of phospholipid bilayers using neutron spin echo spectroscopy. *J. Phys. Chem. Lett.* 8, 4679–4684. doi: 10.1021/acs.jpclett.7b01830

Nagle, J. F., and Tristram-Nagle, S. (2000). Structure of lipid bilayers. *Biochim. Biophys. Acta* 1469, 159–195. doi: 10.1016/S0304-4157(00)00016-2

Naumann, C., Dietrich, C., Lu, J., Thomas, R., Rennie, A., Penfold, J., et al. (1994). Structure of mixed monolayers of dipalmitoylglycerophosphocholine and polyethylene glycol monododecyl ether at the air/water interface determined by neutron reflection and film balance techniques. *Langmuir* 10, 1919–1925. doi: 10.1021/la00018a051

Nawroth, T., Conrad, H., and Dose, K. (1989). Neutron small angle scattering of liposomes in the presence of detergents. *Phys. B* 156, 477–480. doi: 10.1016/0921-4526(89)90708-4

Nguyen, M. H., DiPasquale, M., Rickeard, B. W., Doktorova, M., Heberle, F. A., Scott, H. L., et al. (2019). Peptide-induced lipid flip-flop in asymmetric liposomes measured by small angle neutron scattering. *Langmuir* 35, 11735–11744. doi: 10.1021/acs.langmuir.9b01625

Nickels, J. D., Chatterjee, S., Stanley, C. B., Qian, S., Cheng, X., Myles, D. A., et al. (2017). The *in vivo* structure of biological membranes and evidence for lipid domains. *PLoS Biol.* 15:e2002214. doi: 10.1371/journal.pbio.2002214

Nickels, J. D., Cheng, X., Mostofian, B., Stanley, C., Lindner, B., Heberle, F. A., et al. (2015). Mechanical properties of nanoscopic lipid domains. *J. Am. Chem. Soc.* 137, 15772–15780. doi: 10.1021/jacs.5b08894

Oliver, R. C., Pingali, S. V., and Urban, V. S. (2017). Designing mixed detergent micelles for uniform neutron contrast. *J. Phys. Chem. Lett.* 8, 5041–5046. doi: 10.1021/acs.jpclett.7b02149

Op den Kamp, J. A. F. (1979). Lipid asymmetry in membranes. *Annu. Rev. Biochem.* 48, 47–71. doi: 10.1146/annurev.bi.48.070179.000403

Pan, J., Cheng, X., Monticelli, L., Heberle, F. A., Kučerka, N., Tieleman, D. P., et al. (2014b). The molecular structure of a phosphatidylserine bilayer determined by scattering and molecular dynamics simulations. *Soft Matter* 10, 3716–3725. doi: 10.1039/c4sm00066h

Pan, J., Heberle, F. A., Petruzielo, R. S., and Katsaras, J. (2013). Using small-angle neutron scattering to detect nanoscopic lipid domains. *Chem. Phys. Lipids* 170, 19–32. doi: 10.1016/j.chemphyslip.2013.02.012

Pan, J., Marquardt, D., Heberle, F. A., Kučerka, N., and Katsaras, J. (2014a). Revisiting the bilayer structures of fluid phase phosphatidylglycerol lipids: Accounting for exchangeable hydrogens. *Biochim. Biophys. Acta Biomembr.* 1838, 2966–2969. doi: 10.1016/j.bbamem.2014.08.009

Pan, J., Tristram-Nagle, S., and Nagle, J. F. (2009). Effect of cholesterol on structural and mechanical properties of membranes depends on lipid chain saturation. *Phys. Rev. E* 80:021931. doi: 10.1103/PhysRevE.80.021931

Pencer, J., and Hallett, F. (2000). Small-angle neutron scattering from large unilamellar vesicles: an improved method for membrane thickness determination. *Phys. Rev. E* 61:3003. doi: 10.1103/PhysRevE.61.3003

Pencer, J., Krueger, S., Adams, C. P., and Katsaras, J. (2006). Method of separated form factors for polydisperse vesicles. *J. Appl. Crystallogr.* 39, 293–303. doi: 10.1107/S0021889806005255

Pencer, J., Mills, T., Anghel, V., Krueger, S., Epand, R. M., and Katsaras, J. (2005). Detection of submicron-sized raft-like domains in membranes by small-angle neutron scattering. *Eur. Phys. J. E* 18, 447–458. doi: 10.1140/epje/e2005-00046-5

Perissinotto, F., Rondelli, V., Parisse, P., Tormena, N., Zunino, A., Almásy, L., et al. (2019). GM1 ganglioside role in the interaction of alpha-synuclein with lipid membranes: morphology and structure. *Biophys. Chem.* 255, 106272. doi: 10.1016/j.bpc.2019.106272

Perozo, E., Cortes, D. M., Sompornpisut, P., Kloda, A., and Martinac, B. (2002). Open channel structure of MscL and the gating mechanism of mechanosensitive channels. *Nature* 418, 942–948. doi: 10.1038/nature00992

Pfefferkorn, C. M., Heinrich, F., Sodt, A. J., Maltsev, A. S., Pastor, R. W., and Lee, J. C. (2012). Depth of α-synuclein in a bilayer determined by fluorescence, neutron reflectometry, and computation. *Biophys. J.* 102, 613–621. doi: 10.1016/j.bpj.2011.12.051

Pfeiffer, W., König, S., Legrand, J., Bayerl, T., Richter, D., and Sackmann, E. (1993). Neutron spin echo study of membrane undulations in lipid multibilayers. *Europhys. Lett.* 23:457. doi: 10.1209/0295-5075/23/6/013

Phillips, R., Ursell, T., Wiggins, P., and Sens, P. (2009). Emerging roles for lipids in shaping membrane-protein function. *Nature* 459, 379–385. doi: 10.1038/nature08147

Reynwar, B. J., Illya, G., Harmandaris, V. A., Müller, M. M., Kremer, K., and Deserno, M. (2007). Aggregation and vesiculation of membrane proteins by curvature-mediated interactions. *Nature* 447, 461–464. doi: 10.1038/nature05840

Richter, R. P., Bérat, R., and Brisson, A. R. (2006). Formation of solid-supported lipid bilayers: an integrated view. *Langmuir* 22, 3497–3505. doi: 10.1021/la052687c

Rickeard, B. W., Nguyen, M. H., DiPasquale, M., Yip, C. G., Baker, H., Heberle, F. A., et al. (2020). Transverse lipid organization dictates bending fluctuations in model plasma membranes. *Nanoscale* 12, 1438–1447. doi: 10.1039/C9NR07977G

Rondelli, V., Brocca, P., Motta, S., Messa, M., Colombo, L., Salmona, M., et al. (2016). Amyloidβ Peptides in interaction with raft-mime model membranes: a neutron reflectivity insight. *Sci. Rep*. 6:20997. doi: 10.1038/srep20997

Rondelli, V., Del Favero, E., Brocca, P., Fragneto, G., Trapp, M., Mauri, L., et al. (2018). Directional K^+ channel insertion in a single phospholipid bilayer: Neutron reflectometry and electrophysiology in the joint exploration of a model membrane functional platform. *Biochim. Biophys. Acta Biomembr*. 1862, 1742–1750. doi: 10.1016/j.bbagen.2018.05.007

Sani, M. A., Le Brun, A. P., and Separovic, F. (2020). The antimicrobial peptide maculatin self assembles in parallel to form a pore in phospholipid bilayers. *Biochim. Biophys. Acta Biomembr*. 1862:183204. doi: 10.1016/j.bbamem.2020.183204

Schmiedel, H., Jörchel, P., Kiselev, M., and Klose, G. (2001). Determination of structural parameters and hydration of unilamellar POPC/C12E4 vesicles at high water excess from neutron scattering curves using a novel method of evaluation. *J. Phys. Chem. B* 105, 111–117. doi: 10.1021/jp001712e

Seigneuret, M., and Devaux, P. F. (1984). ATP-dependent asymmetric distribution of spin-labeled phospholipids in the erythrocyte membrane: relation to shape changes. *Proc. Natl. Acad. Sci. U.S.A*. 81, 3751–3755. doi: 10.1073/pnas.81.12.3751

Sharma, V. K., Mamontov, E., Anunciado, D. B., O'Neill, H., and Urban, V. S. (2015). Effect of antimicrobial peptide on the dynamics of phosphocholine membrane: role of cholesterol and physical state of bilayer. *Soft Matter* 11, 6755–6767. doi: 10.1039/C5SM01562F

Sharma, V. K., and Qian, S. (2019). Effect of an antimicrobial peptide on lateral segregation of lipids: a structure and dynamics study by neutron scattering. *Langmuir* 35, 4152–4160. doi: 10.1021/acs.langmuir.8b04158

Shekhar, P., Nanda, H., Lösche, M., and Heinrich, F. (2011). Continuous distribution model for the investigation of complex molecular architectures near interfaces with scattering techniques. *J. Appl. Phys*. 110:102216. doi: 10.1063/1.3661986

Simons, K., and Ikonen, E. (1997). Functional rafts in cell membranes. *Nature* 387, 569–572. doi: 10.1038/42408

Simons, K., and Toomre, D. (2000). Lipid rafts and signal transduction. *Nat. Rev. Mol. Cell Biol*. 1, 31–39. doi: 10.1038/35036052

Singer, S. J., and Nicolson, G. L. (1972). The fluid mosaic model of the structure of cell membranes. *Science* 175, 720–731. doi: 10.1126/science.175.4023.720

Smith, B. D., and Lambert, T. N. (2003). Molecular ferries: membrane carriers that promote phospholipid flip-flop and chloride transport. *Chem. Commun*. 2261–2268. doi: 10.1039/b303359g

Smith, M. B., McGillivray, D. J., Genzer, J., Lösche, M., and Kilpatrick, P. K. (2010). Neutron reflectometry of supported hybrid bilayers with inserted peptide. *Soft Matter* 6, 862–865. doi: 10.1039/b915800f

Soranzo, T., Martin, D. K., Lenormand, J. L., and Watkins, E. B. (2017). Coupling neutron reflectivity with cell-free protein synthesis to probe membrane protein structure in supported bilayers. *Sci. Rep*. 7, 1–10. doi: 10.1038/s41598-017-03472-8

Svergun, D. I., Koch, M. H., Timmins, P. A., and May, R. P. (2013). *Small Angle X-ray and Neutron Scattering From Solutions of Biological Macromolecules*, Vol. 19. Oxford: Oxford University Press.

Tian, A., Capraro, B. R., Esposito, C., and Baumgart, T. (2009). Bending stiffness depends on curvature of ternary lipid mixture tubular membranes. *Biophys. J*. 97, 1636–1646. doi: 10.1016/j.bpj.2009.07.012

Toppozini, L., Armstrong, C. L., Barrett, M. A., Zheng, S., Luo, L., Nanda, H., et al. (2012). Partitioning of ethanol into lipid membranes and its effect on fluidity and permeability as seen by X-ray and neutron scattering. *Soft Matter* 8, 11839–11849. doi: 10.1039/c2sm26546j

van Helvoort, A., Smith, A. J., Sprong, H., Fritzsche, I., Schinkel, A. H., Borst, P., et al. (1996). MDR1 P-glycoprotein is a lipid translocase of broad specificity, while MDR3 P-glycoprotein specifically translocates phosphatidylcholine. *Cell* 87, 507–517. doi: 10.1016/S0092-8674(00)81370-7

Van Meer, G., Voelker, D. R., and Feigenson, G. W. (2008). Membrane lipids: where they are and how they behave. *Nat. Rev. Mol*. 9, 112–124. doi: 10.1038/nrm2330

Verkleij, A., Zwaal, R., Roelofsen, B., Comfurius, P., Kastelijn, D., and Van Deenen, L. (1973). The asymmetric distribution of phospholipids in the human red cell membrane. A combined study using phospholipases and freeze-etch electron microscopy. *Biochim. Biophys. Acta Biomembr*. 323, 178–193. doi: 10.1016/0005-2736(73)90143-0

Wacklin, H. P., Bremec, B. B., Moulin, M., Rojko, N., Haertlein, M., Forsyth, T., et al. (2016). Neutron reflection study of the interaction of the eukaryotic pore-forming actinoporin equinatoxin II with lipid membranes reveals intermediate states in pore formation. *Biochim. Biophys. Acta Biomembr*. 1858, 640–652. doi: 10.1016/j.bbamem.2015.12.019

Wiener, M., Suter, R., and Nagle, J. (1989). Structure of the fully hydrated gel phase of dipalmitoylphosphatidylcholine. *Biophys. J*. 55, 315–325. doi: 10.1016/S0006-3495(89)82807-3

Wiener, M. C., and White, S. H. (1991a). Fluid bilayer structure determination by the combined use of x-ray and neutron diffraction. I. Fluid bilayer models and the limits of resolution. *Biophys. J*. 59, 162–173. doi: 10.1016/S0006-3495(91)82208-1

Wiener, M. C., and White, S. H. (1991b). Fluid bilayer structure determination by the combined use of x-ray and neutron diffraction. II. "Composition-space" refinement method. *Biophys. J*. 59, 174–185. doi: 10.1016/S0006-3495(91)82209-3

Wiener, M. C., and White, S. H. (1992). Structure of a fluid dioleoylphosphatidylcholine bilayer determined by joint refinement of X-ray and neutron diffraction data. III. Complete structure. *Biophys. J*. 61, 434–447. doi: 10.1016/S0006-3495(92)81849-0

Williamson, P., Christie, A., Kohlin, T., Schlegel, R. A., Comfurius, P., Harmsma, M., et al. (2001). Phospholipid scramblase activation pathways in lymphocytes. *Biochemistry* 40, 8065–8072. doi: 10.1021/bi001929z

Wong, J. Y., Majewski, J., Seitz, M., Park, C. K., Israelachvili, J. N., and Smith, G. S. (1999). Polymer-cushioned bilayers. I. A structural study of various preparation methods using neutron reflectometry. *Biophys. J*. 77, 1445–1457. doi: 10.1016/S0006-3495(99)76992-4

Woodka, A. C., Butler, P. D., Porcar, L., Farago, B., and Nagao, M. (2012). Lipid bilayers and membrane dynamics: insight into thickness fluctuations. *Phys. Rev. Lett*. 109:058102. doi: 10.1103/PhysRevLett.109.058102

Yang, S. T., Kreutzberger, A. J., Lee, J., Kiessling, V., and Tamm, L. K. (2016). The role of cholesterol in membrane fusion. *Chem. Phys. Lipids* 199, 136–143. doi: 10.1016/j.chemphyslip.2016.05.003

Yap, T. L., Jiang, Z., Heinrich, F., Gruschus, J. M., Pfefferkorn, C. M., Barros, M., et al. (2015). Structural features of membrane-bound glucocerebrosidase and α-synuclein probed by neutron reflectometry and fluorescence spectroscopy. *J. Biol. Chem*. 290, 744–754. doi: 10.1074/jbc.M114.610584

Yi, Z., Nagao, M., and Bossev, D. P. (2009). Bending elasticity of saturated and monounsaturated phospholipid membranes studied by the neutron spin echo technique. *J. Condens. Matter Phys*. 21:155104. doi: 10.1088/0953-8984/21/15/155104

Yu, J., Mao, J., Nagao, M., Bu, W., Lin, B., Hong, K., et al. (2020). Structure and dynamics of lipid membranes interacting with antivirulence end-phosphorylated polyethylene glycol block copolymers. *Soft Matter* 16, 983–989. doi: 10.1039/C9SM01642B

Zilman, A., and Granek, R. (1996). Undulations and dynamic structure factor of membranes. *Phys. Rev. Lett*. 77:4788. doi: 10.1103/PhysRevLett.77.4788

Conflict of Interest: The authors declare that the research was conducted in the absence of any commercial or financial relationships that could be construed as a potential conflict of interest.

The reviewer NK declared a past co-authorship with the authors JJK, HS, JK to the handling Editor.

frontiers in Chemistry

ORIGINAL RESEARCH
published: 29 April 2021
doi: 10.3389/fchem.2021.630152

ApoE and ApoE Nascent-Like HDL Particles at Model Cellular Membranes: Effect of Protein Isoform and Membrane Composition

*Sarah Waldie[1,2,3], Federica Sebastiani[1], Martine Moulin[2,3], Rita Del Giudice[1], Nicolò Paracini[1], Felix Roosen-Runge[1], Yuri Gerelli[2,4], Sylvain Prevost[2], John C. Voss[5], Tamim A. Darwish[6], Nageshwar Yepuri[6], Harald Pichler[7,8], Selma Maric[9], V. Trevor Forsyth[2,3,10], Michael Haertlein[2,3] and Marité Cárdenas[1]**

[1] Department of Biomedical Science and Biofilms—Research Center for Biointerfaces, Malmö University, Malmö, Sweden, [2] Institut Laue-Langevin, Grenoble, France, [3] Partnership for Structural Biology (PSB), Grenoble, France, [4] Department of Life and Environmental Sciences, Marche Polytechnic University, Ancona, Italy, [5] Department of Biochemistry and Molecular Medicine, University of California, Davis, Davis, CA, United States, [6] National Deuteration Facility, Australian Nuclear Science and Technology Organisation, Lucas Heights, NSW, Australia, [7] Austrian Centre of Industrial Biotechnology, Graz, Austria, [8] Graz University of Technology, Institute of Molecular Biotechnology, NAWI Graz, BioTechMed Graz, Graz, Austria, [9] MAX IV Laboratory, Lund, Sweden, [10] Faculty of Natural Sciences, Keele University, Staffordshire, United Kingdom

Apolipoprotein E (ApoE), an important mediator of lipid transportation in plasma and the nervous system, plays a large role in diseases such as atherosclerosis and Alzheimer's. The major allele variants ApoE3 and ApoE4 differ only by one amino acid. However, this difference has major consequences for the physiological behaviour of each variant. In this paper, we follow (i) the initial interaction of lipid-free ApoE variants with model membranes as a function of lipid saturation, (ii) the formation of reconstituted High-Density Lipoprotein-like particles (rHDL) and their structural characterisation, and (iii) the rHDL ability to exchange lipids with model membranes made of saturated lipids in the presence and absence of cholesterol [1,2-dimyristoyl-sn-glycero-3-phosphocholine (DMPC) or 1-palmitoyl-2-oleoyl-glycero-3-phosphocholine (POPC) with and without 20 mol% cholesterol]. Our neutron reflection results demonstrate that the protein variants interact differently with the model membranes, adopting different protein conformations. Moreover, the ApoE3 structure at the model membrane is sensitive to the level of lipid unsaturation. Small-angle neutron scattering shows that the ApoE containing lipid particles form elliptical disc-like structures, similar in shape but larger than nascent or discoidal HDL based on Apolipoprotein A1 (ApoA1). Neutron reflection shows that ApoE-rHDL do not remove cholesterol but rather exchange saturated lipids, as occurs in the brain. In contrast, ApoA1-containing particles remove and exchange lipids to a greater extent as occurs elsewhere in the body.

Keywords: ApoE isoforms, lipid exchange, reconstituted HDL, model membranes, neutron reflection, small-angle neutron scattering

OPEN ACCESS

Edited by:
Olaf Holderer, Julich-Forschungszentrum, Helmholtz-Verband Deutscher Forschungszentren (HZ), Germany

Reviewed by:
Amiya Kumar Panda, Vidyasagar University, India
David Hoogerheide, National Institute of Standards and Technology, United States

***Correspondence:**
Marité Cárdenas
marite.cardenas@mau.se

Specialty section:
This article was submitted to Physical Chemistry and Chemical Physics, a section of the journal Frontiers in Chemistry

Received: *16 November 2020*
Accepted: *30 March 2021*
Published: *29 April 2021*

Citation:
Waldie S, Sebastiani F, Moulin M, Del Giudice R, Paracini N, Roosen-Runge F, Gerelli Y, Prevost S, Voss JC, Darwish TA, Yepuri N, Pichler H, Maric S, Forsyth VT, Haertlein M and Cárdenas M (2021) ApoE and ApoE Nascent-Like HDL Particles at Model Cellular Membranes: Effect of Protein Isoform and Membrane Composition. Front. Chem. 9:630152. doi: 10.3389/fchem.2021.630152

INTRODUCTION

Disorders in lipid metabolism are related to a range of diseases, among them atherosclerosis and Alzheimer's disease (AD). In atherosclerosis, the leading cause of death in western society, elevated levels of high-density lipoproteins (HDL) are thought to have counter-atherosclerotic properties (Gordon et al., 1989). However, the presence of HDL has more recently been shown to play a neutral (Voight et al., 2012) or even negative (Madsen et al., 2017) role in aiding the prevention of this disease. Even though HDL has been used to help combat the onset of atherosclerosis (*via* HDL therapy or plaque remodelling therapy) (Gille et al., 2014; Van Capelleveen et al., 2014), some recent medical trials have failed to prove HDL's effectiveness against atherosclerosis (Angeloni et al., 2013; Toth et al., 2013).

In general, HDL consist of a core of triglycerides and cholesterol esters, encased in a monolayer of lipids and cholesterol, surrounded by protein. There are many different subclasses of HDL each with slightly varying size and composition (Jonas, 2002). In particular, the lipid-poor, nascent HDL (also known as Preβ-HDL) is thought to be discoidal in shape and transforms into a spherical, mature HDL particle upon esterification of cholesterol and transfer into its lipid core. While ApolipoproteinA1 (ApoA1) constitutes around 70% of total protein content in human HDL, there are various other proteins which are also key to the structure and function of HDL particles (Jonas, 2002). One of these is ApolipoproteinE (ApoE) (Utermann, 1975) which is found in most HDL subfractions but mainly in the largest, most buoyant mature subfraction (HDL2) that contains triglycerides and are lipid rich (Davidson et al., 2009). ApoE is also the most commonly found apolipoprotein in cerebrospinal fluid (Ladu et al., 2009). It plays a large role in cholesterol transport while maintaining local homeostasis of cholesterol within the brain (Mahley, 2016b).

In humans, ApoE allelic variants result in three isoforms E2, E3, and E4, with respective frequencies of 8.4, 77.9, and 13.7% and varying at only two amino acid residues, 112 and 158 (E2: 112Cys, 158Cys; E3: 112Cys, 158Arg; E4: 112Arg, 158Arg) (Weisgraber et al., 1981). These differences in the amino acid sequence largely contribute to the proteins' structure and function and determine their behaviour in the body (Chou et al., 2005; Mahley et al., 2009), and especially in the roles they play in certain diseases such as atherosclerosis and AD. The presence of ApoE2 is associated with very low risk of AD (Wu and Zhao, 2016; Reiman et al., 2020) and generally thought to be protective against atherosclerosis, apart from in the case of type III hyperlipoproteinemia which is associated with increased atherosclerotic risk. On the other hand, ApoE3 levels are neutral in both diseases while the presence of ApoE4 is indicative of both atherosclerotic advancement and the onset of AD (Mahley et al., 2009).

Lipids are important to these diseases as they coexist in both atherosclerotic and AD plaques (Kiskis et al., 2015; Sergin et al., 2016). Understanding the difference in the interaction of ApoE variants with model cellular membranes is key to deciphering the specific roles they play in the development of these diseases. The roles of lipoproteins in the development of atherosclerosis and, most likely in AD, directly involve lipid exchange. The type of lipid exchange occurring— namely deposition or removal— highly depends on the lipoprotein type present (Browning et al., 2017). Previously, HDL was shown to remove lipids from the cell membrane giving rise to the idea behind HDL therapy. Reconstituted HDL (rHDL), comparable to discoidal Preβ-HDL, exhibits similar lipid transfer properties to that of mature HDL (Davidson et al., 1995), and is used to mimic this, discoidal nanoparticles of phospholipids solubilised by encircling ApoA1 are used as artificial HDL or rHDL as a strategy in HDL therapy (Gille et al., 2014; Van Capelleveen et al., 2014). While less is known about the lipid exchange properties of ApoE, ApoE-containing rHDL (ApoE-rHDL) were shown to have potential for atherosclerosis treatment (Valanti et al., 2018), although further testing is needed.

In this paper, the initial interaction of ApoE3 and ApoE4 with saturated and unsaturated supported lipid bilayers (SLBs) is explored using neutron reflectometry (NR). Then, ApoE-rHDL are formed based on the vesicle solubilisation method often used to make ApoA1-rHDL. The ApoE-rHDL structure is further characterised using small angle neutron scattering (SANS). Finally, the lipid exchange capacity for ApoE-rHDL with model membranes is explored by NR. As ApoE is the main apolipoprotein in the brain, where there is a local homeostasis of cholesterol, the model membranes in question are in the absence or presence of cholesterol to determine the potential differences between these interactions. Comparisons are made between to ApoA1-based rHDL and mature HDL pooled from three healthy male volunteers [mature HDL is replotted from Waldie et al. (2020)].

MATERIALS AND METHODS

Materials

MilliQ water (18.2 MΩ cm) was used for all experiments, solvent preparations and cleaning procedures. D_2O (99.9% deuterated, Sigma-Aldrich) was provided by the Institut Laue-Langevin (ILL), Grenoble, France. Bradford reagent, calcium chloride ($CaCl_2$) and Tris buffer saline (TBS) tablets were from Sigma-Aldrich. Tris buffer (50 mM Tris, 150 mM NaCl, pH 7.4: TBS) was prepared by dissolving a tablet in H_2O as specified by the producer or D_2O to the same concentration. 1,2-dimyristoyl-sn-glycero-3-phosphocholine (>99%, hDMPC), 1,2-dimyristoyl-d54-sn-glycero-3-phosphocholine (>99%, dDMPC) and cholesterol (h-cholesterol; >98%) were from Avanti Polar Lipids (Alabaster, AL). Tail deuterated 1-palmitoyl, 2-oleoyl-sn-glycero-3-phosphocholine (d67; overall tail deuteration 95%, dPOPC) was provided by the deuteration facility at ANSTO, produced and purified as previously described (Yepuri et al., 2016).

Protein Expression and Purification

BL21DE3 *Escherichia coli* cells were transformed with pET-32a(+) plasmids containing either ApoE3 or ApoE4 and ampicillin resistance. Cells were cultivated in Terrific Broth medium (12 g L^{-1} tryptone, 24 g L^{-1} yeast extract, 4 mL L^{-1} glycerol, 9.4 g L^{-1} dipotassium phosphate and 2.2 g L^{-1}

potassium dihydrogen phosphate) at 37°C. When cultures reached an OD_{600} nm of 0.6–0.8, protein expression was induced by adding 1 mM isopropyl-beta-thiogalactopyranoside (IPTG) in the culture medium and incubated for a further 90 min. The cells were then harvested by centrifugation (19,000 rpm, JLA 9.1000 rotor 20 min, 4°C) after which the cell pellets were resuspended in TBS buffer and sonicated on ice for 10 min (50% power, 30 s on, 30 s off). hDMPC was suspended in water by bath sonication for 30 min and then added to the protein at a concentration of 100 mg per 1 L of culture and dialysed against TBS at room temperature overnight. The hDMPC is added to protect the hinge region of ApoE when cleaving with thrombin. After dialysis, thrombin was added in excess for 6 h at 37°C. The sample was analysed by SDS-PAGE to ensure all fusion protein had been cleaved. Potassium bromide was added to the ApoE-DMPC mixture to a density of ∼1.21 g mL^{-1}. Ultra-clear tubes (Beckman) were filled two-thirds with a ∼1.12 g mL^{-1} density solution (16% w/v potassium bromide solution dissolved in 20 mM Tris pH 7.4 and 0.05% w/v sodium azide) and underlayed with the lysate solution. Samples were spun for 16 h at 38,000 rpm in a SW41 rotor (Beckman) at 15°C with the break off to preserve the gradient. The resulting "floating pellet" was recovered and dialysed against TBS to remove the potassium bromide salts. The ApoE-DMPC complexes were lyophilised and frozen at −20°C. When fresh protein was required the pellets were delipidated against methanol and resuspended in 6 M Guanidine Hydrochloride (GuHCl) 50 mM Tris pH 8 and 0.5% beta-mercaptoethanol (BME), dialysed against 4 M GuHCl, 10 mM Tris pH 7.5, 1 mM EDTA, and 0.1% BME; further against 100 mM ammonium bicarbonate; and finally into TBS. The protein was then purified *via* gel-permeation column chromatography on 2 S200 columns in series and ready to use.

Protein-Lipid Particle Production and Purification

To form the ApoE-rHDL particles, equal volumes of fresh protein are mixed with freshly extruded hDMPC vesicles at a final molar ratio of 1:100 ApoE:DMPC. The hDMPC vesicles were produced by first forming a thin lipid film (in small vials, under nitrogen flow under manual rotation) that was suspended in TBS first by vortexing, then by bath sonication for 1 h. The lipid suspension was extruded 41 times using an Avanti extruder and a filter of 100 nm pore size (Millipore). The solution was incubated at 24°C for 12 h or overnight. Verification of the particle formation was carried out *via* dynamic light scattering due to a slight reduction in the peak intensity for the 100 nm vesicles and the presence of a small peak at roughly 10–15 nm. The rHDL particles were purified *via* gel filtration chromatography using a Superose 6 10/300 column.

Deuterated Cholesterol Production

The production of tailor-deuterated cholesterol made use of the Deuteration Laboratory within the Life Sciences Group (Haertlein et al., 2016) at the ILL. Based on previous developments for the production of perdeuterated cholesterol (Moulin et al., 2018), matchout-deuterated cholesterol (d-cholesterol) was produced and purified as reported previously (Waldie et al., 2019). The Pichia pastoris strain CBS7435 Δhis4Δku70 Δerg5::pPpGAP-ZeocinTM-[DHCR7] Δerg6::pGAP-G418[DHCR24] was grown in 100% deuterated basal salts medium in the presence of non-deuterated glycerol as the sole carbon source. The batch phase was complete after 7 days in a fermenter at 28°C; the fed-batch phase was initiated by constant feeding of glycerol for a further 12 days. The cells were harvested and then isolated using an organic solvent extraction method followed by HPLC to obtain pure cholesterol, verified by GCMS.

Model Membrane Preparation

Lipid films were prepared in small glass vials from chloroform stocks of dDMPC, dPOPC, h- and d-cholesterol. Twenty mol% cholesterol was incorporated into the cholesterol-containing films. The films were dried under a stream of nitrogen under manual rotation, and placed under vacuum overnight. Before use, the lipid films were hydrated in MilliQ water, vortexed and bath sonicated for 1 h. Immediately prior to injection the lipids were tip sonicated for 5 min (20% power, 5 s on, 5 s off), mixed with an equal volume of 4 mM $CaCl_2$ and injected into the pre-equilibrated NR solid-liquid flow cells by a syringe port (Browning et al., 2017; Waldie et al., 2019). The presence of 2 mM $CaCl_2$ and concentration of 0.1 mg mL^{-1} of lipids were used to optimise vesicle fusion (Åkesson et al., 2012a; Waldie et al., 2018). The lipids were incubated for 20 min before rinsing with water, followed by 50 mM Tris saline buffer, pH 7.4. This process leads to a supported lipid bilayer or "model membrane."

Scattering

SANS and NR data were collected; scattered intensity and reflectivity, respectively, were measured as a function of momentum transfer, $q = 4\pi sin(\theta)/\lambda$, where θ is half the scattering angle for SANS and the incident angle for NR and λ is the neutron radiation wavelength for both.

Neutron Reflectometry

Neutron reflectometry data were collected on the time-of-flight reflectometer FIGARO (Campbell et al., 2011, 2015) at the ILL (Grenoble, France). Momentum transfer ranges of $0.01 > q > 0.3$ $Å^{-1}$ were measured using wavelengths $2 < \lambda < 20$ Å and two incident angles, 0.8 and 2.3°, with a spatial resolution ($\Delta q/q$) of 7%. The area exposed to the neutron beam was 30 × 60 mm^2. The experiments were carried out in reflection-up mode to ensure no aggregated particles could settle on the surface being measured. The analysis of specular reflectivity data allowed a scattering length density (SLD) profile perpendicular to the surface, to be obtained.

The silicon (111) blocks were treated with Piranha solution (H_2SO_4:H_2O_2, 7:3) for 10 min at 80°C before extensive rinsing with MilliQ water (Warning: Piranha solution reacts violently with organic materials and should be handled with extreme caution). The polyether ether ketone (PEEK) and O-ring components of the cells were thoroughly cleaned in Hellmanex 2% (v/v) solution and MilliQ water twice *via* bath sonication, with rinsing of MilliQ water between each sonication. Solvent contrasts were changed *in situ via* HPLC pump. Three isotopic

contrasts were used: 100% h-TBS (TBS made using H_2O), 100% d-TBS (TBS made using D_2O) and 38% d-TBS (or cmSi) to contrast-match the silicon block.

The MOTOFIT programme (Nelson, 2006) was used to simultaneously fit the three isotopic contrasts for each experimental data set, and the Monte Carlo error analysis using genetic optimisation within the software was used to determine the error of the fits. The significance of pairwise parameters were calculated using an *F*-test assuming normal distributed errors. The clean silicon surfaces were characterised initially to determine the thickness and roughness of the oxide layer. After bilayer deposition, data was fitted using a symmetrical leaflet model (heads-tails-heads) using either a four- or five-layer model for the membranes since some samples required an extra solvent layer between the silicon oxide and the bilayer. Symmetry implies that the thickness, coverage and SLD of both headgroup layers are the same, and the roughness was constrained across all regions of the bilayer. The models were constrained to have the same mean molecular area (MMA), within error, across the different lipid bilayer layers. This fitting approach gives equivalent results to the molecularly constrained model (for which MMA is used as a fitting parameter instead). For example, POPC bilayers measured at 25°C were reported to be 62 $Å^2$ (Luchini et al., 2019) and 62 $Å^2$ (Åkesson et al., 2012a) fitting individual thicknesses or MMA, respectively.

After bilayer characterisation, the ApoE protein or protein-lipid particles were introduced into the solid-liquid flow cells *via* syringe pump at a rate of 1 mL min^{-1}. The protein and rHDL concentrations were 0.075 mg mL^{-1} and 0.132 mg mL^{-1}, respectively. After either 6 or 8 h of incubation, the bilayers were rinsed with buffer and re-characterised in all buffer contrasts. When fitting the bilayers post-interaction, the initial parameters were used as a starting point (**Table 1**) while keeping constant the silicon oxide layer parameters. For some bilayers, acceptable fits were obtained by varying only the SLB coverage and lipid tail SLD. For other bilayers, this approach gave no suitable fits forcing the use of the thickness of these regions as an additional fitting parameter. Moreover, an extra layer on top of the bilayer was necessary in all cases corresponding to either the protein or rHDL particles still attached to the bilayer.

Small-Angle Neutron Scattering

SANS data were collected on the D11 instrument at the ILL (Lindner and Schweins, 2010). The experiments were carried out at 25°C with a momentum transfer range of $0.002 < q < 0.3$ $Å^{-1}$ by using detector distances of 1.4, 8, and 39 m at constant wavelength $\lambda = 6$ Å (fwhm 9%).

The protein-lipid particles were measured in three contrasts: 100% h-TBS, 100% d-TBS and 42% d-TBS to contrast-match the protein. The data were corrected for the empty cell, background and the absolute scale was obtained from the attenuated direct beam measurement and validated from the level of water (1 mm, H_2O), used as a secondary standard. The cells were 1 mm path-length QS quartz glass Hellma SANS cuvettes (Hellma GmbH, Müllheim, Germany) and the data reduction was carried out using LAMP. The SasView programme was used to fit the experimental data[1]. The three contrasts were fitted simultaneously to constrain the fit.

RESULTS

In this work, the overall journey of ApoE is followed from its interactions with model membranes in the lipid-poor form, to the formation of a nascent-like HDL particle, and finally to the characterisation of the lipid exchange capacities for saturated lipids in the presence or absence of 20 mol% cholesterol. NR and SANS are ideal techniques for this task as they can distinguish between deuterated and non-deuterated components. Therefore, the use of deuteration in lipid-protein complexes allows highlighting of specific components within the system, together with the use of contrast variation (based on the different content of D_2O-based buffers, denoted as d-TBS) to visualise the differences between the components (Clifton et al., 2020). Here, the model cellular membranes are made up of tail-deuterated lipids and, in some membranes, the presence of non-deuterated or specifically matchout-deuterated cholesterol. The matchout deuterated cholesterol allows no net coherent scattering to be seen for this component in 100% D_2O-based buffer conditions. The protein and rHDL particles, instead, are unlabelled. The differences between the components in the membrane and the protein/rHDL allows NR to be used in determining: (1) the level of protein incorporation or lipid exchange, through the change in the scattering length density (SLD) of the tail region, (2) the amount of lipids that were removed and replaced by protein or solvent, through the change in the solvent quantity in the tail region, and (3) the amount of extra protein/rHDL bound on top of the model membrane. During the kinetics of interaction, the samples were measured in H_2O-based buffer (100% h-TBS) as this gives the best contrast against the deuterated membrane layer, while full characterisation in three contrasts (100% h-TBS, 100% d-TBS and 38% d-TBS) of the model membranes before and after kinetics were measured to increase the sensitivity and accuracy of the structural and compositional information obtained. The layer models describing the model membranes are determined from simultaneous fitting of the isotopic contrasts and allow for the analysis of the membrane composition and the decoupling of the information regarding protein incorporation/lipid exchange and lipid removal as described in the methods section and the **Supporting Information**. **Figure 1** gives schematic representations of protein and nanodisc interactions with the bilayers. Representative structural parameters for the pristine SLBs are summarised in **Table 1** and are in agreement with those reported in the literature for DMPC (Browning et al., 2018), POPC (Åkesson et al., 2012b; Waldie et al., 2020), 20 mol% cholesterol containing DMPC and POPC measured at 37°C (MMA increases with temperature and the reported values cannot be compared to MMA measured at 25°C (Åkesson et al., 2012a). POPC is fond to adopt a thicker, more expanded SLB structure than DMPC given its longer tail and the presence of double bonds that bend the acyl tails. Here, the thickening and

[1]http://www.sasview.org/.

TABLE 1 | Representative structural parameters for the SLB used.

	Head group thickness/ Å	Tail thickness/ Å	Headgroup coverage / %	Tail coverage / %	Mean molecular area / Å^2
dDMPC	9.0 ± 0.1	27.2 ± 0.2	62 ± 1	96 ± 1	59 ± 2
dPOPC	8.8 ± 0.2	28.6 ± 0.4	54 ± 2	86 ± 1	71 ± 5
dDMPC d-cholesterol*	8.5 ± 0.2	32.1 ± 0.2	71 ± 1	98 ± 1	52 ± 4
dDMPC h-cholesterol*	7.7 ± 0.4	30.7 ± 0.5	85 ± 5	94 ± 1	51 ± 4

*Corresponding NR profiles and best fits are given in the **Supplementary Information**.*
**The model membranes containing cholesterol had a nominal composition of 80:20 mol %, and its real cholesterol content was determined to be the nominal one within error (Waldie et al., 2018). d- and h- cholesterol refer to deuterated and hydrogenated cholesterol respectively.*

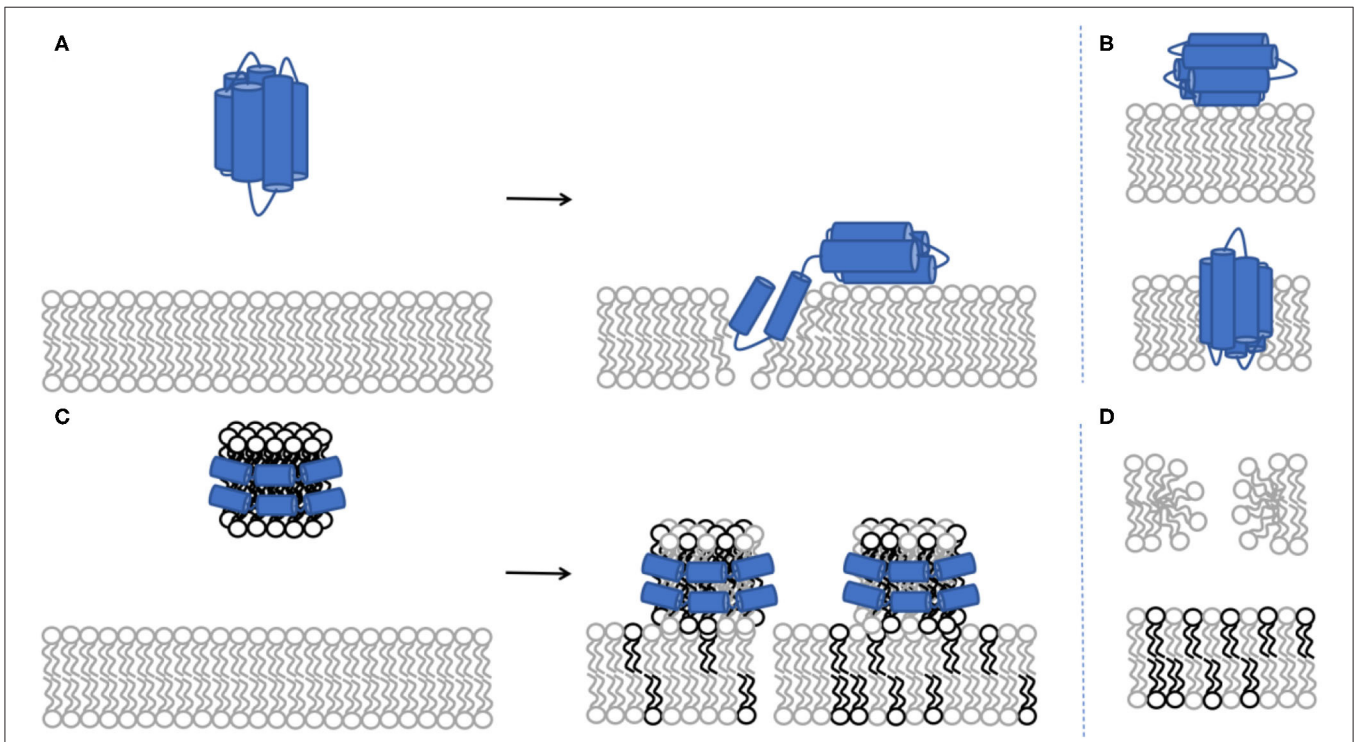

FIGURE 1 | Schematic representation of protein incorporation into the phospholipid bilayer **(A)**. NR cannot distinguish between the conformation of the protein upon binding to the model membrane: whether there are two individual protein molecules adsorbing either in the core or the headgroup region vs. a single individual protein molecule bending across the membrane **(B)**. Schematic representation for lipid exchange between the rHDL and the phospholipid bilayer **(C)**. Lipid exchange represents the combination of lipid removal from the model membrane and lipid deposited by the rHDL particles **(D)**. The light grey colour represents deuterated lipids while the black colour represents non-deuterated lipids. Both DMPC and POPC lipids were used above their melting temperature, giving fluid supported lipid bilayers. Addition of 20 mol% cholesterol to either POPC or DMPC give SLBs with fluid properties (Waldie et al., 2020).

compacting effect of cholesterol on fluid membranes is observed in agreement with previous reports (Gallová et al., 2004; Hung et al., 2007; Waldie et al., 2018, 2019). Moreover, the cholesterol molecules are expected to be fully miscible within these model membranes (Knoll et al., 1985; Barrett et al., 2013).

The samples measured by SANS (all unlabelled) were measured in three contrasts: 100% h-TBS, 100% d-TBS and 42% d-TBS. The different buffers used give varying levels of isotopic contrast; for example, the 42% d-TBS and 100% h-TBS highlight the lipids and the proteins respectively, whereas the 100% d-TBS buffer gives the largest contrast against the sample as a whole. Analysing all three contrasts simultaneously allows for higher sensitivity in the structural determination.

Initial Apolipoprotein Interaction With Model Membranes

The binding of ApoE3 or ApoE4 to model membranes comprised of saturated or unsaturated phospholipids was followed by NR as a function of the saturation level in the bilayer at 37°C in Tris buffer, pH 7.4 (**Figure 2**). For this, we used saturated, tail deuterated dDMPC and unsaturated, tail deuterated dPOPC. As shown in **Figure 2A**, in the case of the saturated lipids (dDMPC), ApoE4 presents a slightly stronger interaction with

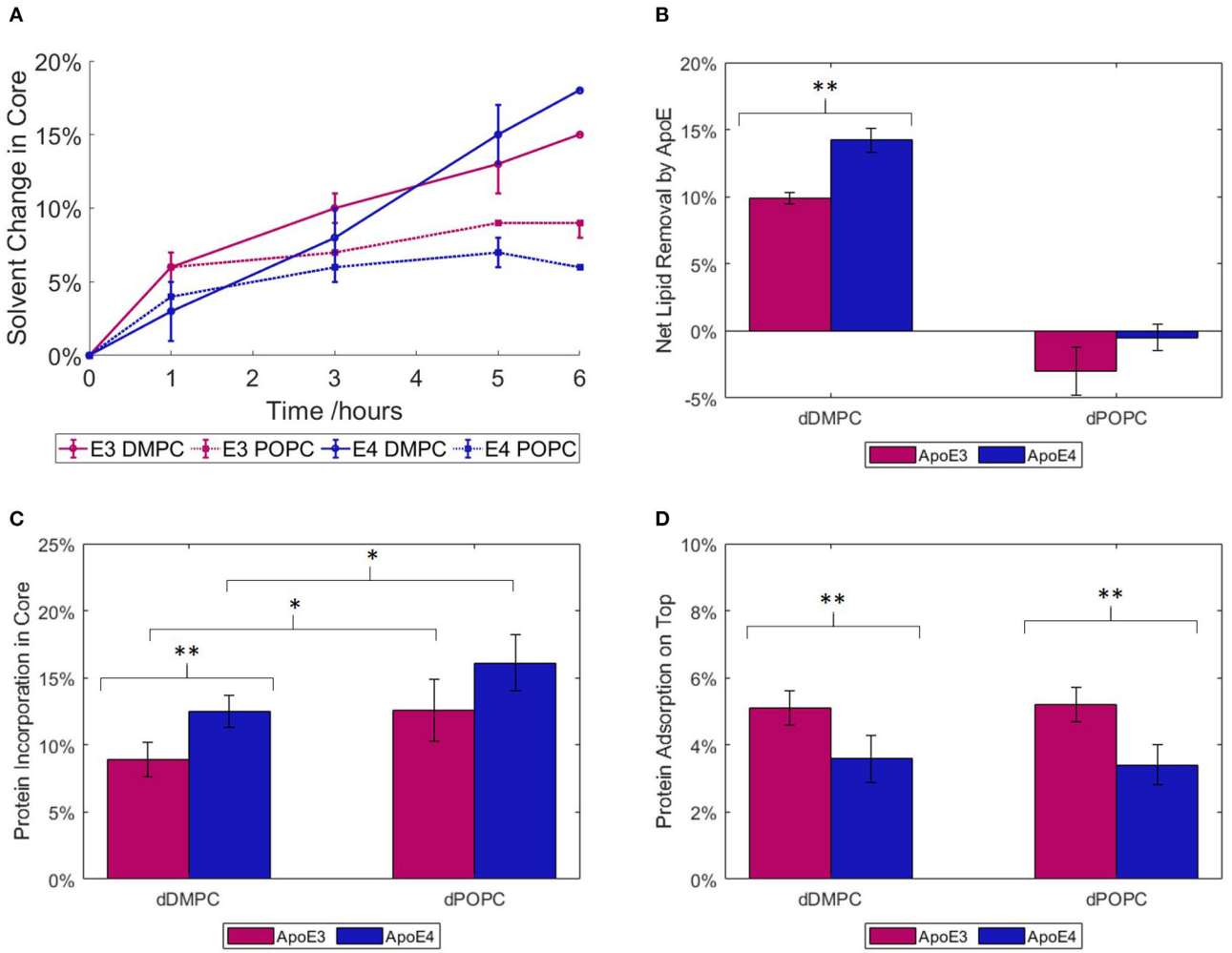

FIGURE 2 | ApoE interaction with saturated (dDMPC) or unsaturated (dPOPC) model membranes measured at 37°C, in Tris-buffer at pH 7.4: kinetics of lipid replacement in terms of the relevant change in solvent penetration of the lipid core, taking into account SLD change also, are given for ApoE3 and ApoE4 **(A)**. Net lipid removal calculated as the difference in solvent coverage within the bilayers before and after 6 h incubation with apolipoproteins **(B)** and volume fractions of protein binding within the core **(C)** or on top of **(D)** the SLBs upon 6 h of incubation and rinsing with Tris buffer. The NR profiles and best fits are shown in the **Supplementary Figures 1, 2.** *Statistically different assuming $p = 0.1$; **Statistically different assuming $p = 0.05$.

the lipids than ApoE3 in terms of lipid removal and lipid replacement by protein adsorption (reflected by the solvent change in the membrane core), whereas the opposite trend can be observed for the unsaturated lipids (dPOPC). In terms of kinetics, most of the binding to unsaturated membranes occurs within the first hour of incubation for both ApoE isoforms (**Figure 2A**). For saturated lipids, the two ApoE variants show a slightly different behaviour. On one hand, ApoE3 shows a similar initial pattern to that of unsaturated lipids but this is followed by a slower increase, possibly suggesting a gradual and slower removal of saturated lipids over longer time periods. On the other hand, ApoE4 follows a more linear increase with time. This implies a difference in the mode of interaction of the proteins with the model membranes and this interaction seems to be variant-dependent and sensitive to the level of lipid saturation.

Following the incubation period, NR data were collected using three isotopic contrasts to enable quantification of lipid removal (calculated from change in solvent penetration), protein binding to the membrane hydrophobic core and adsorption on top of the membrane (**Figures 2B–D**). This additional 28 Å layer represents most of the compact protein in a lipid-free state, allowing for some part to rearrange and integrate itself into the bilayer (Chen et al., 2011). The main lipid-binding region is the C-terminal (Li et al., 2003), thus it is possible that the protein could rearrange itself to allow maximum binding of lipids to this area. For membranes incubated with ApoE3, few changes were required from the pristine membrane (lipid bilayer) structure: the lipid head and tail thicknesses remained constant, while there were minor changes in the lipid tail SLD and both head and tail solvation. On the other hand, interaction with ApoE4 required additional changes in the head

and tail thicknesses to obtain better fits to the NR data. The increased membrane modifications seen with both isoforms correlate to the increased levels of embedded protein. When looking at the net lipid removal (or increase in solvation) and protein insertion (due to changes in SLD of the membrane hydrophobic core) upon incubation with ApoE, both variants showed a preference for the removal of saturated lipids rather than unsaturated ones (**Figure 2B**). Lipids were removed and replaced by protein insertion into the bilayer core (**Figure 2C**) with more protein incorporation into unsaturated than saturated membranes. The latter, in turn, indicates that the protein is more prone to remain bound to the unsaturated membrane without actually removing lipids. Additionally, a further protein layer is formed on top of the SLB (**Figure 2D**). This layer has a greater coverage, or protein volume fraction, for ApoE3 than for ApoE4 regardless of membrane type. This indicates that ApoE3 preferentially interacts with the lipid headgroups compared to ApoE4. Interestingly, and regardless of membrane type, the protein fraction that binds to the lipid bilayer core is larger for ApoE4 than ApoE3. Indeed, 70 and 76% of the ApoE4 protein co-localised within the core of the saturated and unsaturated membranes respectively, while these fractions decreased to 54 and 62% for ApoE3. NR can though not distinguish whether it is the same protein stretching across the core and the heads, or different individual proteins occupying either the head or tail region in the SLB. In summary, even though both ApoE variants displayed more binding to unsaturated bilayers, the NR data highlight a difference between the variants. In particular, the ApoE4 isoform binds to a larger extent to the lipid core than the ApoE3 isoform and the conformation of this fraction is less sensitive to the type of lipid in the model membrane.

ApoE-Containing Nascent-Like HDL Particle Structure

rHDL made of ApoE and hDMPC were prepared using the vesicle solubilisation approach and purified by size exclusion chromatography (**Figure 3A**). The resulting rHDL particles were structurally characterised by SANS in three isotopic contrasts to highlight different parts of the particle and to increase the accuracy of the fit (**Figure 3B**). For the fitting, the "nanodisc" like structure model was adopted, which consists of an elliptical bilayer encased by protein (inset of **Figure 3A**) and both fitted and calculated values can be found in **Table 2**. These discs resemble nascent HDL. HDL are mainly present in cerebrospinal fluid but are also important for the clearance of lipids in the liver *via* binding to ApoE receptors (Pitas et al., 1987).

The calculated values from **Table 2** are determined as follows. The equation used for circumference determination takes into account the ellipticity of the particles as used previously (Skar-Gislinge et al., 2010):

$$Circumference = 2\pi\sqrt{[(r_{minor}+d_{belt})^2+(r_{major}+d_{belt})^2]/2} \quad (1)$$

where r_{minor}, d_{belt} and r_{major} are the radius of the short axis, the width of the protein belt and the radius of the major axis respectively. This can be used for the determination of the number of amino acids in contact with the bilayer by using an average length per amino acid of 1.5 Å. With 299 residues per ApoE molecule, this gives a maximum circumference of ∼448 Å which is slightly larger than what was calculated here, however leaves room for flexibility in the protein and possible expansion. Previously reported data on related particles prepared with similar proteins have also allowed for some residues to not be in contact with the bilayer: about 20 amino acids per protein were estimated not to be in direct contact with the lipid core (Denisov et al., 2004; Skar-Gislinge et al., 2010). The resulting area of the lipid bilayer region gives 139 lipid molecules per leaflet for both ApoE3 and ApoE4, and each disc contains two proteins, one per leaflet. This value is in agreement with the one measured by phosphate analysis (145 and 151 lipids per leaflet for ApoE3 and ApoE4, respectively). This number of lipids per leaflet agrees with data provided for similar length apolipoprotein-like proteins (Bayburt and Sligar, 2010). The mean molecular area for the heads and tails was calculated to be ∼56 Å^2 with ∼30% hydration in the heads which agrees well with the NR data presented and values found in the literature (Bayburt and Sligar, 2010). The disc diameter is larger compared to ApoA1 discs prepared in a similar manner (Midtgaard et al., 2015); however, ApoE (34 kDa) is substantially longer than ApoA1 (28 kDa) (Lund-Katz and Phillips, 2010), thus resulting in larger discs. The diameter of the particles is in agreement with dynamic light scattering data measured for both ApoE3 and ApoE4 based discs which gave values between 10 and 15 nm prior to SANS measurements (results not shown). Both ApoE3 and ApoE4 gave similar structured discs with the same number of lipid molecules per leaflet and number of proteins. This is not surprising due to the same protein length and very similar sequence, only differing in one amino acid. The main structural difference in the discs found between the ApoE variants was the ellipticity, with ApoE3-rHDL being less elliptical than ApoE4-rHDL. Finally, allowing the bilayer core thickness to vary between a reasonable range did not significantly improve the fit quality, thus it was kept fixed at 28 Å as it was similar to the value seen with the NR. The use of atomic force microscopy can also be beneficial to measure such thicknesses (Bayburt and Sligar, 2002).

ApoE-Containing rHDL at Model Membranes

As ApoE isoforms play different roles in the onset and development of atherosclerosis and AD, with lipids found in both atherosclerotic and AD plaques, we therefore used NR to determine how the nascent-like rHDL of each isoform behave in the exchange or removal of lipids. To this end, ApoE-rHDL particles were incubated with model membranes composed of dDMPC, in the absence or presence of cholesterol, at 37°C in Tris buffer at pH 7.4, and their interactions were followed by NR (**Figure 4**). Both hydrogenous (h-cholesterol) and deuterated cholesterol (d-cholesterol) were used to determine whether ApoE particles specifically targeted the cholesterol molecules.

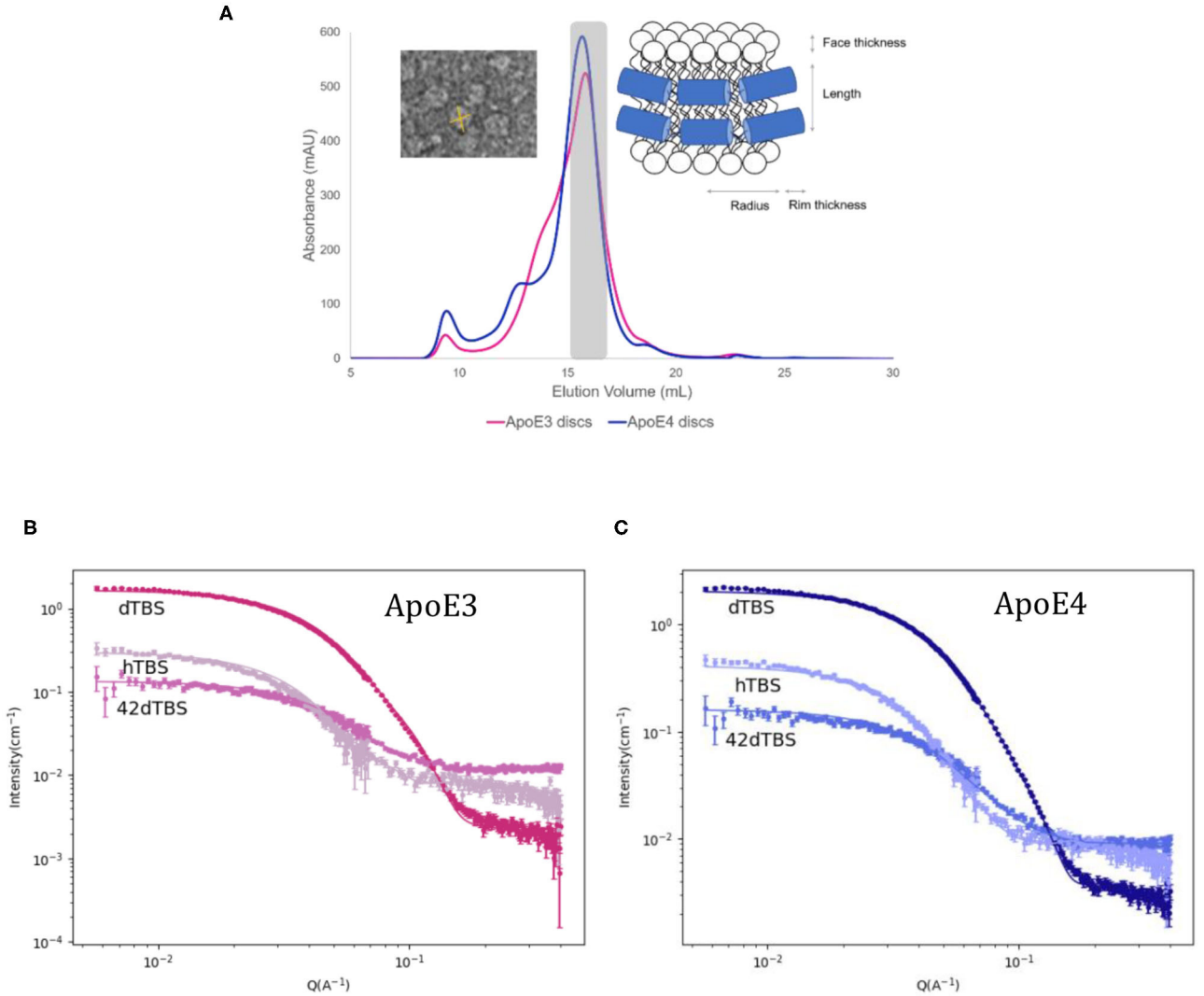

FIGURE 3 | Size exclusion chromatograms for ApoE3 and ApoE4 discs with inset of model used for fitting and negative stained TEM images for ApoE3-rHDL **(A)** SANS data and best fits in three contrasts for the ApoE3- **(B)** and ApoE4-rHDL **(C)** measured at 25°C in Tris buffer pH 7.4. The parameters used for the best fits shown are listed in **Table 2**.

As shown in **Figure 4A**, there was little change in the surface coverage of the model membrane upon interaction with ApoE-rHDL as all SLBs started with at least 95% coverage and finished with no less than 90% coverage. At similar protein concentration, such small capacity for lipid removal cannot be compared to mature HDL (purified from 3 male, healthy adult donors) (Waldie et al., 2020), which can remove about 40% of the model membrane (Waldie et al., 2020) in the absence of cholesterol. This shows that, while some lipids were removed in certain cases, lipid removal is not the main role of the ApoE nascent-like HDL. HDL particles contain a large number of apolipoproteins (Maric et al., 2019), with ApoA1 being the most abundant in serum. Thus, the interaction of ApoA1-rHDL (also prepared by the vesicle solubilisation method (Del Giudice et al., 2017a,b) with a cholesterol containing saturated membrane was also investigated (Del Giudice et al., 2017a,b). In the case of ApoA1-rHDL, significant lipid removal occurred, though to a lesser extent than mature HDL. Lipid removal was double for ApoA1-rHDL and as much as five times for mature HDL as compared to ApoE-rHDL samples. This suggests that more than just the increased incubation time (ApoA1-rHDL and HDL were incubated for 8 h rather than 6 h) is at play. Additionally, kinetics of lipid exchange show that equilibrium was reached after 6 h for ApoE3-rHDL (**Figure 4C**) and ApoA1 (**Supplementary Figure 5**) while continuous increase was observed for ApoE4-rHDL (**Figure 4D**), regardless of membrane composition.

Lipid exchange (**Figure 4B**) is hereby defined as lipids removed from the model membrane and replaced with lipids from the rHDL particles, and is calculated from the SLD change within the lipid tail region. In this case, a significant proportion

TABLE 2 | Fitted and calculated parameters for the protein-DMPC particles.

Parameters	ApoE3	ApoE4
Radius* Å	42.0 ± 0.4	38.1 ± 0.2
Ellipticity ratio*	1.4	1.7
Protein rim thickness* Å	11.0 ± 0.8	8.6 ± 0.3
Lipid headgroup thickness* Å	9.0 ± 0.1	9.0 ± 0.1
Bilayer core thickness*** Å	28	28
Short-long axis disc diameter** Å	106–139.6	93.4–146.7
Disc circumference** Å	389	386
No. amino acids**	260	258
Area per lipid** $Å^2$	55.9	55.9
No. lipids per leaflet**	139	139
No. proteins per disc**	2	2

*Fitted values. **Calculated values. ***Fixed value.

of the lipids were exchanged by ApoE-rHDL and the extent of which was similar regardless of the ApoE isoform present. In the absence of cholesterol, 40.4 ± 0.5% and 37.2 ± 0.6% lipid exchange occurred for ApoE3- and ApoE4-rHDL respectively. However, in the presence of cholesterol, 30.0 ± 0.5% and 29.1 ± 0.5% lipid exchange took place for ApoE3- and ApoE4-rHDL respectively. Bearing in mind the difference in incubation time (ApoE3-rHDL were incubated 2 h longer than ApoE4-rHDL, see **Figures 4C,D**), this suggests that ApoE4-rHDL have the ability to exchange more lipids than ApoE3-rHDL. This is confirmed when observing the quantities of lipids exchanged in the membranes containing d-cholesterol for which the samples were incubated for the same time period (6 h). In this case, the final exchange values differ more drastically: 16.7 ± 0.8% and 25 ± 1% for ApoE3 and ApoE4, respectively. The trend is clear that ApoE4-rHDL exchanged more lipids than the ApoE3-rHDL regardless of membrane composition. In **Figure 4B**, the extent of lipid exchange for both ApoA1-rHDL and mature HDL upon 8 h incubation has similar lipid exchange capacity to ApoE3-rHDL, while ApoE4-rHDL has significantly greater affinity for lipid exchange than any of the other samples tested.

To be able to determine if cholesterol was being preferentially exchanged by either ApoE variant, both deuterated and non-deuterated cholesterol were used. If cholesterol was exchanged preferentially over the phospholipids, a net difference would be seen in the final quantity of lipids exchanged across these two membranes due to lack of contrast between h-cholesterol and the hydrogenous lipids in the rHDL or mature HDL samples. No difference was seen as shown in **Figures 4C,D** (dotted and dashed lines), which suggests that the phospholipid molecules were primarily exchanged rather than the cholesterol molecules.

Mirroring the NR data for protein incubation alone on model membranes (**Figure 2**), the model membranes exposed to ApoE4-rHDL required greater structural and compositional changes to obtain a satisfactory fit to the experimental data. Membranes exposed to ApoE3-rHDL were fitted with head and tail region thicknesses kept constant, whereas ApoE3-rHDL on dDMPC + d-cholesterol and all membranes exposed to ApoE4-rHDL required changes to the head and tail thicknesses to find suitable fits. All variations were tested: from keeping them all the same, to only altering the head thickness or to varying all regions. It was found that better fits were possible when allowing greater variation when incubated with ApoE4-rHDL, again indicating greater level of interaction occurring in the presence of ApoE4 compared to ApoE3. This could in part be due to slight embedding of ApoE4 into the hydrophobic core of the membrane, although the resulting membranes were found to maintain, within error, a constant area per molecule across heads and tails. This suggests that the lipid bilayer structure was retained in all cases, however it cannot be disregarded that protein insertion could be balanced in the lipid heads and tails in such a manner that the SLB structure holds. Finally, similar levels of rHDL particles on top of the model membranes were found regardless of ApoE isoform or bilayer composition (approximately 1%).

DISCUSSION

While the structural difference between the ApoE isoforms is subtle (Chou et al., 2005), clear differences can be seen in their behaviour upon interaction with lipid bilayers. In particular, ApoE4 binds to a larger extent to the membrane core than ApoE3 (**Figure 2C**), although about the same amount of protein sits on top of the membrane regardless of the lipid type, for each isoform, respectively (**Figure 2D**). These changes impact the ability of ApoE to bind lipids. In particular, ApoE4 has a greater ability to bind lipids due to structural differences in the helical segments of the C-terminal. This difference leads to a reduced ability to form tetramers, which are less capable than the monomer of binding lipids (Garai et al., 2011; Chetty et al., 2017). ApoE4's increased affinity for lipid binding is also suggested by the fact that ApoE4 preferentially binds to VLDL (for which its surface is about 60% lipids) rather than HDL, whereas ApoE3 binds preferentially to HDL (for which its surface is about 80% protein). Furthermore, ApoE4 lacks flexibility in its C-terminal domain leading to a preference for the lower curvature of the VLDL particles (Hatters et al., 2005; Nguyen et al., 2010). The increased affinity for VLDL leads to an increased clearance of VLDL from plasma *via* ApoE receptors in the liver. However, this in turn leads to LDL receptors being downregulated, raising overall levels of plasma LDL and leading to an increased risk for atherosclerosis (Dong and Weisgraber, 1996; Mahley, 2016a).

Here, we observed that most protein incorporation into bilayers (**Figure 2A**) occurred within the first hour for the unsaturated lipids but there was further increase with time for saturated ones. Earlier reports on the rate of lipid binding and vesicle solubilisation showed a biexponential decay when solubilising DMPC vesicles at their melting temperature of 24°C (Segall et al., 2002), with ApoE4 presenting a higher rate constant than ApoE3. Another study showed that ApoE4 displays an increased ability to disrupt DMPC vesicles compared to ApoE3 by measuring the release of fluorescent dye (Ji et al., 2002).

Recently, our group showed that native HDL, through its apolipoproteins, present a lower ability to exchange and replace unsaturated lipids as compared to saturated ones (Waldie et al.,

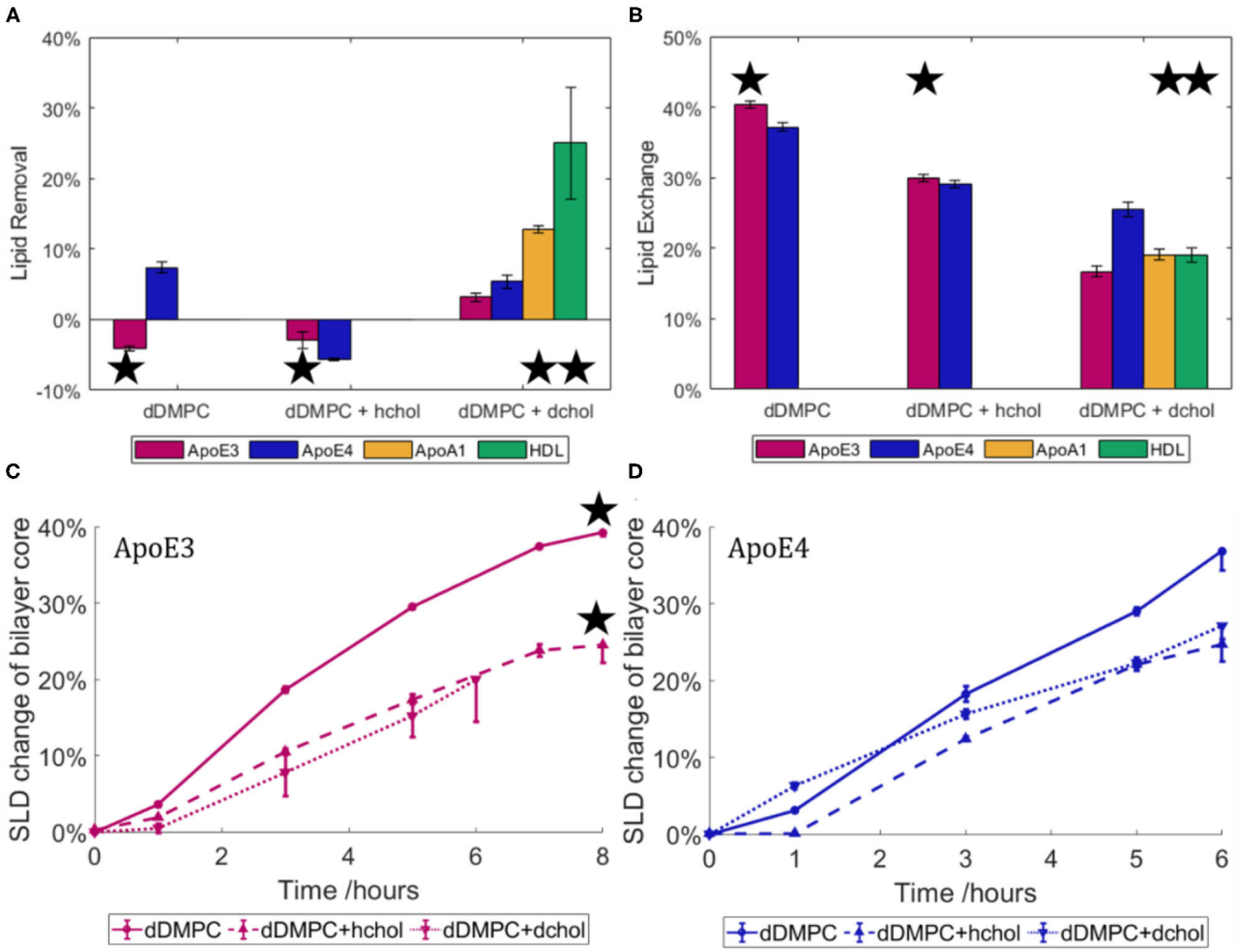

FIGURE 4 | Lipid removal **(A)** and lipid exchange **(B)** across model membranes for ApoE3- and ApoE4-rHDL. Three model membranes were used: saturated lipids (dDMPC) in the absence or presence of hydrogenous or deuterated cholesterol. Data for mature HDL and ApoA1-rHDL against the cholesterol containing bilayers (Waldie et al., 2020) are also included. The asterisk indicates an incubation time of 8 h compared to 6 h for those without. Kinetics of lipid exchange for rHDL containing ApoE3 **(C)** and ApoE4 **(D)** in terms of the relative change in SLD of the solvated lipid core over time. HDL data is replotted from Haertlein et al. (2016). The NR profiles and best fits are given in the **Supplementary Figures 4**, **5**. All statistically different assuming $p = 0.05$ apart from dDMPC + hchol for lipid exchange **(B).**

2020). Both ApoE variants mirror this trend since these proteins remove more saturated than unsaturated lipids. Atherogenic and amyloid plaques are rich in saturated lipids and cholesterol (Touboul and Gaudin, 2014; Kiskis et al., 2015). In a recent study, a link between AD and the disruption of the metabolism of unsaturated fats such as omega 3 was found, which could provide an explanation for ApoE4's higher affinity for the unsaturated membrane (Snowden et al., 2017). Indeed, a previous report states that supplementing mono- and poly-unsaturated fats in the diet reduce the risk to AD, whereas the introduction of saturated fats increase this risk (Morris, 2004).

The fact that a larger fraction of ApoE4 binds the lipid core compared to ApoE3 and that it displays less sensitivity to the lipid type in the membrane (**Figures 2C,D**) could be linked to a decreased protein flexibility although NR cannot distinguish whether different ApoE molecules bind to the core and the head or if a single protein bends over across tails and heads. Indeed, ApoE4's greater rigidity forces it to maintain a more compact conformation around the lipid core which, in turn, could render it less able to bind to HDL. Earlier, ApoE4 was shown to disrupt the lipid membrane to a larger extent than ApoE3 (Mahley et al., 2009), in agreement with our results that show larger ApoE4 incorporation into the bilayers and greater structural changes in the SLBs required to fit the NR data after protein incubation. Indeed, ApoE4 could retain a more compact structure folded back on itself due to the Arg-61:Glu-255 salt bridge that could restrain the protein's structure even when associated with lipids (Raussens et al., 1998; Drury and Narayanaswami, 2005; Hatters et al., 2009).

Regarding the rHDL structure, the reports on ApoE-containing particles mainly involve electron microscopy and spectroscopic studies for structural determination

(Narayanaswami et al., 2004; Newhouse et al., 2005); and ultracentrifugation (Raussens et al., 1998) and native gel electrophoresis (Raussens et al., 1998; Narayanaswami et al., 2004) for size determination. These reports are in agreement with the size of particles reported here: 10–15 nm in diameter (**Figure 3** and **Table 2**). Contrary to ApoE-rHDL, ApoA1- or membrane scaffold protein (MSP)-based nanodiscs form particles that are about 8–12 nm in diameter (Denisov et al., 2004; Bayburt and Sligar, 2010; Skar-Gislinge et al., 2010; Del Giudice et al., 2017a). A variety of models have been presented to describe protein-lipid particles from the picket-fence model (Jonas et al., 1989), to the double superhelix (Wu et al., 2009) or double belt-like structure (Segrest et al., 1999; Midtgaard et al., 2015), though some of these have faced opposition within the nanodisc community (Jones et al., 2010; Gogonea, 2016). Ellipticity is the main structural feature which differed between the ApoE rHDL, with ApoE4 forming more elongated discs. Our data agree well with the double belt structure since the data suggest that there are two proteins present per nanodisc, also in agreement with ApoA1-rHDL. Previously reported data on ApoE-rHDL show the presence of two or more proteins per disc (Raussens et al., 1998; Narayanaswami et al., 2004; Yamamoto et al., 2008). There has been some debate as to whether ApoE3 and ApoE4 form nanodiscs in a different manner giving structural differences to the protein conformation (de Chaves and Narayanaswami, 2008) and, in turn, their lipid exchange ability. The hypotheses suggested include ApoE3 forming more of an extended belt conformation around the whole perimeter of the disc due to increased flexibility (Narayanaswami et al., 2004). The more compact structure of ApoE4 could lead to potentially more ApoE4 molecules per nanodisc compared to ApoE3 (Gong et al., 2002). However, the same number of molecules were found to be present in both nanodisc variants presented here. The NR lipid exchange data (**Figure 4**), on the other hand, suggest that the proteins adapt slightly different conformations giving rise to their differing exchange capabilities.

Where some reports have shown an incremental size increase of nanodiscs with increasing protein length (Denisov et al., 2004, 2005), it is of no surprise that the ApoE-rHDL particles reported here are of a slightly larger size than previously reported for ApoA1-rHDL, as the ApoE protein is longer. In turn, the number of lipid molecules per nanodisc is also higher for ApoE- than ApoA1-containing nanodiscs which does not seem to have an effect on the ability of these nanodiscs to exchange lipids: the similar size of ApoE3- and ApoE4-rHDL does not translate into similar functional capabilities, as clear differences were observed in their lipid exchange and removal affinity (**Figures 4A,B**). Moreover, the lipid exchange (**Figure 4B**) was similar between ApoE3- and ApoA1-rHDL while it was different between ApoE isoforms, despite them being of similar size but larger than ApoA1 (since the nanodisc concentration was constant across samples, smaller discs imply lower lipid concentration in the case of ApoA1). Therefore, it is clear that the rHDL size (area of the lipid nanodisc) does not determine the extent of lipid exchange; rather, specific apolipoprotein-lipid interactions must be behind the observed phenomena.

ApoA1 and ApoE have similar structures comprising amphipathic alpha-helices that enable them to form nascent HDL-like structures by solubilising phospholipids (Lund-Katz and Phillips, 2010). However, neither ApoE3 nor ApoE4 remove further lipids from the membrane than those exchanged, to a significant degree. This contrasts from what is observed for ApoA1-rHDL, which instead remove a notable quantity of lipids, although to a lesser extent than mature HDL (**Figure 4A**). The results obtained for ApoA1 are not surprising since it is the more abundant serum HDL protein, whose function is to clear lipids. Our results suggest that the function of ApoE cannot be mainly related to the lipid exchange, but rather to binding ApoE-receptors in the liver. Indeed, the fact that the structure of ApoE4 is more compact than ApoE3 might affect how it binds to ApoE- and other LDL receptors in the liver (Ruiz et al., 2005). However, ApoE-HDL serve as the primary brain lipoproteins, being produced there and lacking the ability to cross the blood-brain barrier (Pitas et al., 1987). The ApoE in the brain is the second most abundant place for ApoE production in the body after the liver (Mahley, 2016a). ApoE plays an important role in maintaining the homeostasis of cholesterol concentration in the brain, where this lipid comprises about 20–25% of the body's total cholesterol (Michikawa, 2006). Whilst HDL in the rest of the body participate in cholesterol efflux thereby removing cholesterol from artery walls, ApoE-HDL in the brain maintain constant cholesterol levels (Mahley, 2016b). Indeed, the current data clearly show that lipid exchange was not affected by the level of deuteration in cholesterol (**Figure 4**), suggesting that ApoE does not interact with cholesterol significantly. Instead, these results suggest that ApoE-enriched HDL rather transport saturated lipids over cholesterol and unsaturated lipids. By regulating the ratio of saturated lipids in cellular membranes, ApoE-HDL may help maintain membrane elasticity, which is key for the healthy function of the cell. Interestingly, cholesterol crystal nucleation starts sooner in unsaturated than saturated model biles (Halpern et al., 1993), which suggests a higher free cholesterol concentration is achieved in membranes comprised of saturated lipids. Thus, ApoE4 can potentially favour an increase in membrane saturation with cholesterol by exchanging and removing more saturated fats than ApoE3, which could potentially lead to cholesterol crystallisation in the brain.

Even though ApoE4 has a higher affinity to bind lipids than ApoE3 as demonstrated here and elsewhere (Saito et al., 2003), the ability of ApoE isoforms to catalyse the efflux of cholesterol has been disputed: some studies conclude the process is not ApoE isoform dependent (Krimbou et al., 2004) while others have found that ApoE4 has a lesser ability to perform cholesterol efflux compared to ApoE3, especially in relation to neurons in the brain (Huang et al., 1995; Gong et al., 2002; Michikawa et al., 2007). This lack of ability of ApoE4 to remove and deposit cholesterol in the brain efficiently has been proposed to be one of the main reasons for the onset of AD (Gong et al., 2002; de Chaves and Narayanaswami, 2008). Our simplified model shows that neither ApoE isoform has a special affinity for taking up cholesterol and it is therefore hypothesised that there is no significant difference in their capacity to efflux cholesterol.

CONCLUSIONS

Neutron reflection results suggest that ApoE4 adopts a different conformation to ApoE3 at model membranes, and that this conformation differs between saturated and unsaturated membranes for ApoE3 only. Moreover, neither ApoE isoform removes a significant amount of unsaturated lipids from the model membrane used but they were able to remove saturated lipids to similar extents. Small-angle neutron scattering was used to demonstrate that the structure of nascent-like rHDL particles made with DMPC and either ApoE3 or ApoE4 is similar, forming elliptical disc-like structures. Neutron reflection was then used to quantify the extent of lipid exchange and lipid removal by nascent-like rHDL particles and model membranes. The data show that either ApoE3- or ApoE4-rHDL particles have a low ability to remove saturated lipids as compared to ApoA1-rHDL or mature HDL. The extent of lipid exchange, on the other hand, is similar between the isoforms and is impaired by the presence of cholesterol. Finally, ApoE does not exchange or remove cholesterol molecules but rather saturated lipids. The results here mirror the physiological roles of ApoE-HDL and ApoA1-HDL particles in the brain and in serum respectively. This demonstrates that our models are suitable to study the function of these particles in a range of experimental conditions.

DATA AVAILABILITY STATEMENT

The datasets presented in this study can be found in online repositories. The names of the repository/repositories and accession number(s) can be found at: DOIs: 10.5291/ILL-DATA.9-13-807 (FIGARO, June, September 2019), 10.5291/ILL-DATA.9-13-894 (FIGARO, February 2020) and 10.5291/ILL-DATA.8-03-979 (D11, September 2020).

AUTHOR CONTRIBUTIONS

SW produced the ApoE and ApoE-rHDL, participated in the planning of the experiments, performed all experiments, analysed all of the NR and SANS data and wrote the initial draft of this article. FS, NP, YG, SP, and MC participated in performing some of the experiments. FS, FR-R, and MC supported the data analysis. SW and MM produced the deuterated cholesterol and HP purified it. RDG produced the ApoA1-rHDL. TD and NY produced the POPC used. MM, SM, VF, MH, and MC participated in the planning of the experiments. MM, MH, and VF supervised activities in the ILL's Life Sciences Group. MC obtained the funding and supervised the work. All authors contributed to the discussions and editing of the manuscript.

FUNDING

MC thanks the Swedish Research Council, Grant Number 2014-2981. VF thanks the EPSRC for grants GR/R99393/01 and EP/C015452/1 which funded the creation of the Deuteration Laboratory in ILL's Life Science Group. The National Deuteration Facility in Australia is partly funded by The National Collaborative Research Infrastructure Strategy (NCRIS) an Australian Government initiative. This work was also partly funded by a PhD studentship at the ILL.

ACKNOWLEDGMENTS

We thank the ILL neutron facility for granted beamtimes with DOIs: 10.5291/ILL-DATA.9-13-807 (FIGARO, June, September 2019), 10.5291/ILL-DATA.9-13-894 (FIGARO, February 2020) and 10.5291/ILL-DATA.8-03-979 (D11, September 2020) and the Partnership for Soft Condensed Matter at the ILL for the use of sample preparation facilities. This work benefited from the use of the SasView application, originally developed under NSF award DMR-0520547. SasView contains code developed with funding from the European Union's Horizon 2020 research and innovation programme under the SINE2020 project, grant agreement No 654000. This work used the EM facilities at the Grenoble Instruct-ERIC Center (ISBG; UMS 3518 CNRS CEA-UGA-EMBL) with support from the French Infrastructure for Integrated Structural Biology (FRISBI; ANR-10-INSB-05-02) and GRAL, a project of the University Grenoble Alpes graduate school (Ecoles Universitaires de Recherche) CBH-EUR-GS (ANR-17-EURE-0003) within the Grenoble Partnership for Structural Biology. The IBS Electron Microscope facility is supported by the Auvergne Rhône-Alpes Region, the Fonds Feder, the Fondation pour la Recherche Médicale and GIS-IBiS.

SUPPLEMENTARY MATERIAL

The Supplementary Material for this article can be found online at: https://www.frontiersin.org/articles/10.3389/fchem.2021.630152/full#supplementary-material

REFERENCES

Åkesson, A., Lind, T., Ehrlich, N., Stamou, D., Wacklin, H., and Cárdenas, M. (2012a). Composition and structure of mixed phospholipid supported bilayers formed by POPC and DPPC. *Soft Matter*. 8, 5658–5665. doi: 10.1039/c2sm00013j

Åkesson, A., Lind, T. K., Barker, R., Hughes, A., and Cárdenas, M. (2012b). Unraveling dendrimer translocation across cell membrane mimics. *Langmuir* 28, 13025–13033. doi: 10.1021/la3027144

Angeloni, E., Paneni, F., Landmesser, U., Benedetto, U., Volpe, M., Sinatra, R., et al. (2013). Lack of protective role of HDL-C in patients with coronary artery disease undergoing elective coronary artery bypass grafting. *Eur. Heart. J.* 34, 3557–3562. doi: 10.1093/eurheartj/eht163

Barrett, M. A., Zheng, S., Toppozini, L. A., Alsop, R. J., Dies, H., Wang, A., et al. (2013). Solubility of cholesterol in lipid membranes and the formation of immiscible cholesterol plaques at high cholesterol concentrations. *Soft Matter*. 9, 9342–9351. doi: 10.1039/c3sm50700a

Bayburt, T. H., and Sligar, S. G. (2002). Single-molecule height measurements on microsomal cytochrome P450 in nanometer-scale phospholipid bilayer

disks. *Proc. Natl. Acad. Sci. U.S.A.* 99, 6725–6730. doi: 10.1073/pnas.062565599

Bayburt, T. H., and Sligar, S. G. (2010). Membrane protein assembly into Nanodiscs. *FEBS Lett.* 584, 1721–1727. doi: 10.1016/j.febslet.2009.10.024

Browning, K. L., Lind, T. K., Maric, S., Barker, R. D., Cárdenas, M., and Malmsten, M. (2018). Effect of bilayer charge on lipoprotein lipid exchange. *Colloids Surfaces B Biointerfaces*. 117–25. doi: 10.1016/j.colsurfb.2018.01.043

Browning, K. L., Lind, T. K., Maric, S., Malekkhaiat-Häffner, S., Fredrikson, G. N., Bengtsson, E., et al. (2017). Human lipoproteins at model cell membranes: effect of lipoprotein class on lipid exchange. *Sci. Rep*. 7:7478. doi: 10.1038/s41598-017-07505-0

Campbell, R. A., Wacklin, H. P., Sutton, I., Cubitt, R., and Fragneto, G. (2011). FIGARO: the new horizontal neutron reflectometer at the ILL. *Eur. Phys. J. Plus*. 126:107. doi: 10.1140/epjp/i2011-11107-8

Campbell, R. A., Wacklin, H. P., Sutton, I., Cubitt, R., and Fragneto, G. (2015). Erratum to: FIGARO: the new horizontal neutron reflectometer at the ILL. *Eur. Phys. J. Plus* 130:220. doi: 10.1140/epjp/i2015-15220-4

Chen, J., Li, Q., and Wang, J. (2011). Topology of human apolipoprotein E3 uniquely regulates its diverse biological functions. *PNAS* 108, 14813–14818. doi: 10.1073/pnas.1106420108

Chetty, P. S., Mayne, L., Lund-Katz, S., Englander, S. W., and Phillips, M. C. (2017). Helical structure, stability, and dynamics in human apolipoprotein E3 and E4 by hydrogen exchange and mass spectrometry. *PNAS* 114, 968–973. doi: 10.1073/pnas.1617523114

Chou, C.-Y., Lin, Y.-L., Huang, Y.-C., Sheu, S.-Y., Lin, T.-H., Tsay, H.-J., et al. (2005). Structural variation in human apolipoprotein E3 and E4: secondary structure, tertiary structure, and size distribution. *Biophys. J.* 88, 455–466. doi: 10.1529/biophysj.104.046813

Clifton, L. A., Campbell, R. A., Sebastiani, F., Campos-Terán, J., Gonzalez-Martinez, J. F., Björklund, S., et al. (2020). Design and use of model membranes to study biomolecular interactions using complementary surface-sensitive techniques. *Adv. Colloid Interface Sci.* 277:102118. doi: 10.1016/j.cis.2020.102118

Davidson, W. S., Rodrigueza, W. V., Lund-Katz, S., Johnson, W. J., Rothblat, G. H., and Phillips, M. C. (1995). Effects of acceptor particle size on the efflux of cellular free cholesterol. *J. Biol. Chem*. 270, 17106–17113. doi: 10.1074/jbc.270.29.17106

Davidson, W. S., Silva, R. A. G. D., Chantepie, S., Lagor, W. R., Chapman, M. J., and Kontush, A., (2009). Proteomic analysis of defined HDL subpopulations reveals particle-specific protein clusters: relevance to antioxidative function. *Arterioscler Thromb. Vasc. Biol.* 29, 870–876. doi: 10.1161/ATVBAHA.109.186031

de Chaves, E. P., and Narayanaswami, V. (2008). Apolipoprotein E and cholesterol in aging and disease in the brain. *Fut. Lipidol.* 3, 505–530. doi: 10.2217/17460875.3.5.505

Del Giudice, R., Domingo-Espín, J., Iacobucci, I., Nilsson, O., Monti, M., Monti, D. M., et al. (2017a). Structural determinants in ApoA-1 amyloidogenic variants explain improved cholesterol metabolism despite low HDL levels. *BBA-Mol. Basis Dis*. 1863, 3038–3048. doi: 10.1016/j.bbadis.2017.09.001

Del Giudice, R., Nilsson, O., Domingo-Espín, J., and Lagerstedt, J. O. (2017b). Synchrotron radiation circular dichroism spectroscopy reveals structural divergences in HDL- bound apoA-1 variants. *Sci. Rep*. 7:13540. doi: 10.1038/s41598-017-13878-z

Denisov, I. G., Grinkova, Y. V., Lazarides, A. A., and Sligar, S. G. (2004). Directed self-assembly of monodisperse phospholipid bilayer nanodiscs with controlled size. *J. Am. Chem. Soc.* 126, 3477–3487. doi: 10.1021/ja0393574

Denisov, I. G., McLean, M. A., Shaw, A. W., Grinkova, Y. V., and Sligar, S. G. (2005). Thermotropic phase transition in soluble nanoscale lipid bilayers. *J. Phys. Chem. B* 109, 15580–15588. doi: 10.1021/jp051385g

Dong, L.-M., and Weisgraber, K. H. (1996). Human apolipoprotein E4 domain interaction. *J. Biol. Chem*. 271, 19053–19057. doi: 10.1074/jbc.271.32.19053

Drury, J., and Narayanaswami, V. (2005). Examination of lipid-bound conformation of apolipoprotein E4 by pyrene excimer fluorescence. *J. Biol. Chem*. 15, 14605–14610. doi: 10.1074/jbc.M414019200

Gallová, J., Uhríková D., Hanulová M., Teixeira, J., and Balgavý P. (2004). Bilayer thickness in unilamellar extruded 1,2-dimyristoleoyl and 1,2-dierucoyl phosphatidylcholine vesicles: SANS contrast variation study of cholesterol effect. *Colloids Surfaces B Biointerfaces* 38, 11–14. doi: 10.1016/j.colsurfb.2004.07.012

Garai, K., Baban, B., and Frieden, C. (2011). Dissociation of apoE oligomers to monomers is required for high affinity binding to phospholipid vesicles. *Biochemistry* 50, 2550–2558. doi: 10.1021/bi1020106

Gille, A., Easton, R., Andrea, D., Wright, S. D., and Shear, C. L. (2014). CSL112 enhances biomarkers of reverse cholesterol transport after single and multiple infusions in healthy subjects. *Arterioscler Thromb. Vasc. Biol.* 34, 2106–2114. doi: 10.1161/ATVBAHA.114.303720

Gogonea, V. (2016). Structural Insights into high density lipoprotein: old models and new facts. *Front. Pharmacol.* 6:318. doi: 10.3389/fphar.2015.00318

Gong, J.-S., Kobayashi, M., Hayashi, H., Zou, K., Sawamura, N., Fujita, S. C., et al. (2002). Apolipoprotein E (ApoE) isoform-dependent lipid release from astrocytes prepared from human ApoE3 and ApoE4 knock-in mice. *J. Biol. Chem*. 277, 29919–29926. doi: 10.1074/jbc.M203934200

Gordon, D. J., Probstfield, J. L., Garrison, R. J., Neaton, J. D., Castelli, W. P., Knoke, J. D., et al. (1989). High-density lipoprotein cholesterol and cardiovascular disease four prospective American studies. *Circulation* 79, 8–15. doi: 10.1161/01.CIR.79.1.8

Haertlein, M., Moulin, M., Devos, J. M., Laux, V., Dunne, O., and Forsyth, V. T. (2016). Biomolecular deuteration for neutron structural biology and dynamics. *Methods Enzymol.* 566, 113–157. doi: 10.1016/bs.mie.2015.11.001

Halpern, Z., Moshkowitz, M., Laufer, H., Peled, Y., and Gilat, T. (1993). Effect of phospholipids and their molecular species on cholesterol solubility and nucleation in human and model biles. *Gut*. 34, 110–115. doi: 10.1136/gut.34.1.110

Hatters, D. M., Budamagunta, M. S., Voss, J. C., and Weisgraber, K. H. (2005). Modulation of apolipoprotein E structure by domain interaction: Differences in lipid-bound and lipid-free forms. *J. Biol. Chem*. 280, 34288–34295. doi: 10.1074/jbc.M506044200

Hatters, D. M., Voss, J. C., Budamagunta, M. S., Newhouse, Y. N., and Weisgraber, K. H. (2009). Insight on the molecular envelope of lipid-bound apolipoprotein e from electron paramagnetic resonance spectroscopy. *J. Mol. Biol.* 386, 261–271. doi: 10.1016/j.jmb.2008.12.040

Huang, Y., von Eckardstein, A., Wu, S., and Assmann, G. (1995). Effects of the apolipoprotein E polymorphism cell-derived cholesterol in plasma. *Am. Soc. Clin. Investig.* 96, 2693–2701. doi: 10.1172/JCI118336

Hung, W.-C., Lee, M.-T., Chen, F.-Y., and Huang, H. W. (2007). The condensing effect of cholesterol in lipid bilayers. *Biophys. J.* 92, 3960–3967. doi: 10.1529/biophysj.106.099234

Ji, Z.-S., Miranda, R. D., Newhouse, Y. M., Weisgraber, K. H., Huang, Y., and Mahley, R. W. (2002). Apolipoprotein E4 potentiates amyloid β peptide-induced lysosomal leakage and apoptosis in neuronal cells. *J. Biol. Chem*. 277, 21821–21828. doi: 10.1074/jbc.M112109200

Jonas, A. (2002). Lipoprotein structure. *Biochem. Lipids Lipoprot. Membranes* 483–504. doi: 10.1016/S0167-7306(02)36020-4

Jonas, A., Kézdy, K. E., and Wald, J. H. (1989). Defined apolipoprotein A-I conformations in reconstituted high density lipoprotein discs. *J. Biol. Chem*. 264, 4818–4824. doi: 10.1016/S0021-9258(18)83664-X

Jones, M. K., Zhang, L., Catte, A., Li, L., Oda, M. N., Ren, G., et al. (2010). Assessment of the validity of the double superhelix model for reconstituted high density lipoproteins. *J. Biol. Chem*. 285, 41161–41171. doi: 10.1074/jbc.M110.187799

Kiskis, J., Fink, H., Nyberg, L., Thyr, J., Li, J.-Y., and Enejder, A., (2015). Plaque-associated lipids in Alzheimer's diseased brain tissue visualized by nonlinear microscopy. *Sci. Rep*. 5:13489. doi: 10.1038/srep13489

Knoll, W., Schmidt, G., Ibel, K., and Sackmann, E. (1985). Small-angle neutron scattering study of lateral phase separation in dimyristoylphosphatidylcholine-cholesterol mixed membranes. *Biochemistry* 24, 5240–5246. doi: 10.1021/bi00340a043

Krimbou, L., Denis, M., Haidar, B., Carrier, M., Marcil, M., and Genest, J. Jr. (2004). Molecular interactions between apoE and ABCA1: impact on apoE lipidation. *J. Lipid Res.* 45, 839–848. doi: 10.1194/jlr.M300418-JLR200

Ladu, M. J., Reardon, C., Van Eldik, L., Fagan, A. M., Bu, G., Holtzman, D., et al. (2009). Lipoproteins in the central nervous system. *Ann. NY Acad. Sci*. 903, 167–175. doi: 10.1111/j.1749-6632.2000.tb06365.x

Li, X., Kypreos, K., Zanni, E. E., and Zannis, V. (2003). Domains of apoE Required for Binding To apoE receptor 2 and to phospholipids: implications for the functions of apoE in the brain. *Biochemistry* 42, 10406–104017. doi: 10.1021/bi027093c

Lindner, P., and Schweins, R. (2010). The D11 small-angle scattering instrument: a new benchmark for SANS. *Neutron News* 21, 15–18. doi: 10.1080/10448631003697985

Luchini, A., Nzulumike, A. N. O., Lind, T. K., Nylander, T., Barker, R., Arleth, L., et al. (2019). Towards biomimics of cell membranes: structural effect of phosphatidylinositol triphosphate (PIP3) on a lipid bilayer. *Colloids Surfaces B Biointerfaces* 173, 202–209. Available online at https://www.sciencedirect.com/science/article/pii/S0927776518306428

Lund-Katz, S., and Phillips, M. C. (2010). High density lipoprotein structure-function and role in reverse cholesterol transport. *Subcell Biochem*. 51, 183–227. doi: 10.1007/978-90-481-8622-8_7

Madsen, C. M., Varbo, A., and Nordestgaard, B. G. (2017). Extreme high high-density lipoprotein cholesterol is paradoxically associated with high mortality inmen and women: Two prospective cohort studies. *Eur. Heart J*. 38, 2478–2486. doi: 10.1093/eurheartj/ehx163

Mahley, R. W. (2016a). Apolipoprotein E: from cardiovascular disease to neurodegenerative disorders. *J. Mol. Med.* 94, 739–746. doi: 10.1007/s00109-016-1427-y

Mahley, R. W. (2016b). Central nervous system lipoproteins: ApoE and regulation of cholesterol metabolism. *Arterioscler Thromb. Vasc. Biol*. 36, 1305–1315. doi: 10.1161/ATVBAHA.116.307023

Mahley, R. W., Weisgraber, K. H., and Huang, Y. (2009). Apolipoprotein E: structure determines function, from atherosclerosis to Alzheimer's disease to AIDS. *J. Lipid Res.* 50, S183–S188. doi: 10.1194/jlr.R800069-JLR200

Maric, S., Lind, T. K., Raida, M. R., Bengtsson, E., Fredrikson, G. N., Rogers, S., et al. (2019). Time-resolved small-angle neutron scattering as a probe for the dynamics of lipid exchange between human lipoproteins and naturally derived membranes. *Sci. Rep*. 9:7591. doi: 10.1038/s41598-019-43713-6

Michikawa, M. (2006). Role of cholesterol in amyloid cascade: cholesterol-dependent modulation of tau phosphorylation and mitochondrial function. *Acta Neurol. Scand*. 114(Suppl. 185), 21–26. doi: 10.1111/j.1600-0404.2006.00681.x

Michikawa, M., Fan, Q.-W., Isobe, I., and Yanagisawa, K. (2007). Apolipoprotein e exhibits isoform-specific promotion of lipid efflux from astrocytes and neurons in culture. *J. Neurochem*. 74, 1008–1016. doi: 10.1046/j.1471-4159.2000.0741008.x

Midtgaard, S. R., Pedersen, M. C., and Arleth, L. (2015). Small-angle X-ray scattering of the cholesterol incorporation into human ApoA1-POPC discoidal particles. *Biophys. J.* 109, 308–318. doi: 10.1016/j.bpj.2015.06.032

Morris, M. C. (2004). Diet and Alzheimer's disease: what the evidence shows. *MedGenMed* 6, 48.

Moulin, M., Strohmeier, G. A., Hirz, M., Thompson, K. C., Rennie, A. R., Campbell, R. A., et al. (2018). Perdeuteration of cholesterol for neutron scattering applications using recombinant Pichia pastoris. *Chem. Phys. Lipids* 212, 80–87. doi: 10.1016/j.chemphyslip.2018.01.006

Narayanaswami, V., Maiorano, J. N., Dhanasekaran, P., Ryan, R. O., Phillips, M. C., Lund-Katz, S., et al. (2004). Helix orientation of the functional domains in apolipoprotein E in discoidal high density lipoprotein particles. *J. Biol. Chem*. 279, 14273–14279. doi: 10.1074/jbc.M313318200

Nelson, A. (2006). Co-refinement of multiple-contrast neutron/X-ray reflectivity data using MOTOFIT. *J. Appl. Crystallogr*. 39, 273–276. doi: 10.1107/S0021889806005073

Newhouse, Y., Peters-Libeu, C., and Weisgraber, K. H. (2005). Crystallization and preliminary X-ray diffraction analysis of apolipoprotein E-containing lipoprotein particles. *Acta Crystallogr. Sect. F Struct. Biol. Cryst. Commun. F* 61, 981–984. doi: 10.1107/S1744309105032410

Nguyen, D., Dhanasekaran, P., Nickel, M., Nakatani, R., Saito, H., Phillips, M. C., et al. (2010). Molecular basis for the differences in lipid and lipoprotein binding properties of human apolipoproteins E3 and E4. *Biochemistry* 49, 10881–10889. doi: 10.1021/bi1017655

Pitas, R. E., Boyles, J. K., Lee, S. H., Hui, D., and Weisgraber, K. H. (1987). Lipoproteins and their receptors in the central nervous system. *J. Biol. Chem*. 262, 14352–14360. doi: 10.1016/S0021-9258(18)47945-8

Raussens, V., Fisher, C. A., Goormaghtigh, E., Ryan, R. O., and Ruysschaert, J.-M. (1998). The low density lipoprotein receptor active conformation of apolipoprotein E. *J. Biol. Chem*. 273, 25825–25830. doi: 10.1074/jbc.273.40.25825

Reiman, E. M., Arboleda-Velasquez, J. F., Quiroz, Y. T., Huentelman, M. J., Beach, T. G., Caselli, R. J., et al. (2020). Exceptionally low likelihood of Alzheimer's dementia in APOE2 homozygotes from a 5,000-person neuropathological study. *Nat. Commun*. 11:667. doi: 10.1038/s41467-019-14279-8

Ruiz, J., Kouiavskaia, D., Migliorini, M., Robinson, S., Saenko, E. L., Gorlatova, N., et al. (2005). The apoE isoform binding properties of the VLDL receptor reveal marked differences from LRP and the LDL receptor. *J. Lipid Res*. 46, 1721–1731. doi: 10.1194/jlr.M500114-JLR200

Saito, H., Dhanasekaran, P., Baldwin, F., Weisgraber, K. H., Phillips, M. C., and Lund-Katz, S., (2003). Effects of polymorphism on the lipid interaction of human apolipoprotein E. *J. Biol. Chem*. 278, 40723–40729. doi: 10.1074/jbc.M304814200

Segall, M. L., Dhanasekaran, P., Baldwin, F., Anantharamaiah, G. M., Weisgraber, K. H., Phillips, M. C., et al. (2002). Influence of apoE domain structure and polymorphism on the kinetics of phospholipid vesicle solubilization. *J. Lipid Res*. 43, 1688–1700. doi: 10.1194/jlr.M200157-JLR200

Segrest, J. P., Jones, M. K., Klon, A. E., Sheldahl, C. J., Hellinger, M., Loof, H., De, et al. (1999). A Detailed molecular belt model for apolipoprotein A-I in discoidal high density lipoprotein. *J. Biol Chem*. 274, 31755–31758. doi: 10.1074/jbc.274.45.31755

Sergin, I., Bhattacharya, S., Emanuel, R., Esen, E., Stokes, C. J., Evans, T. D., et al. (2016). Inclusion bodies enriched for p62 and polyubiquitinated proteins in macrophages protect against atherosclerosis. *Sci. Signal*. 9:ra2. doi: 10.1126/scisignal.aad5614

Skar-Gislinge, N., Simonsen, J. B., Mortensen, K., Feidenhans'l, R., Sligar, S. G., Lindberg Møller, B., et al. (2010). Elliptical structure of phospholipid bilayer nanodiscs encapsulated by scaffold proteins: Casting the roles of the lipids and the protein. *J. Am. Chem. Soc*. 132, 13713–13722. doi: 10.1021/ja1030613

Snowden, S. G., Ebshiana, A. A., Hye, A., An, Y., Pletnikova, O., O'Brien, R., et al. (2017). Association between fatty acid metabolism in the brain and Alzheimer disease neuro- pathology and cognitive performance: a nontargeted metabolomic study. *PLoS Med*. 14:e1002266. doi: 10.1371/journal.pmed.1002266

Toth, P. P., Barter, P. J., Rosenson, R. S., Boden, W. E., Chapman, M. J., Cuchel, M., et al. (2013). High-density lipoproteins : a consensus statement from the National Lipid Association. *J. Clin. Lipidol.* 7, 484–525. doi: 10.1016/j.jacl.2013.08.001

Touboul, D., and Gaudin, M. (2014). Lipidomics of Alzheimer's disease. *Bioanalysis* 6, 41–61. doi: 10.4155/bio.13.346

Utermann, G. (1975). Isolation and partial characterization of an arginine-rich apolipoprotein from human plasma very-low-density lipoproteins: apolipoprotein E. *Hoppe Seylers Z Physiol. Chem*. 356, 1113–1121. doi: 10.1515/bchm2.1975.356.2.1113

Valanti, E. K., Dalakoura-Karagkouni, K., and Sanoudou, D. (2018). Current and emerging reconstituted HDL-apoA-I and HDL-apoE approaches to treat atherosclerosis. *J. Pers. Med*. 8:34. doi: 10.3390/jpm8040034

Van Capelleveen, J. C., Brewer, H. B., Kastelein, J. J. P., and Hovingh, G. K. (2014). Novel therapies focused on the high-density lipoprotein particle. *Circ. Res.* 114, 193–204. doi: 10.1161/CIRCRESAHA.114.301804

Voight, B. F., Peloso, G. M., Orho-Melander, M., Frikke-Schmidt, R., Barbalic, M., Jensen, M. K., et al. (2012). Plasma HDL cholesterol and risk of myocardial infarction: a mendelian randomisation study. *Lancet* 380, 572–580. doi: 10.1016/S0140-6736(12)60312-2

Waldie, S., Lind, T. K., Browning, K., Moulin, M., Haertlein, M., Forsyth, V. T., et al. (2018). Localization of cholesterol within supported lipid bilayers made of a natural extract of tailor-deuterated phosphatidylcholine. *Langmuir* 34, 472–479. doi: 10.1021/acs.langmuir.7b02716

Waldie, S., Moulin, M., Porcar, L., Pichler, H., Strohmeier, G. A., Skoda, M., et al. (2019). The production of matchout-deuterated cholesterol and the study of bilayer-cholesterol interactions. *Sci. Rep*. 9:5118. doi: 10.1038/s41598-019-41439-z

Waldie, S., Sebastiani, F., Browning, K., Maric, S., Lind, T. K., Yepuri, N., et al. (2020). Lipoprotein ability to exchange and remove lipids from model membranes as a function of fatty acid saturation and presence of cholesterol. *Biochim. Biophys. Acta Mol. Cell. Biol. Lipids* 1865:158769. doi: 10.1016/j.bbalip.2020.158769

Weisgraber, K. H., Rall, S. C., and Mahley, R. W. (1981). Human E apoprotein heterogeneity. *J. Biol. Chem*. 256, 9077–9083. doi: 10.1016/S0021-9258(19)52510-8

Wu, L., and Zhao, L. (2016). ApoE2 and Alzheimer's disease: time to take a closer look. *Neural. Regen. Res*. 11, 412–413. doi: 10.4103/1673-5374.179044

Wu, Z., Gogonea, V., Lee, X., Wagner, M. A., Li, X.-M., Huang, Y., et al. (2009). Double superhelix model of high density lipoprotein. *J. Biol. Chem*. 284, 36605–36619. doi: 10.1074/jbc.M109.039537

Yamamoto, T., Choi, H. W., and Ryan, R. O. (2008). Apolipoprotein E isoform-specific binding to the low-density lipoprotein receptor. *Anal. Biochem*. 372, 222–226. doi: 10.1016/j.ab.2007.09.005

Yepuri, N. R., Darwish, T. A., Krause-Heuer, A. M., Leung, A. E., Delhom, R., Wacklin, H. P., et al. (2016). Synthesis of perdeuterated 1-Palmitoyl-2-oleoyl-sn-glycero-3-phosphocholine ([D82]POPC) and characterisation of Its lipid bilayer membrane structure by neutron reflectometry. *Chempluschem* 81, 315–321. doi: 10.1002/cplu.201500452

Conflict of Interest: The authors declare that the research was conducted in the absence of any commercial or financial relationships that could be construed as a potential conflict of interest.

The reviewer DH declared a past co-authorship with one of the authors VF.

frontiers in Chemistry

ORIGINAL RESEARCH
published: 04 May 2021
doi: 10.3389/fchem.2021.631277

Adhesion Process of Biomimetic Myelin Membranes Triggered by Myelin Basic Protein

*Benjamin Krugmann[1,2], Alexandros Koutsioubas[1], Luman Haris[2,3], Samantha Micciulla[4], Didier Lairez[5], Aurel Radulescu[1], Stephan Förster[3] and Andreas M. Stadler[2,3]**

[1] Jülich Centre for Neutron Science at MLZ, Forschungszentrum Jülich GmbH, Garching, Germany, [2] Institute of Physical Chemistry, RWTH Aachen University, Aachen, Germany, [3] Jülich Centre for Neutron Science (JCNS-1) and Institute for Biological Information Processing (IBI-8), Forschungszentrum Jülich GmbH, Jülich, Germany, [4] Institut Laue-Langevin, Grenoble, France, [5] Laboratoire des Solides Irradiés, École Polytechnique, CEA, CNRS, Institut Polytechnique de Paris, Palaiseau, France

The myelin sheath—a multi-double-bilayer membrane wrapped around axons—is an essential part of the nervous system which enables rapid signal conduction. Damage of this complex membrane system results in demyelinating diseases such as multiple sclerosis (MS). The process in which myelin is generated *in vivo* is called myelination. In our study, we investigated the adhesion process of large unilamellar vesicles with a supported membrane bilayer that was coated with myelin basic protein (MBP) using time-resolved neutron reflectometry. Our aim was to mimic and to study the myelination process of membrane systems having either a lipid-composition resembling that of native myelin or that of the standard animal model for experimental autoimmune encephalomyelitis (EAE) which represents MS-like conditions. We were able to measure the kinetics of the partial formation of a double bilayer in those systems and to characterize the scattering length density profiles of the initial and final states of the membrane. The kinetics could be modeled using a random sequential adsorption simulation. By using a free energy minimization method, we were able to calculate the shape of the adhered vesicles and to determine the adhesion energy per MBP. For the native membrane the resulting adhesion energy per MBP is larger than that of the EAE modified membrane type. Our observations might help in understanding myelination and especially remyelination—a process in which damaged myelin is repaired—which is a promising candidate for treatment of the still mostly incurable demyelinating diseases such as MS.

Keywords: neutron reflectometry, adhesion energy, lipid membranes, myelin basic protein, vesicle fusion, random sequential adsorption, myelin sheath

OPEN ACCESS

Edited by:
Maikel Rheinstadter, McMaster University, Canada

Reviewed by:
Yuri Gerelli, Marche Polytechnic University, Italy
Ravindra Pandey, University of Texas at Austin, United States

***Correspondence:**
Andreas M. Stadler
a.stadler@fz-juelich.de

Specialty section:
This article was submitted to Physical Chemistry and Chemical Physics, a section of the journal Frontiers in Chemistry

Received: *19 November 2020*
Accepted: *01 April 2021*
Published: *04 May 2021*

Citation:
Krugmann B, Koutsioubas A, Haris L, Micciulla S, Lairez D, Radulescu A, Förster S and Stadler AM (2021) Adhesion Process of Biomimetic Myelin Membranes Triggered by Myelin Basic Protein. Front. Chem. 9:631277. doi: 10.3389/fchem.2021.631277

INTRODUCTION

The biological membrane is an important component of cellular function and metabolism. Investigation of biological membrane components, characterization of their physico-chemical properties and the study of their interactions with membrane binding proteins can answer important questions that are central for human health and disease. Several human diseases are directly connected to modification of cellular membranes (Evans, 1980; Maret et al., 1983; Vignini et al., 2007). Degeneration of the well-ordered myelin sheath that exists around nerve

cells in the human brain, for instance, results in nerve conduction failure and neurodegeneration (Love, 2006; Weil et al., 2016). This phenomenon is called demyelination. Myelin basic protein (MBP) stabilizes the myelin membrane multi-layer and is an integral part of the myelin sheath (Boggs, 2006). Of particular relevance is the interaction of MBP with cytoplasmic leaflets of oligodendrocytes. Those cells are assembled to each other by MBP to generate a double bilayer membrane unit which envelopes the axons as a multi-membrane stack forming compact myelin (Quarles et al., 2006). Multiple sclerosis (MS) is a chronic inflammatory disease of the central nervous system, correlated with demyelination through membrane de-adhesion, swelling, and ultimately vesiculation of the myelin sheath (Weil et al., 2016). The lipid compositions of native (healthy) and modified (diseased) myelin sheaths have been investigated in an animal model (Ohler et al., 2004). While the native lipid composition occurs in healthy cytoplasmic myelin sheaths, the diseased lipid composition has been found in animals having experimental autoimmune encephalomyelitis (EAE), which is an animal model to study diseases such as e.g., MS that are connected to demyelination (Ohler et al., 2004). Structural properties of biomimetic native-like and EAE-diseased membranes have been investigated *in vitro* in a biosynthetic approach as oriented membrane bilayers or in the vesicle state (Min et al., 2009, 2011; Shaharabani et al., 2016, 2018; Raasakka et al., 2017). Recently, we found a direct connection between the bending stiffness of large unilamellar vesicles (LUV) having either EAE-diseased or native-like lipid composition and the formation of multilamellar structure which is mediated by the binding strength of MBP with the respective membrane types (Krugmann et al., 2020b).

While most of the above-mentioned studies have investigated structural aspects of those biomimetic myelin-like model membranes in their equilibrium state, knowledge about molecular properties that regulate the kinetics of the assembly process of the myelin sheath is currently still largely missing. A detailed molecular understanding of the formation of the myelin membrane systems is required both from a fundamental biological and biophysical point-of-view as well as to develop novel approaches for medical treatment of neurodegenerative diseases using a process known as remyelination. Remyelination is a process during which a degenerated myelin membrane is replaced by a new sheath, which seems to be thinner than the original, but it is still capable to maintain biological function of myelin (Prineas and Connell, 1979; Franklin and Ffrench-Constant, 2008). There are high expectations to utilize this natural process for the treatment of human demyelinating disorders such as, for instance, MS. Therefore, many efforts are made to understand the molecular mechanism of this process in detail. Currently, knowledge regarding the details of the molecular process of remyelination using vesicle fusion is still missing.

In our study, we investigated molecular aspects of the myelin formation process by using biomimetic membrane systems. We first produced a supported membrane bilayer (SMB) mimicking native or diseased-like cytoplasmic myelin on a silicon substrate and coated it with a dense MBP layer on top. The adsorption kinetics of LUV having the same lipid composition as those bilayers were then studied using neutron reflectometry (NR) as a function of incubation time. NR experiments performed under steady-state conditions at different stages of the assembly process allowed us to gain structural information of the oriented membrane systems orthogonal to the membrane plane with resolution on the nm length-scale. The kinetic adhesion mechanism of the LUV could be modeled by a random sequential adsorption (RSA) process. As the maximal adsorption area of RSA process is known as well as the bending rigidity of the LUV membrane, we could calculate the interaction energy per MBP protein. This parameter was found to be larger for native lipid composition as compared to the EAE-diseased membranes. A perspective for a future application of our approach would be to form myelin-like multilayers by LUV fusion, which would be an interesting mechanism to externally trigger remyelination by LUV fusion.

TABLE 1 | Lipid compositions of native and EAE modified cytoplasmic myelin membranes (Krugmann et al., 2020b).

Lipid type	Native (mol %)	EAE modified (mol %)
PC	25.9	20.1
PE	29.0	32.9
PS	7.0	7.4
SM	6.2	2.2
Cholesterol	31.6	37.4

MATERIALS AND METHODS

Materials

Porcine brain lipids (PC, PE, PS, and SM) and ovine cholesterol were purchased from Avanti Polar Lipids (Alabaster, AL, USA) and bovine MBP from Sigma-Aldrich (St. Louis, MO, USA).

Liposome Preparation

Porcine brain lipids (PC, PE, PS, and SM) with chain compositions given on the Avanti webpage[1] and ovine cholesterol have been separately dissolved in chloroform, or bought in chloroform. The lipids are mixed in ratios found in native and EAE modified myelin (**Table 1**; Krugmann et al., 2020b) and afterwards the chloroform is evaporated using a gentle nitrogen stream followed by vacuum annealing at 50°C overnight. The lipids are then dissolved in D_2O-buffer [150 mM NaCl, 10 mM 3-(N-morpholino) propanesulfonic acid (MOPS)]. The solution is shaken until the lipid cake is no longer stuck at the glass surface. If necessary remaining lipid cake is removed by pipetting. In the following the solution is sonicated for 30 min at 40°C and freeze-thawed 5 consecutive times. To remove remaining large aggregates or giant vesicles the solution is centrifuge-filtered through a 0.45 μm for 10 min at 10,000 g-force. Finally, the solution is extruded through a 100 nm membrane 21 × at 50°C.

[1]https://avantilipids.com/ (accessed March 1, 2021).

Supported Bilayer Preparation

Polished silicon blocks were cleaned by subsequent immersion in chloroform, acetone, ethanol and water under sonication for 20 min each, followed by UV/ozone irradiation for 30 min and rinsing in H_2O to verify hydrophilicity. All silicon substrates were stored in water until utilization to prevent contamination. For the neutron reflectometry measurements, each substrate was sealed in a solid/liquid cell. In detail, the bottom part of the cell is equipped with a PEEK through, which represents the liquid reservoir, while the upper part is an aluminum/Teflon lid. The silicon block is sandwiched between the two parts and the trough (reservoir) filled with Milli-Q water by injection through Teflon tubes (0.5 mm inner diameter), closed by valves. Prior to liposomes solution injection, the cell was pre-heated at 50°C to promote vesicle fusion. When the liposomes were in contact with the hydrophilic SiO surface, a supported membrane bilayer (SMB) was formed and residual liposomes were removed by rinsing with buffer solution.

NR Protocol

Neutron reflectivity measurements were performed on the neutron reflectometer D17 at the Institut Laue-Langevin (ILL, Grenoble, France) (Saerbeck et al., 2018; Krugmann et al., 2020a) operated in time-of-flight mode. The instrumental resolution $\Delta Q/Q$ was varying between 2 and 10% along the full q-range (0.006 0.35 A^{-1}) with accessible wavelengths from 2 to 30 Å and two angles of incidence (0.8 and 3.2°).

The footprint length (in the beam direction) and width (in the perpendicular direction) were $L = 60$ mm and $W = 35$ mm, respectively.

The samples were deposited at the solid/liquid interface of a silicon substrate sealed inside a solid/liquid cells with 1 mL liquid reservoir which was kept at 50°C to promote vesicle fusion; during the rest of the experiment a constant temperature of 37°C was maintained via a thermostatic bath. Contrast variation was carried out via an automatized pumping system at a flow rate of 1 mL/min for a full volume exchange of 20 mL. Firstly, the silicon blocks are characterized in three contrasts (D_2O-buffer, H_2O-buffer, silicon matched water (SMW)-buffer (38% D_2O). Afterwards the respective SMB is formed using the protocol described above. Now, the SMBs are characterized in the same three contrasts. We inject MBP in the cells to coat the SMB as described in Krugmann et al. (2020b). To remove remaining MBP solution the cells are flushed. Again, the membrane is measured at the three contrasts. Finally, the vesicles are injected and the adsorption kinetics is monitored (in D_2O). To enable very fast acquisition the beam divergence is increased and a time resolution of 1 min can be achieved (Cubitt et al., 2015).

NR Data Analysis

For the specular NR, the data first has been reduced using the COSMOS tool in the LAMP software of the ILL. The fitting of those reduced datasets was done using the Anaklasis package based on python (Koutsioubas, 2021). This software allows co-refining multiple datasets as e.g., the same sample at different contrasts or the same sample in D_2O at different steps of the kinetic process. The model assumed is a stratified layer model, while an additional adjustable multiplicative parameter is used for the proper scaling of the reflectivity curves. During data reduction a normalization factor is set accounting for neutron beam attenuation as defined by a direct beam measurement. In the pristine membrane samples only a small deviation to unity is observed which could be explained by a not perfect sample alignment. In the later steps the deviation from unity increases especially in the samples with attached vesicles. This might be accounted to diffuse scattering in these samples. Therefore, less signal is scattered specular and a value smaller than unity needs to be chosen as scaling factor. For the bare membrane we assume the layer order head|chain|head|. This layer sequence will just be called membrane in the following. When adding MBP an additional layer is added and the order is changed to membrane|MBP. After injection of the vesicles the order is changed to membrane|MBP|membrane|diffuse vesicle layer. The diffuse vesicle layer accounts for the 3D structure of the attached vesicles and has a SLD of $0.7 \cdot 10^{-6}$ Å^{-2} between the one of the chain and the head section. As front end we use in all cases Si|SiO|buffer and as back end buffer. Obtained membrane thicknesses are compiled in **Table 2**.

TABLE 2 | Coverage of the second membrane bilayer η, thicknesses of the membrane parts, MBP concentrations in the protein layers, and MBP layer thickness d_{MBP}.

	Native01	Modified01	Modified1
c^*_{MBP} (mg/ml)	0.1	0.1	1
η	0.26 ± 0.02	0.34 ± 0.02	0.39 ± 0.02
d_{head} (Å) (inner)	7.9 ± 1.6	11.1 ± 2.0	8.1 ± 1.4
(outer)	9.8 ± 1.5	11.5 ± 1.7	11.3 ± 1.3
d_{chain} (Å)	31.2 ± 0.8	32.6 ± 0.8	31.6 ± 0.7
$d_{MBP,SBL}$ (Å)	77 ± 68	64 ± 44	72 ± 20
$d_{MBP,DBL}$ (Å)	30.6 ± 2.0	26.4 ± 1.6	24.6 ± 1.3
$c_{MBP,SBL}$ (vol. %)	3 ± 2	5 ± 3	7 ± 2
$c_{MBP,DBL}$ (vol. %)	1 ± 3	0 ± 4	11 ± 3

**MBP concentration in the injected buffer solution. The errors of the fitted parameters are taken from the fit.*

Random Sequential Adsorption Simulation

The RSA simulation is modified from Erban and Chapman (2007) for our system. As starting point we take a test volume (x-y-z = 1 µm – 1 µm – 1 mm) with a constant concentration of vesicles in z-direction. In practice a test area (x-y) is defined. The x-y-surface at $z = 0$ is the adhesive surface. Then we define vesicles in z-direction. Since the concentration should be uniform in x-y-direction we only have to calculate the diffusion of vesicles in z-direction and only initialize the x-y-position in the case that the vesicles touch the surface.

Now we start the diffusion simulation. Therefore, we calculate the diffusion of each vesicle in time steps Δt by

$$z_{new} = z_{old} + \sqrt{2D\Delta t} \cdot \chi \quad (1)$$

Here, D is the diffusion constant and χ is a normal distributed random number.

In the case that the vesicles diffuse to the adhesive surface and no other adhered vesicle is overlapped in *x*-*y*-position they get adsorbed by a certain probability and are removed from the simulation. This is done in the simulation in the case that one of two conditions are fulfilled. The first condition is that the end *z*-position is negative. If this condition is fulfilled the vesicle adsorbs with the probability:

$$p = P \cdot \sqrt{\Delta t} \tag{2}$$

In Erban and Chapman (2007) P describes a positive constant which can be related to the rate constant of the chemical reaction between the virus surface and diffusing polymers. As the geometry of our system is similar in our case P is related to the interaction of vesicles and the MBP coated membrane surface. The second condition checks if the vesicles *z*-position was negative during the step. The adsorption probability is given by:

$$p = \exp\left(-z_{old}\frac{z_{new}}{D\Delta t}\right) \cdot P \cdot \sqrt{\Delta t} \tag{3}$$

At the beginning only, the vesicle concentration close to the surface gets perturbed by the surface adhesion. Therefore, only vesicle diffusion close to the surface is calculated in the beginning. The affected *z*-range $L(t)$ increases is given by:

$$L(t) = 2 \cdot \mathrm{erf}^{-1}0.99 \cdot \sqrt{tD} \tag{4}$$

In this model we assumed the vesicles with diameter $d = 100 \pm 30$ nm as spherical hard shells which exclude the area $A_{ex} = \frac{\pi}{4}d^2$ when attached to the membrane. The simulation has been run 10 consecutive times and the results have been averaged. The time step was set to $\Delta t = 1$ s. We estimated a value $P = 0.015 \cdot 1/\sqrt{t}$ leading to a quite convincing agreement with the measured data. The maximum coverage of such a system has been determined before (Wang, 1994; Cieśla and Nowak, 2016; Cieśla and Ziff, 2018) to be 55.47% for monodisperse disks—which is a good description of the 2D-projection of the vesicles on the membrane surface. In case of polydispersity this value increases as vesicles with smaller diameter can fit in smaller holes (Adamczyk et al., 1997). We simulated the effect for a polydispersity of 0.3 (**Supplementary Figure 1**) which we measured for vesicles of the same compositions and almost identical extrusion procedure via SANS and SAXS (Krugmann et al., 2020b). The coverage seems to be almost completely stable over time—at a time range relevant for the incubation time of the vesicles until the static measurements were started (native ∼20 h, EAE modified ∼10 h). After 1 day we simulated a steric vesicle coverage of 0.60 ± 0.05 (the error was estimated from the incubation time range of the samples) which is used in the further calculations as explained in the following chapter. Here, we used a time step $\Delta t = 10$ s in the simulation. The concentration of vesicles was chosen to be 1 mg/ml. From this value the number concentration was calculated by estimating the weight of one vesicle.

Accessing the Adhesion Constant k_a

Free Energy of a Vesicle

Let us consider a vesicle of area A, supposed to be constant upon deformation, adsorbed onto a plane. Its free energy reduces to two terms:

$$E_{free} = E_a + E_b \ \ with \begin{cases} E_a = -k_a \cdot \alpha_f A \\ E_b = \frac{\kappa}{2}\int (c_1(s) + c_2(s))^2 \, ds \end{cases} \tag{5}$$

The first term E_a is the adhesion energy potential, with k_a the adhesion constant and α_f the area-fraction of the vesicle surface that is flat and adheres to the plane. This term decreases with increasing adhesive-area fraction α_f.

The second term E_b is the bending elastic potential that can be viewed as the variance of the local curvatures $c_1(s)$ and $c_2(s)$ of the surface element ds, with κ the mean-curvature modulus of the bilayer. This term increases as the shape deviates from the sphere, i.e., for increasing flat part given by α_f .

For a given set (α_f, k_a, κ), the vesicle adopts the shape with local curvatures ($c_1(s)$, $c_2(s)$) allowing $\int (c_1(s) + c_2(s))^2 \, ds$ to be minimized with the constraint of curvature-continuity at the boundary of the flat area. Since this constraint depends only on α_f, so does the least-energy shape of the vesicle. Determining this least-energy surface is the first step for the calculation of E_{free}. For this we followed the procedure described in Koutsioubas et al. (2017). The fundamental assumption is the following: the least-energy surface of an adsorbed vesicle is a solid of revolution with a generatrix that is itself a least-energy curve. The main advantage of this method is to reduce the problem to a 1D-problem that can be exactly solved with a minimum computing-time consumption. Actually, the mean-curvature modulus k_c can be independently measured or kept from the literature. So that, E_{free} can be finally computed in the plane (k_a, α_f) (see **Supplementary Figure 2**). For a given adhesion constant k_a, vesicles adopt the value for the adhesive-area fraction α_f allowing E_{free} to be minimized, i.e., in the valley of **Supplementary Figure 2**. Conversely, by measuring α_f one can determine the corresponding value for k_a. The bending rigidity κ of native and EAE-diseased membranes was determined by NSE previously (Krugmann et al., 2020b) and the values of κ are compiled in **Table 3**. Obtained values of α_f and k_a determined in this study are summarized in **Table 3** as well.

Combining RSA Simulations and Neutron Reflectivity Measurements to Access α_f

"From the top" point of view (RSA):

In the RSA model, the addition of a new particle is sensitive to the steric hindrance of particles already adsorbed. Let us denote A_{ex} the maximum extension area parallel to the plane of a vesicle, i.e., its projection area on the plane, and define the "steric coverage density" ρ as:

$$\rho = N \cdot \frac{A_{ex}}{A_{tot}} \tag{6}$$

where N is the number of adsorbed vesicles and A_{tot} the total area of the plane.

"From the bottom" point of view (neutron reflectivity):

On the other side, neutron reflectivity is sensitive to the area of vesicle that adheres and is directly in contact with the plane. Let us denote A_f this area with no curvature per vesicle and define the "adhesive coverage density" η as:

$$\eta = N \cdot \frac{A_f}{A_{tot}} \tag{7}$$

Dividing Equation (6) by Equation (7) gives:

$$\frac{\rho}{\eta} = A_{ex}/A_f \tag{8}$$

TABLE 3 | Values of the bending rigidity κ, the membrane coverage η, the fraction of the vesicles which are flat α_f, the calculated adhesion energy k_a, the area per MBP molecule A_{MBP} and the adhesion energy per MBP molecule ϵ_{MBP}.

	Native01	Modified01
κ ($10^{-19}J$)$^{\#}$	1.44 ± 0.10	1.16 ± 0.06
η	0.26 ± 0.02	0.34 ± 0.02
α_f	0.138 ± 0.022	0.198 ± 0.028
k_a (mJ/m^2)	0.36 ± 0.06	0.45 ± 0.10
A_{MBP} (nm^2)$^{\$}$	156 ± 172	113 ± 103
A_{MBP} (nm^2)$^{\#}$	86 ± 17	50 ± 15
ϵ_{MBP} ($10^{-19}J$)	0.31 ± 0.08	0.23 ± 0.08

$^{\#}$*Values of the bending rigidity and area per MBP are taken from Krugmann et al. (2020b).*
$^{\$}$*Values of area per MBP calculated from fit results in* ***Table 2****.*

By definition, A_f writes:

$$A_f = \alpha_f A \tag{9}$$

But actually, the flatter the vesicle, the wider it is, so that A_{ex} also depends on α_f. For a spherical vesicle of radius R, one has $A_{ex,a_f=0} = \pi R^2$ and for a completely flattened vesicle $A_{ex,a_f=0.5} = A/2 = 2\pi R^2 = 2A_{ex,\alpha_f=0}$. The computation of the least-energy surface as a function of α_f shows that the departure from the linearity between these two extremities is negligible (see **Supplementary Figure 3**).

This leads to

$$A_{ex} \simeq A \cdot (1 + 2\alpha_f)/4 \tag{10}$$

Equations (8) and (10) give: $\rho/\eta = (1 + 2\alpha_f)/4\alpha_f$ leading to

$$\alpha_f \simeq \frac{1}{4\left(\frac{\rho}{\eta}\right) - 2} \tag{11}$$

Considering the situation at time $t \to \infty$ with $\rho_\infty = 0.60 \pm 0.05$ is estimated from the simulations, one can deduce α_f from the neutron reflectivity measurement of η_∞.

RESULTS AND DISCUSSION

To precisely analyze the interaction of MBP coated membranes with other membranes we choose to rely on neutron reflectometry (NR). Information is obtained perpendicular to the membrane plane by detection of the specular NR signal

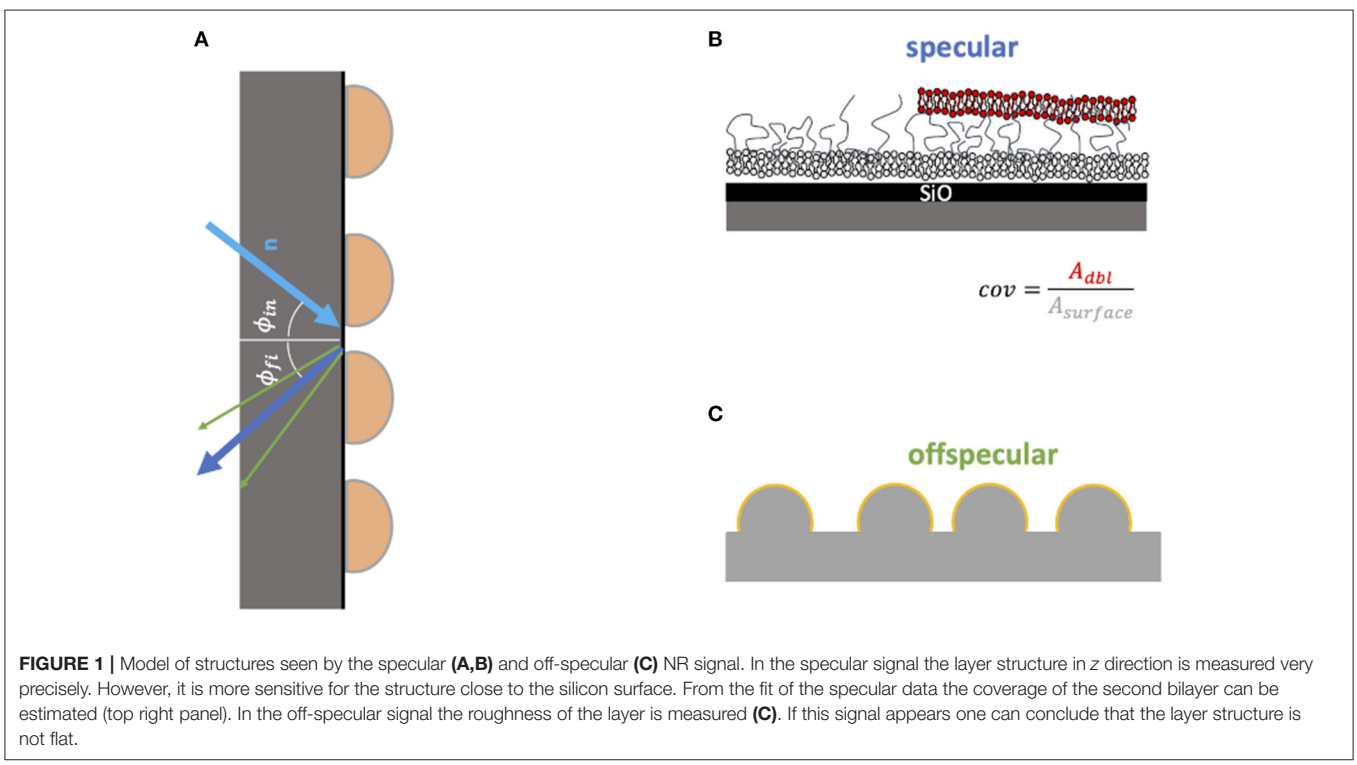

FIGURE 1 | Model of structures seen by the specular **(A,B)** and off-specular **(C)** NR signal. In the specular signal the layer structure in *z* direction is measured very precisely. However, it is more sensitive for the structure close to the silicon surface. From the fit of the specular data the coverage of the second bilayer can be estimated (top right panel). In the off-specular signal the roughness of the layer is measured **(C)**. If this signal appears one can conclude that the layer structure is not flat.

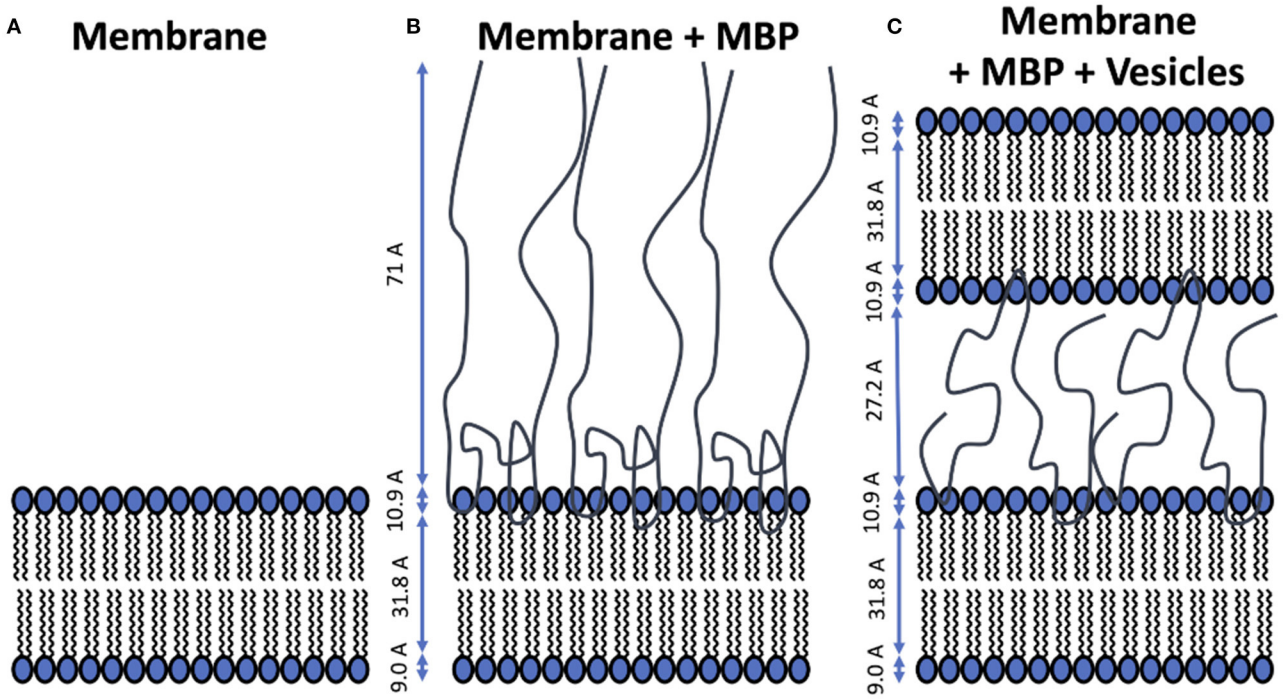

FIGURE 2 | Schematic representation of structural models for the different stages of the experiment. The averaged thickness values of the membrane components are indicated in the figure panels. **(A)** Supported membrane bilayer formed by vesicle fusion on silicon wafer. **(B)** MBP-coated membrane formed after injection of protein solution and incubation. **(C)** Double-layer membrane structure connected by a dense MBP phase in between that is formed upon adhesion of the LUVs.

in combination with in-plane resolution by also measuring off-specular NR data (Zhou and Chen, 1995; Jablin et al., 2011). This is shown schematically in **Figure 1**. The reflected neutron beam is mostly scattered specular—meaning that the final angle Φ_{fi} is equal to the initial angle Φ_{in}. The specular signal is determined by the structure perpendicular to the surface and has a resolution in the order of a few Ångstrom. However, if there is also in plane structure in the sample—in most cases roughness—a part of the beam is reflected at a different angle. This fraction is called off-specular and is only sensitive to parts of the sample which have in-plane structure.

Preparation of the Membrane System and Steady-State Characterization

The system of interest is a supported membrane bilayer (SMB) coated with MBP which is kept in a liquid cell. Into this cell large unilamellar vesicles (LUV) are injected which can diffuse toward the SMB surface and adhere to it. The main purpose of our study was to investigate the mechanism of that adhesion process. Prior to that we validated the structural properties of the membrane components—an essential prerequisite for the interpretation of the kinetic NR experiments. The different stages of the preparation process are schematically depicted in **Figure 2** alongside with the average thicknesses of the membrane components.

As a first step the SMB was created by vesicle fusion on a hydrophilic silicon substrate (**Figure 2A**; Stroumpoulis et al., 2006; Rondelli et al., 2017). The neutron reflectometry curves were measured on the neutron reflectometer D17 at the ILL (Saerbeck et al., 2018) at three different contrasts having buffer compositions of 100% D_2O, 100% H_2O and a mixture (38%/62% v/v) D_2O/H_2O which matches the SLD of silicon being abbreviated as silicon matched water (SMW) in the following. The NR data are shown for a native and EAE modified SMB in **Figures 3A**, **4A**, respectively. The fit of a simple head—chain—head layer sequence can reproduce the measured NR data nicely (see **Figures 3A**, **4A**). A SMB with native-like lipid composition and two SMBs with EAE modified lipid composition referred to as Native01, Modified01 and Modified1 SMBs were characterized. The obtained thicknesses of the head (d_{head}) and chain sections (d_{chain}) of those three SMBs are reported in **Table 2** and the respective water penetration values are given in **Supplementary Table 1**. The respective SLD profiles are shown in **Figure 3B** of the Native01 membrane and in **Figure 4B** of the Modified01 SMB.

As a next step MBP was injected in the liquid cell at either a concentration of $c_{\text{MBP}} = 0.1$ mg/ml for the Native01 and Modified01 SMBs or at 1 mg/ml for the Modified1 SMB. Due to electrostatic interaction, it interacts with the negatively charged membrane and forms a dense protein layer on top of the membrane (see **Figure 2B**). The data of the Native01 membrane with 0.1 mg/ml MBP in combination with a fit is shown in **Figure 3C**. The respective data of EAE modified membrane Modified01 with 0.1 mg/ml MBP including theoretical fit is

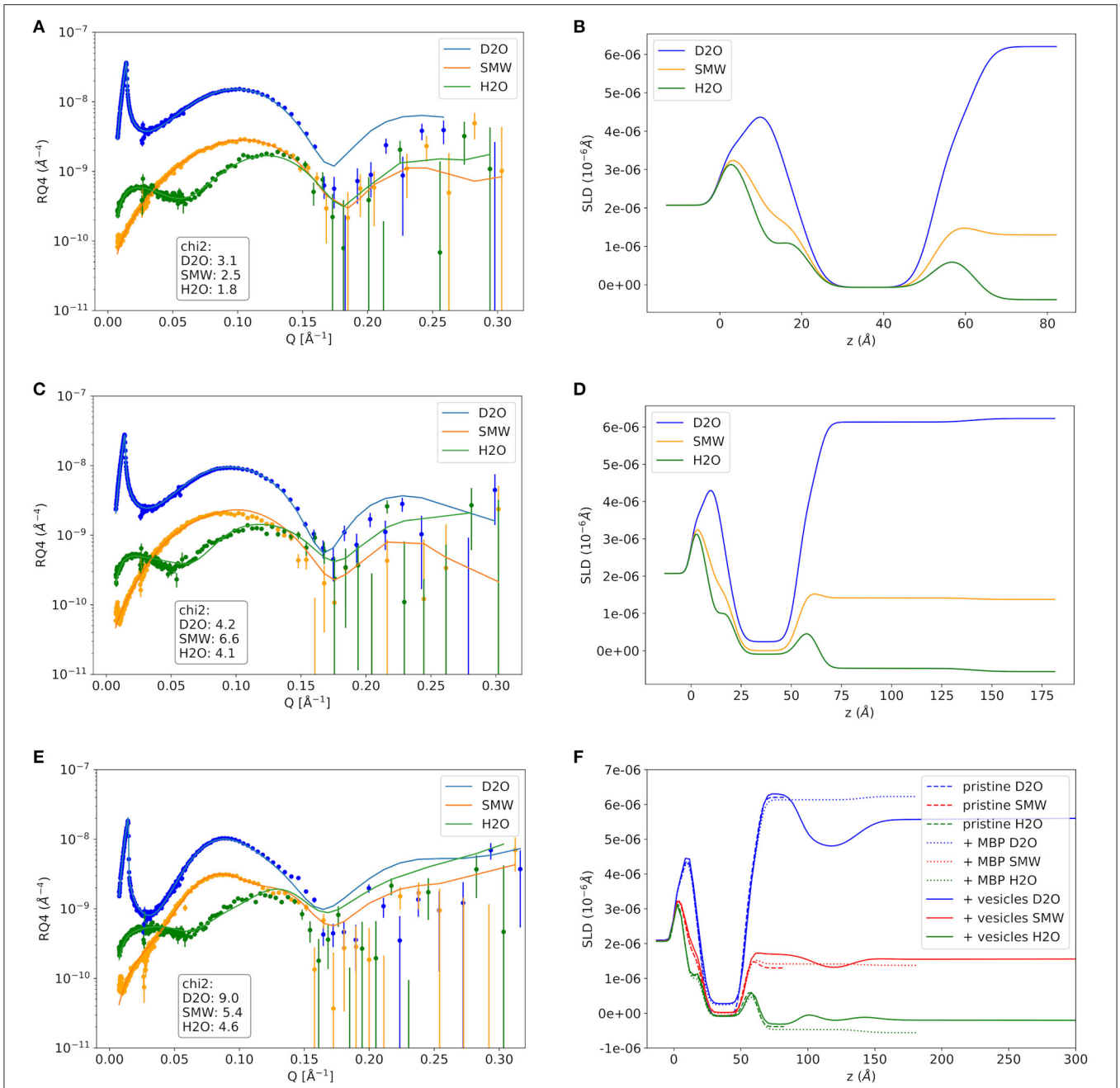

FIGURE 3 | Neutron reflectivity curves and respective SLD profiles of the Native01 sample. **(A,B)** The pure native membrane without MBP, **(C,D)** the supported membrane with MBP protein layer on top that was formed by addition of protein solution with 0.1 mg/ml MBP, and the double-membrane structure with dense intramembrane MBP-layer that was formed after vesicle adhesion in **(E,F)**. In **(F)** the SLD profiles of the pristine membrane and the MBP coated membrane are shown as comparison. NR data was measured on the D17 neutron reflectometer.

shown in **Figure 4C**. Those datasets have been fitted as a layer sequence head—chain—head and an additional dense MBP layer on top of the membrane with thickness $d_{\mathrm{MBP,SBL}}$ and concentration $c_{\mathrm{MBP,SBL}}$. During these fits the fitted values of d_{head} and d_{chain}, water penetration and roughness between the layers from the SMB without MBP were used and constrained in ±5% of the best value around those values, while the thickness of the MBP layer $d_{\mathrm{MBP,SBL}}$ (constrained for Modified01: 60–100 Å, otherwise: 70–100 Å) and its water penetration were fitted. The water penetration of the chain section was left free between 0 and 5%. The SLD of MBP was estimated with the primary structure of bovine MBP using the Biomolecular Scattering Length Density Calculator[2] considering 90% exchange of labile hydrogen atoms.

[2]*Biomolecular Scattering Length Density Calculator*. http://psldc.isis.rl.ac.uk/Psldc (accessed March 17, 2021).

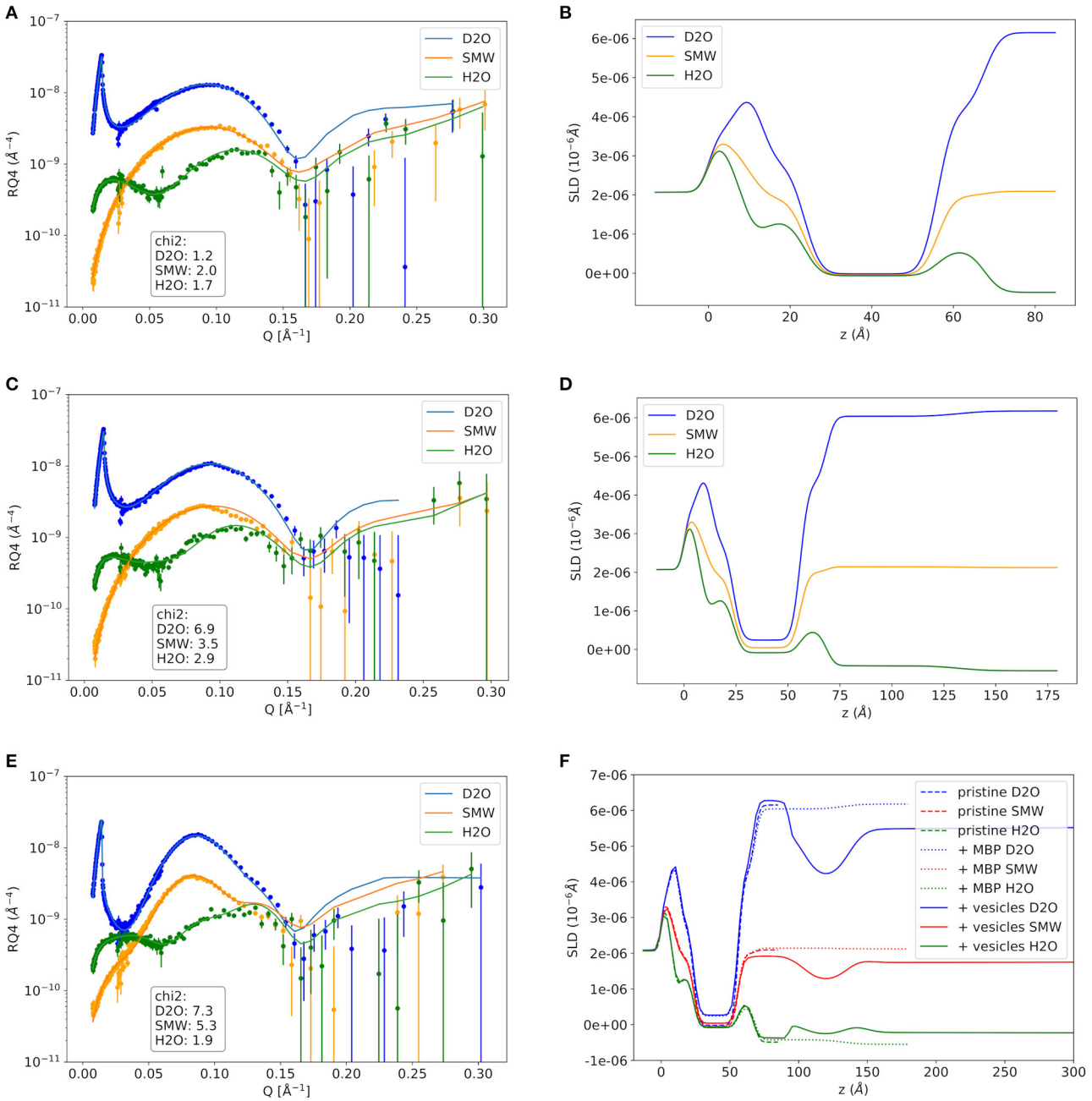

FIGURE 4 | Neutron reflectivity curves and respective SLD profiles of the EAE Modified01 sample. **(A,B)** The pure EAE membrane without MBP, **(C,D)** the supported EAE membrane with MBP protein layer on top that was formed by addition of protein solution with 0.1 mg/ml MBP, and the double-EAE-membrane structure with dense intramembrane MBP-layer that was formed after vesicle adhesion in **(E,F)**. In **(F)** the SLD profiles of the pristine membrane and the MBP coated membrane are shown as comparison. NR data was measured on the D17 neutron reflectometer.

These values are in D_2O $\rho_{D_2O} = 3.45 \cdot 10^{-6} A^{-2}$, in SMW $\rho_{SMW} = 2.55 \cdot 10^{-6} A^{-2}$, and in H_2O $\rho_{H_2O} = 2.00 \cdot 10^{-6} A^{-2}$. The respective SLD profiles of the Native01 and Modified01 SMB are depicted in **Figures 3D**, **4D**. The fit results are reported in **Table 2**, the corresponding buffer penetration values are given in **Supplementary Table 1**. We got a convincing fit with a MBP layer with thickness between $d_{\mathrm{MBP,SBL}} = 60$–$80$ Å (the determined parameters are characterized by large error bars, due to the dilute nature of the MBP layer) and a protein concentration in the range of $c_{\mathrm{MBP,SBL}} = 3$–7% vol/vol (corresponding to MBP concentrations of around 22 and 51 mg/ml, respectively, when a protein specific volume of 0.73 ml/mg is considered) for both membrane types and both injected MBP concentrations of 0.1 and 1 mg/ml. The MBP layer thicknesses and concentrations

as reported in this study are in agreement with previous observations (Krugmann et al., 2020b).

Vesicles were injected onto the MBP/SMB systems and the interaction process was studied with kinetic NR acquisition. The kinetic data will be discussed in the next section, but beforehand we take a look at the steady state specular NR measurement after an almost constant state is reached after 1–2 h. A schematic visualization of that steady-state membrane system in shown in **Figure 2C**. Experimental NR data of native and EAE modified conditions under steady-state conditions are shown in **Figures 3E**, **4E** including theoretical fits. We can see a strong change in the reflectivity profiles in comparison to the membranes without adhered vesicles. As a fit model we assume a double-bilayer system because the vesicles diffuse to the membrane and adhere to it. In this case, the specular NR profile should be a double bilayer as specular NR only is sensitive for the z-structure close to the Si-surface since the penetration depth of the neutrons under such small angle is quite low. However, to account for the part of unfused adsorbed vesicles that extends into the solution, we add in our model a long 800 Å diffuse vesicle layer as last layer with a SLD of $0.7 \cdot 10^{-6}$Å^{-2} and high roughness and buffer penetration. The thickness of the MBP layer in the double bilayer model has been fitted to $d_{\mathrm{MBP,DBL}} \approx 30$ Å which is close to what we have measured before in between 2 bilayers in small-angle X-ray scattering experiments (Krugmann et al., 2020b). The fitted values of d_{head} and d_{chain}, water penetration and roughness between the layers from the SMB without MBP were again used and constrained in ±5% of the best value around those values. The thicknesses of the second membrane layer (d_{chain}, $d_{\mathrm{head,inner}}$, and $\mathrm{d_{head,outer}}$) are fixed to the values d_{chain} and $d_{\mathrm{head,outer}}$ of the first layer. They are fixed to $d_{\mathrm{head,outer}}$ as they are both not attached to the silicon substrate and therefore less ordered. Fitted parameters are the buffer penetration value corresponding to the MBP concentration between the bilayer $c_{\mathrm{MBP,DBL}}$. The fitted buffer penetration values are given in **Supplementary Table 1** and the MBP concentrations in $c_{\mathrm{MBP,DBL}}$ in **Table 2**. The SLD-profiles we attain form those fits are shown in **Figures 3F**, **4F**.

The fitted structural models of the three stages of the experiment are summarized visually in **Figure 2** including the averaged thickness values of the membrane components. Overall, our characterization by NR of the assembly process under steady-state conditions yields a coherent picture of the assembly process. MBP that is injected as a rather dilute concentration interacts strongly with the first SMB and forms a concentrated fluid phase with concentration in the range of 3–7% and a thickness of 60–80 Å. Upon formation of the second membrane layer the MBP layer thickness is reduced to around half of its initial thickness (∼30 Å) and a concentration of 0–1% vol/vol for the 0.1 mg/ml samples and 11% for 1 mg/ml sample. This MBP layer is, hence, regulating the assembly and fusion process of the LUV with the SMB. However, due to the complexity of the system in its final state and the dilute nature of the MBP layer, it appears that our modeling is sensitive only to the thickness of the MBP layer, leading to relative underestimation on protein concentration.

Furthermore, from the buffer penetration value $h_{chain,2}$ of the second chain section (given in **Supplementary Table 1**) it is possible to calculate the coverage η of the second bilayer as the hydrophobic chain section is nearly water free in both cases. Therefore, it is possible to calculate the coverage as $\eta = 1 - h_{chain,2}$. The definition of the coverage η can be expressed mathematically as the area of the second bilayer A_{dbl} divided by the total area A_{tot} of the first bilayer of the sample

$$\eta = \frac{A_{dbl}}{A_{tot}}. \tag{12}$$

In **Table 2** the coverage values of η are given for the investigated membrane systems.

In **Figure 5A** the 2D off-specular map of an EAE-modified sample in the final steady-state of LUVs bound to the MBP-coated SMB measured at the MARIA reflectometer is given. For technical details of the instrument MARIA, we refer to the instrument paper (Mattauch et al., 2018). In **Figure 5B** the 2D image of an EAE modified sample of LUVs bound to the MBP-coated SMB measured using the D17 reflectometer is shown. Clearly, an off-specular signal is visible in both cases. This off-specular signal is proof that the samples have strong surface roughness which is an indication for vesicles adhered to its surface (Ott and Kozhevnikov, 2011).

Kinetics of the Vesicle Adhesion Process

Time-resolved NR experiments were carried out to understand the process of adhesion. In **Figure 6A** an exemplary kinetic NR measurement of a modified membrane is shown. To maximize the NR signal and to reduce the incoherent background, time-resolved NR experiments have been performed only at one contrast in 100% D_2O buffer. Clearly, in the time range of one to a few hours the adhesion process is happening. The off-specular data is growing in this time as well. The specular curves in **Figure 6A** can be fitted by the earlier explained double bilayer model. Here, only the coverage ($\eta = 1 - h_{chain,2}$), water penetration of the diffuse vesicle layer its roughness and the scaling factor are fitted, while the rest of the remaining parameter values are fixed to the ones obtained from the static measurements of the membrane with adhered vesicles. The influence of the head section is not that strong as the contrast to D_2O is higher to the chain section. In **Figure 6B** the respective SLD profiles are depicted. In **Figure 6C** the normalized coverage (scaled to the RSA simulation curve) from the specular fit, the normalized off-specular signal (scaled to the RSA simulation curve with subtracted background) and the behavior represented by the RSA simulation curve are plotted together. The important observation here is that the normalized experimental coverage values obtained from both specular and off-specular NR data are identical within the statistical uncertainty and their time-dependence can be reproduced by the theoretical model of an RSA simulation.

RSA is a model in which particles diffuse and adhere to a surface and cannot detach from it. The details of the RSA simulation are explained in the Materials and Methods section. Strikingly, the kinetics of the specular data—representing the formation of a double bilayer—and the off-specular data—representing the adhesion of vesicles to the surface—follow

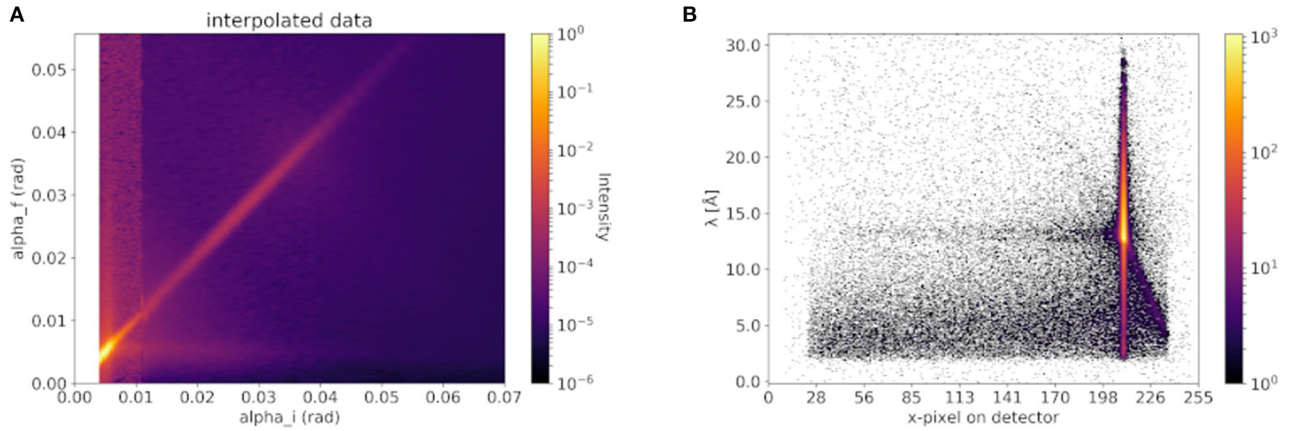

FIGURE 5 | Off-specular signal of vesicle coated membranes seen by **(A)** classical monochromatic and **(B)** TOF neutron reflectometer. In **(A)** an exemplary measurement at the classical monochromatic instrument MARIA (Mattauch et al., 2018) from an EAE-modified sample of our previous paper (Krugmann et al., 2020b) is shown. And in **(B)** an exemplary measurement of an EAE modified membrane at the TOF reflectometry mode using an incident polychromatic neutron beam of the D17 instrument is shown as comparison.

the same trend and can both be described by the same RSA simulation. We can conclude here that both signals are governed by the same kinetic time constant of the diffusion driven adhesion of the vesicles. The deformation of the vesicles which is responsible for the double bilayer formation is, therefore, quasi-instantaneous in comparison to the adhesion process. In RSA the vesicles that adsorb to the membrane are described as disks that—when adsorbed—exclude a certain area A_{ex}. After waiting for an infinite amount of time ($t = \inf$) the coverage of vesicles $\rho(t)$–which is different from η as not the whole excluded diameter is in contact with the membrane—a coverage $\rho(\inf)$ is reached. To verify if RSA is the correct kinetic process to describe our data we plot the logarithm of $\rho(\inf)$-$\rho(t)$ over the logarithm of time in **Figure 6D**. This should give a slope of $-1/2$ for an RSA process of disks on a surface, which is indeed the case of our NR data when we exclude the first initial time points (Hinrichsen et al., 1986).

Calculation of Adhesion Energy per MBP

From the above-mentioned results, it is possible to estimate the adhesion energy per area k_a. This is achieved by minimizing the free energy which is constituted of the bending energy and the adhesion energy (see section Free Energy of a Vesicle). By accounting for some geometrical assumptions (see section Combining RSA simulations and neutron reflectivity measurements to access α_f) we can estimate the adhesion energy per area k_a of the native and modified membranes with 0.1 mg/ml MBP. Values of k_a are given in **Table 3**. With this we can calculate the interaction energy per MBP molecule ϵ_{MBP}.

$$\epsilon_{MBP} = k_a \cdot A_{MBP}, \tag{13}$$

where A_{MBP} is the area per MBP molecule we take from Krugmann et al. (2020b) calculated with the MBP molecule volume from Stadler et al. (2014). Input values of A_{MBP} and the obtained values of ϵ_{MBP} are compiled in **Table 3** for the native and EAE-diseased membranes. We can see that the so-estimated adhesion energy per MBP-molecule in native membranes—calculated by this model—is larger as in EAE modified membranes which might explain the formation of a stable myelin sheath. The A_{MBP} values calculated from fits of D17 data that are presented in this publication have large statistical uncertainty, but they are in agreement with values of A_{MBP} that we have reported previously (Krugmann et al., 2020b). The large error bars of the D17 fit parameters A_{MBP} (**Table 3**) lead to high errors of ϵ_{MBP} as well. Therefore, it is not possible to draw any conclusions on the difference between native and EAE-diseased membranes using these values.

In the case of the EAE modified membrane with 1 mg/ml MBP concentration, we have a coverage fraction η_{dbl} of around 39%. This would lead to a high value of k_a in the range of the value of silicon $k_a\,(Si) = 0.5 - 1\ mJ/m^2$ where we already observe vesicle fusion triggered by the strong adhesion (Anderson et al., 2009). Therefore, we believe that it is unphysical and probably we have partial vesicle fusion occurring. This case is not covered in our model and would of course increase η_{dbl} without the vesicles needing to be flattened as much. Therefore, the calculated k_a would decrease dramatically. Partial vesicle fusion might also happen in the lower protein concentration case where the values are close to those measured in silica. In that case our calculated values of k_a and ϵ_{MBP} might be overestimated.

CONCLUSIONS

In this manuscript, we report on the adhesion mechanisms of LUV onto a supported membrane that was coated with an MBP layer. Structural characterization at the different stages of membrane assembly process has been performed under steady-state conditions, while the vesicle fusion process has been monitored as function of the incubation time. The overall aim was to investigate differences between native and

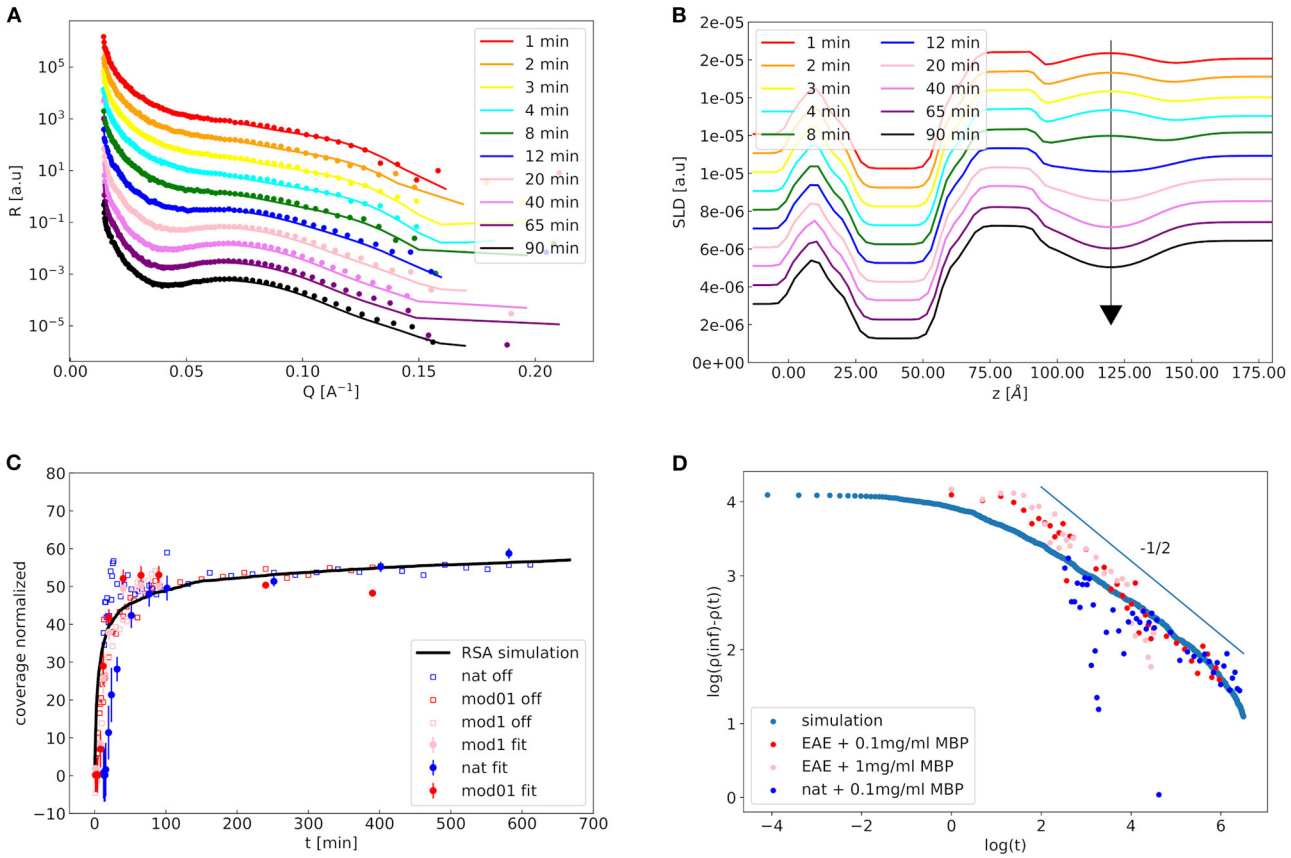

FIGURE 6 | Kinetics of the reflectivity measurements: In **(A)** a waterfall plot of the kinetic reflectivity measurements of the EAE modified membrane with 1 mg/ml MBP is shown (sample Modified1). Experimental NR data are represented by symbols as a function of incubation time. Solid lines are theoretical fits using the double-membrane bilayer model with intramembrane-MBP layer and diffuse vesicle layer for 3D structure of the attached vesicles. Structural parameters of the membrane profile were kept fixed during the individual fits and only the coverage fraction of the second membrane layer (and the diffuse vesicle layer water content and roughness) was fitted. In **(B)** the respective SLD profiles are shown. In **(C)** the kinetics of the off-specular signal of the three membranes (empty symbols), the kinetics of the coverage fit parameter of the three membranes obtained from specular NR data (filled symbols) and an RSA simulation of vesicles with 50 nm radius and 15 nm polydispersity (solid black line) are shown. In **(D)** the log-log-plot of the vesicle coverage ρ (inf) $-$ $\rho(t)$ over the time is shown for the off-specular experimental values and the RSA simulation. The thin line indicates power-law behavior with a slope of $-1/2$, which is the theoretical prediction of an RSA process of flat disks on a surface (Adamczyk et al., 1997).

EAE modified biomimetic cytoplasmic myelin membranes and to gain information on the myelin sheath assembly process at a molecular scale. From the steady-state experiments we demonstrate that a concentrated MBP layer is formed on top of a single SMB with a protein concentration of around 3–7%. Adhesion of LUV with local formation of a second membrane bilayer results in an MBP layer that is reduced in thickness. Concerning the LUV adhesion kinetics, we show that the adhesion of the vesicles can be modeled by an RSA simulation. In addition, we provide evidence that the vesicles are reshaping after the adhesion. Their contact surface with the membrane is maximized until the elasticity of the membrane leads to a force in opposite direction and an equilibrium state is established. Our measurements show that this process depends on both membrane type and MBP concentration, while its kinetics is entirely limited by the diffusion of the vesicles toward the membrane surface agreeing with the observed RSA mechanism. In combination with the bending rigidity of those membranes, which we investigated in earlier studies (Krugmann et al., 2020b), we can provide an estimate of the interaction force per MBP molecule: In the native-like membrane case it is larger than in the EAE-diseased membranes. Our new results can also help with the interpretation of our last paper (Krugmann et al., 2020b). In that study, we have seen that LUV having EAE modified lipid composition tend to stick to each other by a strong attractive interaction being mediated by the binding strength of MBP. As we show in here, this seems not to be because of a stronger interaction of MBP with these EAE-diseased membranes as the adhesion energy per MBP-molecule is higher for native membrane than for the EAE-diseased membrane. Instead, the driving force of that effect appears to be due to the higher MBP concentration in the MBP layer on top of EAE modified membranes as compared to that of native-like membranes.

We found indications that partial vesicle fusion is occurring when EAE membranes were treated with the higher MBP

concentration of 1 mg/ml. By applying external stimuli like osmotic shock or temperature shocks it might be possible to achieve complete vesicle fusion resulting in a perfect double bilayer system with an intercalated MBP layer in between the two bilayers. This would be a significantly improved model system to study the initial growth process of the myelin sheath from a molecular perspective, and it would allow us to study basic biophysical properties of artificial biomimetic nerve cells *in vitro*.

DATA AVAILABILITY STATEMENT

The datasets analyzed for this study can be found in the ILL data repository (data.ill.eu) (Krugmann et al., 2020a).

AUTHOR CONTRIBUTIONS

AS, AR, AK, and SF designed the research. BK, AK, LH, and SM performed the research. BK and AK analyzed the data. DL contributed analytical modeling. BK and AS wrote the manuscript with input from all other authors. All authors read and approved the finalized manuscript.

ACKNOWLEDGMENTS

This work was based upon experiments performed on the instruments MARIA operated by Jülich Centre for Neutron Science at the Heinz Maier-Leibnitz Zentrum, Garching, Germany and on D17 at the Institut Laue-Langevin, Grenoble, France. The authors acknowledge the PSCM at the ILL for the use of the preparation laboratories and for the preliminary sample characterization during the beamtime.

SUPPLEMENTARY MATERIAL

The Supplementary Material for this article can be found online at: https://www.frontiersin.org/articles/10.3389/fchem.2021.631277/full#supplementary-material

REFERENCES

Adamczyk, Z., Siwek, B., Zembala, M., and Weroński, P. (1997). Influence of polydispersity on random sequential adsorption of spherical particles. *J. Colloid Interface Sci.* 185, 236–244. doi: 10.1006/jcis.1996.4540

Anderson, T. H., Min, Y., Weirich, K. L., Zeng, H., Fygenson, D., and Israelachvili, J. N. (2009). Formation of supported bilayers on silica substrates. *Langmuir* 25, 6997–7005. doi: 10.1021/la900181c

Boggs, J. M. (2006). Myelin basic protein: a multifunctional protein. *Cell. Mol. Life Sci. CMLS* 63, 1945–1961. doi: 10.1007/s00018-006-6094-7

Cieśla, M., and Nowak, A. (2016). Managing numerical errors in random sequential adsorption. *Surf. Sci.* 651, 182–186. doi: 10.1016/j.susc.2016.04.014

Cieśla, M., and Ziff, R. M. (2018). Boundary conditions in random sequential adsorption. *J. Stat. Mech. Theory Exp.* 2018:043302. doi: 10.1088/1742-5468/aab685

Cubitt, R., Saerbeck, T., Campbell, R. A., Barker, R., and Gutfreund, P. (2015). An improved algorithm for reducing reflectometry data involving divergent beams or non-flat samples. *J. Appl. Crystallogr.* 48, 2006–2011. doi: 10.1107/S1600576715019500

Erban, R., and Chapman, S. J. (2007). Time scale of random sequential adsorption. *Phys. Rev. E* 75:41116. doi: 10.1103/PhysRevE.75.041116

Evans, W. H. (1980). Hepatic plasma-membrane modifications in disease. *Clin. Sci.* 58, 439–444. doi: 10.1042/cs0580439

Franklin, R. J. M., and Ffrench-Constant, C. (2008). Remyelination in the CNS: from biology to therapy. *Nat. Rev. Neurosci.* 9, 839–855. doi: 10.1038/nrn2480

Hinrichsen, E. L., Feder, J., and Jøssang, T. (1986). Geometry of random sequential adsorption. *J. Stat. Phys.* 44, 793–827. doi: 10.1007/BF01011908

Jablin, M. S., Zhernenkov, M., Toperverg, B. P., Dubey, M., Smith, H. L., Vidyasagar, A., et al. (2011). In-plane correlations in a polymer-supported lipid membrane measured by off-specular neutron scattering. *Phys. Rev. Lett.* 106:138101. doi: 10.1103/PhysRevLett.106.138101

Koutsioubas, A. (2021). *Anaklasis: A Compact Software Package for Model Based Analysis of Specular Neutron and X-Ray Reflectometry Datasets*. Journal of Applied Crystallography. Available online at: https://github.com/alexandros-koutsioumpas/anaklasis (accessed April 1, 2021).

Koutsioubas, A., Appavou, M. S., and Lairez, D. (2017). Time-resolved neutron reflectivity during supported membrane formation by vesicle fusion. *Langmuir* 33, 10598–10605. doi: 10.1021/acs.langmuir.7b02459

Krugmann, B., Gutfreund, P., Haris, L., Koutsioubas, A., Micciulla, S., Radulescu, A., et al. (2020a). *Kinetics of Myelin Membrane Fusion Triggered by Myelin Basic Protein*. Grenoble: Institut Laue-Langevin (ILL). doi: 10.5291/ILL-DATA.8-02-870

Krugmann, B., Radulescu, A., Appavou, M. S., Koutsioubas, A., Stingaciu, L. R., Dulle, M., et al. (2020b). Membrane stiffness and myelin basic protein binding strength as molecular origin of multiple sclerosis. *Sci. Rep.* 10:16691. doi: 10.1038/s41598-020-73671-3

Love, S. (2006). Demyelinating diseases. *J. Clin. Pathol.* 59, 1151–1159. doi: 10.1136/jcp.2005.031195

Maret, A., Potier, M., Salvayre, R., and Douste-Blazy, L. (1983). Modification of subunit interaction in membrane-bound acid β-glucosidase from Gaucher disease. *FEBS Lett.* 160, 93–97. doi: 10.1016/0014-5793(83)80943-0

Mattauch, S., Koutsioubas, A., Rücker, U., Korolkov, D., Fracassi, V., Daemen, J., et al. (2018). The high-intensity reflectometer of the Jülich Centre for Neutron Science: MARIA. *J. Appl. Crystallogr.* 51, 646–654. doi: 10.1107/S1600576718006994

Min, Y., Alig, T. F., Lee, D. W., Boggs, J. M., Israelachvili, J. N., and Zasadzinski, J. A. (2011). Critical and off-critical miscibility transitions in model extracellular and cytoplasmic myelin lipid monolayers. *Biophys. J.* 100, 1490–1498. doi: 10.1016/j.bpj.2011.02.009

Min, Y., Kristiansen, K., Boggs, J. M., Husted, C., Zasadzinski, J. A., and Israelachvili, J. (2009). Interaction forces and adhesion of supported myelin lipid bilayers modulated by myelin basic protein. *Proc. Natl. Acad. Sci. U.S.A.* 106, 3154–3159. doi: 10.1073/pnas.0813110106

Ohler, B., Graf, K., Bragg, R., Lemons, T., Coe, R., Genain, C., et al. (2004). Role of lipid interactions in autoimmune demyelination. *Biochim. Biophys. Acta* 1688, 10–17. doi: 10.1016/j.bbadis.2003.10.001

Ott, F., and Kozhevnikov, S. (2011). Off-specular data representations in neutron reflectivity. *J. Appl. Crystallogr.* 44, 359–369. doi: 10.1107/S0021889811002858

Prineas, J. W., and Connell, F. (1979). Remyelination in multiple sclerosis. *Ann. Neurol.* 5, 22–31. doi: 10.1002/ana.410050105

Quarles, R. H., Macklin, W. B., and Morell, P. (2006). "Myelin formation, structure and biochemistry," in *Basic Neurochemistry, Molecular, Cellular and Medical Aspects, 7th Edn.,* ed S. Brady (Amsterdam: Academic Press), 51–71.

Raasakka, A., Ruskamo, S., Kowal, J., Barker, R., Baumann, A., Martel, A., et al. (2017). Membrane association landscape of myelin basic protein portrays formation of the myelin major dense line. *Sci. Rep.* 7:4974. doi: 10.1038/s41598-017-05364-3

Rondelli, V., Brocca, P., Tranquilli, N., Fragneto, G., Del Favero, E., and Cantù, L. (2017). Building a biomimetic membrane for neutron reflectivity investigation: complexity, asymmetry and contrast. *Biophys. Chem.* 229, 135–141. doi: 10.1016/j.bpc.2017.04.011

Saerbeck, T., Cubitt, R., Wildes, A., Manzin, G., Andersen, K. H., and Gutfreund, P. (2018). Recent upgrades of the neutron reflectometer D17 at ILL. *J. Appl. Crystallogr*. 51, 249–256. doi: 10.1107/S160057671800239X

Shaharabani, R., Ram-On, M., Avinery, R., Aharoni, R., Arnon, R., Talmon, Y., et al. (2016). Structural transition in myelin membrane as initiator of multiple sclerosis. *J. Am. Chem. Soc*. 138, 12159–12165. doi: 10.1021/jacs.6b04826

Shaharabani, R., Ram-On, M., Talmon, Y., and Beck, R. (2018). Pathological transitions in myelin membranes driven by environmental and multiple sclerosis conditions. *Proc. Natl. Acad. Sci. U.S.A*. 115, 11156–11161. doi: 10.1073/pnas.1804275115

Stadler, A. M., Stingaciu, L., Radulescu, A., Holderer, O., Monkenbusch, M., Biehl, R., et al. (2014). Internal nanosecond dynamics in the intrinsically disordered myelin basic protein. *J. Am. Chem. Soc*. 136, 6987–6994. doi: 10.1021/ja502343b

Stroumpoulis, D., Parra, A., and Tirrell, M. (2006). A kinetic study of vesicle fusion on silicon dioxide surfaces by ellipsometry. *AIChE J*. 52, 2931–2937. doi: 10.1002/aic.10914

Vignini, A., Nanetti, L., Moroni, C., Tanase, L., Bartolini, M., Luzzi, S., et al. (2007). Modifications of platelet from Alzheimer disease patients: a possible relation between membrane properties and NO metabolites. *Neurobiol. Aging* 28, 987–994. doi: 10.1016/j.neurobiolaging.2006.05.010

Wang, J.-S. (1994). A fast algorithm for random sequential adsorption of discs. *Int. J. Mod. Phys. C* 05, 707–715. doi: 10.1142/s0129183194000817

Weil, M.-T., Möbius, W., Winkler, A., Ruhwedel, T., Wrzos, C., Romanelli, E., et al. (2016). Loss of myelin basic protein function triggers myelin breakdown in models of demyelinating diseases. *Cell Rep*. 16, 314–322. doi: 10.1016/j.celrep.2016.06.008

Zhou, X. L., and Chen, S. H. (1995). Theoretical foundation of X-ray and neutron reflectometry. *Phys. Rep*. 257, 223–348. doi: 10.1016/0370-1573(94)00110-O

Conflict of Interest: The authors declare that the research was conducted in the absence of any commercial or financial relationships that could be construed as a potential conflict of interest.

frontiers in Physics

ORIGINAL RESEARCH
published: 14 May 2021
doi: 10.3389/fphy.2021.628219

Influence of NaCl on the Structure and Dynamics of Phospholipid Layers

Sebastian Jaksch[1,2]*, *Olaf Holderer*[1], *Henrich Frielinghaus*[1], *Alexandros Koutsioubas*[1], *Piotr Zolnierczuk*[3], *Dominic William Hayward*[1], *Stephan Förster*[4] and *Peter Müller-Buschbaum*[2,5]

[1]Jülich Centre for Neutron Science (JCNS) at Heinz Maier-Leibnitz Zentrum (MLZ), Forschungszentrum Jülich, Garching, Germany, [2]Heinz Maier-Leibnitz Zentrum (MLZ), Technische Universität München, Garching, Germany, [3]Jülich Centre for Neutron Science (JCNS) at Spallation Neutron Source (SNS), ORNL, Oak Ridge, TN, United States, [4]Jülich Centre for Neutron Science (JCNS-1), Forschungszentrum Jülich, Jülich, Germany, [5]Lehrstuhl für Funktionelle Materialien, Physik-Department, Technische Universität München, Garching, Germany

We present a structural and dynamical analysis of the influence of NaCl on multilayer stacks of phospholipids on a solid surface. To this end, multilayer stacks of phospholipids (L-α-phosphatidylcholine, abbreviated as SoyPC) are investigated with neutron reflectometry, grazing-incidence small-angle neutron scattering (GISANS) and grazing-incidence neutron-spin echo spectroscopy (GINSES). We show both that the NaCl influence on the structure is predominantly on water-head group interface and also, that the change in dynamics is restricted to an associated change in the inter-plane viscosity. Using this knowledge, it is possible to model the dynamical behavior of a phospholipid membrane in response to a salt concentration of the solvent using only a single parameter, namely the in-plane viscosity. The excellent agreement with our previously published model also strongly supports the existence of a thermally excited surface mode in phospholipid membranes for close-to-physiological conditions.

Keywords: phospholipids, salt, dynamics, structure, GISANS, neutron reflectometry, neutron spin-echo, GINSES

OPEN ACCESS

Edited by:
Doo Soo Chung,
Seoul National University, South Korea

Reviewed by:
Victoria Garcia Sakai,
ISIS Facility, United Kingdom
Sadafara Anand Pillai,
P P Savani University, India

***Correspondence:**
Sebastian Jaksch
s.jaksch@fz-juelich.de

Specialty section:
This article was submitted to Physical Chemistry and Chemical Physics, a section of the journal Frontiers in Physics

Received: *11 November 2020*
Accepted: *30 April 2021*
Published: *14 May 2021*

Citation:
Jaksch S, Holderer O, Frielinghaus H, Koutsioubas A, Zolnierczuk P, Hayward DW, Förster S and Müller-Buschbaum P (2021) Influence of NaCl on the Structure and Dynamics of Phospholipid Layers. Front. Phys. 9:628219. doi: 10.3389/fphy.2021.628219

INTRODUCTION

Phospholipids are a major constituent of the plasma membranes in the vast majority of biological organisms. These membranes play a crucial role in a wide variety of important mechanisms and properties from drug delivery [1] to permeability in cellular membranes [2]. In the case of the latter, the interplay between dynamics and structure is of particular importance. The structure and dynamics of phospholipid membranes has been the subjects of a wide array of investigations ranging from light-scattering [2] and AFM studies [3] over X-ray scattering [4–10] to elastic [11–13] and inelastic neutron scattering [14–17]. An overview of the interplay between structure and dynamical behavior was published by Tanaka [18], and reviews focusing on neutron and X-ray scattering were published by Rheinstädter and Fragneto [19], and Salditt [8]. Moreover, an overview focused on grazing incidence methods on similar systems was given before [20].

In this study, we use elastic neutron scattering methods, reflectometry and grazing-incidence small-angle neutron scattering (GISANS), to evaluate the structure of a phospholipid membrane stack when NaCl is introduced to the solvent. NaCl addition introduces ions to the system and can be understood as an approach to getting closer to physiological conditions. It can be used to separate possible effects observed in unadulterated (i.e. in the absence of salt) *in vitro* experiments and examine their applicability to real-life systems. A previous investigation on the effects of various salts on the structure of lipid membranes found that the inter-lamellar spacing increases on addition of

TABLE 1 | Summary of samples used and their respective NaCl concentrations. If no salt was added to the sample, it was measured in pure D_2O.

sample	D_2O/mg	Salt/mg	Experiment
No salt		N/A	Reflectometry
1 M ($M: mol/L$)	44,450	2,340	Reflectometry, GISANS
2 M ($M: mol/L$)	44,280	4,680	Reflectometry, GISANS
No salt		N/A	GINSES
2 M ($M: mol/L$)	18,015	1894	GINSES

NaCl [21] However, in this work, we find that the overall dimensions of the membranes remain stable and there is little change in the bilayer thickness due to the salt concentration. We attribute this difference to a different approach of data evaluation. Hishida et al. used one single main peak position to determine the bilayer thickness. Using inverse Fourier transform we are able to show that an additional peak (Q = 0.05 $Å^{-1}$), which appears for higher NaCl concentrations at lower Q-values, is actually connected to the changes at the phospholipid-water interface of the bilayer. The same is true for the peak splitting (Q = 0.09 $Å^{-1}$). This more complicated reflectometry data probably cannot be adequately analyzed by using only a single peak position.

In an earlier work, focusing on the grazing-incidence small-angle neutron-spin echo spectroscopy (GINSES) technique [17], we demonstrated the existence of a hitherto unknown surface mode in a phospholipid membrane stack system which did not include any salt. Here we extend this investigation to systems with an NaCl-containing solvent, and examine the impact of the NaCl-ions on the membrane. This surface mode we postulate in our previous work is a long-range in-plane correlation, which is on the order of a few hundred Angstroms (Q~0.01 A^{-1}) with an energy transfer in the μeV range [16, 17, 22]. One of the questions that we try to answer in this study is, whether this phenomenon is only restricted to very pure phospholipid systems, or whether this is a general phenomenon in phospholipid membranes, also at closer to physiological conditions as described here.

The measurements presented here show that the effects of NaCl concerning structure is mostly concentrated on the interface between the phospholipid headgroups and the water layer, while not fundamentally impacting on the membrane stack nature of the samples.

Concerning the dynamical behavior such systems we show that the description put forward in our previous manuscript for the pure multilayer stack system also holds in case of NaCl introduction to the system. Only the intramembrane viscosity changes. This finding proves the existence of the previously shown surface mode being present in the phospholipid systems. Furthermore, it increases the predictive power of our model to systems, which are very close to those found under physiological conditions.

MATERIALS AND METHODS

Materials

The materials used in the experiments reported here are L-α-phosphatidycholine, 95% (SoyPC) procured from Avanti Lipids, NaCl obtained from SigmaAldrich and D_2O (99.8 atom-% D) from Deutero.

The sample preparation was identical in all cases, irrespective of the experiments being performed. A solution of 5 g SoyPC in 34 g of isopropanol (pA) was prepared. This was done at room-temperature (RT) and the mixture was shaken for at least 20 min. This always resulted in a clear solution with a slight yellow tinge.

In parallel, a silicon (Si) block with a neutron-resonator was prepared by cleaning it for at least 2 h in a 2% Hellanex solution. The resonating structure improved the scattering characteristics in for the GINSES measurements, without impeding those in the case of neutron reflectometry or GISANS [23]. The resonator is a layered structure of sputtered platinum and titanium, which provides a constructive interference for neutrons within an acceptable windows in terms of wavelength and incoming angle. This increases the probability of interaction of the neutrons with the sample. For the complete procedure, we followed the well-established protocol of our previous publications [13, 24].

In short, 12 ml SoyPC solution was solution cast onto the silicon block and dried overnight at a pressure of 250 mbar at room temperature to allow for ideal self-assembly conditions.

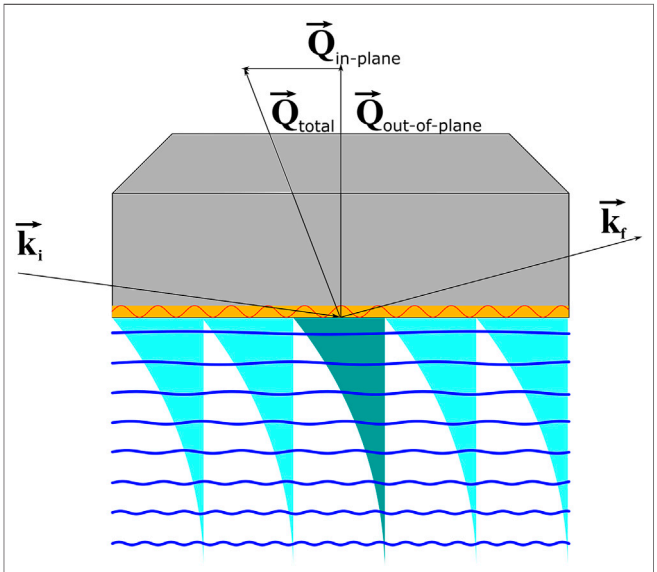

FIGURE 1 | Sketch of the applied scattering geometry: For reflectometry the incoming wavevector k_i and outgoing wavevector k_f are identical. Hence, the total scattering vector Q is an out-of-plane vector perpendicular to the sample surface. For GISANS, a range of scattering angles are collected on the detector and therefore there are both in and out-of-plane components of the Q-vector, depending on the position on the detector. In case of the GINSES measurement, k_i and k_f are strictly different (incoming angle 0.2°, outgoing angle 8°) which leads to an in-plane component of $Q_{in\text{-}plane}$ = 0.0072 $Å^{-1}$. However, since the active detector area of 10 cm width at 4 m sample detector distance is involved into data collection the uncertainty of outgoing angle is 0.25 mrad, which results in the uncertainty described in the text.

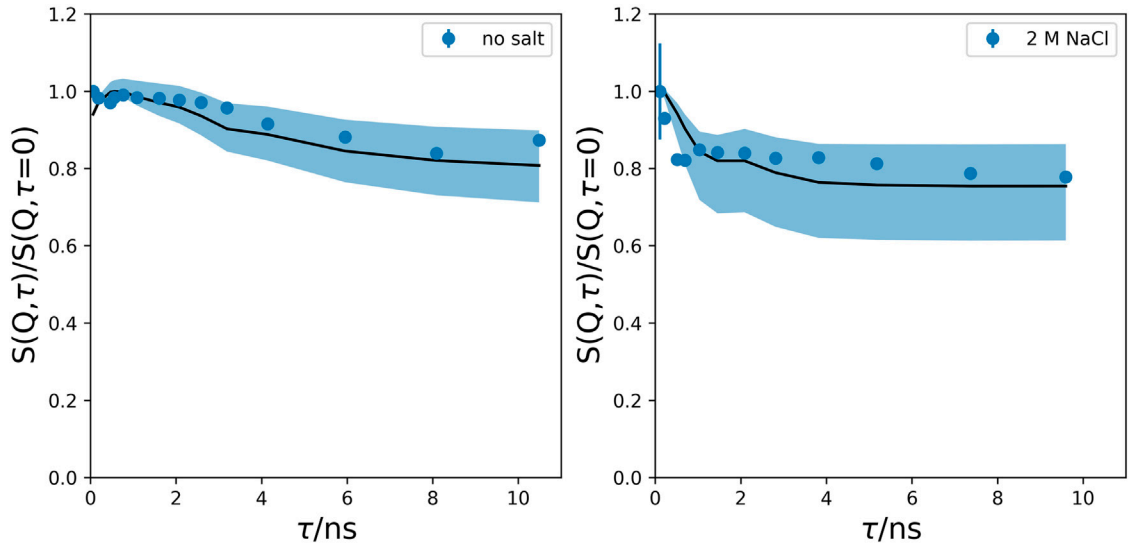

FIGURE 2 | GINSES data for sample without **(left panel)** salt and a sample with a 2 M NaCl concentration in the solvent **(right panel)**. The black lines represent the data either calculated from fits in our previous publication [17]. The shaded areas represent the confidence areas using the uncertainties for the in-plane Q. The extremely good correspondence, even without a fit (see text) corroborates our earlier and current use of the Romanov layer model and the existence of the surface mode shown in our previous publications. The very fast decay for short times in the case of a 2 M NaCl concentration we attribute to a facilitated sliding of the membrane layers against each other for short times.

For the measurements, the prepared Si-blocks were fixed into a sample holder that provided a confined, water-tight space above the sample film on the surface. Finally, D_2O containing the appropriate salt concentrations (as indicated in **Table 1**) were injected into the cell.

Sample Block and Geometry

A sketch of the sample block and the resulting geometry are given in **Figure 1**. It is important to note that the neutrons always impinge onto the phospholipid sample from the silicon side, at the solid/liquid interface. This provides an excellent orientation of the sample and a very smooth surface for the self-assembly of the phospholipid layer stack.

In terms of orientation a distinction must be made between the set-up for the GISANS and reflectometry experiments versus that for the GINSES experiment. The GISANS and reflectometry experiments were carried out on a single wavelength instrument, using either a reflectometry geometry, where the Q-vector is perfectly perpendicular to the sample surface or a GISANS geometry where the incoming angle is fixed and therefore a set of Q-values is probed, including lateral information. GINSES on the other hand was performed on a time-of-flight instrument with a wavelength spread of the incoming neutrons. Since the in-plane Q-vector is defined by the difference between the incoming and the outgoing angle of the neutrons, and the outgoing angle and Q-values are a function of each other, this in-plane Q-vector carries a systematical error of $2.5 \cdot 10^{-4}$ Å^{-1} due to the pixel size of the detector (3.75 cm pixels at 4 m sample detector distance). The impact of this uncertainty can be seen by the shaded areas in the GINSES data in **Figure 2**.

GISANS and Reflectometry

GISANS and neutron reflectometry measurements were performed on the MARIA [25] reflectometer of JCNS at MLZ, FRM2, Garching, Germany. The temperature was controlled by a Julabo water thermostat. Temperature calibration was done by calibrating the Julabo temperature to a direct measurement of the temperature of the sample block. Incident angles for GISANS were always $\alpha_i = 0.2^\circ$, with a neutron wavelength of $\lambda = 5$ Å.

GISANS and conversely grazing-incidence x-ray scattering (GISAXS) have been established since long as valuable tools for the investigation of surfaces and interfaces [20]. Due to the shallow incident angle (below or close to the critical angle of total external reflection) there is a large footprint of the beam, which allows that a large area average is made. In comparison to reflectometry, where the information may be extracted for similar average surface areas, GISANS and GISAXS analyze also non-specular intensities, which probe in-plane correlations, such as patches along the surface, to be investigated.

GINSES

GINSES measurements were performed at on the SNS-NSE [26] neutron spin-echo spectrometer of JCNS at SNS, ORNL, Oak Ridge (TN), USA. Temperature was controlled by a Julabo with a temperature sensor directly connected to the Si-sample block. Also here, the incident angle was set to $\alpha_i = 0.2^\circ$ as well. The exit angle was 8°, which leads to an in-plane scattering vector of $Q_{in-plane} = \sin(\alpha_f - \alpha_i/2) \times Q_{total} = 0.0072$ Å^{-1}.

There are two aspects for using a grazing incidence geometry for neutron spin-echo spectroscopy (NSE): 1) Since incoming and

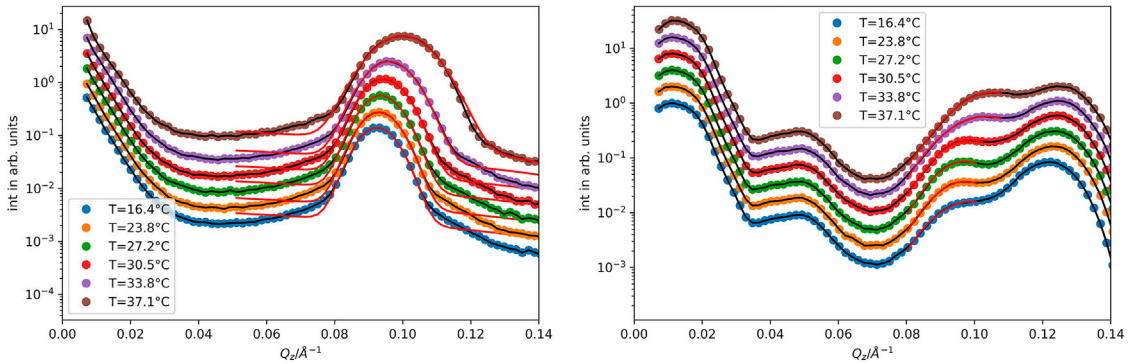

FIGURE 3 | Reflectometry data of SoyPC samples with 1 M **(left panel)** and 2 M **(right panel)** NaCl in the D_2O solvent. The black lines represent fits obtained by inverse FFT analysis, while the red lines represent Gaussian fits to determine the correct peak positions. The curves are shifted along the intensity axis for clarity of the representation.

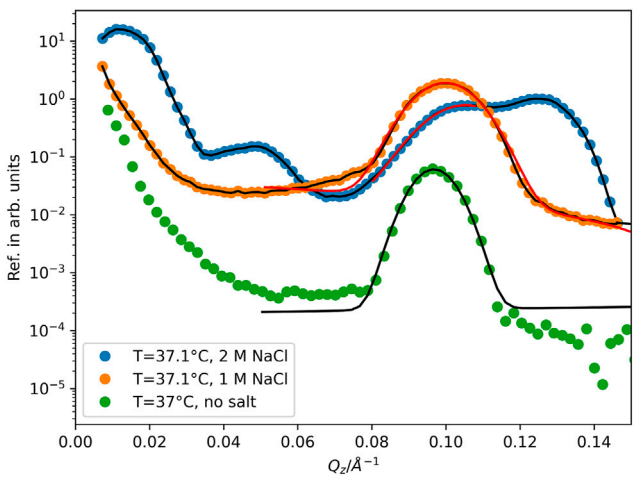

FIGURE 4 | Reflectometry data for different NaCl concentrations at physiological temperatures. The curves are shifted along the intensity axis for clarity of the presentation.

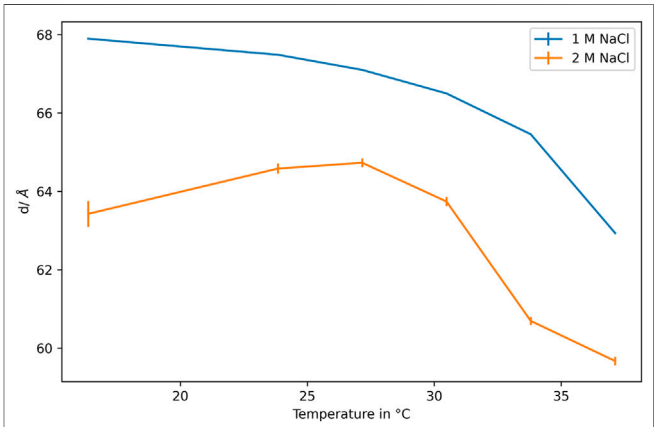

FIGURE 5 | Double layer distances *d* from reflectometry data over temperature. The error bars are vanishingly small for the 1 M NaCl concentration.

outgoing angle are not identical, very small in-plane Q-values are accessible (see **Figure 1**), which are usually hidden to NSE, due to the rather large primary beam, and the detectors usually not being able to work under full beam conditions. The other reason 2) is to exploit the same advantages in surface scattering as GISANS and GISAXS, namely averaging over a large surface area and thereby enabling the investigation of films and interfaces. The authors gave an extensive overview of the technique in a previous publication [23].

Inverse FFT

The inverse FFT analysis used in the present data analysis is based on a self-written code by the authors using the approaches presented by Stroud and Li [27, 28]. While the resulting fits reproduce the data extremely well, due to boundary condition effects this method obtains most of the resulting neutron scattering length density (SLD) data directly from the area around the peaks. Accordingly, although the shape of the individual multilayer is well reproduced, no information about the layer-to-layer distance is included. This information is then obtained by the classical use of the peak position.

RESULTS

The results are split in sections for GISANS/reflectometry and GINSES to make a distinction between structural and dynamic behavior, which is investigated with the different measurements. As an overall observation it can be stated that the stacked, lamellar nature of the phospholipid membranes, as was reported also in earlier investigations, is rather stable. The investigated salt concentrations of 1 and 2 M NaCl do not drive the system into a non-lamellar phase.

Reflectometry

Representative neutron reflectometry data is shown in **Figure 3** and **Figure 4**. The most apparent feature is that for the 1 M salt

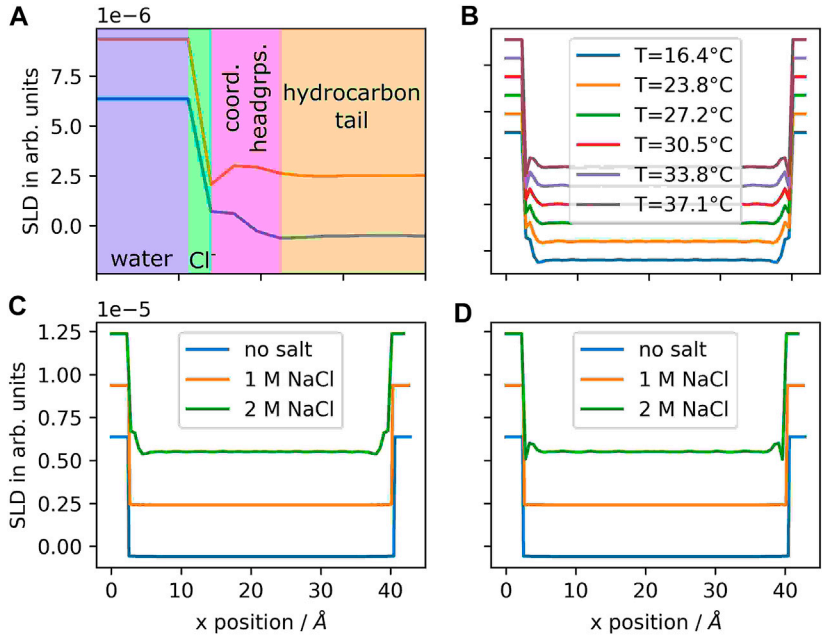

FIGURE 6 | SLD profiles determined from reflectometry data via inverse FFT analysis; **(A)**: 2 M, lowest and highest temperature zoom-in. The water area (D_2O SLD = 6.3 10^{-6} $Å^{-2}$) is shaded blue, the area where chlorine ions are enriched is shaded green, the area where sodium ions interact with the phospholipid head groups, causing a temperature dependent coordination is shaded magenta and the area of the hydrocarbon tail ($C_{10}H_{22}$ SLD = $-0.49 \cdot 10^{-6}$ $Å^{-2}$); **(B)**: 2 M all temperatures, **(C)**: all concentrations 1 and 2 M at 16.4°C, salt-free at 37°C; **(D)**: all concentrations 1 and 2 M at 37.1°C, salt-free at 37°C. Upper limit in all cases is 6.3 10^{-6} $Å^{-2}$ for D_2O and −0.49 10^{-6} $Å^{-2}$ for the pure hydrocarbon tails of the phospholipids. Curves are shifted against each other for better visibility.

concentration there is little distortion of the primary peak (Q ≈ 0.09 to 0.1 $Å^{-1}$) of the lamellar order, while in case of the 2 M concentration, this peak is split into two peaks (Q ≈ 0.09 $Å^{-1}$ and Q ≈ 0.12 $Å^{-1}$). Moreover, an additional peak appears closer to the primary beam position in case of 2 M (Q ≈ 0.05 $Å^{-1}$).

In order to analyze the double layer thickness, we analyzed the peak positions of for the 1 M salt concentration and the peak position of the corresponding forward peak for the 2 M concentration. Both the peak positions and the resulting double layer thicknesses d ($d = 2\pi/Q_{max}$, where Q_{max} is the position of the peak maximum) are given in **Figure 5**. The 1 M salt concentration is consistently slightly thicker (compares to 60 Å in the case of pure water at 37°C [13]) at about d = 68 Å vs. d = 64 Å for 2 M NaCl. The consistent change over temperature follows a phase diagram as already measured for the samples without salt, exhibiting the stacked tail region below 25°C, a coexistence phase of liquid and stacked tails above 20°C and a fully gel like/liquid tail region above 30°C, which also very well compares to literature values for similar samples without salt.

The more complex structure at the 2 M salt concentration necessitated an inverse Fourier transform algorithm for analysis of the reflectivity data. Previous attempts to use the Parrat algorithm for the data analysis only worked for the condition 1 M, but were unsuccessful in finding a solution that was both algorithmically stable, in combination with the physical assumptions about the SLDs and thicknesses in the model, as well as describing the data fairly well. The resulting SLD profiles are

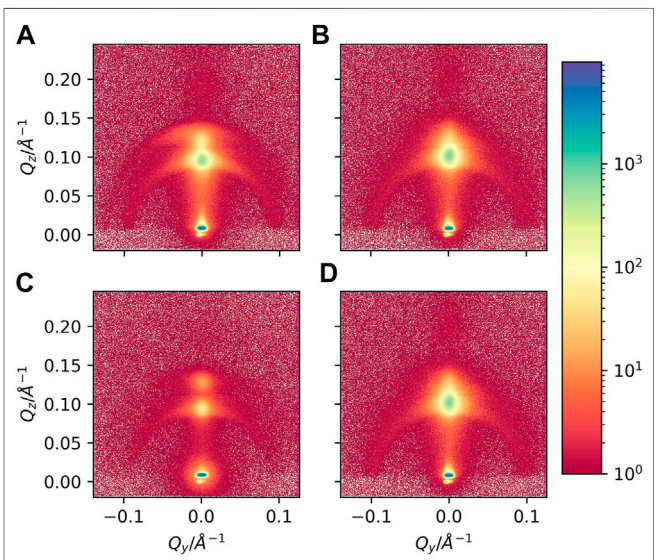

FIGURE 7 | Representative GISANS images of samples with 1 M NaCl (**A**: 16.4°C and **B**: 37.1°C) and 2 M NaCl (**C**: 16.4°C and **D**: 37.1°C).

shown in **Figure 6**. From those data it is apparent the thickness of the single lipid layer is constant with respect to temperature. The most pronounced difference is visible for the water/lipid interface, where the headgroup of the phospholipid is located. There a pronounced step is visible for the 2 M NaCl sample at low

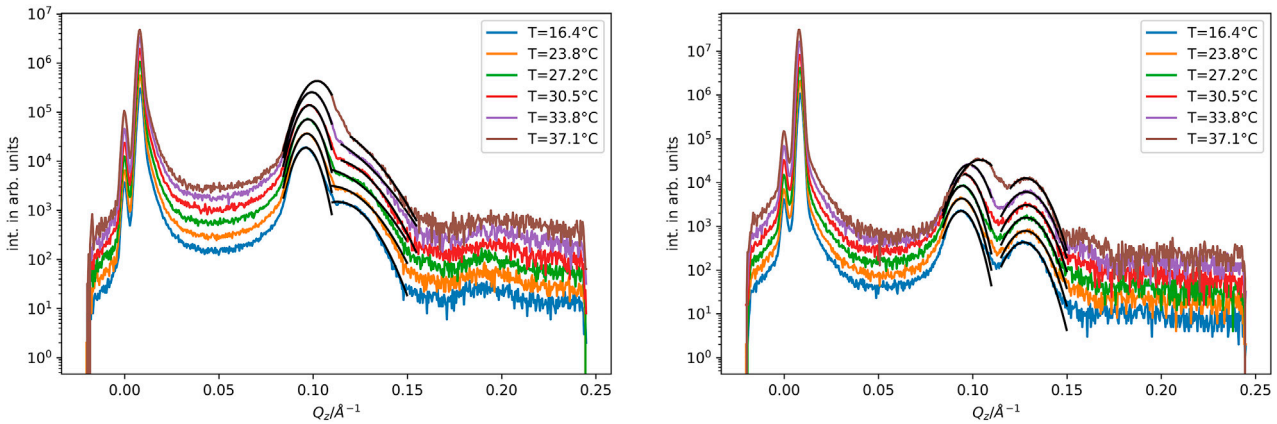

FIGURE 8 | Vertical line cuts of the 2D GISANS data, taken at $Q_y = 0$ for 1 M **(left panel)** and 2 M **(right panel)** NaCl concentration. Black lines are Gaussian fits to extract peak positions. Curves are shifted along the intensity axis for clarity of the presentation.

temperatures, while there is an additional undulation in case of high temperatures. The 1 M NaCl sample and the sample without salt do not exhibit this additional step, but have a single step between the SLD of the phospholipid and water region respectively.

GISANS

In addition to the reflectometry measurements probing structure information along the surface normal, GISANS measurements allow to probe in-plane features [29]. Such in-plane features could hint at an additional order or a phase transition in the in-plane direction. Representative GISANS data are shown in **Figure 7**.

In the GISANS data, the only off-specular features are Debye-Scherrer rings. This observation clearly indicates, that apart from a slight disordering of the membrane stack in-plane, there is no structure formed upon the addition of NaCl salt. The additional secondary peak slightly above the primary lamellar peak is more pronounced at low temperatures. For 1 M salt concentration it is hard to be distinguished and only visible at low temperatures, while it is more pronounced and visible at all temperatures for the 2 M salt concentration. In addition, the secondary lamellar peak is visible. This secondary peak is extremely weak, but still an excellent guide to find the correct lamellar distance. For such a weak peak, splitting is impossible to see, so we use it only to identify the primary peak position, which otherwise is challenged by the additional splitting. This approach also helps to identify the correct peak position for the reflectivity data, which is apparently the one at lower Q-values. The distances extracted from vertical line cuts of the 2D GISANS data (**Figure 8**) confirm the distances obtained from the reflectometry data.

One difference between the reflectometry and vertical line cut data is the relative intensity of the secondary peak, which we attribute to the peak-splitting caused by SLD-variations close to the head-group of the phospholipids. Due to the different collimation conditions for reflectometry and GISANS the interplay between those two peaks is considerably more complex in the GISANS case, where an overlap of the two peaks occurs due to no collimation slits after the sample. This leads to a slight apparent shift of those peaks, as well as to a difference in relative intensity when compared with the peak at lower Q-values.

TABLE 2 | Parameters used to calculate curves for the GINSES description. Only viscosity is fitted. Within the errorbars, the remaining parameters returned to the given values taken from the previous publication.

parameter	No salt (reproduced from previous paper)	2 M NaCl
B/Pa	$3.4\ 10^6$	$3.4\ 10^6$
γ/N m	0.01	0.01
η_3/Pa s	0.00765	0.0023 ± 0.00044
κ/k_B T	22.4	22.4
d/Å	60	60

GINSES

In the GINSES measurements, we compare measurements of SoyPC membrane stacks without NaCl in the D_2O solvent, and those with a 2 M NaCl concentration.

The respective data is shown in **Figure 2**. Both experiments were performed at physiological temperatures (37°C) and, apart from the presence of salt in the solvent, identical conditions with a scattering vector of $Q = 0.106\ Å^{-1}$ and an in-plane scattering vector of $Q_{in\text{-}plane} = 0.0072\ Å^{-1}$. It is immediately apparent that the most prominent feature is the fast decay below $\tau = 1$ ns for the sample with the 2 M salt concentration. We are able to fit the data with exactly the same parameters as in our previous publications for both samples [16, 17]. This evaluation was based on a theory by Romanov et at [30] and treated the membrane stack as a number of elastic layers close to a solid substrate, where wave modes govern the dynamic behavior of the membrane.

Romanov et al. solved the coupled equations of motion for infinitely thin membranes adjacent to a solid substrate, based on the assumption of a smectic liquid crystal, where thermal fluctuations (displacement forces), restoring forces and coupling between the membranes were considered. The coupling between the membranes was effected by elastic and

viscous forces, which then related to the bulk viscosity and compressibility. NB, the bulk viscosity is different from the layer sliding viscosity η_3, which was the layer sliding viscosity of the membranes along each other.

The only parameter that changed between the two fits is the in-plane viscosity η_3. All other parameters were directly taken from our previous publication and are shown in **Table 2**. These parameters were not fitted, however if left free reverted to similar values. Thus, the difference in dynamic behavior can be attributed solely to a change in the viscosity of the system along the membrane surface. The value of $\eta_3 = 0.0023$ Pa s is approximately a third of the value for the salt-free system.

DISCUSSION

We investigated the influence of NaCl salt concentration on the structure and dynamical behavior of phospholipid membrane systems (SoyPC) using neutron reflectometry, GISANS and GINSES.

Concerning the structure, the major impact of introducing NaCl into the system happens around the headgroup of the phospholipids. While for 1 M salt concentration the splitting of the primary lamellar peak is still difficult to be distinguished in the reflectometry data, in GISANS the splitting is more prominent, due to the different collimation conditions. We attribute this splitting to the onset of enrichment of ion-counter ion pairs along the head groups of the phospholipid.

Increasing the NaCl concentration to 2 M leads to a very prominent peak splitting and we find an enrichment of ion-counter ion pairs at the interface between the phospholipid and the D_2O. This finding is corroborated by the temperature behavior of the SLD-undulation at the interface. The much smaller ions are a lot more mobile at higher temperatures, leading to a more distinctive ion-counter ion pair at higher temperatures causing a sharper contrast than at lower temperatures. A similar behavior has been observed in MD-simulations, where the sodium ions were mostly located at the head group of the phospholipid and the chlorine ions were mostly located in water directly adjacent to the phospholipid layer and did not change the overall structure of the membrane [31, 32]. The increase of the layer thickness upon addition of NaCl to PC multilayers, as reported in another study, cannot be confirmed by our data [21]. We assume that the change in thickness was attributed to the choice made which of the two split peaks was chosen for a simple single peak to double layer thickness correlation in the previous work. In the present work, however, we show that this splitting can be attributed to the difference in structure of the interface, due to the NaCl ion-counter ion pairs at the head groups of the phospholipids, and that it is not necessary to include an additional assumption about double layer distance to interpret the data, which is continuously evolving with temperature in a manner consistent with literature [33–35]. The change in thickness as can be expected from the phase changes (essentially a phase transition of the tail groups from liquid crystalline to liquid) is as pronounced (approx. 4 Å in each instance) as is the effect of the NaCl concentration.

We attribute the more pronounced difference between low and high temperature concerning the structure close to the head group-water interface, which is nearly negligible for 1 M NaCl concentration and only visible for the 2 M NaCl concentration to the more pronounced coordination as reported by Böckmann et al. [31]. Not only does this make a the more pronounced wriggling (instead of the nearly box-like profile for 1 M NaCl) at 2 M NaCl better understandable, but also the temperature sensitivity, since the coordination as such is a transient state and therefore more sensitive to thermal excitation.

The GINSES results corroborate the findings from our previous publication, in that without additional fitting the case of the salt-free sample can be reproduced within the experimental uncertainty. In addition, by only adjusting the in-plane viscosity η_3 to a lower value, the measurements of a sample with a 2 M NaCl concentration are reproduced very well. This compares to bulk values from literature, where the viscosity of pure water also changes upon the addition of NaCl from 1.002 Pa s to 1.250 Pa s for a 2 M salt concentration [36]. Thus, it can be seen, that even though the viscosity for bulk water increases, the interface effect seems to dominate, such that the sliding of the membranes against each other is facilitated by the ion-ion interaction and the in-plane viscosity decreases. In addition, a higher coordination as reported by Böckmann et al. [31] for higher NaCl concentrations improves the in-plane ordering, which might facilitate the sliding of two membranes against one another. Since the bulk viscosity of water is changing a lot weaker than the in-plane viscosity, and in the opposite direction, we assume this a structural effect due to the influence of the ordering of the membranes.

This allows also to understand the interplay between the dynamics and the structure of the sample. Since the NaCl ion-counter ion pairs are located at the water-phospholipid interface they can also be expected to have a profound impact of the viscosity of these layers against each other. Essentially, they decrease the resistance of the water layer against sliding along the phospholipid layer.

Due to experimental limitations (each GINSES curve takes 3–4 days without setup) we are not able to test this behavior as a function of temperature, but from the present data it seems reasonable to assume that the location and interpenetration of the phospholipid headgroups and the ion-counter ion pairs change their mobility in the surface as they also change their spatial arrangement.

Summarizing, this study shows both the influence on the structure of phospholipid membranes upon the addition of NaCl salt. The principal effect of salt addition is the incorporation of ions close to the headgroup-water interface, which is to be expected, since there they find the highest charge density in the overall system. This is in line with the very short ranged dipolar field of the zwitterionic head group that is barely shielded by NaCl ions on long ranges but has short range compensations [37] compared to isolated ions in the Debye-Hückel [38] theory ($\kappa^{-1} = 2.2$ Å). So the only effect of the NaCl ions is on the viscosity of the water and only weakly changes the dipole field effect on the bending rigidity in contrast to simply charged head groups [39, 40]. This can be understood as the small-scale analogue of rough surfaces sliding against each other. As soon as the roughness of the surface is overcome by a lubricant, even if this effect is small compared to the overall thickness, there is a profound impact on the overall system.

This behavior has also been observed in MD simulations [31]. Such a change in the structure, and the location of the ions, then

lead to a distinctly different dynamic behavior. The previously postulated dynamic surface mode is still present and can be reproduced in our newer measurements. Moreover, by changing only the in-plane viscosity and keeping all other parameters constant, the behavior of the membrane can be correctly described. This finding strongly supports both the existence of the surface mode and their description and treatment using the Romanov theory.

It is interesting to speculate, what impact this surface mode has on the *in vivo* behavior of biological membranes. Since this surface mode seems to be universally present and the Romanov model also develops predictive powers. The extent to which such modes play a role in the functioning of living organisms is intriguing and warrants and requires substantial further research.

DATA AVAILABILITY STATEMENT

The original contributions presented in the study are included in the article, further inquiries can be directed to the corresponding author.

AUTHOR CONTRIBUTIONS

SJ planned and conducted the experiments, performed data analysis and was primary author of the manuscript. OH, HF, AK, and PZ planned and conducted the experiments, participated in data analysis and the writing of the manuscript. DH, SF and PM-B participated in data analysis and the writing of the manuscript.

FUNDING

This research was carried out on internal funding of the Jülich Center for Neutron Science institute. PM-B acknowledges funding by German Research Foundation (MU 1487/).

ACKNOWLEDGMENTS

The authors acknowledge being awarded beamtime by the JCNS on the MARIA and SNS-NSE instruments.

REFERENCES

1. Cevc G. Drug Delivery across the Skin. *Expert Opin Investig Drugs* (1997) 6(12):1887–937. doi:10.1517/13543784.6.12.1887
2. Touitou E, Dayan N, Bergelson L, Godin B, and Eliaz M. Ethosomes - Novel Vesicular Carriers for Enhanced Delivery: Characterization and Skin Penetration Properties. *J Controlled Release* (2000) 65(3):403–18. doi:10.1016/s0168-3659(99)00222-9
3. Butt H-J, Cappella B, and Kappl M. Force Measurements with the Atomic Force Microscope: Technique, Interpretation and Applications. *Surf Sci Rep* (2005) 59(1–6):1–152. doi:10.1016/j.surfrep.2005.08.003
4. Constantin D, Brotons G, Salditt T, Freyssingeas E, and Madsen A. Dynamics of Bulk Fluctuations in a Lamellar Phase Studied by Coherent X-Ray Scattering. *Phys Rev E* (2006) 74(3):31706. doi:10.1103/physreve.74.031706
5. Pabst G, Katsaras J, Raghunathan VA, and Rappolt M. Structure and Interactions in the Anomalous Swelling Regime of Phospholipid Bilayers†. *Langmuir* (2003) 19(5):1716–22. doi:10.1021/la026052e
6. Safinya CR, Roux D, Smith GS, Sinha SK, Dimon P, Clark NA, et al.Steric Interactions in a Model Multimembrane System: a Synchrotron X-Ray Study. *Phys Rev Lett* (1986) 57(21):2718–21. doi:10.1103/physrevlett.57.2718
7. Safinya CR, Sirota EB, Roux D, and Smith GS. Universality in Interacting Membranes: the Effect of Cosurfactants on the Interfacial Rigidity. *Phys Rev Lett* (1989) 62(10):1134–7. doi:10.1103/physrevlett.62.1134
8. Salditt T. Thermal Fluctuations and Stability of Solid-Supported Lipid Membranes. *J Phys Condens Matter* (2005) 17(6):R287–R314. doi:10.1088/0953-8984/17/6/r02
9. Malaquin L, Charitat T, and Daillant J. Supported Bilayers: Combined Specular and Diffuse X-Ray Scattering. *Eur Phys J E* (2010) 31(3):285–301. doi:10.1140/epje/i2010-10578-2
10. Reusch T, Mai D, Osterhoff M, Khakhulin D, Wulff M, and Salditt T. Nonequilibrium Collective Dynamics in Photoexcited Lipid Multilayers by Time Resolved Diffuse X-Ray Scattering. *Phys Rev Lett* (2013) 111(26):268101. doi:10.1103/physrevlett.111.268101
11. Schneck E, Rehfeldt F, Oliveira RG, Gege C, Demé B, and Tanaka M. Modulation of Intermembrane Interaction and Bending Rigidity of Biomembrane Models via Carbohydrates Investigated by Specular and Off-Specular Neutron Scattering. *Phys Rev E* (2008) 78(6):61924. doi:10.1103/physreve.78.061924
12. Jaksch S, Koutsioubas A, Mattauch S, Holderer O, and Frielinghaus H. Measurements of Dynamic Contributions to Coherent Neutron Scattering. *Colloids Inter* (2018) 2(3):31. doi:10.3390/colloids2030031
13. Jaksch S, Lipfert F, Koutsioubas A, Mattauch S, Holderer O, Ivanova O, et al.Influence of Ibuprofen on Phospholipid Membranes. *Phys Rev E* (2015) 91(2):9. doi:10.1103/physreve.91.022716
14. Armstrong CL, Toppozini L, Dies H, Faraone A, Nagao M, and Rheinstädter MC. Incoherent Neutron Spin-Echo Spectroscopy as an Option to Study Long-Range Lipid Diffusion. *ISRN Biophys* (2013) 2013:439758. doi:10.1155/2013/439758
15. Armstrong CL, Häußler W, Seydel T, Katsaras J, and Rheinstädter MC. Nanosecond Lipid Dynamics in Membranes Containing Cholesterol. *Soft matter* (2014) 10(15):2600–11. doi:10.1039/c3sm51757h
16. Holderer O, Jaksch S, Zolnierczuk P, Ohl M, and Frielinghaus H. Phospholipid Membrane Dynamics at the Solid–Liquid Interface Studied with Grazing Incidence Neutron Spin Echo Spectroscopy. *J Phys Conf Ser* (2019) 1316:012001. doi:10.1088/1742-6596/1316/1/012001
17. Jaksch S, Holderer O, Gvaramia M, Ohl M, Monkenbusch M, and Frielinghaus H. Nanoscale Rheology at Solid-Complex Fluid Interfaces. *Scientific Rep* (2017) 7(1):1–7. doi:10.1038/s41598-017-04294-4
18. Tanaka M. Physics of Interactions at Biological and Biomaterial Interfaces. *Curr Opin Colloid Interf Sci* (2013) 18(5):432–9. doi:10.1016/j.cocis.2013.07.002
19. Fragneto G, and Rheinstädter M. Structural and Dynamical Studies from Bio-Mimetic Systems: an Overview. *Comptes Rendus Physique* (2007) 8(7–8):865–83. doi:10.1016/j.crhy.2007.09.003
20. Jaksch S, Gutberlet T, and Müller-Buschbaum P. Grazing-incidence Scattering-Status and Perspectives in Soft Matter and Biophysics. *Curr Opin Colloid Interf Sci* (2019) 42:73–86. doi:10.1016/j.cocis.2019.04.001
21. Hishida M, Yamamura Y, and Saito K. Salt Effects on Lamellar Repeat Distance Depending on Head Groups of Neutrally Charged Lipids. *Langmuir* (2014) 30(35):10583–9. doi:10.1021/la502576x
22. Jaksch S, Koutsioubas A, Mattauch S, Holderer O, and Frielinghaus H. Long-range Excitations in Phospholipid Membranes. *Chem Phys Lipids* (2019) 225:104788. doi:10.1016/j.chemphyslip.2019.104788
23. Frielinghaus H, Gvaramia M, Mangiapia G, Jaksch S, Ganeva M, Koutsioubas A, et al.New Tools for Grazing Incidence Neutron Scattering Experiments Open Perspectives to Study Nano-Scale Tribology Mechanisms. *Nucl. Instrum. Methods Phys. Res. A* (2017) 871:72–6. doi:10.1016/j.nima.2017.07.064
24. Jaksch S, Holderer O, Gvaramia M, Ohl M, Monkenbusch M, and Frielinghaus H. Nanoscale Rheology at Solid-Complex Fluid Interfaces. *Scientific Rep* (2017) 7(1):4417. doi:10.1038/s41598-017-04294-4
25. Mattauch S, Koutsioubas A, Rücker U, Korolkov D, Fracassi V, Daemen J, et al.The High-Intensity Reflectometer of the Jülich Centre for Neutron Science: MARIA. *J Appl Cryst* (2018) 51(3):646–54. doi:10.1107/s1600576718006994

26. Ohl M, Monkenbusch M, Arend N, Kozielewski T, Vehres G, Tiemann C, et al. The Spin-Echo Spectrometer at the Spallation Neutron Source (SNS). *Nucl Instr Methods Phys Res Section A: Acc Spectrometers, Detectors Associated Equipment* (2012) 696:85–99. doi:10.1016/j.nima.2012.08.059
27. Stroud RM, and Agard DA. Structure Determination of Asymmetric Membrane Profiles Using an Iterative Fourier Method. *Biophysical J* (1979) 25(3):495–512. doi:10.1016/s0006-3495(79)85319-9
28. Li M, Möller MO, and Landwehr G. Fitting of X-ray or Neutron Specular Reflectivity of Multilayers by Fourier Analysis. *J Appl Phys* (1996) 80(5): 2788–90. doi:10.1063/1.363196
29. Müller-Buschbaum P, Gutmann JS, Cubitt R, and Stamm M. Probing the In-Plane Composition of Thin Polymer Films with Grazing-Incidence Small-Angle Neutron Scattering and Atomic Force Microscopy. *Colloid Polym Sci* (1999) 277(12):1193–9. doi:10.1007/s003960050509
30. Romanov VP, and Ul'yanov SV. Dynamic and Correlation Properties of Solid Supported Smectic-A Films. *Phys Rev E* (2002) 66(6):9. doi:10.1103/physreve.66.061701
31. Böckmann RA, Hac A, Heimburg T, and Grubmüller H. Effect of Sodium Chloride on a Lipid Bilayer. *Biophysical J* (2003) 85(3):1647–55. doi:10.1016/s0006-3495(03)74594-9
32. Valley CC, Perlmutter JD, Braun AR, and Sachs JN. NaCl Interactions with Phosphatidylcholine Bilayers Do Not Alter Membrane Structure but Induce Long-Range Ordering of Ions and Water. *J Membr Biol* (2011) 244(1):35–42. doi:10.1007/s00232-011-9395-1
33. Cornell BA, and Separovic F. Membrane Thickness and Acyl Chain Length. *Biochim Biophys Acta (BBA) - Biomembranes* (1983) 733(1):189–93. doi:10.1016/0005-2736(83)90106-2
34. Jaksch S, Lipfert F, Koutsioubas A, Mattauch S, Holderer O, Ivanova O, et al.Influence of Ibuprofen on Phospholipid Membranes. *Phys Rev E* (2015) 91(2):022716. doi:10.1103/physreve.91.022716
35. Lvov J, Mogilevskij L, Fejgin L, Györgyi S, Ronto G, Thompson K, et al.Structural Parameters of Phosphatidylcholine Bilayer Membranes. *Mol crystals liquid crystals* (1986) 133(1-2):65–73. doi:10.1080/00268948608079561
36. Sharqawy MH, Lienhard JH, and Zubair SM. Thermophysical Properties of Seawater: a Review of Existing Correlations and Data. *Desalination Water Treat* (2010) 16(1-3):354–80. doi:10.5004/dwt.2010.1079
37. Ramshaw JD. Debye-Hückel Theory for Rigid-dipole Fluids. *J Chem Phys* (1976) 64(9):3666–9. doi:10.1063/1.432730
38. Debye Pv., and Hückel E. Zur Theorie der Elektrolyte: I. Gefrierpunktserniedrigung und verwandte Erscheinungen; II. Das Grenzgesetz für die elektrische Leitfähigkeit (On the theory of electrolytes: I. Lowering of the freezing point and related phenomena; II. The limiting laws for the electrical conductivity). *Phys Z* (1923) 24:185.
39. Lekkerkerker HNW, Kegel WK, and Overbeek JTG. Phase Behavior of Ionic Microemulsions. *Berichte der Bunsengesellschaft für physikalische Chem* (1996) 100(3):206–17. doi:10.1002/bbpc.19961000305
40. Lekkerkerker HNW. Contribution of the Electric Double Layer to the Curvature Elasticity of Charged Amphiphilic Monolayers. *Physica A: Stat Mech its Appl* (1989) 159:319–28. doi:10.1016/0378-4371(89)90400-7

Conflict of Interest: The authors declare that the research was conducted in the absence of any commercial or financial relationships that could be construed as a potential conflict of interest.

Advantages of publishing in Frontiers

OPEN ACCESS
Articles are free to read for greatest visibility and readership

FAST PUBLICATION
Around 90 days from submission to decision

HIGH QUALITY PEER-REVIEW
Rigorous, collaborative, and constructive peer-review

TRANSPARENT PEER-REVIEW
Editors and reviewers acknowledged by name on published articles

Frontiers
Avenue du Tribunal-Fédéral 34
1005 Lausanne | Switzerland

Visit us: www.frontiersin.org
Contact us: frontiersin.org/about/contact

REPRODUCIBILITY OF RESEARCH
Support open data and methods to enhance research reproducibility

DIGITAL PUBLISHING
Articles designed for optimal readership across devices

FOLLOW US
@frontiersin

IMPACT METRICS
Advanced article metrics track visibility across digital media

EXTENSIVE PROMOTION
Marketing and promotion of impactful research

LOOP RESEARCH NETWORK
Our network increases your article's readership